Flame propagation and autoignition in a high pressure optical engine

by

Zhengyang Ling

BEng MSc

Submitted in accordance with the requirements
for the degree of Doctor of Philosophy

UNIVERSITY OF LEEDS

School of Mechanical Engineering

September 2014

To Mom and Dad

Intellectual Property and Publication Statements

The candidate confirms that the work submitted is his/her own, except where work which has formed part of jointly authored publications has been included. The contribution of the candidate and the other authors to this work has been explicitly indicated below. The candidate confirms that appropriate credit has been given within the thesis where reference has been made to the work of others.

In the following three papers, the candidate completed all experimental studies, evaluation of data and preparation of publications. All authors contributed to proof reading of the articles prior to publication.

Part of Chapter 6 of the thesis is based on a jointly-authored conference extended abstract paper: Zhengyang Ling, A.A. Burluka. **Effect of increased initial pressure on premixed turbulent flame development in SI Engines**, *in the 7th Biennial Meeting for the Scandinavian-Nordic Section*, Cambridge, England, March 27-28, 2014.

Part of Chapter 7 of the thesis is based on a jointly-authored conference paper: Zhengyang Ling, A.A. Burluka. **Self-ignition and knock in normally aspirated and strongly charged SI engine**, *in European Combustion Meeting 2013*, Lund, Sweden, June 25-28, 2013.

Appendix C contains: a jointly-authored paper: Zhengyang Ling, A.A. Burluka, U. Azimov. **Knock Properties of Oxygenated Blends in Strongly Charged and Variable Compression Ratio Engines**, *in SAE 2014 international Powertrain, Fuels&Lubricants Meeting*, Birmingham, UK, October 20-30, 2014. SAE Technical Paper, 2014-01-2608.

The candidate undertook part of PIV data analysis, in particular, probability distribution function and integral length scales calculation in the jointly-authored journal paper:

Burluka, A.A.; El-Dein Hussin, A.M.T.A.; Ling, Z. Y.; and Sheppard, C.G.W., 2012, **Effects of large-scale turbulence on cyclic variability in spark-ignition engine**, *Experimental Thermal and Fluid Science* 43, 13-22.

Acknowledgements

It is unlikely to complete a doctoral dissertation without the help and support of many people. The acknowledgments resulted the hardest part to write, because it was not simple to find the right words to express my gratitude for those people, who support and accompany me throughout these years.

First and foremost, I am grateful to my supervisor, Dr. Alexey Burluka, for his patience and guidance during the writing process and through the period of research. At many stages I have benefited from his advices, especially in the lab for exploring new ideas, and giving me the freedom to pursue my interests in the combustion group.

I would like to thank Dr. Kexin Liu, who introduced me to this exciting group, and Prof. Derek Bradley for valuable advises.

I would like to thank the technical staff in the Thermodynamics Laboratory: Paul Banks, Brian Leach, Mark Batchelor, for the help during the preparation of the experiment.

My gratitude also goes to my PhD colleagues: Graham Conway, Ahmed Faraz, Nini Chen, Dominic Moffat, Richard Mumby. Former research fellows: Dr. Junfeng Yang, Dr. Ulugbek Azimov, Dr. Jin Xiao, for providing me insightful discussions and ideas, and the pleasure of working together. Thanks in particular to Ahmed M. T. A. E. Hussin, who helped me to "survive" in the first year in Leeds and take care of me as a member of family.

I am also grateful to Prof. Heng Cao, and Prof. Qi An at East China University of Science and Technology, for their encouragements throughout my doctoral research. I would not start my PhD study without the fundamental knowledge and skills I learned from them.

I also want to thank many friends: Xianwei Meng, Mingfu Guan, Wei Jiang, Xijin Hua, Yue Zhang, Jun Zhu, Nicolas Delbosc and all members in the Office 2.47. My warmest grateful to Leigang Cao, who is the one I could always call if I need any help.

I wish to thank China Scholarship Council for financial support which enabled me to pursue my studies at University of Leeds.

At last, I will be forever thankful to my parents, Chengzu Ling and Yan Cheng, who always believe in me and give me the best care. Thanks to my love, Rossella Sorte for her love and for the happiness she has brought to my life. Things always become easy when they are around me.

Abstract

"Downsizing" engines with a turbo-charger is considered a promising way to realize the reduction of CO_2 emissions and the improvement of fuel efficiency. Understanding high pressure engine combustion and knock is a prerequisite of developing any "Downsizing" Spark Ignition (SI) engine. Nevertheless, the lack or inconsistent of experimental data about dynamic behaviours of premixed flame and autoignition at elevated pressure hinder further research. The aims of this study are developing an optical experimental boosted spark-ignition engine, and applying advanced diagnostic tools for investigation of flame propagation and autoignition.

In this study, the optical engine LUPOE (Leeds University Ported Optical Engine) was employed, which was supercharged using electronically controlled exhaust valves. The controlled exhaust valves can increase the back pressure and extend the inlet boosting time, to raise the initial pressure without changing the inlet flow rate. This new experimental boosting configuration enables the intake mass flow rate and the initial pressure to be independently varied. New engine control and data acquisition systems also were developed to fulfill the requirements of the high pressure experiments.

This new boosting method has further been deployed to investigate the influence of a highly boosted initial environment (inlet pressure was up to 2.5 bar) on the flame development. These studies have been conducted at almost the same conditions of turbulence intensity. The turbulence intensities, and the integral length scales, were measured by using two dimensional Particle Image Velocimetry (PIV). The turbulent flame development was recorded with high speed CH* chemiluminescence. In addition to the image analysis, "reverse" thermodynamic analysis was applied to derive the in-cylinder charge state and mass burning rate. The results show that an inlet pressure rise from 1.6 bar to 2.0 bar decreases the flame burning velocity weakly. However, it has different effects upon the flame acceleration at the early stage, and flame deceleration when the flame approaches the side walls. Burning velocity still shows a slight raise with the pressure increasing at the "fully developed" stage. The structure of the flame at high pressure and its response to pressure effects also were investigated. A laser sheet visualization technique was applied, and a new image processing algorithm was developed to derive the detailed cross section flame front topology. Wrinkle and curvature of the flame front were characterized to compare the flame shapes under different boosted initial pressures. "Self-similar" properties of flames were evaluated with mean progress variables. The results show that the initial pressure has only a slight effect on the flame structure. Flames at high pressure have the same "self-similar" properties as that observed at low pressure.

Further analysis and modelling of turbulent combustion requires information on the laminar flame speed. In order to gain the iso-octane laminar flame speed at high igni-

tion temperatures and pressures up to 600 K and 15 bar, the LUPOE engine was operated at extremely low engine speeds, i.e. at an engine speed of 100 rpm. A turbulent-free condition was attained and confirmed by PIV measurement, the flame speeds in engine-relevant conditions were collected. By comparing these data with the laminar burning velocities from the correlations calculation and chemical mechanisms simulation, the measured burning velocities could be twice faster than that of unstretched and stable flame. This is possibly caused by flame surface wrinkling, induced by hydrodynamic instabilities at high pressure.

Finally, knock characteristics were examined in the strongly boosted SI engine. Images of different knock development processes provide a detailed understanding of the pressure oscillation in relation to in-cylinder phenomena. It was found that the extreme knock events, observed during the strongly charged operation, occurred at lower pressures, and larger mass fractions burned compared with knock at the normally aspirated operation. The gas dynamics of autoignition, and flame-autoignition interaction played an important role for the pressure oscillations. The reaction front initiated by the autoignition events propagated at velocities much lower than the speed of sound at the extreme knock onset.

Contents

List of Figures

List of Tables

Nomenclature

Roman and Greek Symbols

Symbol	Units	Description
A	m^2,	Area
A	–	Zimont burning velocity model constant
a	m/s	Speed of sound in a gas
α	1/s	Stretch rate
α	m^2/s	Thermal diffusivity
$\bar{c}$	–	Mean progress variable
δ_L	mm	Laminar flame thickness
d	m	Diameter
D	m	Engine bore
D	m^2/s	Mass diffusivity
Da	–	Damkhöler number
ϵ	–	The rate of dissipation of the kinetic energy
f_d	–	Flame acceleration coefficient
f_w	–	Flame deceleration coefficient
I_0	–	Stretch factor
I	–	Image intensity
Ka	–	Karlovitz number
k	m^2/s^2	Turbulent kinetic energy
κ	m^{-1}	Wave number
κ_c	m^{-1}	Curvature rate
L_b	–	Markstein length
Le	–	Lewis number
L_i	mm	Turbulent integral length scale
L_λ	mm	Turbulent Taylor length scale

L_η	mm	Turbulent Kolmogorov length scale
L_a	mm	Flame integral length scale
M_a	–	Markstein number
M	–	Image magnification
P	Pa	Pressure
ϕ	–	Equivalence Ratio
m	kg	Mass
$\dot{m}$	kg/s	Mass flow rate
ρ	kg / m^3	Density
R	J/(mol*K)	gas constant
R_e	mm	Flame entrainment radius
Re	-	Reynolds Number
S_l^0	m/s	Unstretched laminar flame speed
S_f	m/s	Flame speed
S_t	m/s	Turbulent flame speed
S	m/s	velocity magnitude
T	K	Temperature
θ	^{o}	Crank angle
t	s	Time
τ_i	s	Integral time scale
τ_λ	s	Taylor time scale
τ_η	s	Kolmogorov time scale
υ	m^2/s	kinematic viscosity
V	m/s	Flow velocity
U_l	m/s	Laminar burning velocity
U_e	m/s	Entraiment buring velocity
u	m/s	Burning Velocity
u'	m/s	Rms turbulent velocity
u'_k	m/s	Effective rms turbulent velocity
x	m	distance

Abbreviations

aTDC	After top dead centre
bTDC	Before top dead centre

^{o}CA	Degrees of crank angle rotation
CR_{static}	Static compression ratio
$CR_{dynamic}$	Dynamic compression ratio
CCD	Charge coupled device
CMOS	Complementary metaloxide semiconductor
DAQ	Data acquisition
DNS	Direct numerical simulation
ECU	Electronic control unit
EGR	Exhaust gas recirculation
EPC/EVC	Exhaust port closure / exhaust valve closure
FFT	Fast fourier transform
fps	Frames per second
HCCI	Homogeneous charge compression ignition
HWA	Hot wire anemometry
IMEP	Indicated mean effective pressure
IPC/IVC	Intake port closure / intake valve closure
K	Kalghatgi octane index correction factor
LDV	Laser doppler velocimetry
LSPI	Low speed pre-ignition
LUPOE 2D	Leeds university ported optical engine (Mk II) disc configuration
LUSIE	Leeds university spark ignition engine (simulation software)
LUSIEDA	Leeds university spark ignition engine data analysis
MATLAB	Matrix Laboratory
MON	Motor octane number
NTC	Negative temperature coefficient
NA	Naturally Aspirated
ON	Octane Number
PIV	Particle image velocimetry
POD	Proper Orthogonal Decomposition
PLIF	Planar Laser Induced Fluoresence
PRF	Primary reference fuel
rev / min	Revolutions per minute
rms	Root mean square

RON	Research octane number
SI	Spark ignition
TDC	Top dead centre
WOT	Wide open throttle

Subscripts

b	–	Burnt
i	–	Intake
l	–	Laminar
t	–	Turbulent
r	–	Reaction (burnt)
u	–	Unburnt

Chapter 1

Topic introduction and scope of thesis

1.1 Motivation

Internal combustion (IC) engines, the core part of vehicles, have been developed for more than a century. At present, the energy crisis and environmental pollution are two major challenges for their further development. The price of fuel is expected to continue to rise owing to the limitation of crude oil reserves, which will be consumed in a few decades (DoE [2014]). Governments have also strictly legislated the emissions of pollutants from IC engines such as nitrogen oxides, NO_x, carbon dioxide, CO_2, and unburned hydrocarbons, UHC (Sounasis [2013]). Under these financial and political pressures, engine researchers and manufacturers are seeking cost-effective solutions to increase engine efficiency and reduce pollution emissions. More compact engines, which consume less fuel is a direct way to achieve these targets, especially for reducing the CO_2 generation. This is the concept of "Downsizing" engine (Lake et al. [2004]), designed to reduce the engine displacement volume while keeping the same power performance as compared with the initial larger engine. Such decrease of swept volume leads to an improvement in engine efficiency as well as a reduction in CO_2 emissions. Boosting system, such as a turbocharger, is usually employed in the process of engine downsizing to increase the density of the fluid in the inlet above ambient conditions, in order to achieve high specific engine

power output. A reduction in the number, or size, of cylinders also reduces pumping, friction, and heat transfer losses. In the short to medium term, "Downsizing" engine is an efficient way to improve fuel economy with a good cost to benefit ratio (Fraser et al. [2009]).

Flame propagation directly affects the heat release and pressure development in the combustion process in Spark Ignition (SI) engines. A smaller capacity engine with external boosting system means an increase of the in-cylinder pressure during the combustion process [1]. Therefore, demands for improvements in "Downsizing" Spark Ignition engines require major efforts for understanding the fundamental principles of combustion at elevated pressure environments. This includes the aspects of premixed laminar flames and turbulent flames. Although laminar and turbulent premixed flames have been investigated very extensively in the fundamental combustion experiments, such as ones using a constant volume vessel, most of these studies concern combustion at atmospheric or low pressure range (1-10 bar), while combustion phenomena at high pressures, about 20 bar or above related to supercharged SI engines condition are still poorly understood. The previous experimental works concluded that laminar flame speeds were reduced by pressure for typical hydrocarbon-air mixtures, while turbulent flame speeds were increased by pressure (Lipatnikov and Chomiak [2002]). However, these results obtained from various experiments are not consistent, and there are not sufficient data of high pressure flame speeds in supercharged SI engines condition.

Another important area in engine studies is to characterise auto-ignition in SI engines. The further development of a higher compression ratio, boosted engine is limited by abnormal combustion phenomena, such as knock and pre-ignition, which in turn limit the maximum efficiency of the engine. A random heavy knock has been observed in recently strongly supercharged engine experiments (Dahnz and Spicher [2010]), this could cause severe engine damage. With the increasing of initial inlet pressure at low speed, the maximum amplitude of knock pressure tends to be extremely high, compared to the knock combustion pressure in a naturally aspirated engine. Although, these extreme knock events[2] have been recorded in a number of "Downsizing" engine experiments, the mechanism of it is still an open subject.

[1] It may also increase temperature and turbulence intensity.

[2] Previous works referred to these abnormal ignition events as Super Knock (Inoue et al. [2012], Mega Knock (Attard et al. [2010]), or Extreme knock (Dahnz and Spicher [2010]). The term "Extreme knock" was adopted in this study.

1.2 Scope of the current work

This study aims at contributing to the knowledge of the flame propagation and autoignition process in highly supercharged Spark Ignition engines. Although some prototype "Downsizing" Spark Ignition engines have been tested (Attard et al. [2010]; Lecointe and Monnier [2003]; Shahed and Bauer [2009]), and significant amount of data were generated to analyze engine performance, the information on the detailed flame structure and development at elevated pressure in a strongly supercharged engine environment is deficient. For this reason, a study for applying advanced flow visualization and high speed flame imaging methods into an optical boosted experimental SI engine is conducted here, in order to acquire a view inside the combustion and knock phenomena in a supercharged engine.

The first objective of the present work is to develop a new optical boosted engine apparatus. It is based on the single cylinder Leeds University Ported Optical Engine 2D (LUPOE 2D), which could provide a full-bore optical access and a well-controlled mixture composition preparation. LUPOE 2D gas exchange system was designed to avoid complex turbulence flows, in such a way that a growing flame sees a homogeneous flow field, in order to simplify the effects of turbulence on flame growth and put more emphasis on the combustion process.

In order to achieve high pressures in the engine cylinder and avoid complex coupling between the turbocharging and combustion processes, a simulated boosting method is developed to increase the inlet pressure. In the majority of experiments with boosted engines, a high pressure is accompanied by an increase of the inlet flow rate, thus simultaneously high pressure and stronger turbulence may arise at highly boosted conditions. This results in the flame development being affected by both high pressure and turbulence. In order to overcome this problem, a new supercharging method should yield the mean and root-mean-square (rms) flow velocities in the cylinder at the spark timing at the same level while only the pressure increases. Ideally, the supercharged optical engine will also achieve a high peak motoring pressure value, higher than most current optical spark ignition engines.

Consequently, turbulent burning velocities at high pressures with different initial inlet pressure are measured. Under the similar turbulence conditions, effects of highly boosted initial pressure on flame unsteady development, flame structure, and flame brush thickness can be studied. These effects need to be assessed at the different combustion phases i.e. initiation, main phase, and termination phase.

The experimental data derived from the LUPOE 2D engine also can be an ideal test-bed for the validation of advanced turbulent combustion models. For the latter, laminar flame speed is required as an important input parameter. Corresponding experimental values at boosted engine-relevant conditions are not available in the literature. As a consequence, experimental investigations on premixed iso-octane flames are conducted in the LUPOE 2D engine with an extremely low engine speed. It is of interest to see whether or not the optical engine in a turbulence-free environment allows one accurately to measure the laminar flame speed at higher pressures.

Autoignition is also investigated in the LUPOE 2D boosted engine. The high speed images of different modes of auto-ignition with corresponding in-cylinder pressure data provide clues to the onset and development of abnormal combustion in the engines. These observed autoignition phenomena also can be used to deduce those knock events with the similar pressure curve shapes without images from other engines. Further data analysis try to gain insight into the effects of boosted inlet pressure on knock characteristics in strongly supercharged spark ignition engines, in particular, to understand the extreme knock.

1.3 Thesis outline

- Chapter 2 - A literature review includes basic concepts of turbulence, combustion and autoignition in Spark Ignition engines related to this study. The emphases are put on the methods to characterize turbulence flow, the definition of laminar, turbulent flame burning velocities with their measurement issues and a discussion of experimental results in the literature about pressure effects on flame propagation and autoignition.

- Chapter 3 - A detailed description of the developed boosted Leeds University Ported Optical Engine. Two kinds of boosting methods were compared and an exhaust valve design scheme was presented. A new micro-controller based engine control system was also developed. In addition, a brief introduction of LUSIEDA (Leeds University Spark Ignition Engine Data Analysis), a reverse thermodynamic code used to derive the unburned pressure/temperature history from experimental pressure trace is given.

- Chapter 4 - Flow velocities and flame development measurement methods inside the engine cylinder are presented in this chapter. The basic principles of Particle Image Velocimetry (PIV), flame chemiluminescence, and laser sheet visualization

techniques are described, with a description of their experimental operation and data process details.

- Chapter 5 - An attempt to direct measurement of the laminar flame speed from an optical engine with extremely low engine speed is presented in this chapter. The nearly turbulence-free condition was validated by using PIV technique. By comparing the existing laminar flame speed data and correlation equations in the literature to the current experimental data, the accuracy of laminar flame speed measurement in a turbulence-free engine chamber is discussed.

- Chapter 6 - Results of the turbulence flame measurement are presented in this chapter. The performance of designed boosted system was evaluated by using PIV measurement. 5 experimental conditions were selected to compare the effects of pressure on different flame development stages. The detailed flame structures derived from laser sheet images also were investigated.

- Chapter 7 - A number of different autoignition development processes were observed and shown in this Chapter. The reaction front velocities were calculated to clarify if detonation could be generated from a hot spot directly. 4 typical autoignition cycles representing the transition from weakly self-ignition to strong knock were analyzed, based on simultaneously images and pressure data. At last, correlations between knock characteristic parameters were conducted to show the different knock properties in naturally aspirated and strongly boosted engine.

- Chapter 8 - The conclusions of the present work are summarized, together with recommendations for future studies.

Chapter 2

Background to SI engine combustion

Presented in this Chapter is the literature review of basic concepts of turbulence, premixed flame, and autoignition. Following, the prior optical spark ignition engines for characterization of combustion are compared. Autoignition and knock in a spark ignition engine are influenced by the pressure and temperature in the end portion of the unburned gas, these are governed by the turbulent flame propagation. Therefore, a deep understanding of combustion processes in-cylinder, such as the flow structures, laminar and turbulent flame propagation, and stability of flame, is a prerequisite to the understanding of autoignition and knock phenomena. In this Chapter, the above-mentioned concepts are discussed with a particular emphasis on the processes at elevated pressure related to supercharged engines.

2.1 Turbulence

The knowledge of turbulence is a starting point to understand turbulent combustion. Turbulence itself is one of the remaining few unresolved and important problems in classical physics. Turbulent flow is a complex natural phenomenon containing a wide range of vortice scales; they are chaotic in nature (Tennekes and Lumley [1972]). According to Kolomogorov′s theory on eddy cascade hypothesis for homogeneous and isotropic turbulence (Mathieu and Scott [2000]), turbulence might be characterized by a wide range of size of eddies which are generated from large eddies and broken up into smaller eddies. The smallest eddies dissipating during this process are dominated by the viscous forces.

Turbulent flow is referred to as homogeneous when its mean properties do not vary with position. This means that measurements taken at one position are statistically equivalent to measurements taken at any other position. Isotropic turbulence is when the turbulence has no preferential direction. This implies that measurements taken with one particular probe orientation are statistically indistinguishable from measurements taken with any other probe orientation (Mathieu and Scott [2000]).

The turbulence in an engine is greatly determined by the engine geometry and breathing system design (Tabaczynski [1976]). During engine air charging process, the inlet system usually generates two types of large scale turbulent flow: swirl and tumble (Heywood [1988]). The swirl is a rotation of the bulk air around the cylinder axis, while the tumble is a rotation of the air charge around the axis which is normal to the cylinder axis. Thereafter, these large bulk air structures are decaying and dissipating into small scale eddies during the compression stroke. These eddies have a major influence on early flame kernel growth and flame propagation. Strong turbulence can lead to an increase of flame speed, resulting in faster burning velocity and reduction of the cyclic variability (Hill and Zhang [1994]). It also can benefit for the extension of lean combustion operation range. Nevertheless, excessively strong turbulence can quench the flame ([Bradley et al., 1992]). In some experimental engines, the breathing system was designed to eliminate the significant bulk flow motion, e.g. swirl or tumble, as well as the flow was nearly isotropic and homogeneous near the end of compression process (Atashkari [1997]).

This section briefly describes and introduces measures of turbulence. Turbulent flow velocity changes continuously in a wide range of length and time scales. Methods using statistics are therefore required to describe and characterize the turbulent flow, including mean velocity, root mean square (rms) turbulent velocity, and various length or time scales.

2.1.1 Reynolds decomposition of velocity

The instantaneous fluid velocity $U(t)$, can be split into mean $\bar{U}(t)$ and fluctuating component $u(t)$ in what known as Reynolds decomposition as follows:

$$U(t) = \bar{U}(t) + u(t) \tag{2.1}$$

The mean velocity can be calculated in a number of different ways. If the flow is considered steady, the mean velocity is time independent and is described as follow:

$$\bar{U} = \lim_{\tau \to \infty} \frac{1}{\tau} \int_{t_o}^{t_o+\tau} U dt \tag{2.2}$$

The fluctuating component can be calculated as root-mean-square quantities:

$$u' = \lim_{\tau \to \infty} \left[\frac{1}{\tau} \int_{t_o}^{t_o+\tau} (U - \bar{U})^2 dt \right]^{1/2} \tag{2.3}$$

u' usually is defined as "turbulent intensity"[1]. By summing the square of turbulent intensities from each of the orthogonal components, turbulent kinetic energy per unit mass of fluid can be obtained:

$$k = \frac{1}{2} \left(u'^2_x + u'^2_y + u'^2_z \right) \tag{2.4}$$

An illustration of the Reynolds decomposition is shown in Figure 2.1. Nevertheless, it is hard to find a steady or isotropic flow in the reciprocated engines because of additional nearly periodic motion introduced by valves and piston movement. A discrete average process can be adopted in this situation (Heywood [1988]; Stone [1999]). An instantaneous turbulence velocity in the i_{th} cycle at crank angle θ can be decomposed as follows:

$$U(\theta, i) = \bar{U}(\theta, i) + u(\theta, i) \tag{2.5}$$

where $\bar{U}(\theta, i)$ and $u(\theta, i)$ are the mean and fluctuating components of the instantaneous velocity. The ensemble-averaged velocity is defined as:

$$\bar{U}_{EA}(\theta) = \frac{1}{N_c} \sum_{i=1}^{N_c} U(\theta, i) \tag{2.6}$$

where N_c is the total number of cycles used in the average calculation.

[1]Strictly speaking, the term of "turbulence intensity" should be $u'/\bar{U}$. However, this definition cannot be applied in the flow where mean velocity tends to be zero.

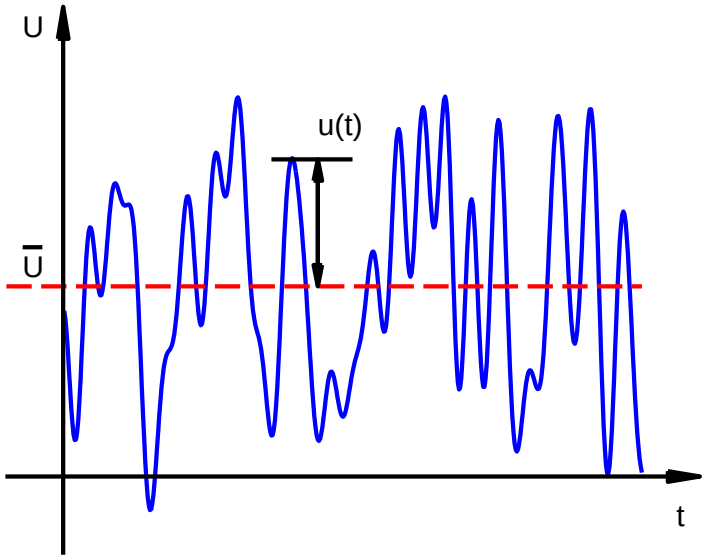

Figure 2.1: Reynolds decomposition for time dependent flow.

The Reynolds number, which evaluates the effects of inertial forces and molecular viscous forces, is widely used to characterize a flow:

$$\mathrm{Re} = \frac{u' L_i}{\upsilon} \tag{2.7}$$

where u' is the root mean square (rms) velocity, υ is the kinematic viscosity of the flow. L_i is the integral length scale which will be introduced in the following section [1].

A large number of turbulence measurement experiments have been done in internal combustion engines (Lancaster [1976]; Roudnitzky et al. [2006]). In a reciprocating engine, in-cylinder turbulence is usually not homogeneous, nor isotropic. Bulk air flow such as swirl and tumble could be generated by the inlet valves, piston, as well as the cylinder walls. The mean flow velocities and turbulence intensity have a high value during induction, and decrease after the intake valve closure (Stone [1999]). It was found that the turbulence intensity tended to be homogeneous in the ported engine, and isotropic in both the ported and valved engines without swirl at the Top Dead Centre (TDC). The magnitude of turbulence intensity is strongly related to mean piston speed and the breathing configuration. Without swirl, the turbulence intensity in a valved engine is slightly smaller than that in a ported engine near TDC (Liou et al. [1984]). Extremely

[1] Reynolds number also can be represented using Taylor length scale L_λ, Kolmogorov length scale L_η.

thin boundary layer regions could be created by the interaction between turbulence and engine walls (Pierce et al. [1992]).

2.1.2 Turbulent length scales

Three length scales are usually used to characterize the size of eddies in turbulent flow: integral length scale, L_i, Taylor length scale, L_λ and Kolmogorov length scale, L_η (Mathieu and Scott [2000]). The definition of these length scales does not have really a precise number, but rather an order of magnitude. The integral length scale is an indication of the large eddies, which contains most of the kinetic energy within the flow. It is defined as the integral of two-point velocity correlation over space:

$$L_i = \int_0^\infty R(r)dt \tag{2.8}$$

where $R(r)$ is the spatial velocity correlation of fluctuating component varying between two different positions. It can be represented as:

$$R(r) = \frac{\overline{u(x)u(x+\delta r)}}{u'(x)u'(x+\delta r)} \tag{2.9}$$

where u' is the fluctuating component of velocity, x is the position in the flow, δr is the offset displacement from point x. The corresponding integral time scale τ_i is simply calculated as:

$$\tau_i = u'/L_i \tag{2.10}$$

Most of the turbulent kinetic energy is generated at the order of the integral scale by the turbulent process, and it is independent from the fluid viscosity. In internal combustion engines, the integral length scale usually depends upon the engine piston bore size and clearance height (Tabaczynski [1976]).

The separation vector between the two points at which velocity correlation is considered, may be aligned with the direction of the velocity components. In this case, the resulting length scale is referred to as longitudinal L_{il} . When the separation vector is normal to the velocity components, the length scale is termed as transverse L_{it} integral scale (Hinze [1975]). This is illustrated in Figure 2.2. The relationship between two integral scales in the case of isotropic and homogeneous flows is:

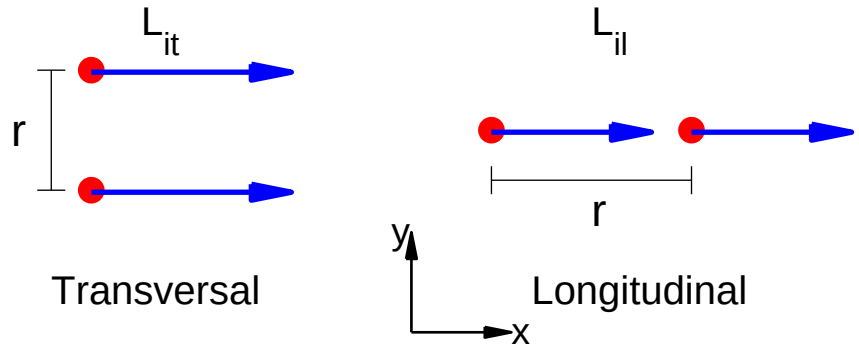

Figure 2.2: Transversal and longitudinal spatial velocity correlations.

$$L_{il} = 2L_{it} \tag{2.11}$$

The autocorrelation function at zero separation can be expanded in a Taylor series to define a further length scale as follows:

$$R(r) = 1 + r\frac{dR}{dr}\bigg|_{r=0} + \frac{r^2}{2!}\frac{d^2R}{dr^2}\bigg|_{r=0} + ... \tag{2.12}$$

Higher order terms can be ignored, and the terms given in Equation 2.12 are from a parabolic approximation to R. This length scale refers to the Taylor microscale (Tennekes and Lumley [1972]):

$$L_\lambda = -\frac{1}{2}\frac{d^2R}{dr^2}\bigg|_{t=0} \tag{2.13}$$

The Taylor microscale L_λ is considered to be a rough measure of the size of the thin shear layer in which viscous dissipation occurs (Mathieu and Scott [2000]). The Kolmogorov length scale L_η represents the smallest eddies surviving at least one characteristic time of its own rotation (Mathieu and Scott [2000]). Its definition is:

$$L_\eta = \left(\frac{\upsilon^3}{\epsilon}\right)^{\frac{1}{4}} \tag{2.14}$$

where υ is the kinematic viscosity, and ϵ is the rate of dissipation of the kinetic energy of the turbulent fluctuation per unit mass of the flow. The relationship between the integral

scales and Taylor, Kolmogorov length scales, can be represented by using the Reynolds number based on the integral length scale (Law [2006]):

$$\frac{L_i}{L_\lambda} = \mathrm{Re}^{\frac{1}{2}} \tag{2.15}$$

$$\frac{L_i}{L_\eta} = \mathrm{Re}^{\frac{3}{4}} \tag{2.16}$$

2.1.3 The spectrum of turbulence

Turbulence can be analyzed using Fourier method to decompose the turbulent fluctuations into sinusoidal components (Mathieu and Scott [2000]). Fourier transform translates the correlation function into a kinetic energy spectrum $S(k)$, representing distribution of a turbulent energy among the different wavelengths and different scales of turbulence. The outcome of Fourier transformation is the density of kinetic energy per unit wave number k. The wave number k is the inverse of the eddy size. The one dimensional frequency power spectral density is defined as:

$$S(k) = \frac{1}{2\pi} \int_{-\infty}^{\infty} exp(-itf)R(t)dt \tag{2.17}$$

A dimensionless power spectrum was suggested by Abdel-Gayed et al. [1987], and later improved by Scott [1992] as a function of Kolmogorov length scales by interpolating a large number of data from Laser Doppler Anemometer (LDA) measurements in the Leeds fan stirred bomb vessel for a stoichiometric octane-air mixture. A homogeneous and isotropic turbulence energy spectrum can be calculated by using the following equation:

$$S(k_\eta) = \frac{0.01668\mathrm{Re}_\lambda^{2.5} + 3.74\mathrm{Re}_\lambda^{0.9} - 70\mathrm{Re}_\lambda^{-0.1}}{1 + (0.127\mathrm{Re}_\lambda^{1.5}k_\eta)^{5/3} + (1.15\mathrm{Re}_\lambda^{0.623}k_\eta)^4 + (1.27\mathrm{Re}_\lambda^{0.35}k_\eta)^7} \tag{2.18}$$

An example of this energy spectrum for a turbulent flow of stoichiometric octane-air mixture at $Re_\lambda = 500$ was plotted in the log-log Figure 2.3 using the Equation 2.18. The small wave numbers are related to large scale eddies, which contain most of the energy and contribute most to the transport of momentum, mass and heat. These large scale eddies correspond to the integral scale, and are caused by the boundary conditions of the flow, such as bulk flow in the engine. In the inertial sub-range, the energy spectrum decreases following a slope of $-5/3$, which can be observed in the energy spectrum Figure 2.3.

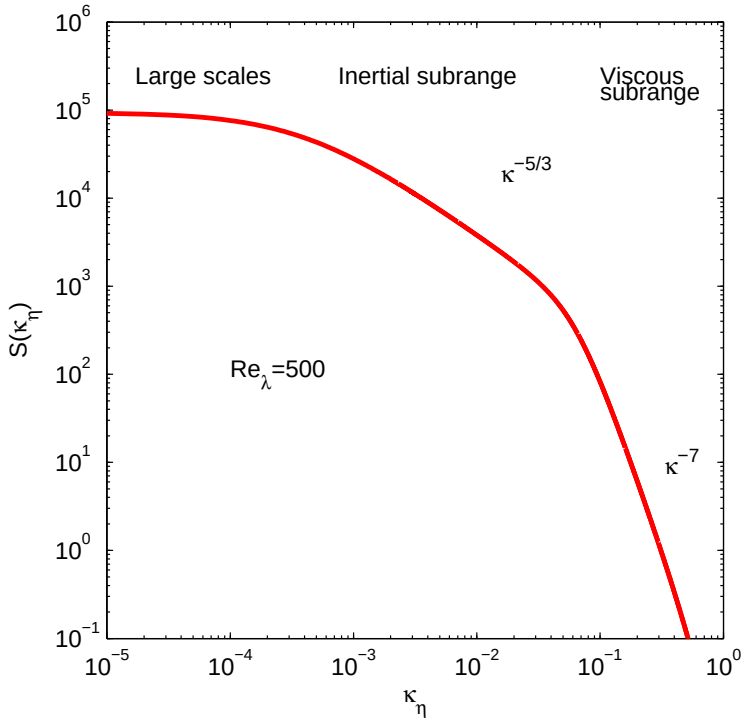

Figure 2.3: Energy spectrum of homogeneous isotropic turbulence using generalized PSD function 2.18 for stoichiometric octane-air based on Kolmogorov length scale.

Turbulent kinetic energy is generated at the large scales, $k \ll 1/L_\eta$, or dissipated at the small scales $k \sim 1/L_\eta$, and it is transferred between different wave numbers for the intermediate k. The smallest Kolmogorov length scales are the most important for energy dissipation. At this length scale, the kinetic energy of the smallest eddies is converted into thermal energy by viscous forces (Mathieu and Scott [2000]).

Following the turbulence spectrum, Abdel-Gayed et al. [1987], proposed an effective turbulence rms velocity u'_k, based on the concept that the initial laminar mode flame kernel is wrinkled by the smallest scales of the turbulence spectrum, while the larger scales vortexes only convect the flame motion. With the flame propagation, the flame experiences the whole spectrum of turbulence, and the turbulent flame develops to its full size. The effective rms turbulent velocity could be obtained by the integral calculation of the power spectral density (PSD) function, against frequency which can be related to elapsed time from spark time, or flame radius development (Scott [1992]).

2.1.4 Influence of pressure on turbulence

Turbulent flow in an engine is usually produced by the breathing system and piston motion. The flow structure and intensity are related to the geometry of the inlet valves for 4 stroke engines and the inlet pipes configuration for 2 stroke engines. Before investigating the pressure effects on turbulence, it is necessary to clarify whether the turbulence is increased by stronger supercharged inlet flow rate, or by pressure. Cruz et al. [2003] found a 10% rise in turbulence intensity when the engine inlet pressure was boosted from 1 bar to 1.5 bar by using calibrated anemometer measurements. Landry et al. [2008] applied Particle Imaging Velocimetry to measure the flow field in an optical single cylinder research engine, and used Proper Orthogonal Decomposition to derive the turbulence intensities and length scales. Both values show a tendency to increase weakly with pressure. However, the observed effects were not strong enough to draw a relationship between turbulence properties and the inlet pressure. Although these researchers have reported that supercharged engines had a higher turbulence intensity, it was not clearly identified whether the increase was generated by the turbocharger or by the raised initial pressure.

The effect of intake charge mass flow rate on the turbulent flow was investigated by Dawood [2010] in a single cylinder two-stroke ported engine. This engine has a similar structure and geometry size with the engine that is used in this study. The results from PIV measurements showed that the inlet flow velocity had greater influence at low engine speed. A 50% increase of inlet flow rate corresponded a 50% increase in mean velocity, and a 25% in Root Mean Square (RMS) velocity. These velocities were measured at TDC position at an engine speed of 750 rpm. This means that the increased turbulence intensity, generated by stronger inlet flow, should be taken into account when the supercharged engine is applied to investigate the pressure effects, especially, if this is a two stroke engine with jet type intakes.

The main pressure effect on turbulence is a decrease of the flow kinematic viscosity $\nu \propto P^{-1}$. This results in an increase of Reynolds number $\mathrm{Re}_l = u' L_i/\nu \propto P$, and in the extension of the energy spectrum to a higher frequency region with smaller eddies, described by the Taylor length scale $L_\lambda \propto L_i \cdot \mathrm{Re}_l^{-1/2}$ and the Kolmogorov length scale $L_\eta \propto L_i \cdot \mathrm{Re}_l^{-3/4}$ (Soika et al. [2003]). An example of this spectra widening was shown in the experiment of Kobayashi et al. [1997], performed with a nozzle-type burner in a high-pressure chamber. The mean flow rate (U = 2.0 m/s), and the turbulent intensity were maintained the same during measurements. It was found that the integral scale tended to remain the same at elevated pressure. Pressure and turbulence intensity u' (rms velocity) had not a linear relationship. Initially, the turbulent intensity decreased

with the pressure, until the latter reached about 1.0 MPa, at which point a further raise of pressure increased u'.

This trend was also observed by Soika et al. [2003]. A premixed bluff-body stabilized burner flame in a high pressure cylindrical chamber was investigated. The inlet flow conditions were well controlled. The premixed flame was ignited at an atmospheric pressure, then an exhaust throttle valve was closed, and the flow mass was increased until the pressure in the chamber reached a desired value. The inlet flow velocity was kept constant during the experiment, thus both the mean flow velocity and turbulent intensity could be thought to be constant when the pressure increased. The flow field was characterized with Laser Doppler Anemometry (LDA). Soika et al. [2003] found that the global flow features were only weakly dependent on pressure. The integral length scale was decreasing when pressure was increased below 0.7 MPa, beyond which it grow with the increased pressure.

In conclusion, it has been shown that the effects of pressure on turbulence are likely to be weak. However,the turbulent flow in a supercharged engine could be affected by both inlet flow rate and pressure. In order to study the pressure effects, the turbulence modification caused by the boosting process, rather than pressure needs to receive attention. This, in particular means the mean velocity and turbulence in the intake flow into the cylinder, plus the pattern of the flow inside the cylinder induced by the intake.

2.2 Combustion

Even though the flame in SI engines is a turbulent flame, laminar premixed flames play a crucial role for turbulent burning velocities. Therefore, this section will introduce the laminar flame phenomena, and a description of turbulent premixed flames. Some concepts such as flame speed, burning velocity, and flame thickness, can be equally applied to explain the turbulent flame.

2.2.1 Laminar premixed flames

A laminar premixed flame is a traveling wave of chemical transformation of fresh gas into combustion products. A simplified structure of unstretched laminar premixed flames can be identified as the preheat zone, the reaction zone, and the product zone, as shown in Figure 2.4 (Griffiths and Barnard [1995]). The unstretched laminar flame speed S_l^0 is usually defined as the velocity of flame front relative to a stationary observer, where

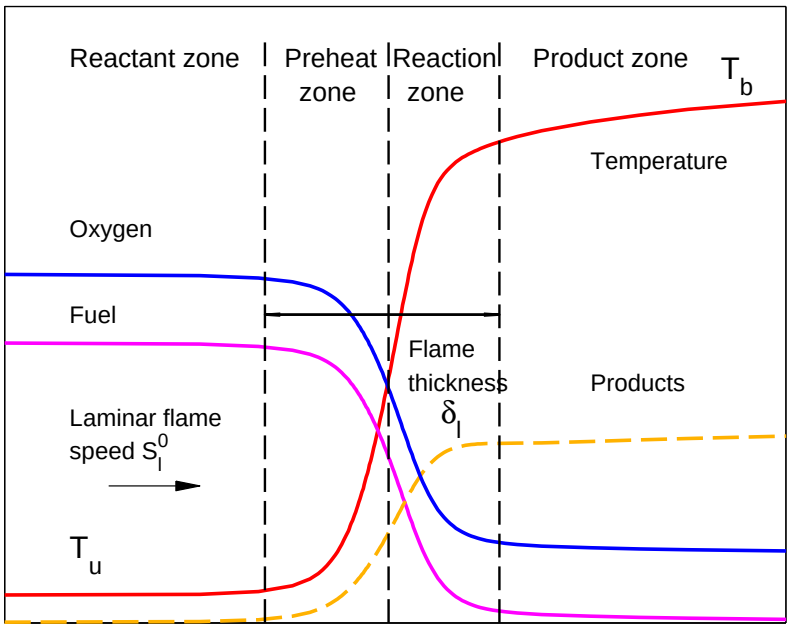

Figure 2.4: Schematic representation of structure of a one dimensional premixed flame.

superscript 0 means that the parameter refers to flame propagating in uniform medium with zero gradients of velocity, temperature or concentration. The flame front follows a preheat zone, where a balance between convection and diffusion exists. The reaction zone is defined as the inner layer, where the fuel is consumed and the radicals are depleted in a usually branched chain reactions. The reaction species such as CH*, C_2*, CHO* are excited to a higher energy level, then they return to a ground state while emitting a certain wavelength light, called flame chemiluminescence. The inner layer temperature is one of the important factors determining the rate of chemical reactions. In the final oxidation layer, primarily CO and H_2 oxidize to CO_2 and H_2O (Griffiths and Barnard [1995]).

The depth of the reaction zone is related to the flame thickness δ_l. Several definitions of flame thickness can be found in the literature (Abraham et al. [1985]). Because the flame reaction zone is thin, the laminar flame thickness can be defined to be approximately equal to the thickness of the preheat zone. A characteristic length can be used to estimate the reaction zone thickness δ_l of flame in the experiment (Bradley et al. [1992]).

$$\delta_l = \nu / U_l \tag{2.19}$$

where ν is the kinematic viscosity and U_l is the laminar burning velocity, which will be introduced in the next Section.

2.2.1.1 Laminar burning velocity

Flame speed and burning velocity are widely used to characterize a flame. In order to illustrate these two definitions, an infinitely thin flame model is usually adopted instead of a finite flame thickness with inner structure. The flame is considered as an interface which separates unburnt and burnt air-fuel mixture at the latter equilibrium state. Figure 2.5 represents both one dimensional steady unstretched laminar infinitely thin flame model, and finite flame thickness model, which is propagating from left to right. The flame speed is assumed to be much lower than the speed of sound. Sub-sonic waves of combustion are sometimes referred to as "deflagration" (Law [2006]). In the infinitely thin flame model the flame front can be represented at iso-level surface, such as temperature or density, the location of which is denoted as x, which usually can be observed directly in the experiment by imaging or schlieren methods. The motion of this flame front over a certain time interval is defined as flame speed S_f in Equation 2.20. It is the speed of this reference surface with respect to the fresh gas:

$$S_f = \frac{dx}{dt} \tag{2.20}$$

This flame propagation speed is the sum of the laminar burning velocity U_l relative to the fresh gas, and the unburned gas's own velocity ν_u:

$$S_f = U_l + \nu_u \tag{2.21}$$

Often the fresh gas velocity ν_u is induced by the thermal expansion of the burnt gas. It should be noted that flame speed is not a fundamental property of fuel, but the burning velocity is. If $S_f = 0$, the flame front remains stationary such as a flame observed in e.g. a Bunsen burner (Rallis and Garforth [1980]). Laminar burning velocity U_l may also be considered as the mass burning rate in the unburnt side U_u per unit flame surface area A, divided by unburnt reactant density. (Rallis and Garforth [1980]).

$$U_l = U_u = \frac{1}{\rho_u}\left(\frac{\dot{m}_u}{A}\right) \tag{2.22}$$

An engine combustion chamber contains unburnt and burnt gases separated by a propagation of spherically infinitely thin flame. The radius of flame is $R(t)$. Because the flame

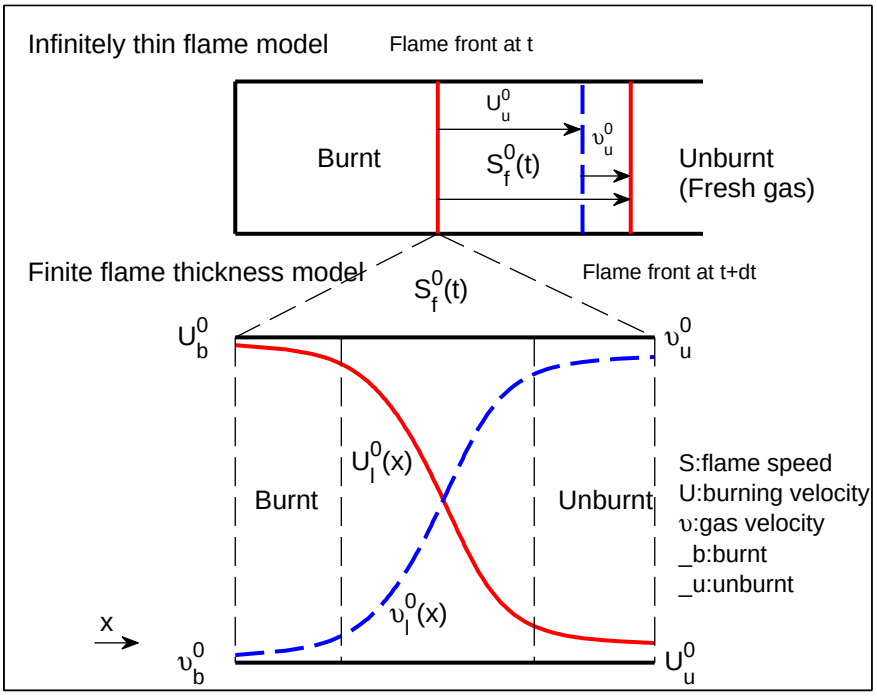

Figure 2.5: Infinitely thin flame model and finite flame thickness model for a one dimensional unstretched flame propagating from left to right.

is subsonic, the pressure non-uniformities dissipate much faster than it propagates, hence the pressure is uniform in the chamber. Mass flows are balanced through the flame front:

$$\dot{m}_u = \rho_u \cdot U_u = \dot{m}_b = \rho_b \cdot U_b \tag{2.23}$$

where $\dot{m}$ is a mass flux per unit flame surface. The subscripts u and b indicate that the parameters refer to the unburnt and bunrnt gas, respectively, thus,

$$U_l = U_u = \frac{\rho_b}{\rho_u} U_b \tag{2.24}$$

By substituting Equations 2.20 and 2.21 in the burnt side into Equation 2.24, we get:

$$U_l = \frac{\rho_b}{\rho_u} \left(\frac{dx}{dt} - \nu_b \right) \tag{2.25}$$

The second item in the bracket is the flow velocity of the burnt gas. Often the burnt gas behind the flame front is stationary or hence a very small velocity, but the expansion of

hot products induces considerable motion of the fresh gas ahead of the flame. Therefore, Equation 2.25 can be simplified with flame radius $R(t)$ as follow:

$$U_l = \frac{\rho_b}{\rho_u}\left(\frac{dR(t)}{dt}\right) = \frac{\rho_b}{\rho_u}S_b \tag{2.26}$$

The exact definition of the laminar burning velocity is important before applying any measurement in the experiment. Equation 2.26 is one possible illustration of how to derive burning velocity from flame radius $R(t)$ recorded by an image acquisition system. Usually, imaging measurement of flame development is employed in constant pressure conditions where pressure change is negligible. An engine burning velocity, can also be calculated from pressure signal, e.g. assuming a linear relationship between the mass fraction of the burnt gas and the pressure rise. Then, a computer model can be used to calculate the burning velocity from pressure information (Marshall et al. [2011]; Metghalchi and Keck [1982]). Generally, pressure rather than images is a direct measurement for burning velocity. However, complexity of models, and a number of input parameters, influenced the accuracy of the final results. In practice, optical techniques are preferred, in fact, image method can provide the geometry information of the flame front and record the initial flame propagation, which is hardly detected by pressure transducer due to the small pressure increase at the beginning.

The another way to measure burning velocity is to make use of Equation 2.21. The second item in Equation 2.21 is the flow velocity in the unburnt side in front of flame, which is usually a large value and can not be neglected. The flow measurement method has been applied to measure directly the gas velocity in front of a flame (Vagelopoulos and Egolfopoulos [1998]), and derive the burning velocity from Equation 2.21. However, the gas velocity is a function of distance from the flame, as shown in the finite flame thickness model, behavior of the burning velocity $U_l(s)$, gas velocity $\nu_l(s)$, and flame propagation velocity $S_f(s)$, is schematically represented as a function of the position in different unstretched flames. Moreover, the spatial resolution of the flow measurement may be not sufficiently high to obtain an accurate velocity. The value of fresh gas velocity is a major part of Equation 2.21, so any imprecise measured of flow velocities would bring a large error in the burning velocity. Therefore, the imaging measurement based on Equation 2.26 will be adopted in this study for both laminar and turbulent flame measurements. The density of unburnt and burnt gas could be calculated from thermodynamic analysis equations with chemical reaction components (Abdi Aghdam [2003]).

2.2.1.2 Flame stretch

One-dimensional flames, described in the previous section, cannot be achieved in practical experimental configurations (Rallis and Garforth [1980]). For example, real flames are often affected by the stretch effects. The stretch rate α can be defined as the time derivative of the flame surface area A and further divided by the area A:

$$\alpha = \frac{1}{A}\left(\frac{dA}{dt}\right) \tag{2.27}$$

For example, for a cylindrical flame of a unit height with radius R, this becomes:

$$\alpha = \frac{1}{A}\left(\frac{dA}{dt}\right) = \frac{1}{2\pi R}\frac{d(2\pi R)}{dt} = \frac{1}{R}S_f \tag{2.28}$$

The equation which relates the stretch rate to flow velocity $\vec{u}$ has been derived in the following form (Law [2006]):

$$\begin{aligned}\alpha &= (\widehat{n}\cdot(\widehat{n}\cdot\nabla)\vec{u} + \nabla\cdot\vec{u}) + S_l\nabla\cdot\widehat{n} \\ &= (\delta_{ij} - n_i n_j)\frac{\partial u_i}{\partial x_j} + S_l\frac{\partial n_i}{x_i} \\ &= \alpha_\tau + \alpha_n + \kappa_c\end{aligned} \tag{2.29}$$

where $\widehat{n}$ is a unit normal outward. α is strain item due to the gradient velocities at the flame surface, and it can be further split into normal straining α_n and tangential straining α_τ. The final item κ_c is the curvature caused by the flame area change during propagation of the curved surface. S_l is the flame speed. The propagating flame surface can be expanded or contracted by the strain and curvature effects under different conditions of curvature, as shown in Figure 2.6.

In the experiment, stretch rate can be obtained from equation 2.28 using flame radius information. It can also be directly measured based on the equation 2.29, where flow field information can be measured. However, 2D flow field measurement will shift the results to a lower value (Lauer and Sattelmayer [2010]), and in order to detect the velocity gradients at the flame front, very high spatial resolution of the velocity measurement is required.

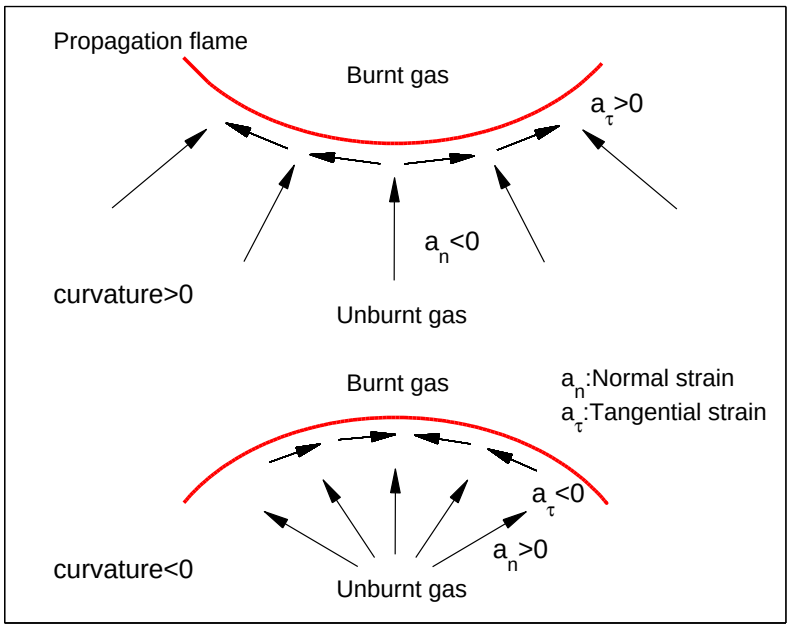

Figure 2.6: Strain and curvature effects on a stretched propagating flame.

The unstretch flame front velocity S_l can be expressed by a linear regression in terms of a Markstein length L_b (Markstein), only for very small stretch rates. The change in the flame speed depending on the stretch rate is given by:

$$S_l - S_n = L_b \alpha \tag{2.30}$$

where S_n is the stretched flame speeds. Markstein number is the Markstein length divided by the laminar flame thickness:

$$M_a = L_b / \delta_l \tag{2.31}$$

The definition of flame front affects both M_a and flame stretch rate. It was found that the burnt edge of a stretched laminar flame is most appropriate to determine the mass burning rate (Groot et al. [2002]). Determination of flame speed and burning velocity at different location within the flame will result in very different values of Markstein length; thus Markstein length for burnt gas, i.e.trailing edge of the flame, is very different from that for fresh gas, i.e. leading edge. This is because of very steeply changing gas velocity (Lipatnikov [1996]). It is also impossible to introduce separate and unique Markstein numbers to characterize the flow straining and curvature, since it changes in different combustion situations (Groot et al. [2002]).

2.2.1.3 Flame instability

At elevated pressures, laminar flames are prone to instability and cellularity; this is likely to result in an increasing flame surface area and enhanced burning velocity. There are also some evidences of "carry-over" of cellularity to turbulent flames (Kobayashi et al. [2002]). However, most studies about flame instability are limited to laminar flame conditions. The cellularity due to flame instability increases the difficulty of accurate measurements of flame speed. There are several mechanisms to explain flame instability: the hydrodynamic instability, also known as Landau-Darrieus (LD) instability, which is caused by thermal expansion from exothermal reaction; diffusive-thermal (DT) instability, due to differential diffusion and disbalance of the temperature or composition in front of flame; and finally Rayleigh-Taylor instability, due to the buoyancy force (Lipatnikov [2013]).

Figure 2.7 shows a thin laminar flame which propagates at a speed S_l subjected to a hydrodynamic flame instability. Due to the expanding hot products, when the flame front becomes concave or convex, the unburnt flow velocity normal to the flame front increases or decreases, respectively. Because of flame surface area change, and the tangential velocity component remaining the same across the flame front, the streamline direction across the flame must be changed. This in turn produces a more wrinkled and cellular flame front.

A disparity between conductive thermal fluxes from the preheat zone, and diffusive mass flux in the reaction zone, leads to thermal-diffusive instability. It highly depends on the Lewis number Le, which is defined as the ratio of thermal conductivity to reactant diffusion (Borghi and Destriau [1998]). Figure 2.8 illustrates schematically the diffusive-thermal unbalance process effects on the local burning velocity with positive and negative curvature. When Le > 1, the heat loss exceeds molecular diffusion, therefore heat loss from the preheat zone is increased by the positive curvature i.e. with the flame convex towards the fresh gas. The flame propagation relies more on the weaker molecular diffusion, and this results in the decrease of the burning velocity. When the curvature is negative, the heat loss from the preheat zone is reduced, thus the reaction rate increases. When Le < 1, the propagation rate is dominated by the molecular diffusion across the reaction and preheat zones, positively curved flames will increase the burning velocity because the flame surface is exposed to a larger area of unburnt reactants, and vice versa.

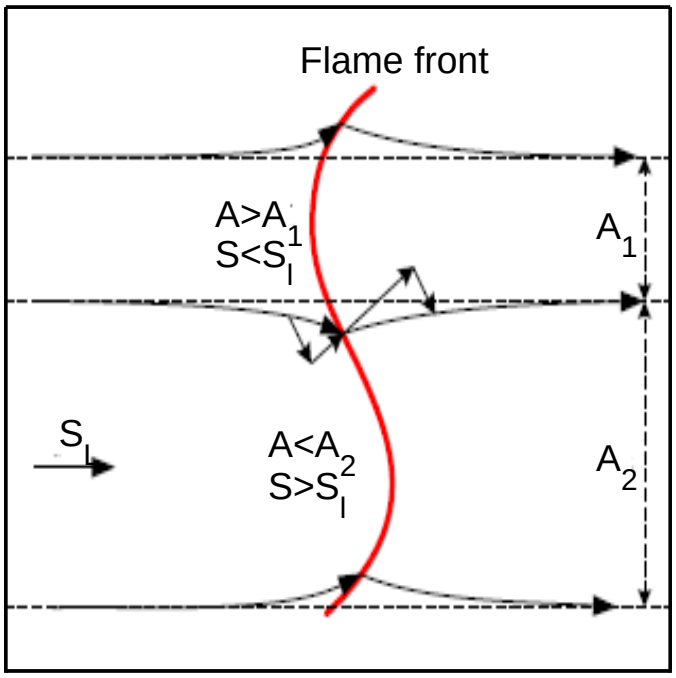

Figure 2.7: Illustration of hydrodynamic flame instability.

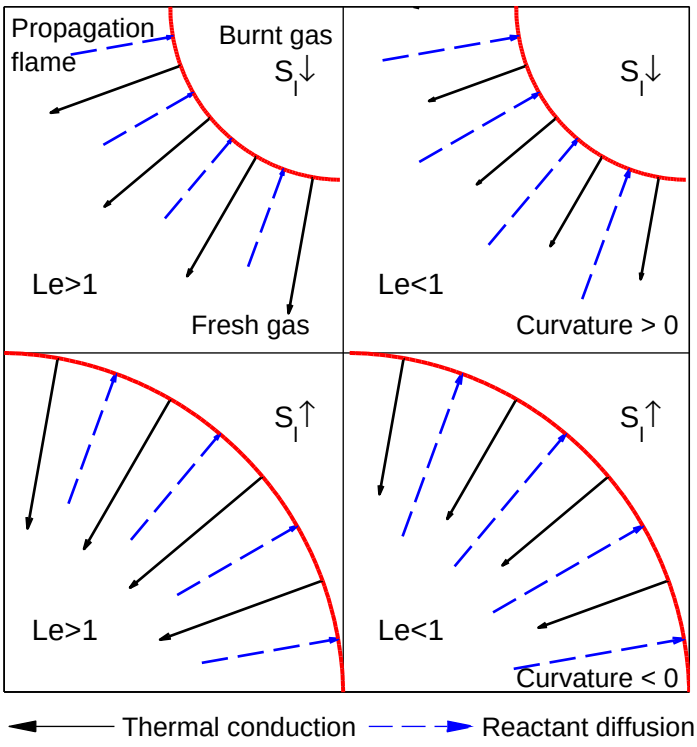

Figure 2.8: Illustration of effects of thermo-diffusion flame instability on laminar propagating flame speeds.

2.2.2 Turbulent premixed flames

Turbulence has been already described in Section 2.1 and the laminar flame structure has been presented in Section 2.2.1. In this Section, the basic concepts of turbulent premixed flames are introduced.

2.2.2.1 Flamelet concept and flame brush thickness

During combustion in SI engine, unburnt and burnt mixtures are separated by the flame front. The aerodynamics of flame front mostly depends on the in-cylinder flow field. A higher degree of turbulence results in a rapid rate of burning due to an increase of flame front surface area and possible modification of the flame structure. Although turbulent burning rates are considerably higher than laminar ones, due to great transfer and mixing of turbulent flow, it is often speculated that turbulent premixed combustion can be described as an array of laminar flame sheets, subjected to stretch and wrinkling in a turbulent flow (Lipatnikov [2013]). If the chemical time scale is shorter than the turbulence integral time scale, the chemistry reaction occurs fast compared to the flow change, it can be supposed that flamelets separate the reacting flow into unburnt reactants and the burnt products as illustrated in Figure 2.9. A flamelet structure is commonly characterized by using the following equation which relates flamelet structure parameters to the turbulent burning velocity S_t (Driscoll [2008]):

$$\frac{S_t}{S_l} = I_o \int_{-\infty}^{\infty} \Sigma d\lambda = I_0 \Sigma_{max} \delta_t \tag{2.32}$$

where Σ is the flame surface area per unit volume. The flame brush thickness δ_t and the stretch factor I_0. S_l is the laminar burning velocity. The interaction of the turbulent flow with flame has two principal and opposing effects on turbulent burning velocity, the turbulent burning velocity increases due to surface area increased by wrinkling, while it is decreased by the effects of flame stretch. The flame brush thickness is a macroscopic parameter defined as a distance between the leading and trailing edges of the flame.

2.2.2.2 Combustion diagram

It has been hypothesized for long time that turbulent combustion can proceed in several regimes. Diagrams defining regimes of premixed turbulent combustion in terms of velocity and length scale ratios have been first proposed by Borghi and Destriau [1998], while

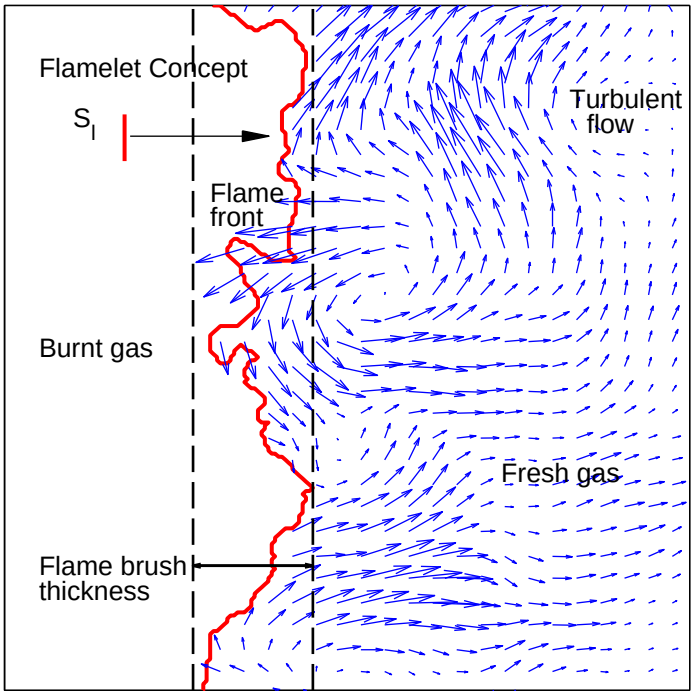

Figure 2.9: Flamelet concept: the turbulent premixed flame consists an array of laminar flame sheets, subjected to stretch and wrinkling in a turbulent flow.

later other scholars presented similar diagrams (Abdel-Gayed et al. [1989]; Chen et al. [1996]; Veynante and Vervisch [2002]). The Borghi combustion regime has been shown in Figure 2.10 with the possible engine combustion region.

In order to describe transitions between the different regimes, two non-dimensional numbers have been defined. These compare the characteristic time and length scales of the chemical reaction to those of the turbulent flow. The Damköhler number describes the ratio of the turbulent τ_t to the chemical τ_c time scales. For turbulent premixed flames, the chemical time scale τ_c, may be estimated as the ratio of the thickness δ_l and the burning velocity U_l of the laminar flame. The turbulent time may be estimated from turbulent integral scale characteristics. The Damköhler number is defined as follow:

$$\mathrm{Da} = \frac{\tau_t}{\tau_c} = \frac{l_l}{\delta_l}\frac{U_l}{u'} \tag{2.33}$$

The flamelet regime, or thin wrinkled flame regime, occurs when the Damköhler number is much large, which means the turbulent flow only distorted and convected the thin

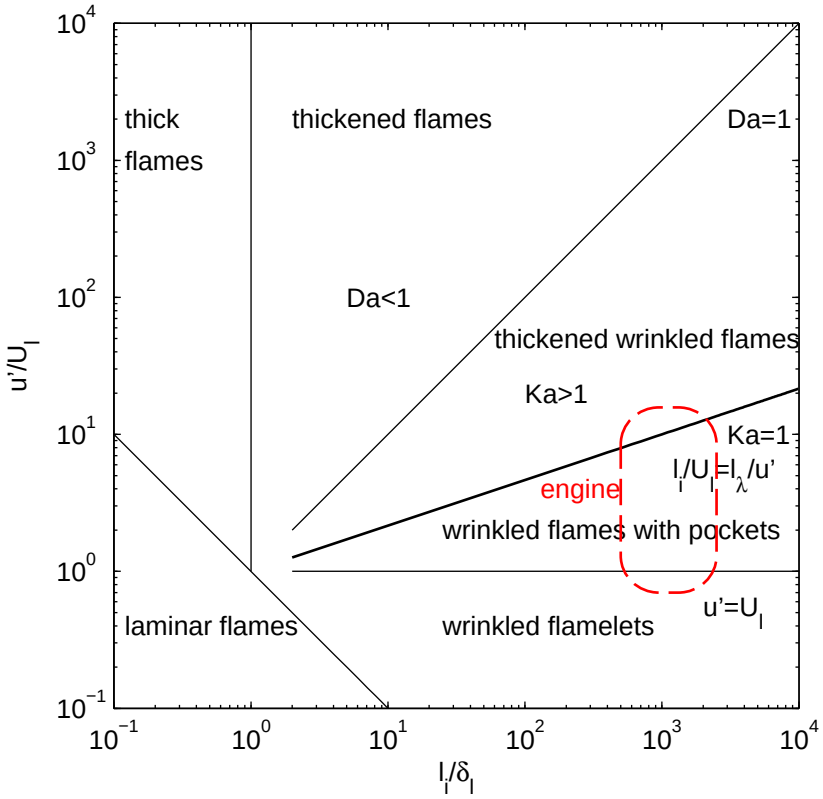

Figure 2.10: Borghi combustion regime diagram with possible engine combustion region.

flame reaction zone. Karlovitz number is defined as the ratio of the chemical time scale to the Kolmogorov time scale (Veynante and Vervisch [2002]):

$$Ka = \frac{\tau_c}{\tau_k} = \frac{\delta_l}{l_k}\frac{u_k}{U_l} = \left(\frac{u'}{U_l}\right)^{3/2}\left(\frac{l_l}{\delta_l}\right)^{-1/2} \tag{2.34}$$

By comparing the chemical time scale τ_c to the Kolmogorov time scale τ_k, different combustion regions can be classified:

- $Ka < 1$: Flamelet regime or thin wrinkled flame regime. Two subdivisions may be proposed depending on the velocity ratio u'/U_l.
  - $u'/U_l < 1$: wrinkled flame. This means the turbulent velocity fluctuations were dominated by the laminar burning velocity U_l. Turbulent eddies are unable to wrinkle flame surface and laminar flame is the predominant flame front propagation.
  - $u'/U_l > 1$: wrinkled flame with pockets ("corrugated flame"). In this regime, the velocities of the large scale eddies are larger than the laminar burning velocity, but the size of smallest eddies are still larger than the laminar flame

thickness, so that eddies are unable to penetrate into the laminar flame structure, leaving chemical and transport processes within the flame structure essentially unchanged.

- $1 < Ka \leq 100$: Thickened wrinkled flame regime or thin reaction zone. In this regime, the smallest eddies are smaller than the laminar flame thickness so that eddies are able to penetrate into the laminar flame structure. But, the smallest eddies are still larger than the thickness of the inner layer so that eddies cannot change the reaction zone.

- $Ka > 100$: Thickened flame regime or well-stirred reactor. In this situation, the smallest eddies are small enough to penetrate into the inner layer, affecting chemical reactions. The premixed flame structure cannot be preserved and local extinction will occur.

2.2.2.3 Flame development and turbulent burning velocity

Combustion in a spark ignition engine is a transient process, both burning velocity and flame brush thickness develop with time after ignition and are influenced by several mechanisms, this process is called flame development (Lipatnikov [2013]).

After spark ignition, a laminar flame would propagate in a smooth spherical manner from the point of ignition. The diffusion mechanism governs the flame propagation and only small eddies can affect it. With the flame developing, the flame surface is wrinkled and distorted by the turbulence, increasing its propagation velocity and brush thickness. The constant burning rate may be observed in a short period before the flame reaches the cylinder walls. This phenomena could be attributed to the flame attaining a "fully developed" state or a balance between flame initial acceleration and the deceleration caused by the interaction of flame and walls (Liu et al. [2013]). At last, the flame speed become slow and quenches when it is approaching the cylinder wall.

Usually, turbulent burning velocities in an engine are referred to the burning velocity at the "fully developed" state. Two definitions of flame burning velocity have been considered by Groff and Matekunas [1980]. One is based on mass rate of entrainment of unburned mixture into the flame (U_e), usually derived from photographic observations (Beretta et al. [1983]). The second definition is related to the rate of production of burnt gas, which is obtained from pressure rise; this may be named mass burning velocity, U_n.

The turbulent burning velocity is the result of the interaction of turbulence and the flame. It is increased by the turbulent wrinkling of the flame, resulting in an en-

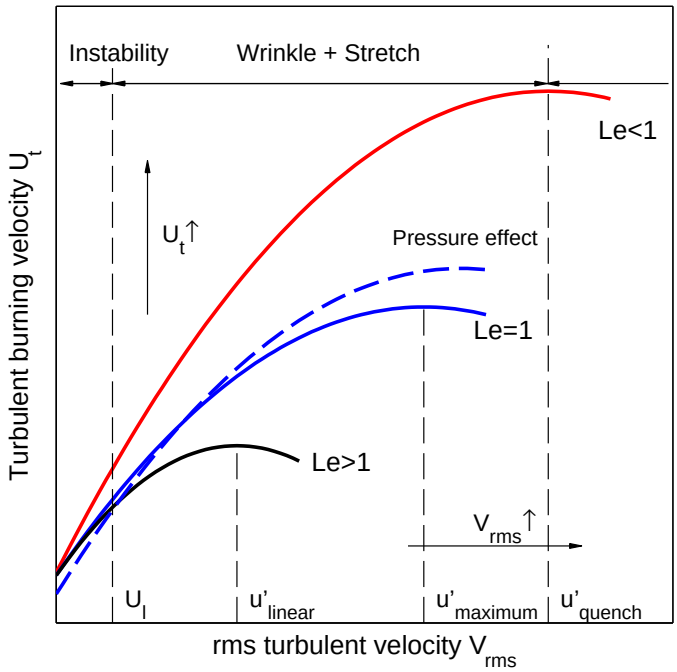

Figure 2.11: The influence of various physical mechanisms on the turbulent burning velocity with root mean square (rms) velocity and the Lewis number Le, reproduced after Lipatnikov [2013].

larged flame surface. However, "collisions and mutual annihilation of self-propagating flamelet " might reduce the surface area (Lipatnikov [2013]). The opposing influence is the flame stretch, which reduces laminar burning velocity. The turbulent burning velocity will increase due to predomination of flame wrinkling, then will tend to decrease, and even partially quench due to flame stretch (Gillespie et al. [2000]), see Figure 2.11. Moreover, turbulent burning velocity may also be influenced by the flame instability. The hydrodynamic and diffusive-thermal instabilities of laminar flamelets may increase the flamelet surface area resulting in increasing turbulent burning velocity. When Le>1 then the diffusive-thermal effects might be able to suppress the hydrodynamic instability, therefore, the flame surface maintains smooth (Lipatnikov [2013]). Turbulent burning velocity is usually increased by pressure despite the decrease in the laminar burning velocity, this will be discussed in the following Section. By analyzing experimental data, Prudnikov [1964] has shown that a "self-similar" regime of turbulent flame propagation exists, where the "distributions of mean temperature and density across the turbulent flame brush collapse to a universal curve" under a very wide range of initial conditions. Further discussion of flame development and the "self-similar" regime are presented in Chapter 6.

2.2.2.4 Influence of pressure on flame propagation

It has been widely observed that pressure has a negative effect on laminar burning velocity from both computation (Soika et al. [2003]) and experiments (Bradley et al. [1998]). Detailed one-dimensional flame calculations using CHEMKIN for a methane/air flame show an approximate relationship $u_l \propto P^{-0.5}$ (Soika et al. [2003]). Experimental results also confirmed that the unstretched laminar burning velocities decrease as $P^{-0.52}$ (Liu et al. [2011]). In addition, the flame thickness is not significantly changed by pressure.

A comprehensive review of pressure effects on laminar flame speed and structure has been done by Law [2006]. It has been shown that effects of pressure on laminar flames can be attributed to several aspects: when the pressure increases, the density of reactant gases at the same temperature increases, consequently higher concentrations of the species are achieved. Diffusion coefficient and thermal diffusivity are inversely proportional to pressure. Strong nonlinearly chemical kinetics may play a key role, especially those pressure-dependent chain mechanisms whose reaction rate can be varied by pressure, through the reaction order, or the pressure exponent (Law [2006]). Detailed description of effects on chemical reaction mechanisms is out of the aims of this study. However, the application of the chemical mechanism validated only at low pressure should be considered cautiously to calculate the burning velocity at high pressure. The adiabatic flame temperature is increased by elevated pressure i.e. adiabatic flame temperature can be increased from 50 to over 100 K by pressure increase from 1 to 100 bar (Law [2006]).

Apart from understanding the pressure effects on a laminar flame, it may be more important gaining accurate laminar burning velocity, since it is a key parameter for studying turbulent combustion. Laminar burning velocities measurements have been made at high pressure, e.g. as demonstrated in the work of Metghalchi and Keck [1982], in which data at high pressure were extracted from pressure rise measurements in a constant volume bomb. A laminar burning velocity correlation equation was proposed based on their experiments with a wide range of temperature and pressure. More details of the correlation equations are presented in Chapter 5. However, the data at elevated pressures are still limited, although there is a rapid growth of the measurements in this area (Jerzembeck et al. [2009]; Marshall et al. [2011]). Recently, the initial pressure in a constant volume bomb experiment was increased to 25 bar in the experiment of Jerzembeck et al. [2009] with schlieren methods. The cellular structure on the flame surface, due to flame instability at elevated pressure, brings the difficulties in the accurate measurement of burning velocity (Lawes et al. [2012]). The onset of cellularity is shifted towards a small flame radius by increased pressure. Cellular shape flame surface induced by instabilities causes

an acceleration of the flame front. How the flame speed is accelerated by the instability in the engine relevant condition, and whether flame instability effects should be included into turbulent combustion modelling, still remains an open question.

The laminar flame speeds under engine relevant conditions (pressure $>$ 15 bar and temperature $>$ 500 K) are difficult to measure directly in the constant volume vessel. Landry et al. [2008] calculated the laminar burning velocity by using detailed chemical mechanisms under engine-like conditions. The results show a decrease of laminar burning velocity with elevated pressure, which might be compensated for by an increase in the temperature. Consequently, the laminar burning velocity remains nearly constant. Hence, it is different between the results observed from steady state experiments and engine experiment, where temperature and pressure are changed together during compression stroke.

For turbulent premixed flames, most experimental results show an increase in turbulent flame speeds and burning velocities by pressure. Kobayashi et al. [2002, 1997] have investigated turbulent premixed flames at a high-pressure environment up to 3.0 MPa. In order to stabilize the flame at high pressure, a bunsen-type burner was used to overcome the unsteady and short duration of flame propagation in combustion vessels. Turbulent burning velocity was measured, and S_t/S_l was also found to be considerably affected by pressure. A power law expression of S_t/S_l with $(P/P_0)(u'/S_l)$ was deduced, and the exponent ratio was found to be 0.4. A finer and more wrinkled structure of the flame with increasing of pressure was found. This is consistent to the observation of Soika et al. [2003]. They found that the flame front contour of high-pressure methane/air flames became strongly wrinkled when the pressure was increased in a bluff-body stabilized burner. However, the results from Griebel et al. [2007] experiment showed that there was no influence of pressure on the mean flame front position, on the flame brush thickness, or on the turbulent burning velocity under the pressure range of 0.5-1.44 MPa. In his work, turbulent flame speeds and flow field of lean premixed methane/air flames were measured by using Particle Image Velocimetry (PIV) and Planar Laser Induced Fluorescence of the OH radical (OH-PLIF) in a high pressure combustor.

In comparison with the results from stationary flames, information for freely propagating turbulent flames may be more relevant to internal combustion engines. Bradley et al. [1998] have investigated turbulent burning velocities for a wide range of initial conditions using a fan-stirred bomb up to 1.2 MPa for turbulent flames. The results showed that the flame curvature and wrinkling were increased due to the onset of instability at high pressure, which made the turbulent burning velocity increase with pressure. The implosion technique (Al-Shahrany et al. [2005]) was developed to measure burning ve-

locities at the final stage of two opposite inward propagation flames, where the pressure can reach 3.0 MPa. A comprehensive measurement of the turbulent burning velocity of iso-octane/air mixtures has been conducted by Lawes et al. [2012]. It was found that the turbulent burning velocity did not change significantly with pressure at a low turbulent intensity (u' = 1 m/s), while at u' = 4 m/s, the increased pressure resulted in an observable rise in turbulent burning velocity in a constant volume combustion bomb from 0.1-1 MPa. In these tests, the pressure was increased while turbulence intensity was kept constant. Liu et al. [2012] argued that the increase of pressure raised the Reynolds number, which caused the increasing of the turbulent burning velocity. Under constant Reynolds number conditions, they found that turbulent burning velocities decreased with increasing of pressure, which was similar to laminar burning velocities. The data were collected from a double-chamber, fan-stirred large premixed turbulent combustion facility at elevated pressure up to 1.2 MPa. However, the turbulent burning velocity increased at any elevated pressure with an increase of Reynolds number.

The results from constant combustion vessel still can not provide all the information about combustion in SI engines due to a number of factors, including piston motion, which leads to higher pressure and temperature before spark ignition and also the flame shape is confined by the geometry of the engine chamber. Only a few studies provided the information about combustion characteristic in a real boosted engine condition. Mounaïm-Rousselle et al. [2013] undertook an investigation into the effect of pressure and dilution on the turbulent burning velocity with intake pressures between 0.7 to 1.5 bar. The turbulent burning velocity was estimated from the mean flame front displacement velocity and the mean flow field velocity, which were determined from the laser tomography images and Particle Image Velocimetry (PIV). It was found that the intake initial pressure, which ranged from 1.0-1.5 bar, seemed to have no effect on turbulence. At the same condition, the turbulent flame speed increased slightly, while the laminar flame speed remained constant. Merola et al. [2007] investigated the flame development and found that the trajectory scope of flame kernel decreased when increasing of the boost pressure, while the path length and speed of it was increased. The initial speed of flame propagation was increased for boosted conditions and it decreased after it reached a maximum speed, due to the increase of pressure in the end gas. The last stage of flame-wall contact information is absent because of the limit of engine's optical access structure.

2.2.2.5 Flame Chemiluminescence

The knowledge of flame chemiluminescence is important for flame imaging measurement. Flame chemiluminescence is a kind of light emission of radicals during their return from an electronically excited state to the ground state (Gaydon [1957]). Chemiluminescence techniques have been applied in a wide combustion research areas, e.g. monitoring fuel-air ratio (Aleiferis et al. [2004]), detecting range of flame position, shape, and structure (Ikeda et al. [2001]), and can also be employed to measure heat release fluctuations (Hardalupas and Orain [2004]). Usually, the excited species are generated by chemical reactions in the flame reaction zone. Thus in typical hydrocarbon-air flames, chemiluminescence intensity from radicals, like CH* and C_2*, can provide information about conditions in the reaction zone. A typical chemiluminescence spectrum in the ultraviolet and visible part of combustion in a spark ignition was shown in Figure 2.12 (Merola et al. [2009]). It can be seen that C_2* has several band systems. The Swan band consists of wavelength near 473.71 nm, 516.52 nm and 563.55 nm. The formation of C_2* is owing to the reactions (Gaydon [1957]):

$$CH_2 + C- > H_2 + C_2* \tag{2.35}$$

$$CH + C- > H + C_2* \tag{2.36}$$

The CH is detected at 430 nm, 290 nm, 314 nm. The strongest is at 430 nm. The formation of excited CH in the flames has been debated for long time (Gaydon [1957]). It was suggested that it might be generated from C_2:

$$C_2 + OH- > CO + CH* \tag{2.37}$$

$$C_2 + O- > CO + CH* \tag{2.38}$$

However, it is difficult to interpret the chemiluminescence signals because of the integrated line of sight information acquired. Furthermore, it is affected by many factors such as pressure, temperature, strain, equivalence ratio and fuel.

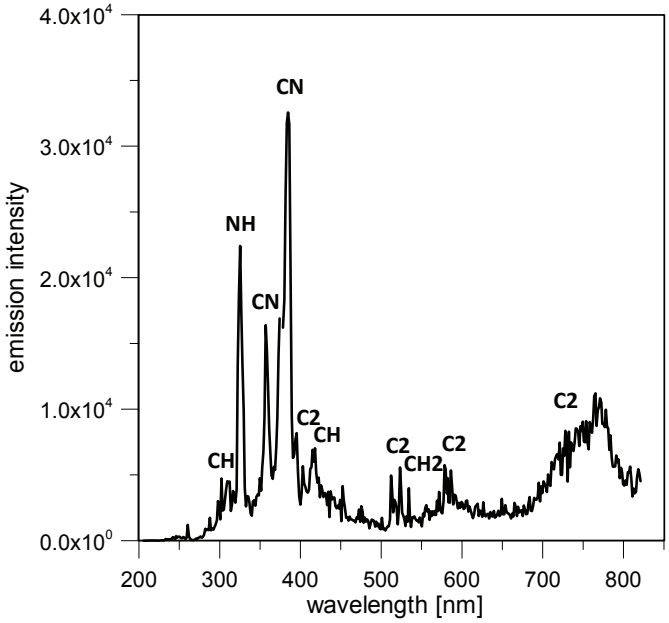

Figure 2.12: Emission spectrum detected at the SI engine (Merola et al. [2009]).

2.3 Autoignition and knock

2.3.1 Types of abnormal combustion

The term ”autoignition” is used to describe a rapid combustion reaction which is initiated without any external ignition source. The autoignition of fuel-air mixture occurs when the reaction heat energy release is larger than the heat loss to the surroundings (Griffiths and Barnard [1995]). The abnormal combustion in the spark ignition engine has been attributed to the autoignition in the gas phase or ignition by an overheated solid surface.

Figure 2.13 illustrates the autoignition in the pre-flame gas occurence with flame propagation in the SI engine. The surface ignition is caused by early autoignition on the over-heated combustion chamber walls and once happened it tends to continue in subsequent cycles (Kalghatgi and Bradley [2012]). It may be eliminated by the cooling system to a certain extent. Autoignition in the gas phase has attracted more attention. It is likely to occur ahead of the flame front, as well as in the end gas region at a varying distance from the walls. Two kinds of autoignition in the gas phase are assumed: ”homogeneous” autoignition, where the end gas is ignited simultaneously and uniformly; ”pinpoint” autoignition, where self-ignition occurs at many point sources. Further evidence demonstrated that knock is usually caused by multiple autoignition points in the

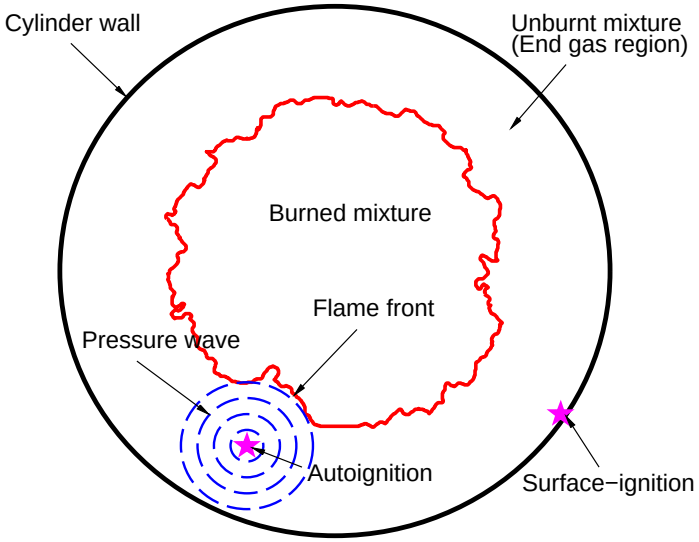

Figure 2.13: Autoignition at a solid surface (cylinder wall) or in the gas phase (unburnt mixture).

inhomogeneous end gas region instead of being a result of spontaneous ignition of a homogeneous end gas (Pan and Sheppard [1994]).

In a spark ignition engine, the compression by the moving flame is much faster than by piston motion, leading to sufficiently high pressures and temperatures in the end-gas; this may result in a rapid release of chemical energy from one or more hot-spots. These "hot spots" are typically caused by inhomogeneities in temperature and composition in the end gas region. Temperature inhomogeneities can arise from combustion chamber wall deposits as well as imperfect turbulent mixing. Zeldovich (Zeldovich [1980]) suggested that inhomogeneity in radical concentration in the end-gas may also be as important as that of temperature. Multi-point autoignitions can reinforce pressure waves, to create the local high pressure and gas velocities (Pan and Sheppard [1994]). In a conclusion, autoignition was influenced by heat conduction, species diffusion and some reaction waves. As a matter of fact, it is the temperature non-uniformity which is the root cause of autoignition.

Autoignition commonly, but not necessarily, results in in-cylinder pressure oscillation and strong noise, known as "knock", a potential cause of damage to the engine, piston and valves (Heywood [1988]). The severity of knock is usually estimated from the amplitude of pressure oscillations. If autoignition happens prior to the initiation of a flame from a spark, it can be called pre-ignition (Dahnz and Spicher [2010]). In the modern supercharged engine, sporadic pre-ignition accompanied by extreme knock has been found (Attard et al. [2010]; Dahnz and Spicher [2010]). However, an extreme knock could

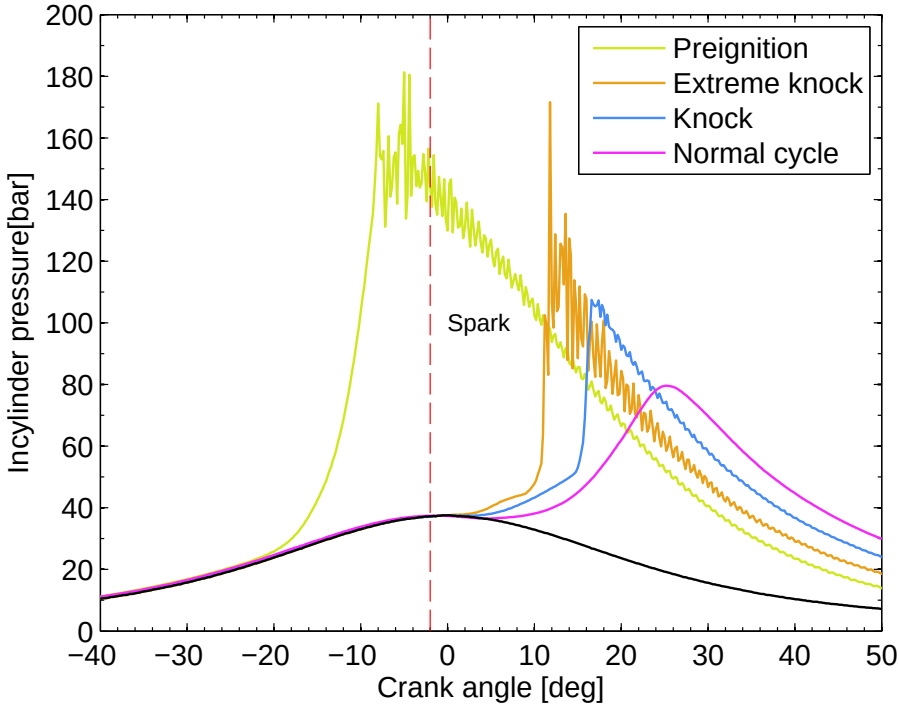

Figure 2.14: Illustration of pressure curves of pre-ignition, extreme knock, knock, and normal combustion, in the LUPOE 2D boosted engine running at speed of 750 rpm and spark timing 2^o bTDC, stoichiometric iso-octane fuel. The intake and head temperature was kept at 323 K. Initial pressure was 2.0 bar.

also occur after spark ignition. The difference between extreme knock and traditional knock is that the former has much higher pressure oscillation amplitude and occurs at random. Thee types of abnormal combustion: pre-ignition, extreme knock and knock were illustrated with a normal combustion cycle in the Figure 2.14, obtained under nominally identical running conditions. Our findings are further discussed in Chapter 7.

It should be mentioned that there is an alternative, fairly old theory of formation of knock, which assumes that the knock is caused by the propagating flame front suddenly accelerating to sonic velocities which leads to the end gas mixture consumed at a rate much faster than normal with a rapid of release of energy (Firey [1957]). Miller [1947] proposed a theory which combined the autoignition with the detonation theories. The knock was classified as light knock which was caused by the autoignition of the end gas and moderate to severe knock which was caused by the autoignition of the end gas followed by development of a detonation-like wave. The detonation theory has been challenged by many investigators, principally because there was not enough experimental data to prove that detonation waves can develop under engine conditions (Bradley and Kalghatgi [2009]).

2.3.2 Autoignition chemistry and the octane number of fuel

The end gas auto- (or self-) igniton originates from a rapid heat release at a single or multiple discrete exothermic centres or hot spots. These appear when the induction time for the end-gas autoignition is less than the time required for the spark-initiated flame to propagate through the cylinder. The chemical induction time is related to fuels ignition behaviour which is mostly governed by the complex chemical mechanisms of fuel oxidation.

Hydrocarbon oxidation generally consists of four steps; initiation, propagation, degenerated branching and termination (Griffiths and Barnard [1995]). The path of the autoignition reaction is related to the history of the unburned gaseous mixture pressure and temperature. There exist three main paths: a "cool" flame reaction at temperatures in the range of 500-800 K, two stage ignition region in which the "cool" flame proceeds to a hot flame (800-1100 K) and a single stage "hot-temperature" ignition ($> 1100\,K$). In the low or intermediate temperature region (500-860 K), Reaction $R + O2 \rightleftharpoons RO2$ is reversible, so synthesis and decomposition occur simultaneously. The Reaction is generally in forward mode and produces the alkylperoxy radicals RO2. When temperature is increased to enter the Negative Temperature Coefficient regime (NTC), $RO2 \longrightarrow R + O2$ reaction is predominately reversed and produces RO2 radicals. At the high temperature, decomposition of branching agent (hydrogen peroxide: $H2O2 \rightleftharpoons OH + OH$) becomes the key reaction. Therefore, at low temperatures, ROOH radicals into a single hydroxyl (OH) radical and partial fuel oxidation dominate the oxidation process while at high temperatures; the HOOH radical becomes the main branching agent. In the Negative Temperature Coefficient (NTC) regime, high temperatures shutdown the pathway of low temperature oxidation and shifting to the hydrogen decomposition and the temperature is not high enough to activate hydrogen peroxide decomposition (Curran et al. [2002]). In engine research using spectroscopic investigations, weak OH* radicals and very weak HCHO* radicals were obtained before autoignition occurred which confirms low-temperature chemical reaction of auto-ignition in the engine (Kawahara et al. [2007]).

Since practical fuels contain many hundreds of components coming from all types of hydrocarbons e.g. alkanes, alkenes, napthenes and aromatics, this makes it difficult to develop an accurate chemical mechanism to explain the knock phenomena. In order to obtain a direct comparison of different fuel tendencies to produce knock, a method for correlating the chemical structure of a species with its octane number was proposed (Heywood [1988]). The Cooperative Fuel Research Committee defined a standard procedure to measure a fuel's octane number (ON). Regardless of how complex the autoignition

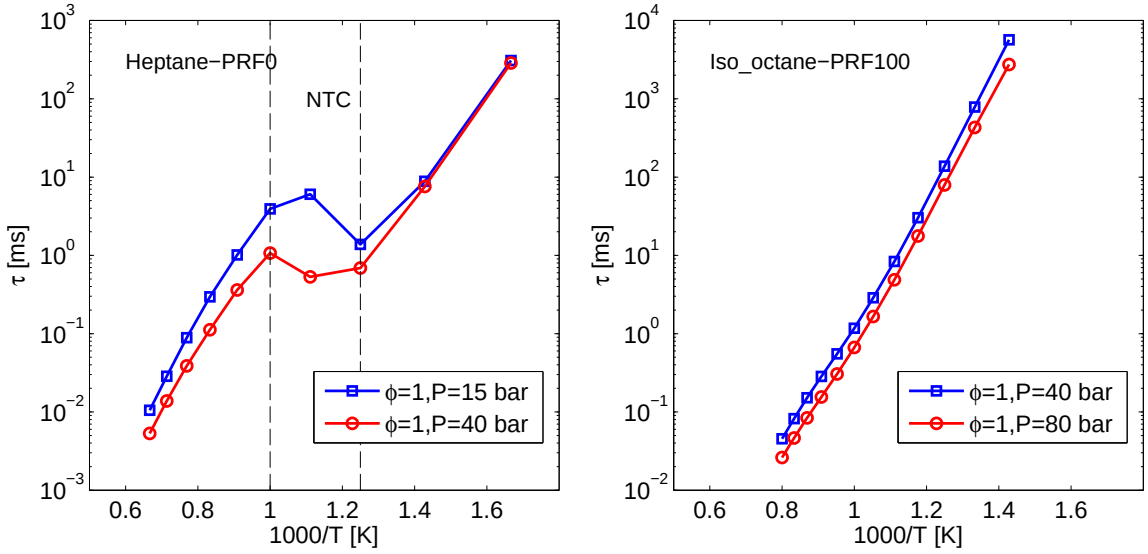

Figure 2.15: Ignition delay time of heptane (MON=RON=0) and iso-octane (MON=ROM=100) at different pressure and temperature. The data are calculated using CHEMKIN II package (Robert [1989]) with chemical reaction mechanism from Jerzembeck et al. [2009].

chemistry is, the fuel behaviour may be compared to that of a mixture of n-heptane/iso-octane called primary reference fuel (PRF) burned in a standard single cylinder CFR engine. It was found that heptane prone to auto-ignition while iso-octane has a good anti-knock characteristic. The ON number of a fuel is the volumetric percentage of iso-octane in the PRF (Primary Reference Fuel) producing knock at the same intensity at the same conditions. Octane number 100 means the fuel has the same anti-knock properties as pure iso-octane.

Figure 2.15 shows ignition delay time of heptane and iso-octane at different pressure and temperature. The data are calculated using CHEMKIN II package (Robert [1989]) with chemical reactions from Jerzembeck et al. [2009]. Generally, ignition delay time decreases with increasing temperature due to the acceleration of chemical reactions rate. The negative temperature coefficient (NTC) behaviour can be observed in the heptane fuel [1]. The influence of pressure on the ignition delay of heptane fuel are found to be not uniform, smallest for low temperatures and tend to be significant in the high-temperature region. With the increasing of pressure, the transition region shifts to higher temperatures and lower ignition delays. The RON and MON are important indications of fuels anti-knock characteristics and they have been established in state standards all over the world. However, they may not be a complete guide for a turbo-charged engine,

[1]NTC can be observed for virtually any fuel except methane or toluene

because of the wider range of operational regimes which may exceed the reference engine (Bradley and Head [2006]).

The calculated ignition delay time for the PRF fuel is often much too long to cause pre-ignition (Dahnz and Spicher [2010]). Recent investigation of pre-ignition in a turbo-charged engine by Dahnz and Spicher [2010] has highlighted effects of lubricant oil droplets released from the cylinder liner promoting autoignition under certain conditions. A further study of Kalghatgi and Bradley [2012] related the autoignition on the engine surface to the minimum critical size of a hot spot for a flame to propagate. It was found the the minimum critical size of a hot spot decreased with the increasing of the initial pressure. The gas-phase autoignition, which is considered as the dominant mode of pre-ignition in modern SI engines, may originate from the hot spot containing long-chain lubricating oil, and this process could possibly be enhanced by small solid particles acting as a catalyst.

These conclusions may imply that while the main cause of end-gas ignition is the homogeneous gas-phase chemistry under naturally aspirated conditions, analysis of auto-ignition under boosted conditions should take into account the role of the lubricant as well. However, such assumptions have not been convincingly validated and the mechanism of lubricant oil droplets inducing pre-ignition is still far from clear, perhaps to some extent because of lack of understanding of autoignition delay times in the presence of lubricating oil mists. Therefore, no attempt is made in this work study potential effects of the lubricant on the abnormal combustion.

2.3.3 Reaction front development from autoignition sites

Three modes of reaction front propagation from hot spots have been proposed to describe the transition from autoignition to knock using modelling method (Gu et al. [2003]). A thermal explosion or homogeneous autoignition would be created when the temperature gradient is small. Although, this is unlikely to be the case in an engine. As the magnitude of temperature gradient increases, weak pressure waves are created from exothermic centres, propagating away from the centre and transiting to deflagration. The end gas is consumed by a reaction front, propagating at subsonic speed, O(10-100) m/s at engine conditions. Knock tends to be moderate in this case. If the temperature gradient of the end gas reaches to some critical value between the deflagration and thermal explosion modes, a stronger shock is formed with a super-sonic reaction front velocity. Intense chemical reaction will be initiated and sustained by this shock and ultimately leads to the development of a detonation. The speed of detonation can reach O(1000) m/s (Gu et al. [2003]). In this mode, severe knock occurs and will damage the engine (Konig and

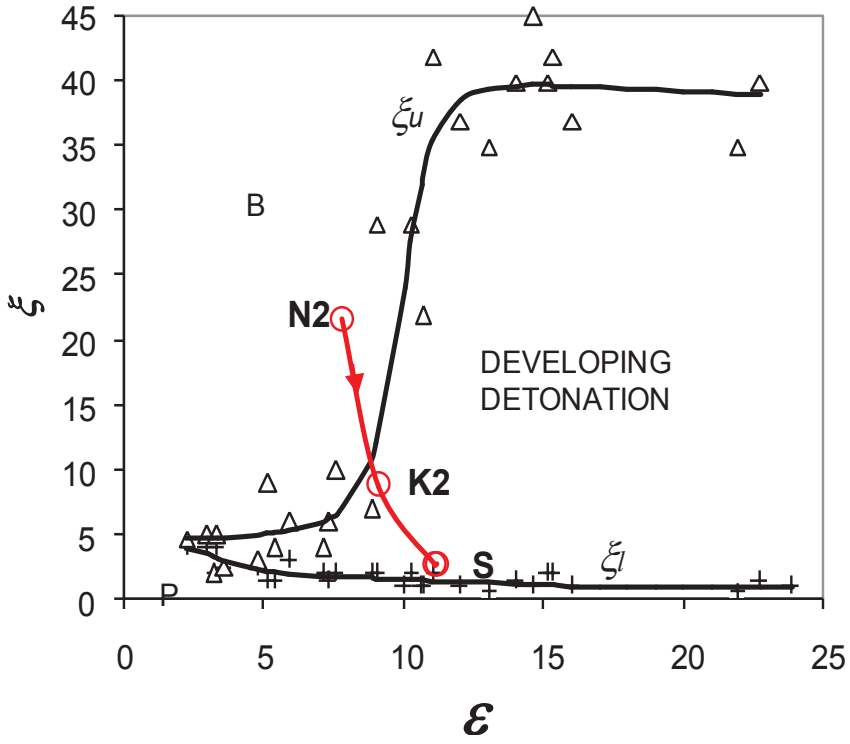

Figure 2.16: Conditions for the occurrence of developing detonations in terms of ξ, and ε. Supersonic and subsonic autoignitive deflagrations occur in the regions marked P and B respectively. Cited from (Kalghatgi and Bradley [2012]).

Sheppard [1990]). Although, detonation in engines has been studied for nearly a century, rare evidence existed to prove it, partially due to the speed of camera is much slower than detonation. Several images were published by Leeds combustion group (Pan et al. [1998]) using a 240,000 frame rate drum camera. A peak velocity about 900 m/s was observed, which is possibly associated with a transition to the developing detonation mode. The amplitude of this knock pressure was much lower than current extreme knock.

In a numerical experiment, Bradley et al. [2002] extend to five modes of reaction front propagation. An analysis method was developed based on the assumption that the propagation mode governed by the coupling between the acoustic pressure wave and the reactive front (Bradley and Kalghatgi [2009]). Two dimensionless parameters have been defined, one, ξ is the ratio of the temperature gradient in the hot spot to the critical one where a mutual amplification occurs between the chemical and acoustic waves. The second parameter ε was defined as the ratio of major heat release loaded into the acoustic wave to that based on excitation time. When both ratios are within a certain range, the chemical reaction wave may reinforce an acoustic pressure wave and generate a developing detonation. These dimensionless parameters can be derived from experimental

ignition delay time $\tau(T, p)$ (Bradley and Kalghatgi [2009]). Kalghatgi and Bradley [2012] investigated several pressure traces of extreme knock, and registered these conditions on the (ξ and ε) coordinates as shown in Figure 2.16, it was found that extreme knock was located in the developing detonation regime and the high knock intensities could be attributed to autoigniton induced further detonation. By using this method, the detonation mode has also been recognized by Rudloff et al. [2013]. However, these conclusions rely on the assumption that the detonation was generated from the hot spot directly and the map used for recognizing detonation and deflagration was based on the DNS calculation using H_2 (Gu et al. [2003]), which has a different ignition delay time with commercial fuel. To identify the extreme knock caused by the huge unburnt mass fraction due to advance of auto-ignition time or the occurrence of developing detonation is one of objectives of this study.

2.4 Optical experimental engines

Pressure signals from an experimental engine only yield the information averaged over the entire combustion chamber. Detailed flow and combustion processes can be acquired from partially transparent engines with optical measurements. Although additional optical windows within an engine may change heat transfer intensity, optical access is useful for fundamental combustion research related to reciprocating engines. Two main kinds of optical engines are described in the literature as shown in Figure 2.17: optical access through the cylinder head, and the optical access through the piston (Zhao and Ladommatos [2001]), in the so-called Bowditch arrangement.

The optical access through the piston engines are more widely used (Beretta et al. [1983]; Foucher and Mounaïm-Rousselle [2005]; Gatowski et al. [1984]; Knaus et al. [1999]), especially in the last twenty years. Mounting an optical window in the piston is compatible with the overhead valves configuration. Fuel injection spray and mixture in modern Gasoline Direct Injector (GDI) engines, which are strongly affected by flow structure generated by lifted valves, can be investigated (Aleiferis et al. [2010, 2004]; Chen et al. [2012]). Ignition and initial flame development can be observed (Peterson et al. [2014]). In order to apply diagnostics to engine, another window in the side of engine, or a totally transparent cylinder body, may need to be used. But above all, the optical access can be employed to observe the combustion phenomena (Aleiferis et al. [2013]; Bates [1991]; Buschbeck et al. [2012]; Ziegler et al. [1988]).

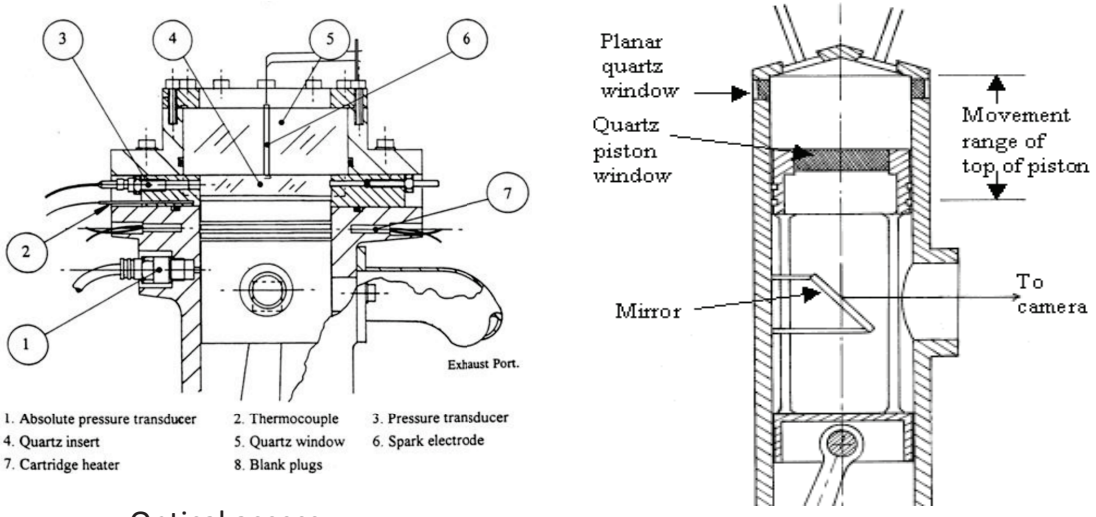

Figure 2.17: Two kinds of configuration of optical engines: optical access through the cylinder head (Hicks et al. [1994]), optical access through the piston (Stone [1999])

Optical access through the cylinder head engine is usually employed in derivatives of a two-stroke engine. By replacing the cylinder head with an optical window, a complete view of the whole combustion chamber form top can be achieved. This configuration can be found in the early engine experiment in the University of Princeton (Zur Loye [1987]), later in the University of Leeds (Hicks et al. [1994]). With the continuous development of the breathing system at the University of Leeds (Dawood [2010]), the flow structure in the engine becomes more homogeneous, and this kind of engine tends to approach some kind of a reciprocating combustion rig, which provides a high pressure combustion experimental method, situated somewhere between constant combustion vessel and a "real" SI engine. In addition, the full bore optical access provides the opportunity to study the phenomenon near the cylinder walls, such as the flame quenching and autoignition in the end large of unburnt gas (Hicks et al. [1994]; Konig and Sheppard [1990]; Schießl and Maas [2003])[1]. Optical access through the cylinder head, also can be found in some valved engines, where fewer than normal valves were installed and this left space for a small window (Ihracska et al. [2014]).

Optical access through the cylinder head engine was adopted in this study to gain deep insight into the combustion and autoignition phenomena at high pressure related to

[1]Some "Bowditch" arrangement engines also can provide full bore optical access (Serras-Pereira et al. [2012])

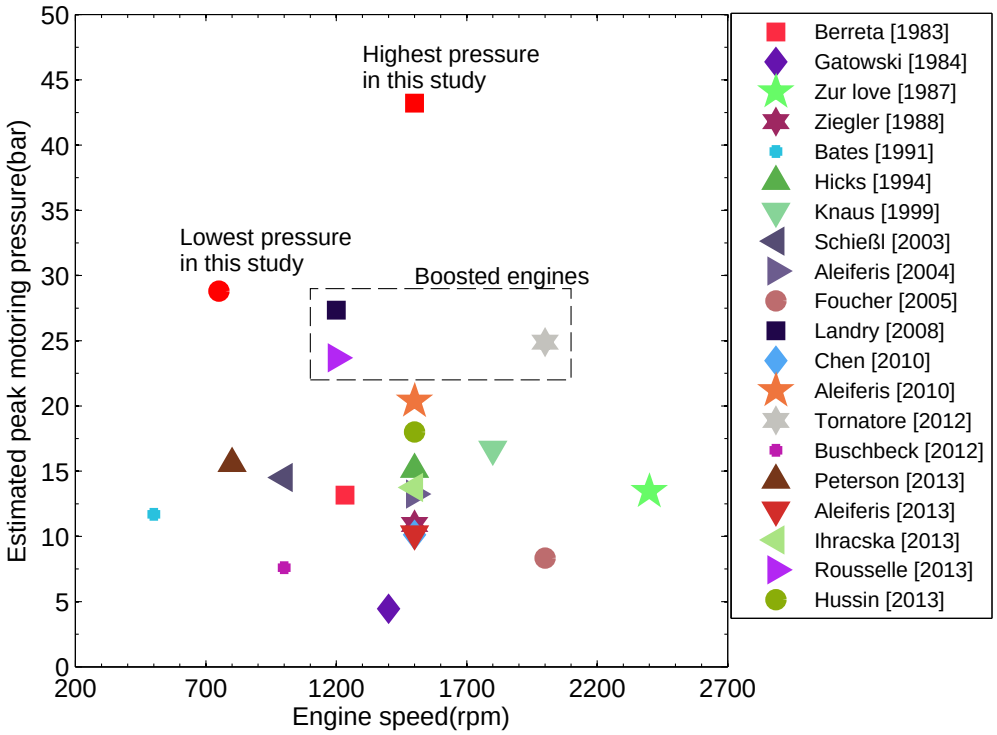

Figure 2.18: Peak motoring pressure and maximum engine speed achieved in this study comparison with previously spark ignition optical engines.

supercharged SI engines. Most relevant work on flame measurements and autoignition investigations in optical engines have been conducted with inlet atmospheric pressure or a low compression ratio. These pressures at ignition were lower than in supercharged engines. Only a few studies are related to boosted conditions, however, these boosted engines run in a narrow initial pressure range (1-1.5bar) (Landry et al. [2008]; Mounaïm-Rousselle et al. [2013]; Tornatore et al. [2012]). Although small changes in the intake air pressure can result in large changes in the peak pressure due to the engine compression process, these initial pressure values and the peak motoring pressure achieved might be not sufficiently high to observe the effect of pressure on the flame development process. Further extension of the initial intake pressure, would be a challenge for this research work. A comparison of peak motoring pressure and maximum engine achieved in most prior optical engine experiments to this study condition is shown in Figure 2.18[1]. The peak motoring pressure was estimated by using polytropic equation with polytropic exponent of 1.25 (Heywood [1988]).

[1]It should be noticed that the values listed here are experimental conditions set, the maximum performance of these engines might be higher than these values.

Chapter 3

Experimental engine and boosting system

In recent years, a large number of excellent naturally aspirated engine experiments have been conducted by the Leeds combustion research group using the Leeds University Ported Optical Engine (LUPOE) (Muard [2006]; Roberts [2010]; Smallbone [2004]). The objective of the current study is to investigate the engine combustion at elevated pressures. With this aim, the naturally aspirated LUPOE 2D engine was modified into a boosted engine. The breathing system of LUPOE 2D was redesigned for the purpose of simulating turbo-charged engine operation condition. The challenge was not only to increase the initial pressure of the engine, but also to control the turbulence in the engine at a certain desired level. Various methods have been applied to increase the initial pressure, including exchanging the position of the intake and exhaust ports, installing intake and exhaust system valves, and increasing the air supply pressure directly. These methods were tested and compared to find an efficient and accurate way to control the inlet pressure. This Chapter also includes the description of LUPOE 2D engine design along with its basic components. The engine controller and data acquisition system were redesigned and are described here. At last, the pressure data process and analysis methods were introduced with a reverse thermodynamic simulation software LUSIEDA (Leeds University Spark Ignition Engine Data Analysis).

3.1 LUPOE 2D research engine

Leeds University Ported Optical Engine, Version 2, Disc-head (LUPOE 2D) was developed on the base of a commercially available Lister Petter-PH1 single cylinder diesel engine, of which the cylinder head, the breathing system were replaced with bespoke components. An overview of the engine setup can be seen in Figure 3.1, and a detailed drawing of the schematic diagram of the LUPOE 2D and optical head have been shown in Figure 3.2. A photograph of the LUPOE 2D engine can be found in Appendix A.

The LUPOE 2D engine is similar to a two-stroke engine, in that it has a disc-shaped combustion chamber with a full-bore overhead optical access. It replaces the overhead valves by side ports to avoid obstructing the full-bore optical access, provided by one top and two opposite side windows. A custom built compact spark plug was located in the center of the cylinder bore; it consists of a 0.5 mm diameter steel anode housed inside a sheathed 3 mm alumina tube. A L-shaped length of brazing rod was connected to the outer brass tube to act as the cathode. The quartz optical window was used in normal combustion experiments, in most cases, but it was replaced by a more robust metal blanking plate to avoid the damage to the quartz window under strongly knocking conditions.

The LUPOE 2D engine has two diametrically opposed intake ports of rectangular cross section and an exhaust passage consisting of either two or four rings of circular exhaust holes drilled in the liner, communicating with a void between a liner and a barrel, leading to one exhaust duct. The liner of the boosted LUPOE 2D engine has 2 rows of exhaust holes, while naturally aspirated version has 4 rows, the reason of this configuration will be explained in the Section "Boosting system". The timings of the port holes opening and closing were controlled by the movement of piston. The specifications of the naturally aspirated LUPOE 2D engine and boosted LUPOE 2D engine are compared in Table 3.1. The employed ported breathing arrangement, in particular the ports dimensions and inclination, allows one to eliminate swirl and tumble motion often existing in valves engines, and to generate in-cylinder flow field uniform in both average and root-mean square properties, thus LUPOE 2D can be considered as a featureless flow engine.

Compression ratio can be adjusted by using a series of metal shims, placed between the top of the engine block and the cylinder head. The specifications of these are detailed in Table 3.2. The shim thickness of 4 mm was only used during initial stage of engine tests to ensure that the engine operation was safe. The shim thickness of 1 mm was mainly used in this study, in order to obtain a similar compression ratio as the naturally aspirated LUPOE 2D engine.

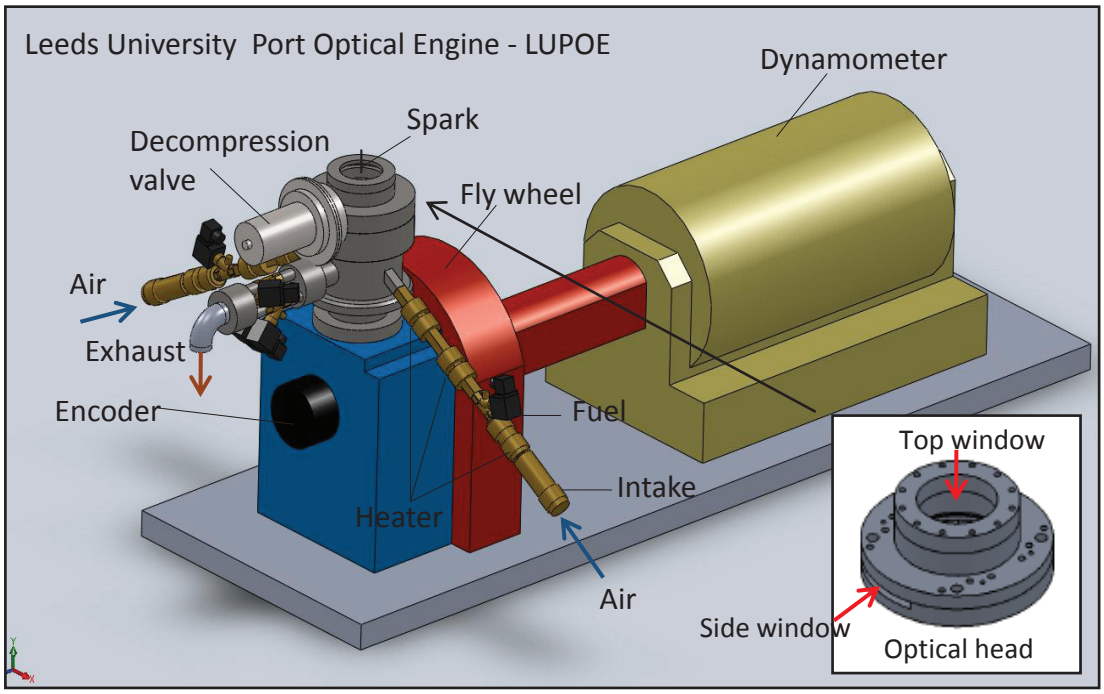

Figure 3.1: 3D view of the LUPOE 2D engine layout with the details of the optical head.

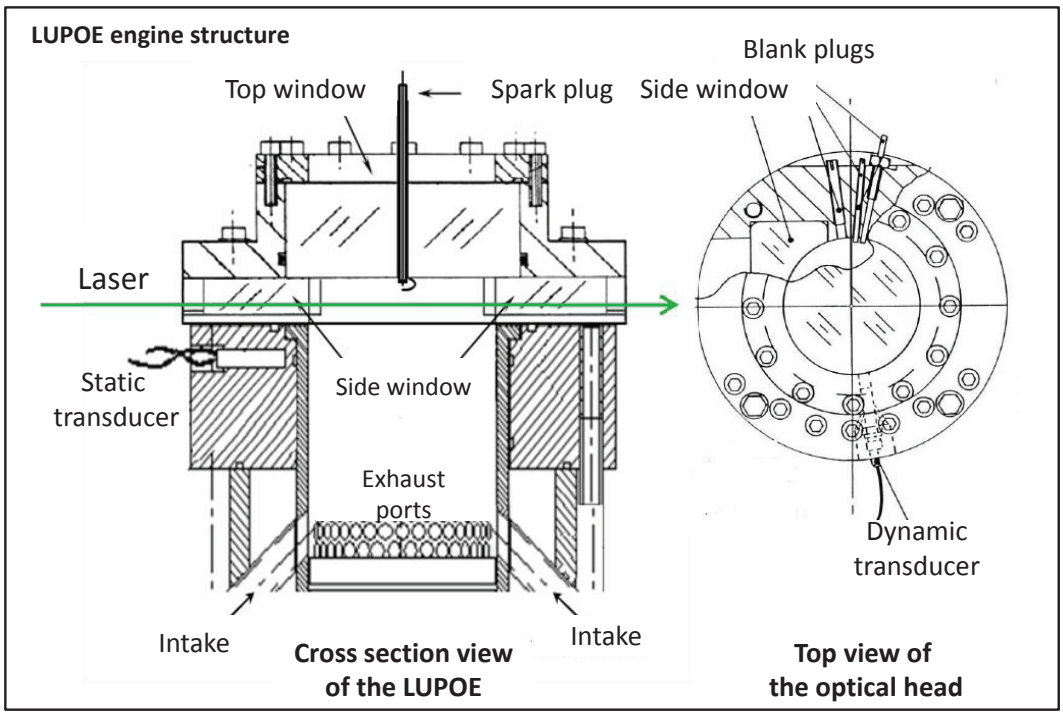

Figure 3.2: Schematic diagram the LUPOE 2D engine modified from Roberts [2010].

Table 3.1: A comparison of the main engine parameters between the LUPOE 2D and LUPOE 2D boosted engines.

Engine Parameter	LUPOE 2D	LUPOE 2D Boosted
Bore (mm)	80.0	80.0
Stroke (mm)	110.0	110.0
Clearance Height (mm)	8.0	8.0
Connection-Rod Length (mm)	232.0	232.0
CR_{Static} / $CR_{Dynamic}$	15.2 / 10.5	15.2 / 11.3
IPO/IPC° aTDC	-101.2	-101.2
EPO/EPC° aTDC	107.0	127.6

Table 3.2: Various effective compression ratios.

Shim thickness	Effective compression ratio
0 (mm)	11.47
1 (mm)	10.24
4 (mm)	7.83

3.2 Air and fuel system

The schematic diagram of the LUPOE 2D engine air and fuel flow system is shown in Figure 3.3. Air used in the experiments was supplied from the laboratory compressed air system and the pressure was maintained at 4 bar by a filtered regulator. Two thermal mass flow meters with feedback control function were employed in the air line, this allowed adapting the change of flow rate induced by pressure fluctuation in inlet manifold during experiment. The maximum measurement can reach to 33 g/s in each intake pipe. To further diminish the flow oscillations, a 5 L surge tank was installed upstream of each inlet pipe to steady the air supply pressure. The thermal flow meter operates based on a principle of heat transfer by sensing the delta-T along a heated section of a capillary tube. The fuel supply system employed a standard automotive filter-pump system. The fuel pressure was maintained at 0.3 MPa using a Bosch regulator. The fuel mass flow rate at each fuel line was controlled using a Series M53 Bronkhorst Coriolis mass flow controller.

Prior to feeding air-fuel mixture to the engine, the air temperature was increased and maintained using a series of five 175 W and one 200 W band heaters installed along each intake to offer sufficient heat flux to vaporise the fuel. Cylinder barrel and head

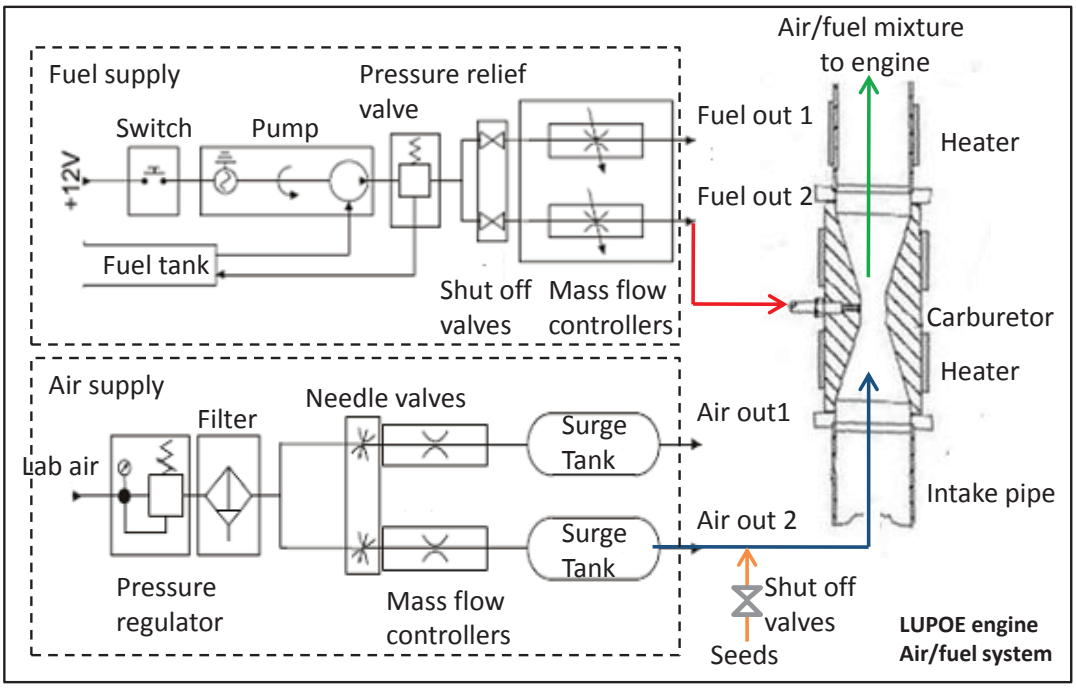

Figure 3.3: Schematic diagram of the LUPOE 2D engine air/fuel flow system modified from Roberts [2010].

heating were maintained using 50 W equally spaced cartridge heaters. The temperature was monitored using a thermocouple positioned immediately upstream of the intake port, the reading of which was processed by a Digitron 4801 control unit.

The fuel was injected in the port before the air and fuel mixture flowed into the cylinder through two separated intake ducts pipes. Cairns [2001] designed the intake duct, in which fuel was injected into a venturi which was located approximately 350 mm from the port. The intake pipes were installed 180^o apart and angled 20^o below the horizontal. The purpose of this kind of design is to create homogeneous mixture and uniform turbulence for the combustion event.

The liquid droplet seeding system, SCITEC LS-10 shown in Figure 3.4 was used in the PIV experiment and laser sheet visualization experiments, olive oil was used for seeding. Lab air was supplied to flow rate controller with four channels. Each channel was connected to several 1 mm diameter Laskin nozzles creating air jets into the oil reservoir. The olive oil was pressurised by air and atomised into fine droplet seeding. This mixture of air and oil droplets was then directly taken from the reservoir to the main air supply pipe, and induced into the engine inlet manifold.

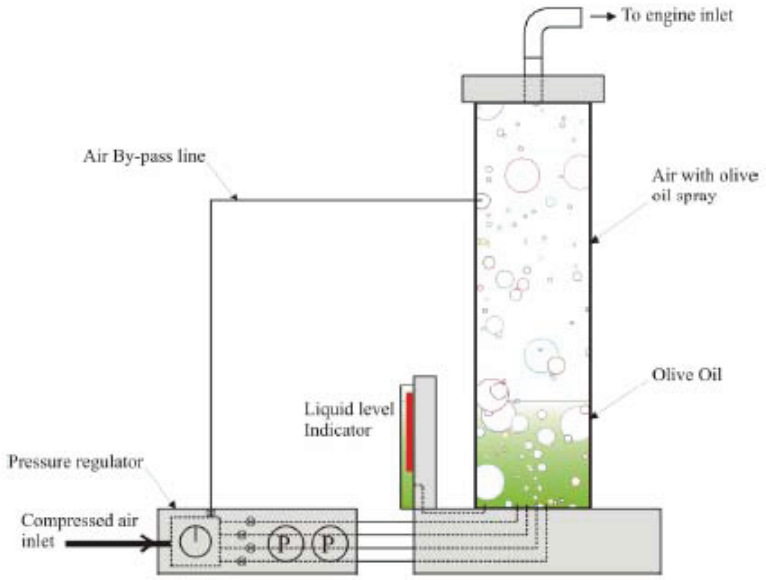

Figure 3.4: Schematic diagram of the LUPOE 2D seeding system, cited from Wu [2006].

3.3 Boosting system

The initial pressure of a commercial turbo-charged engine depends on the exhaust gas powered turbine, driving the inlet air compressor. Since the flow and state of exhaust gas varies during the engine running, it is difficult to keep the inlet initial pressure precisely at a desired value. For the LUPOE 2D engine, there are a number of reasons why turbo-charging or super-charging would not be a suitable boosting system. First is the difficulty of finding a suitable turbocharger: the common passenger cars' turbochargers are designed for engines of at least twice the displacement, and the motorbike engines run at much higher speed, so the mass flow rates are much larger than those required for the small and slow speed LUPOE 2D engine. Secondly, because the exhaust is collected into a large void and the engine barrel is relatively cold, there are very large heat losses from the exhaust, and the turbine efficiency will be very low. Finally, the LUPOE 2D running time are short and even then employ skip firing; the transient performance of a turbo-charger will be poor indeed. Therefore, a novel boosting system should be designed to boost the initial pressure of the LUPOE 2D engine to a stable level.

3.3.1 Initial design of boosting system

The initial pressure may be easily increased in the direct way through increase of the air supply pressure. Unfortunately, this way is of no use for the former LUPOE 2D because

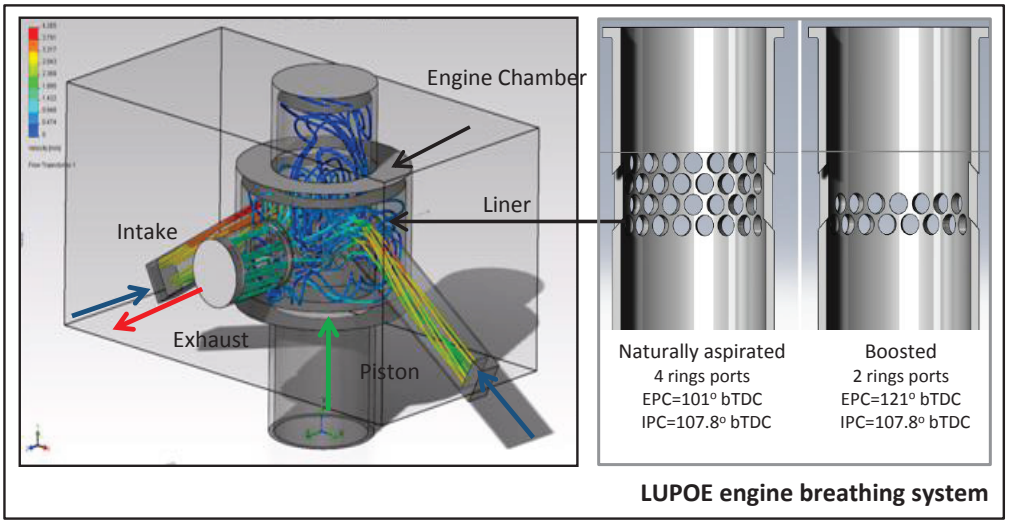

Figure 3.5: 3D view of the LUPOE 2D engine breathing system with liners and its position (The liners are modified from Conway [2013]).

of its ported breathing configuration. A 3D view of breathing system of the LUPOE 2D is shown in the left side of Figure 3.5. Figure 3.5 was made in the software Solidworks, the flow simulation only was used to illustrate the flow travel process with the position of liner. The detailed liner design for two kinds of engine are shown in the right side of Figure 3.5. The naturally aspirated exhaust port consisted of 4 rings of exhaust ports around the cylinder wall. Each orifice has a circular shape of 10 mm diameter. Exhaust gas flowed though these ports into an annular void between the liner and barrel and then into the exhaust pipe connected to the main laboratory exhaust extraction, the latter has a forced draught. In previous experiments, natural aspiration of the engine was kept by locating the exhaust ports above the intake ports. Therefore, during the compression stroke, the exhaust port is the last one to close, so that, the initial pressure was determined by the pressure of the exhaust port. The initial pressure in that arrangement was approximately equal to atmospheric pressure: it was measured that the LUPOE 2D engine has an inlet pressure of approximately 1.15 bar in the naturally aspirated configuration (Roberts [2010]). This was originally to improve scavenging, however, with the new requirement of boosting inlet pressures, this needed to be revised. In order to increase the inlet pressure, the location of intake ports and exhaust ports should be changed. If the intake port was closed later than the exhaust port, the initial pressure would be determined by the pressure of the intake port and the provided flow rates.

This design was done by Conway [2010], who designed a new liner in which two rows of exhaust ports were removed, with the inlet now sitting higher than the top ex-

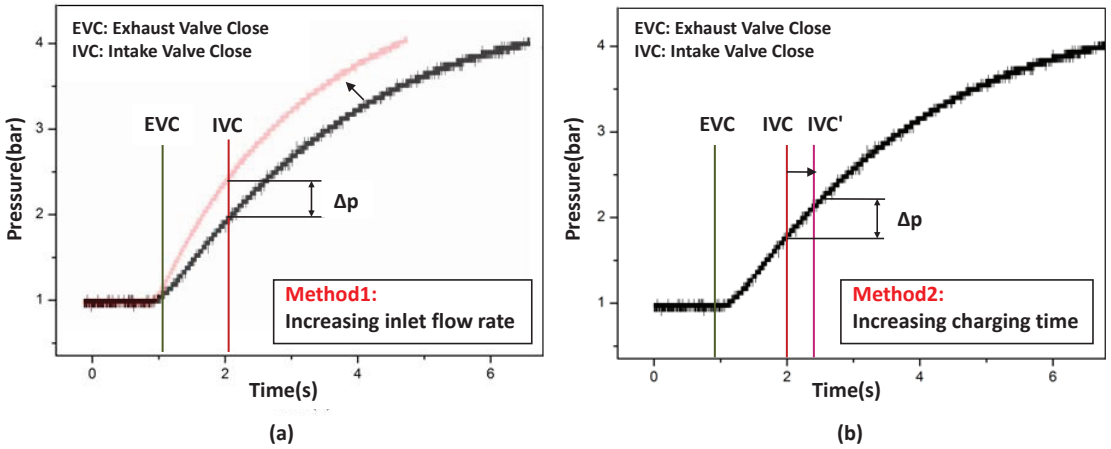

Figure 3.6: Illustration of two methods to super-charge an engine: (a) Increasing the inlet flow rate, (b) increasing the air charging time. The black line is the increasing of the initial inlet pressure measured without piston movement.

haust ring as shown in the left side of Figure 3.5. The new liner has been manufactured and its performance in motoring cycles was tested by author to assess the scavenging characteristics of this new configuration. The results show the initial pressure can achieve 1.6 bar when the air flow mass rate is 7 g/s.

3.3.2 Supercharging system with intake and exhaust valves

In the above Section, a method of changing the position of the intake ports and exhaust ports derived in order to make the intake ports close later than the exhaust ports has been introduced. This method enabled the LUPOE 2D engine initial pressure to rise to approximately 1.6 bar. However, a further design was required to enable the initial pressure value to be adjustable. Figure 3.6 (a) shows the pressure rise history when the exhaust ports were closed, and the piston was at BDC (Bottom Dead Centre),

It could be observed that the initial pressure increases with time before it reaches a peak value equal the air supply pressure (4 bar). It can be concluded that the initial pressure was governed by the intake pressure increase curve, the pressure-charge time and air supply pressure. Based on this principle, two methods could be used to further adjust the initial pressure. The first one is to increase the inlet flow rate as shown in Figure 3.6 (a). The second one is to increase pressure charging time by extending the time between exhaust and intake valves closing, see Figure 3.6 (b).

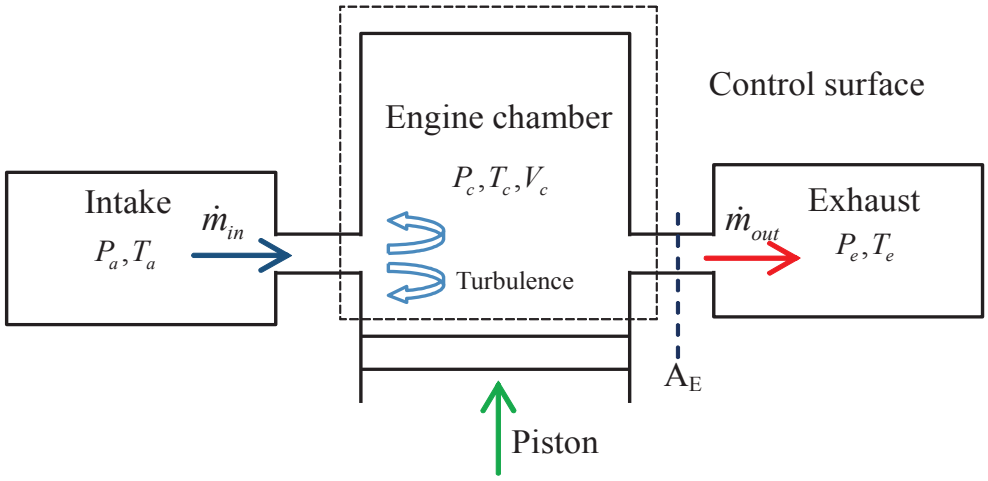

Figure 3.7: Illustration of the initial pressure calculation model with piston movement

Thermodynamics control volume model was used to have a further illustration of these two supercharging process [1]. The control surface consisting of piston and cylinder walls are shown by dotted lines in Figure 3.7. It is connected to two plenum chambers through the inlet and exhaust pipe. The inlet plenum is at high pressure P_a, supplied by the air supply compression; the exit plenum is at a lower pressure P_e, exhausting directly to atmosphere. This model can be described as following Equations:

$$\frac{dP_c}{d\theta} = -\gamma\left(\frac{P_c}{V_c}\frac{dV_c}{d\theta} + \frac{\dot{m}_{in} - \dot{m}_{out}}{m}\right) \tag{3.1}$$

$$\dot{m}_{in/out} = \frac{C_D A_E P_a}{\sqrt{\mathrm{R}T_a}}\left(\frac{P_c}{P_a}\right)^{1/\gamma}\left\{\frac{2\gamma}{\gamma-1}\left[1-\left(\frac{P_c}{P_a}\right)^{(\gamma-1)/\gamma}\right]\right\}^{1/2} \tag{3.2}$$

$$\frac{V_c}{V_0} = 1 + \frac{1}{2}(r_c - 1)\left[R_l + 1 - cos(\theta) - (R_l^2 - sin^2\theta)^{1/2}\right] \tag{3.3}$$

where $\dot{m}_{in}$ is the inlet mass flow rate, $\dot{m}_{out}$ is the exhaust mass flow rate, P_c is the cylinder pressure, V_c is the cylinder volume, θ is the crank angle, ω is the engine speed, A_E is the pipe cross-section area, R is the gas constant, and the ratio of specific heats $\gamma = C_p/C_v$ are constants, P_a is the inlet supply pressure, T_a is the inlet temperature, C_D is a discharge coefficient, R_l is the ratio of connecting rod length to crank radius, r_c is the compression ratio, V_0 is the clearance volume. Equation 3.1 shows the in-cylinder pressure rise induced by piston compression and the difference between mass flow rates in and out

[1] This model is used to illustrate the design concept only, no calculation was presented here.

under assumption of adiabatic compression process, see Appendix B. Equation 3.2 is for one-dimensional steady compressible isotropic flow through an orifice or flow restriction of effective area A_E. Equation 3.3 is the engine volume change (Heywood [1988]). It can be seen that the first method is to increase the $\dot{m}_{in}$ essentially. In order to obtain a higher boosted pressure, the air flow rate has to be increased, it is not an efficient way and a potential drawback is that the large mass flow rate may increase the turbulence in jet-type intake LUPOE 2D engine and further to interfere the observation of pressure effects on flame. The second way to increase the pressure charge time is essentially try to control the $\dot{m}_{out}$ by adjusting the A_E, the most efficiency way is to reduce the A_E , this can be realized by installing a controllable exhaust system valve. This configuration enables the intake mass flow rate $\dot{m}_{in}$ and the initial pressure to be independently varied. The turbulence quantities, which are heavily influenced by inlet flow velocities in the ported engine, can be controlled to the greatest extent. From these reasons, an exhaust system valve was selected to it developed for controlling the boosted initial pressure.

3.3.3 Selection of the exhaust system valve

The challenge for the exhaust valve design is that a contradiction exists between requirements of high flow rate and fast response time. The moving parts of the valve have to be accelerated within a very short period of time to provide a prompt response. Thus the weight of the moving parts that cover the orifice must be kept to a minimum. This reduces the stroke, and flow rate across the valve. Furthermore, the high pressure and temperature of the working fluid also should be taken into account. After a full comparison of different types of valves, a solenoid valve was selected (Ling [2011]). The solenoid valve is controlled by an electric current through a solenoid. The solenoid converts electrical energy into mechanical energy which, in turn, opens or closes the valve mechanically. The pulse signal is very steep which will be enough for fulfilling the requirement of response time. The limitation of solenoid valve is that the flow rate may decrease if the stroke is short. The problem can be solved by using more motoring cycles in an experiment, which means that there will be enough time to allow the fully premixed homogeneous charge from the intake to displace completely the contents of the cylinder.

A commercial solenoid valve with a 12 mm orifice area has been chosen . A test-bed was established to test the air flow rate through the valve, the details have been reported in Ling [2011]. The solenoid valve was installed between the air supply source and the engine intake pipe. A thermal mass flow meter was used to record the flow rate. The solenoid valve opened when it was connected to 24 V power which was controlled by an

Table 3.3: A comparison of the specifications between desired valve and selected valve.

Item	Requirements	Selected valve
Valve cross-section diameter (mm)	36	12
Flow rate (L/min)	400	320
Maximum Pressure (bar)	30	25
Maximum Temperature (^oC)	100	145
Opening/Closing time	24ms@engine speed 1500rpm	5-40ms

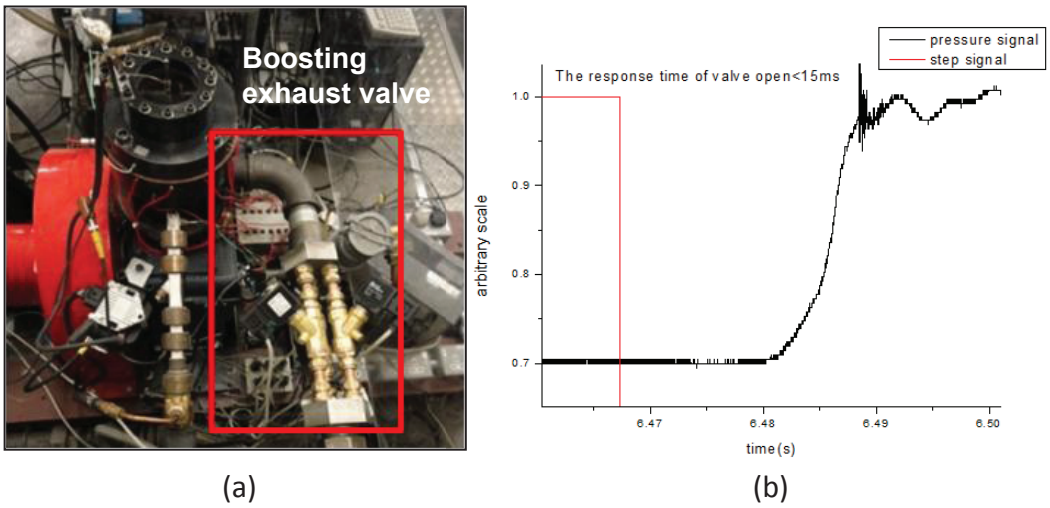

Figure 3.8: (a) Photograph of the installed exhaust system valve on the LUPOE 2D boosted engine. (b) The result of response time test of the selected solenoid valve.

electrical switch. The result showed the flow rate passing by the valve can reach as high as 400 L/min under $\Delta p = 4bar$ [1]. To achieve the required flow rate, three valves were installed in parallel to increase the flow rate. The comparison between requirements and the specification of the selected valve is shown in Table 3.3.

The installed exhaust system valve with the LUPOE 2D boosted engine is shown in Figure 3.8 (a). The exhaust valves are actuated by electromagnets; high traction force and high armature acceleration was required to open valve as rapidly as possible. The response time of the solenoid valve was tested using a pressure signal, and the result is shown in Figure 3.8 (b). It was confirmed that the response time of the valve opening time is shorter than 15 ms, which is sufficient fast for the current application.

[1] It may go higher, but this is the maximum measurement range of the current flow meter

3.4 Engine control and data acquisition system

The control system used on the naturally aspirated LUPOE 2D proved inadequate and unreliable, and a new bespoke system was designed and implemented as a part of this PhD. It is shown in Figure 3.9. It consists of a micro-controller acting as the control system kernel and a personal computer running Labview software for data recording. The use of a micro-controller is an efficient option because it has a simple hardware structure and can easily be programmed. It can be used to replace former complex logical circuits system, reducing the risk of error. The micro-controller Dspic6014A was selected and software MPLAB ICD 3 was used for coding in this study.

The function of micro-controller was to send out trigger signals for ignition, valve operation timing, camera, laser and acquisition system start timing, depending on the input at TDC (Top Dead Centre) and clock signals from the shaft encoder. It also controls the duration time of these devices working and keeps them synchronised. These parameters can be easily changed by setting the values in the micro-controller. In order to keep the experiment safe, the engine running cycles can be pre-set so that the spark and fuel supply would stop once the engine has run the certain pre-programmed number of cycles. An emergency stop function was added in the remote start trigger controller to stop the engine during an experiment. Real-time pressure signal detection also was developed by using the analogue to digital conversion function of the microcontroller. This detection runs at a low scan rate and can stop the engine immediately once it detected the in-cylinder pressure exceeding a safety threshold.

The personal computer was used to record the experiment data. A National Instruments 6110 analogue PCI card, accurate to 12 bits, was connected to convert the analogue signals from dynamic and absolute pressure signals to digital forms. Digital signals were read by a National Instruments DIO-32HS digital PCI card. An operation panel was developed in Labview to achieve synchronous signal recording and visualization. Sampling of all signals was set at 200 kHz. The skip firing method was used in the experiment to improve scavenging and ensure that the firing cycle was free of residual gases. After the firing cycle, several motoring cycles follow, as shown in Figure 3.10. However, this method will waste of the storage memory for recording the useless motoring pressure, so a multi-trigger data recording method was applied in the course of this PhD, as a result of this method, the computer only records the firing cycles and two cycles before and one cycle after the firing cycles.

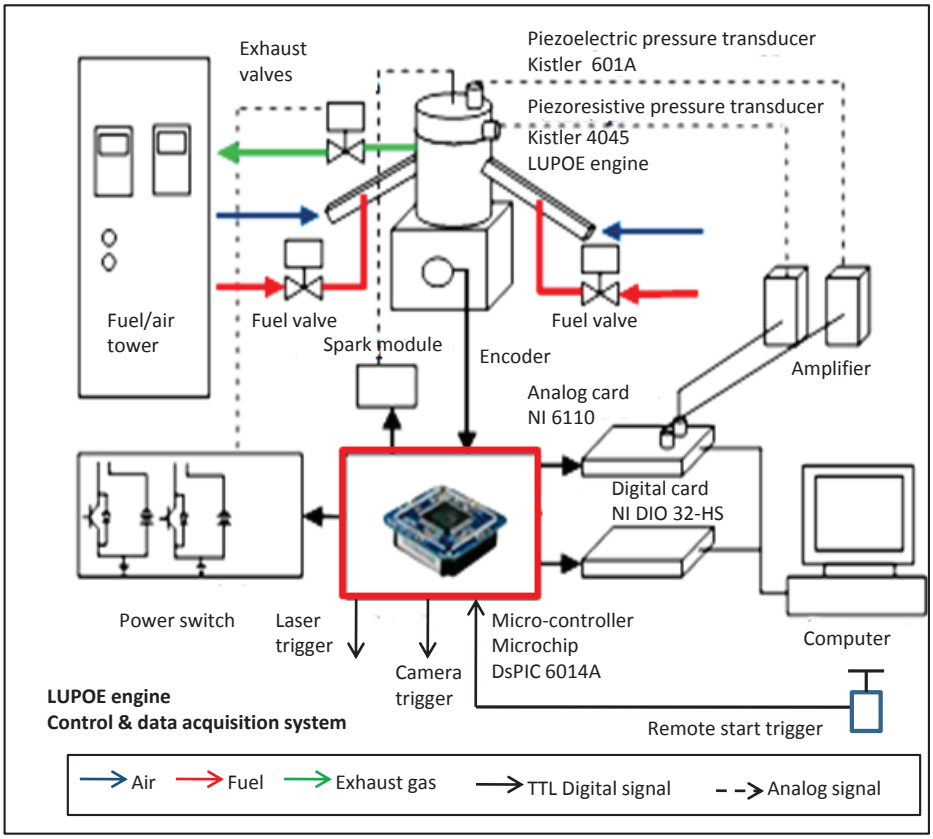

Figure 3.9: Schematic diagram of the LUPOE 2D boosted engine control and data acquisition system.

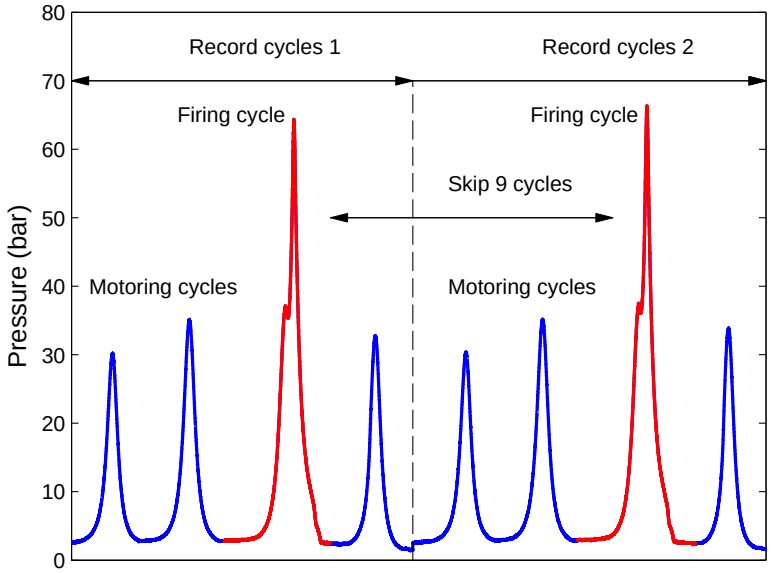

Figure 3.10: Schematic diagram of the engine skip firing and multi-trigger sequence.

3.4.1 Input signals

Two kinds of pressure transducers were used to measure the in-cylinder pressure; one is a piezoresistive 0-2MPa Kistler 4045 A20 referred to as "the absolute transducer" and another is a quartz piezoelectric 0-25 MPa kirstler 601A referred to as "the dynamic transducer". The dynamic transducer has a high response rate to deal with the rapid change in pressure; it was incorporated into the engine head. The charge amplifier Kistler Type 5007 was used to amplify the charge output from transducer ranging from 0-10V. The absolute transducer was mounted at a low point in the engine barrel to measure the pressure during the initial stages of compression as a "reference signal" for dynamic transducer. The absolute transducer signal was amplified using a Kistler Series 4601A piezoresistive amplifier. The mounting position of the absolute transducers was such that it was cut off from the combustion chamber by the ascending piston at 58.6^o bTDC, where pressure was typically 0.25 to 0.3 MPa. Both transducer signals were recorded simultaneously using a data acquisition system. The absolute transducer was calibrated using a dead weight tester where static measurements of voltage against fluid pressure were recorded. The calibration method of the dynamic transducer was performed by applying pressurized nitrogen to the sensor and measuring the voltage output and recording the relation between pressure value and voltage value. The dynamic and absolute pressure signals were converted to an absolute pressure using the following Equation:

$$P_{cyl} = P_{dyn} + (\bar{P}_{abs}(\theta = \theta_{EPC}) - \bar{P}_{dyn}(\theta = \theta_{EPC})) \tag{3.4}$$

where P_{cyl} is cycle pressure, P_{dyn} and P_{abs} are pressure signals from dynamical transducer and absolute transducer respectively. θ_{EPC} is the crank angle at the moment of exhaust port closure. In order to reduce the influence of noise, both the absolute and dynamic pressure transducer signals were averaged over a small time period around exhaust port closure. The results are shown in Figure 3.11. A negligible mis-alignment could be observed during the engine expansion process, which may be caused by a thermal shock.

A Horner 3202 shaft encoder, which produced 1800 pulses per revolution as well as a separate single pulse for Top Dead Centre (TDC), was used to record crank angle (CA) position. Determination of the exact TDC position was crucial for accurate timing. The calibration of shaft encoder had been done before experiment using a capacitive proximity sensor incorporated into the engine head (Ling [2011]).

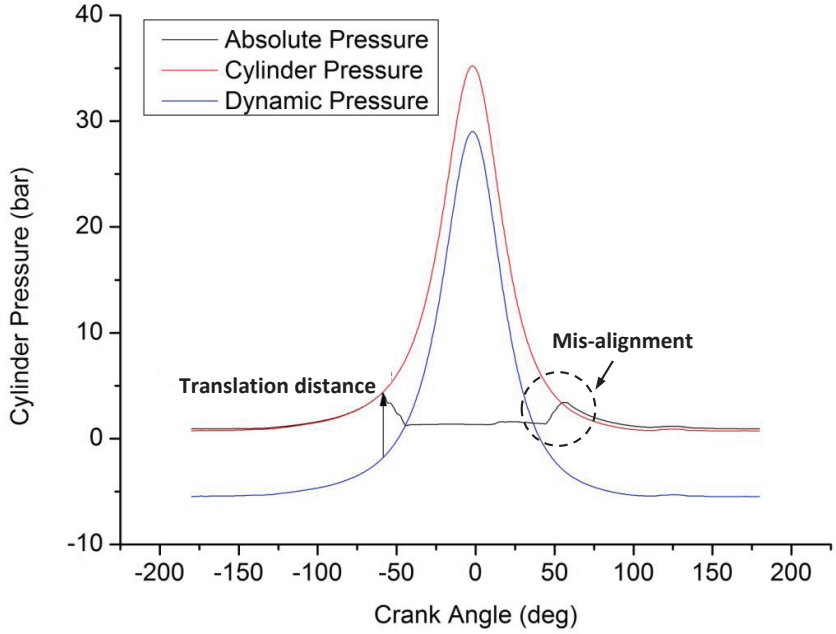

Figure 3.11: Dynamic pressure re-alignment using the absolute pressure signal.

3.4.2 Exhaust valve control scheme

The exhaust valve control timing with measured in-cylinder pressure is illustrated in Figure 3.12. The curves are in-cylinder pressure during motoring and firing cycles. The larger rectangle represents exhaust ports closing time, and the smaller rectangle represents intake ports closing time. Only when the exhaust ports are closed and intake ports are open, can the engine be boosted. It can be seen that this period is very short if exhaust valves were not used. After installing exhaust valves, the exhaust port is closed before the firing cycle in order to prolong the pressure-charge time thus increasing the initial pressure until spark timing. Due to the movement of the piston, which can open and close the ports too, the duration of these closing time, can be used to overlap with the valve closing time. This approach can compensate for the delay time of exhaust valve closure when the piston moves to TDC in a motoring cycle and closes all ports. The initial pressure of firing cycles can be adjusted by controlling the number of motoring cycles during which the exhaust valves were closed. The exhaust valves open again after spark has fired, this allows the exhaust gas to leave the engine chamber. Then the process starts all over again. This boosting method has high efficiency and avoids changing the turbulence level to the greatest extent which will be confirmed in Chapter 6.

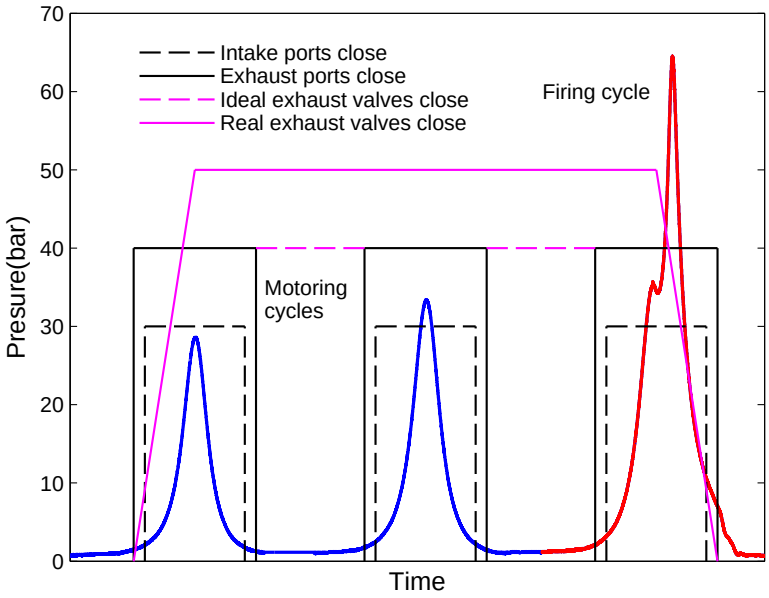

Figure 3.12: Illustration of exhaust vale control scheme.

3.4.3 Micro-control code structure

The structure of the micro-controller program employed a polling method instead of an interrupt method. This is because all inputs and outputs signals have a pre-set timetable, so the polling method is easier to program and maintain. As a sample, Figure 3.13 shows the flow chart of the valve control program with its input and output to the hardware. Other signals such as camera and laser triggers have a similar structure. The purpose of this program is to read the input signal, to determine the valve opening and closing time and to send a signal to the valve. The input signal includes a clock signal and TDC signal. The first reading is from the shaft encoder driven by the engine crankshaft. The resolution of these pulses is 0.2 degree per pulse. Counting of the individual crank angle pulses will provide the control time for valve opening and closing, which is independent of engine speed. The TDC signal is a once-per-cycle pulse signal, it is sent when the piston is at the top dead centre. When the program starts working, it runs a loop to wait for the trigger signal. Once received the start trigger signal, the controller reads the TDC signal to count the number of skip firing cycles. If a cycle corresponds to a firing cycle, it will jump to the next block to read the clock signal, then a counter counts the shaft encoder crank angle degrees and continuously compares the instantaneous count with the desired value for the valve opening, When the count is equal to the desired value, a signal is sent to the power switch which switches the power supply to the electromagnet opening the valve. In the same way, the valve will be closed when the count reaches the desired value at which the electromagnet should be switched off.

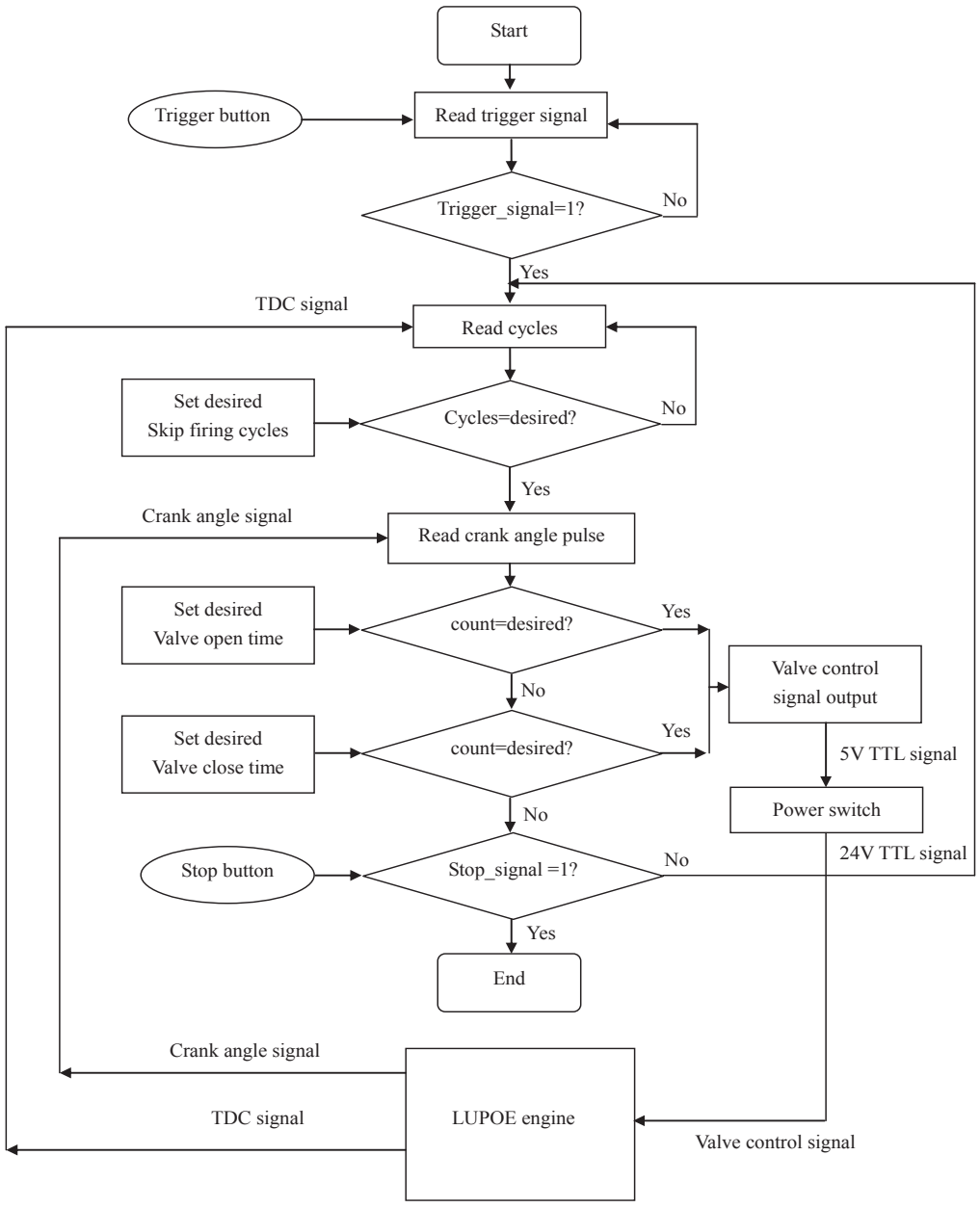

Figure 3.13: Flow chart for the micro-controller code for exhaust valve control.

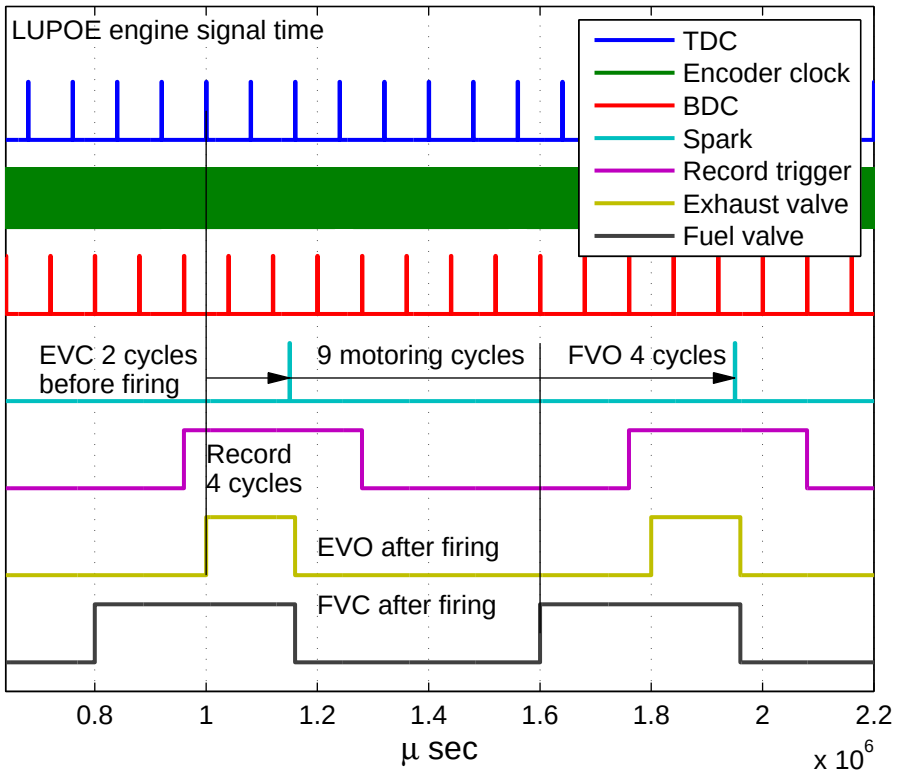

Figure 3.14: The LUPOE 2D boosted engine timing captured by the data acquisition system. EVC: Exhaust valve close, EVO: Exhaust valve open; FVC: Fuel valve close.

3.4.4 Data acquisition system timing

The timing diagram of the LUPOE 2D Data Acquisition System (DAS) is shown in Figure 3.14. The first line is the Top Dead Centre (TDC) signal, the second is crank angle signal, also used as a clock time for the micro-controller code. These two signals are the output signal from the shaft encoder. The Bottom Dead Centre (BDC) signal was calculated based on these two signals. The firing cycle was decided and the spark plug was triggered at the set spark timing by the microcontroller. The exhaust valves were controlled by the scheme described in Section 3.4.3. In most cases, only 4 cycles around a firing cycle were recorded. It should be noted that there is a fuel valve installed between the fuel supply line and the injection port in the each intake pipe, in order to switch off the fuel supply after a firing cycle. The reason for this is that it was found that the hot exhaust gas left in the firing cycle may cause a furious auto-ignition with fresh air-fuel mixture in the subsequent cycle.

3.5 Pressure data processing and analysis

3.5.1 Re-sample of pressure data

The raw data of the absolute and dynamic pressure and TDC, BDC, ignition and shaft encoder clock signals were recorded based on time. A Matlab program has been developed in a previous study (Hattrell [2007]) to achieve re-sampled all raw data into cylinder pressure vs. crank angle format. User input of scan rate was required to finish this process. The incomplete last cycle will be discarded or compensated by using the advance complete cycle data. Since the fluctuation of engine speed, the number of recoded data in each cycle is not same. The largest number of cycle should be found and insert zero into other cycles to make them same, then, the re-sampling of time based into crank angle based data was achieved with 0.2^o CA intervals. Thereafter, the data was chopped into individual cycles using the BDC signal. The flow chart of the pressure data processing is shown in Figure 3.15.

Cycle-to-cycle variations are an intrinsic phenomenon of engine combustion, this is mainly caused by different burn rates, which result in variations in the cylinder pressure and unburnt temperature history in the cylinder. In order to take the cycle-to-cycle phenomena into analysis, peak pressures from each cycle were calculated to obtain the mean and the standard deviation of these values. Then, three regions were classified: close to the mean pressure as a medium cycle and close to the mean pressure plus and minus two standard deviations respectively (plus is fast and minus is slow).

3.5.2 LUSIEDA reverse thermodynamic analysis

The pressure data was further analyzed using a reverse thermodynamic Fortran based code named as LUSIEDA (Leeds University Spark Ignition Engine Data Analysis). Most subroutines used within LUSIEDA are from the LUSIE thermodynamic simulation software (Leeds University Spark Ignition Engine). Both LUSIE and LUSIEDA have been developed over the years by the Combustion group at the University of Leeds. See Abdi Aghdam [2003]; Desoky [1981]; Hattrell [2007]; Hynes [1986]; Langridge [1995] for more details about LUSIE and LUSIEDA software. In this study, LUSIEDA was used solely as a processing tool for calculating burning rates and other combustion parameters. Here below, follows a brief summary of the main features relevant to the study.

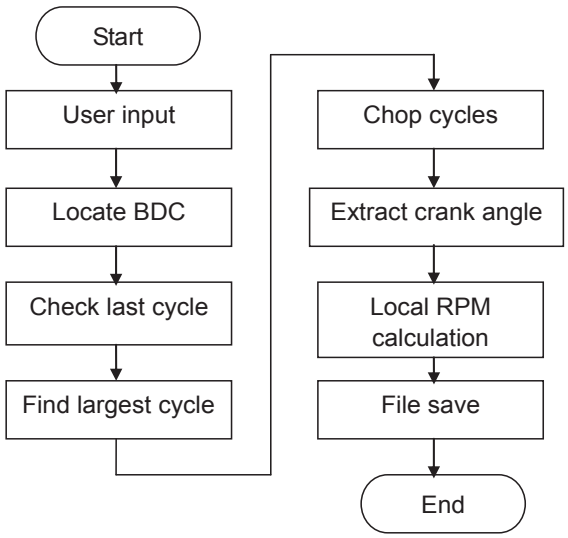

Figure 3.15: Flow chart of pressure signal processing

For a two-zone model application, the assumptions involved with the LUSIEDA are the following ones: (a) In-cylinder mixture has ideal gas behaviour. (b) In-cylinder mixture, temperature and pressure are uniform prior to combustion. (c) The cylinder was separated into two zones i.e. burned gas and unburned gas during combustion, flame has an infinitesimally thin flame thickness. (d) There is no heat transfer between burned and unburned zones. (e) Temperature and chemical composition are homogeneous within both zones. (g) Flame propagation has a spherical shape. Figure 3.16 illustrates the models assumptions and sub-models used in the LUSIEDA. The engine combustion was divided into compression, combustion, and expansion processes. Each process consisted of several basic sub-modules, such as piston motion, heat transfer, blow-by, and pressure equalizing. Each event changes the pressure in the cylinder:

- Piston motion: The temperature and pressure in the cylinder are assumed to be isentropic compression or expansion with a frozen mixture composition during the piston motion. The contribution of piston motion to pressure change is represented as $\triangle P_{pm}$;
- Heat transfer: Woschni [1967] model was adopted, and it was assumed that the heat transfer occured by convection following Newtons law of cooling. The pressure has a decrease of $\triangle P_{ht}$ due to hear release;
- Blow-by: Air-fuel mixture can leave or re-enter the cylinder, through top land crevice volume, piston ring gaps, and inter-ring crevice volumes between the piston and cylinder walls. This process results in a pressure decreasing of $\triangle P_{bb}$.

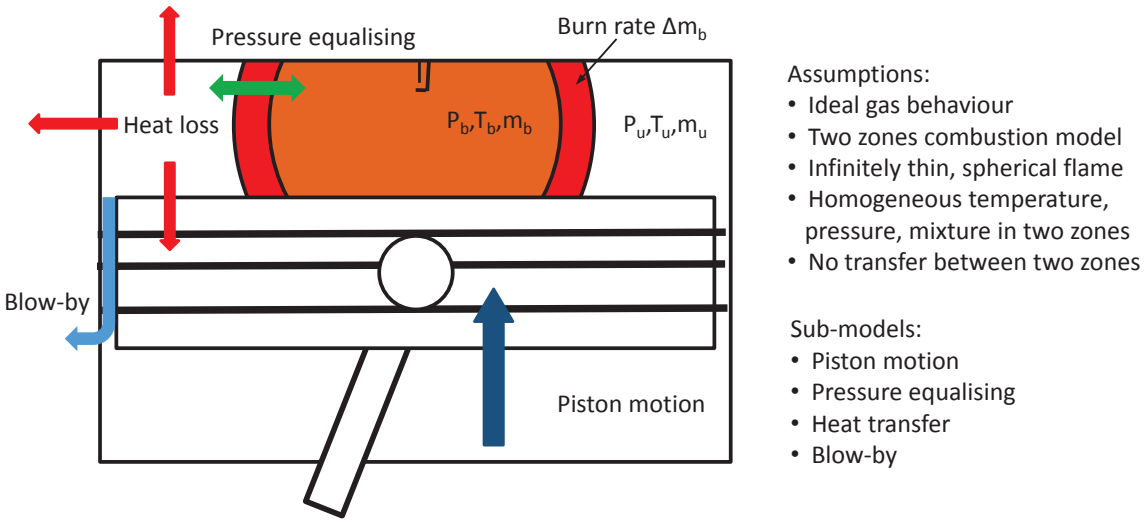

Figure 3.16: Illustration of engine combustion models in the LUSIEDA

A burning rate calculation is the main task of the LUSIEDA code. A certain amount of fuel burned $\triangle m_b$ at two consecutive crank angles causes a change in pressure, which is the difference between measured experimental firing cycle's pressure $\triangle P_{exp}$ and the pressure change $\triangle P'_{mot}$ caused by the engine motoring in the condition of the firing cycle. Furthermore, this motoring pressure change comprised all contributions from piston motion $\triangle P_{pm}$, heat transfer $\triangle P_{ht}$ and blow by $\triangle P_{bb}$:

$$\begin{aligned} \triangle P_{comb}(\triangle m_b) &= \triangle P_{exp} - \triangle P'_{mot} \\ &= \triangle P_{exp} - (\triangle P_{pm} + \triangle P_{ht} + \triangle P_{bb}) \\ &= P_{i+1} - P_i - (\triangle P_{pm} + \triangle P_{ht} + \triangle P_{bb}) \end{aligned} \tag{3.5}$$

where P_{i+1} and P_i are the experimental cylinder pressures at two consecutive crank angles. Once the difference between the simulated pressure and the experimental pressure is larger than a predetermined error ε_{set1}, the firing cycle simulation starts. A certain amount of burned mixture $\triangle m_b$ is guessed, and a P_{sim} was predicted with an assumption of a constant volume adiabatic combustion process. The P_{sim} was compared to the experimental firing pressure to calculate the ε_p, then an iterative bisection method for the determination of $\triangle m_b$ runs until the minimum error ε_{set2} is achieved. Each sub-model needs to be re-calculated with the change of flame geometry and thermodynamic conditions. The "Pressure equalization" subroutine, developed by Abdi Aghdam [2003], was used to keep uniform the pressure in the combustion chamber. Figure 3.17 shows the sequence of events during a firing cycle analysis in LUSIEDA. Before firing cycles analy-

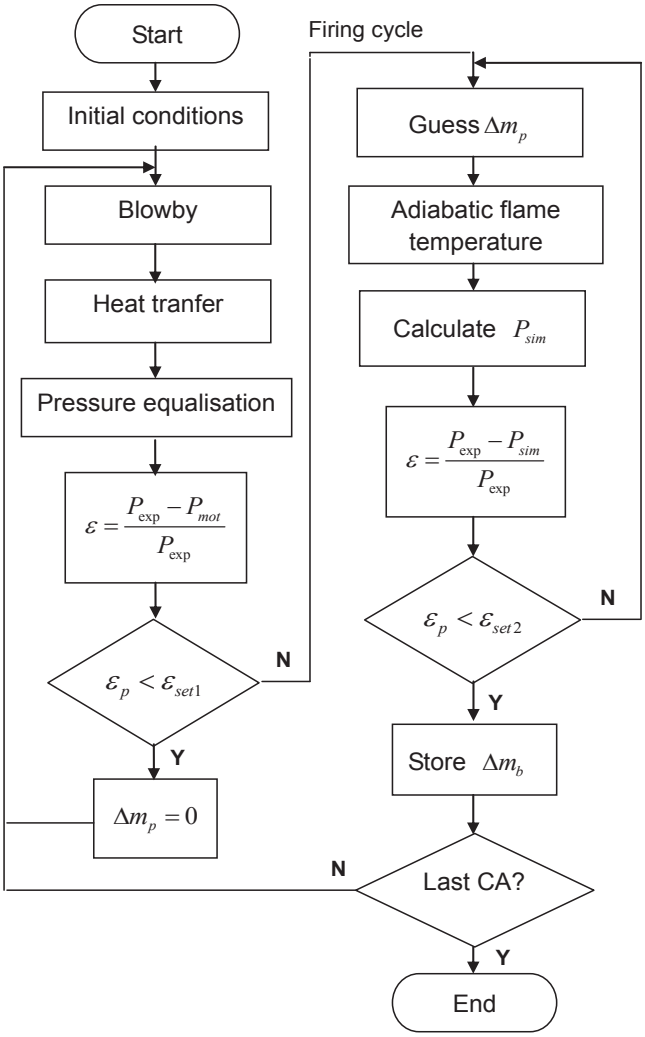

Figure 3.17: Flowchart showing the sequence of events during a firing cycle analysis in LUSIEDA, reproduced from Roberts [2010].

sis, a motoring simulation was required to validate the heat transfer, blow-by, and other engine operation initial conditions parameters setting. Decoupling of the cylinder pressure and temperature rise due to piston motion from that due to combustion have been shown to be vital for a successful LUSIEDA calculation (Roberts [2010]).

Thermodynamic analysis of measured cylinder pressure in LUSIEDA gives a flame radius which lies between the entrainment and end of combustion radius. An example of the burned gas radius calculated from the pressure trace processed by LUSIEDA is shown in the left side of Figure 3.18, where the entrainment flame radius derived from the same cycle's CH*images is also presented. A small radius about 5 mm at the spark timing existed due to the error between the experimental pressure and simulated pressure, only

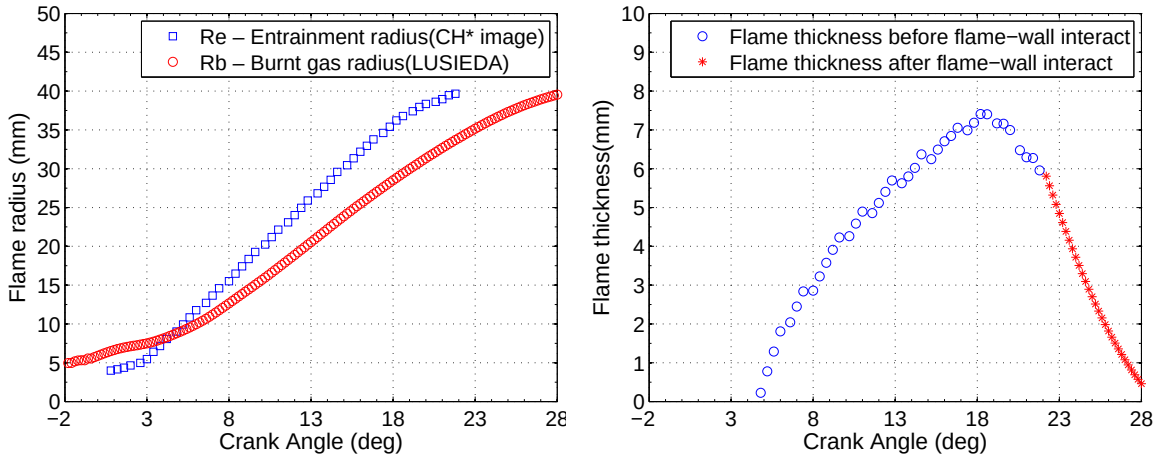

Figure 3.18: Samples of the flame radii derived from LUSIEDA and CH* chemiluminescence image (left), and the flame thickness calculated using the difference between these two flame radii. The data are from the LUPOE 2D boosted engine running at a speed of 750 rpm and a spark timing 2^o bTDC, stoichiometric iso-octane fuel.

a minimum mass could burn at this condition, therefore this error was negligible. It can be seen the difference between flame radii derived from images and pressure, this difference was assumed to be the flame thickness as shown in the right side of Figure 3.18. More descriptions of this flame thickness will be given in Chapter 6.

Chapter 4

Optical measurements and data processing

This Chapter presents the optical measurement techniques and their data processing methods to characterize the flow field and flame propagation process. Firstly, the principles and relevant experimental considerations in the Particle Image Velocimetry (PIV) measurement are introduced. Secondly, two flame imaging methods are described: the CH* chemiluminescence imaging, and a two-dimensional laser sheet visualization technique [1]. Data processing methods for these optical measurements are also developed.

4.1 Flow field measurement

Time-averaged single-point measurements using Laser Doppler Velocimetry (LDV), and Hot Wire Anemometry (HWA), have been applied to the study of in-cylinder flow in internal combustion engines (Witze [1980]), which provided a wealth of useful information. However, flows in-cylinder are highly complex, unsteady, and exhibit cycle-to-cycle variations, hence, single point measurements are not sufficient for the investigation of in-cylinder flows in detail. Therefore, the measurement techniques of the two dimensional flow fields have been developed, such as Particle Image Velocimetry (PIV). This

[1] It was also called "laser tomography" or "Mie scattering" in the literature, the term "laser sheet method" was adopted in this study.

technique provides new insights into flow processes within internal combustion engine cylinders.

Particle Image Velocimetry was first applied to investigate the high axial swirl in an internal combustion engine by Reuss and Rosalik [2000]. This work showed the method to calculate instantaneous vorticity and strain rate fields ahead of the flame front, the resolution achieved was of the order of 1 mm. Subsequently, Reuss and Rosalik [2000] examined the cyclic variability in a semi quantitative manner by capturing the flow field in each cycle. Towers and Towers [2004] applied a high speed PIV system with a framing rate of 13.5 kHz and a spatial resolution of 128 x 128 pixels to study cyclic variability of in-cylinder flows using an optical engine with a head having two inlet valves. The results showed that changing the axial swirl level has a significant influence on the cyclic variability of the flow in the latter half of the compression stroke. The whole field had a maximum velocity of nearly 10 m/s. Fajardo and Sick [2009] developed a high-speed PIV technique using two high-repetition rate diode-pumped Nd:YAG lasers operated at 355 nm and a CMOS camera with a framing rate of 12 kHz and a spatial resolution of 480 x 480 pixels to measurements of velocity fields near the spark plug in a firing engine at a rate of 6 kHz for 500 consecutive cycles.

For a Particle Image Velocimetry system, a continuous or pulsed laser light source is used to illuminate flow mixing particles in a thin measurement plane, traces of the particles are recorded and a comparison between two pictures is conducted using a statistical correlation technique to calculate the velocity of the particles. Significant interpolation or ensemble averaging of many data sets is required to re-construct the information of two dimensional velocities. Since individual particle images do not need to be identified, a high particle seeding density can be used to gain a high resolution two dimensional flow velocity map (Raffel et al. [2007]). Owing to these advantages, PIV was chosen as the two-dimensional flow visualization technique in this research.

4.1.1 PIV experimental setup

The PIV experiment consists of several subsystems: the proper tracer particles, a double-pulse laser, a camera and image evaluation process. Figure 4.1 illustrates the PIV experiment setup for the in-cylinder flows measurement in the LUPOE 2D engine in a two-dimensional horizontal plane, with its data process. In this section, the setup of PIV system is described firstly.

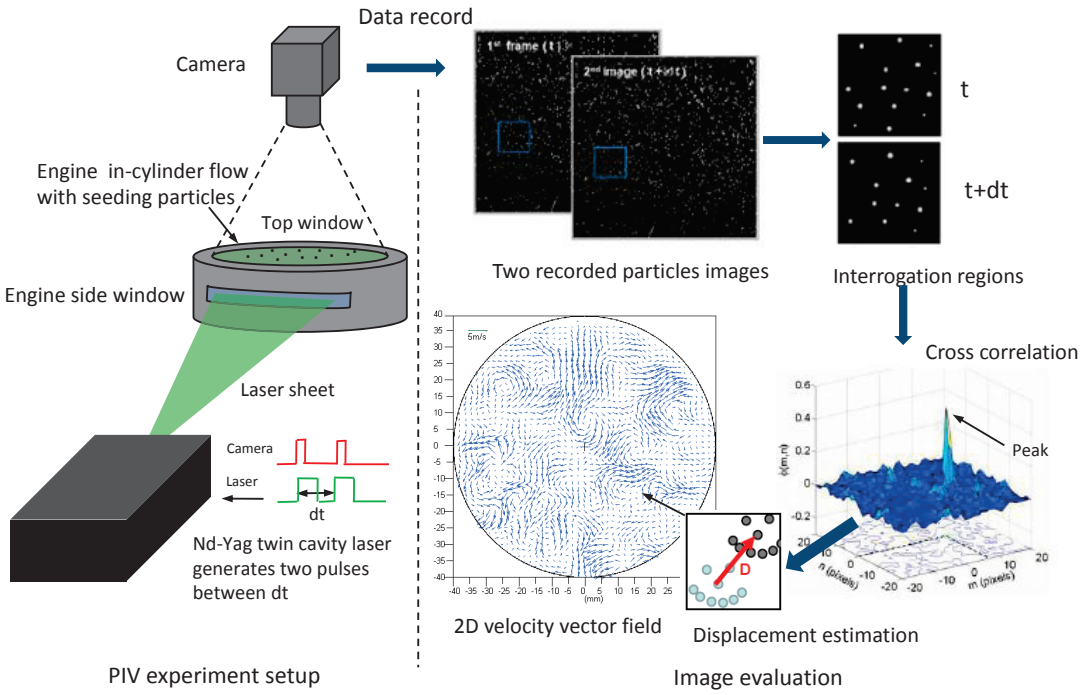

Figure 4.1: A schematic diagram of PIV experiment setup, image evaluation process, and a 2D velocity vector field from LUPOE 2D engine running at 750 rpm.

The seeding particles should be chosen carefully to ensure which they are able to move with local flow velocity, and scatter sufficient light in the Mie region to be recorded. Usually, a compromise between a small particle size for accurate flow tracking, and a large particle size for increased light scattering, should be reached. By using the Equations 4.1 and 4.2, the lag in the velocity between the fluids motion V and the particles motion U, under an acceleration dV/dt in the flow can be estimated. τ is the relaxation time, which must be smaller than characteristic time scale of the flow (Raffel et al. [2007]).

$$U - V = \tau \frac{dV}{dt} \tag{4.1}$$

$$\tau = \frac{d_p^2}{18} \frac{\rho_p}{\mu_f} \left(1 - \frac{\rho_f}{\rho_p}\right) \tag{4.2}$$

where d_p is the diameter of particle, ρ_p is the density of particle, ρ_f is the density of fluid, μ_f is the viscosity of fluid.

In this study, olive oil was used as seeding, it has a density of 920 kg/m^3. The tracer particles are generated by a liquid droplet seeding system, and mixed with air in the intake pipes before they are introduced into the engine chamber. The details of

the seeding generator have been introduced in Section 3.2. The generated diameter of particles is between 0.5-5 μm depending on the experimental conditions. Two nozzles are used, and the amount of air fed to the seeding generator is about 5-10 $\%$ of the total intake air mass flow rate; the pressure drop across the seeding system is kept constant at 1 bar. The air density is 1.23 kg/m^3 and its dynamic viscosity is $17.9\times10^{-6}N.s/m^2$ (Dawood [2010]). By supposing an instantaneous acceleration in the flow of 1000 m/s^2 and using Equations 4.1 and 4.2, the velocity lag is approximately O(10^{-3}) m/s with a relaxation time O(10^{-7}) s. This indicates that the particle movements follow the fluid flow accurately and without lag, while also providing excellent scattering light intensity. The density of seeding needs to be well controlled. In fact, if the particle density is too high, overlapping between particles will occur in the recorded image, resulting in the failure of the correlation calculation. If it is too low, the method becomes a much more laborious PTV measurement. The optimised number of particles in each interrogation grid is about 8 particles (Raffel et al. [2007]).

The tracer particles are introduced into the engine cylinder, and illuminated twice by using a double-pulse laser light sheet through a side window in the LUPOE 2D engine head, see Figure 4.1. A double pulsed Neodymium-doped Yttrium Aluminium Garnet (Nd:YAG) laser producing a 532 nm frequency and maximum output power 400 mJ/pulse laser beam was employed to illuminate the flow field. The laser beam was converted to a sheet using an integrated optics lens system. The configuration of this integrated optics lens system for laser sheet generation is shown in Figure 4.2. It consists of a Plano-concave cylindrical lens with a focal length f_1 = -20 mm, and two telescope lenses which enable the laser beam to reach the focus distance of f_2 = 300-2000 mm. The diameter of the laser beam at the cylindrical lens is about d = 5 mm, therefore, the aperture angle α in the Figure 4.2 can be calculated as 14^o. In order to gain a sheet width close to the diameter of cylinder bore (80 mm), the distance between cylindrical lens and the centre of the cylinder bore was adjusted to 500 mm. Because of the divergence of the laser beam, the laser sheet could not cover the whole area of cylinder chamber plane, thus some flow velocity near the cylinder wall will be lost. Nevertheless, the information on flow velocities, collected in the central region available, could still be used to characterize the whole flow field, as it is the turbulence around the spark region which arguably is the main influence for the flame propagation. It is also important to control the thickness of the light sheet. The thin laser beam ensures that the particles recorded are from a same plane rather than a surrounding volume, and this increases the accuracy of velocity measurement. The thickness of the laser sheet was adjusted to be approximately 1 mm at the focus position inside the cylinder, and it passed between the spark plug and Top Dead Centre position of the piston. This was achieved by adjusting the focus of the telescope

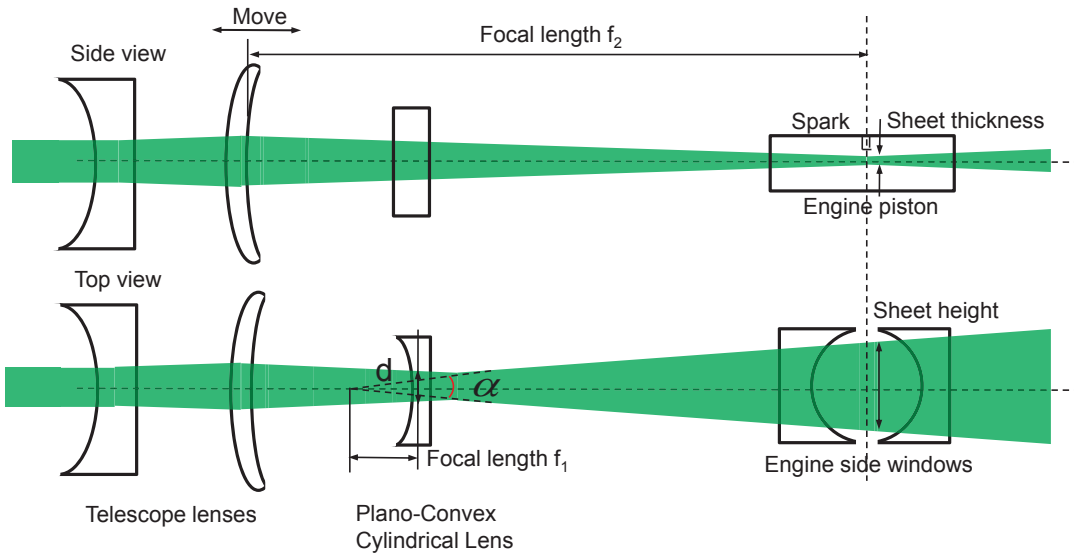

Figure 4.2: The configuration of lens for laser sheet generation.

lenses. The laser beam thickness was calibrated by using black paper to record the laser beam position in the centre of cylinder chamber. The high power laser beam could burn the paper and leave a trace, from which it is possible to detect the position and the size of the laser beam. Usually, the duration of the single laser pulse needs to be short enough to capture the motion of the particles during the pulse exposure. The interval delay time dt between two pulses depends upon the mean flow velocity and the magnification of image. The optimised value should be long enough to allow a particle to move out of a peak pixel size in the image, but shorter than a quarter of the selected interrogation window size.

High-resolution digital, or film cameras, are usually used to record the light scattered from the tracer particles. It is possible to capture more than 1000 PIV recordings per minute with modern charge coupled device (CCD) cameras (1000×1000 sensor elements and more), and even do acquisition in the kHz range with complementary metaloxide semiconductor (CMOS) sensors. For modern digital PIV, the output data can be transferred to a computer directly. In this study, the scattered light was recorded by a CCD camera, Imager Pro VC04. A 50 mm Nikon lens was used and adjusted to view the whole flow field at the top of the laser sheet. The camera has 1600×1200 pixels resolution, the image area is the full piston bore size 80×80 mm. A calibration should be conducted to find the image reference position and magnification ratio. Here, the spatial resolution of the measured velocity field is about 0.067 mm/pixel. An estimation of the resolved minimum flow structure can be obtained by using the mean turbulent velocity and the integral scale of turbulence within a naturally aspirated LUPOE engine. These values

have been measured as about U = 1 - 5 m/s, L_i = 10 mm by Hussin [2012]. The Taylor microscale and Kolmogorov length scale can be estimated as O(0.1) mm from Equations 2.15, and O(0.01) mm from Equation 2.16, respectively. The minimum interrogation size that can be used without accuracy loss is 16 pixels square, with 50% overlap. Thus, the minimum resolution of a vector velocity is about O(0.5) mm. Therefore, it is impossible to study the turbulence structures smaller than Taylor and Kolmogorov length scales. However, for investigating the bulk flow behaviour with the new boosting system, this experimental setup still has sufficient spatial resolution to detect the large flow structures.

There are two images recorded for each engine cycle. The first image shows the initial positions of the particles, and the second records the final positions after the particles movement in the flow. These two trigger signals for the camera are synchronized with the laser pulse, as shown in the Figure 4.1. The software was set up in such a way that the first frame of the PIV image pair was exposed for microseconds and then the second image was exposed for a longer period of time to record the image (Dawood [2010]). The noise could be reduced using a mechanical shutter or preventing external light to reach the camera during the experiment. A low pass optical filter attached to the camera was used to allow the passage of the scattered laser light whilst prevent any illumination produced by the flame. The lab lights should be switched off during the experiment, and black plates covered the space around the engine to reduce the light reflection from the surroundings.

4.1.2 Image evaluation

After the digital PIV images are recorded, interrogation areas are created by dividing the image into many small subareas. It is assumed that all the particles within one interrogation area have homogeneous movements between the two illuminations. Statistical methods, such as auto and cross correlation, are implemented to derive the local displacement vector from each two sets of interrogation regions. In most commercial PIV software, correlation plane calculation is achieved in the frequency domain by using Fast Fourier Transforms (FFT) (Raffel et al. [2007]), it can be represented as:

$$R_{II} \Leftrightarrow \hat{I} \cdot \hat{I}'^{*} \tag{4.3}$$

where $\hat{I}$ and $\hat{I}'$ are the Fourier transforms of the function I and I', respectively. The location of the peak in the correlation plane corresponds to the average particle displacement, see Figure 4.1. Then, a single average particle displacement and velocity could be

Table 4.1: Specifications of PIV setting

Item	Value
Seeding	
Seeding type	Olive oil
Seeding size	1×10^{-6}m
Laser	
Laser type	Nd:Yag laser
Wavelength	532 nm
Pulse Duration	5 ns
Maximum repetition rate	10 Hz
Energy per pulse	400 mJ
Camera	
Camera type	8-bit CCD
Pixel size	$7.4 \times 7.4 \mu m$
Max resolution	1600*1200 pixels
Frame rate	$30 fps$
Operating setting	
Image region width	80×107mm^2
Image time separation (dt)	$60 \mu m$
interrogation regions	32×32 pixels with 50% overlap
Paticle image size	1-2 pixels

calculated. This process of an interrogation area is repeated for the whole PIV images as illustrated in Figure 4.1. Finally, a two-dimensional velocity vector field can be obtained. A commercial software, "Davis", was adopted to process the raw images to a vector image by following the above steps. An overlap of 50% in 39×31 interrogation areas is applied, and 1209 vectors could be generated in the each image. The multi-iteration evaluation also is used to achieve a higher accuracy and signal to noise ratio of each flow field image. An example of a 2D velocity vector field from LUPOE 2D boosted engine running at 750 rpm is shown in Figure 4.1.

It should be noticed that the phenomenon of "Peak locking" might occur when the measured displacement of a particle is biased towards nearest integer pixel value (Raffel et al. [2007]). To overcome this problem, the Gaussian peak fit method is generally applied to appropriate the discrete pixels data, and estimating the true sub-pixel displacement. Thus, this requires the particle image size to be 2 or 3 pixels. However, due to diffraction of the light through the lens, the size of the particle image that is recorded by

the camera does not depend solely upon lens magnification. It is also related to the laser wave length and the lens aperture. The approximate particle image size in a single lens system can be calculated using the equation of light diffraction (Raffel et al. [2007]):

$$d_i = \sqrt{(M \times d_p)^2 + (2.44(M+1)f\lambda)^2} \tag{4.4}$$

where: d_i is the particle image diameter, d_p is the true particle diameter, M is the image magnification, f is the f number of the lens, i.e. ratio of focal length to lens aperture, and λ is the wavelength of incident light. The first item is a geometric image and the second is the point spread function. In order to achieve high accuracy, it has been shown that the optimum particle image size should be larger than two pixels, so that sub-pixel displacement can be resolved and the peak locking can be eliminated. For this study, olive oil particles were used. The image magnification is approximately 0.11. The wavelength of laser is fixed at 523 nm. In order to achieve the full bore size flow field and over 2 pixels of particle size in the image, f-number should be adjusted to be above 10. When increasing the f-number, the light illumination from particles will decrease quickly, thus the laser pulse energy needs to be increased to compensate the loss of scattering from seeding at a high f-number, this will cause the strong laser light reflection from cylinder wall. Under these considerations, the f-number was set at 5.6. The particle image size is about 1-2 pixels, therefore the risk of peak locking exits due to the larger observation area. The evaluated resultant peak locking error is equal to a half value of maximum velocity achieved in one pixel with dt. For an instance, the maximum flow velocity is expected to be 5-10 m/s at 750 rpm. The error caused by peak locking is estimated to be 0.5 m/s. Although this magnitude of error is far from ideal, it is still enough to demonstrate the general flow motion behaviour. Moreover, the practical experimental tests showed better performance of seed recolonization in the image than that from the theory calculation. As a result, this peak locking risk was accepted in this study. The final settings of PIV experiment are listed in Table 4.1.

4.1.3 Data post processing

The results of PIV experiment were stored as a number of matrices, which represent the two-dimensional vector velocities of a flow field. The size of one matrix is equal to the image resolution of 203×154 pixels. Further post-processing is mostly dependent on the purpose of experiment to obtain the desired information. For the description of turbulence in an engine cylinder, the statistical methods presented in the Section 2.1 were used.

In general, the mean velocity varies with time and position, thus there are two methods to evaluate flow field variables: ensemble and spatial averaging (Larsson [2009]). In this study, the ensemble averaging method was adopted. The data calculations have been programmed using Matlab with some functions from an open source package PIVMAT (Moisy [2007]). The ensemble average velocity was calculated at each point on the interrogation grid, and hence the results were often presented as maps, such processing was mostly used to establish the flow properties of the engine. The ensemble mean velocities were calculated as:

$$\bar{U}_x(x,y) = \frac{1}{N_{im}} \sum_{i=1}^{N_{im}} U_x(x,y,i) \tag{4.5}$$

$$\bar{U}_y(x,y) = \frac{1}{N_{im}} \sum_{i=1}^{N_{im}} U_y(x,y,i) \tag{4.6}$$

where $U_x(x,y,i)$, $U_y(x,y,i)$ are the instantaneous velocities at the grid point (x,y) in the x and y direction respectively. i indicates the number of vector flow fields, and the total number of images is N_{im}. Ensemble averaging removed the large-scale flow variation due to turbulence and cyclic variation present in the velocity fields for individual cycles. While the formulation above is written for Cartesian coordinates, it was also possible to use polar coordinates. The velocity magnitude S is defined as:

$$S = \sqrt{U_x^2 + U_y^2} \tag{4.7}$$

The time-average fluctuation components, u_x, u_y are calculated as:

$$u_x(x,y,i) = U_x(x,y,i) - \bar{U}_x(x,y) \tag{4.8}$$

$$u_y(x,y,i) = U_y(x,y,i) - \bar{U}_y(x,y) \tag{4.9}$$

from which the RMS turbulent velocity,$u_x^{'}$ and $u_y^{'}$ are calculated as:

$$u_x^{'}(x,y) = \left\{ \frac{1}{N_{im}} \sum_{i=1}^{N_{im}} [u_x(x,y,i)]^2 \right\}^{\frac{1}{2}} \tag{4.10}$$

$$u_y^{'}(x,y) = \left\{ \frac{1}{N_{im}} \sum_{i=1}^{N_{im}} [u_y(x,y,i)]^2 \right\}^{\frac{1}{2}} \tag{4.11}$$

as was shown in the introduction in Section 2.1, there exist four kinds of integral length scales depending on velocity direction u_x or u_y, and correlation direction "transverse" or "longitudinal" (Hussin [2012]). The corresponding correlation coefficients can be represented as R_{xl}, R_{xt}, R_{yl}, R_{yt}, they are calculated from the fluctuating velocity values at two separated positions (x, y) and $(x + \zeta, y)$ in X-direction or (x, y) and $(x, y + \beta)$ in Y-direction. β and ζ are the variable separation distances. Here, only the equations based on u_x are given:

$$R_{xl}(x, x+\zeta) = \frac{1}{(N_{im}-1)} \sum_{i=1}^{N_{im}} \frac{u_x(x,y,i)u_x(x+\zeta,y,i)}{[u_x'(x,y)u_x'(x+\zeta,y)]} \tag{4.12}$$

$$R_{xt}(y, y+\beta) = \frac{1}{(N_{im}-1)} \sum_{i=1}^{N_{im}} \frac{u_x(x,y,i)u_x(x,y+\beta,i)}{[u_x'(x,y)u_x'(x,y+\beta)]} \tag{4.13}$$

Then the longitudinal integral length scale L_{xl} and transverse integral length scale L_{xt} which have been illustrated in Figure 2.2, are calculated from:

$$L_{xl}(x,y) = \int_0^{\zeta=0} R_{xl}(x, x+\zeta) d\zeta \tag{4.14}$$

$$L_{xt}(x,y) = \int_0^{\beta=0} R_{xt}(y, y+\beta) d\beta \tag{4.15}$$

4.2 Flame imaging

Flame imaging experiments have been applied in optical spark ignition research engines for many years with methods including natural light, schlieren, shadowgraph, laser sheet Mie scatter imaging and Planar Laser Induced Fluorescence (PLIF). Early investigations used the schlieren technique or natural light imaging (Gatowski et al. [1984]) to investigate the combustion phenomena in cylinder.

Shadowgraph and schlieren techniques depend on a refraction index change caused by density gradients in the combustion mixture to generate an image on a screen. A light

source and optical lens are required to generate a parallel beam of light. The entrainment flame front can be obtained from the image due to substantial difference between burnt and unburnt gas densities instead of flame luminosity, the sensitive requirement of camera might be not important. The difficulties of applying the shadowgraphy and schlieren techniques are the requirement of optical access through the cylinder. In an engine, configuration of a mirror installed on the top of the piston crown with an optical head access is often adopted. However, the vibration of mirror during engine running would bring errors into measurement, and the mirror surface degradation caused by combustion makes this method very risky for a supercharged engine.

In natural light imaging, the chemiluminescence, i.e. the emitted light from flame species is the only source for detection. This method has many advantages of application with the exception of low luminosity which is not always sufficient for fast imaging, particularly in the case of lean flames (Dawood [2010]). Different wavelength filters can be used to isolate the light of a certain wavelength. The flame front position and brush thickness can be detected by tracing flame chemiluminescence generated from certain species such as CH*, C_2* in the reaction zone (Ikeda et al. [2001]). However, this is also limited by the low level of luminosity, most applicants only are single-shot image. Modern high speed digital cameras are extremely light sensitive and are capable of using just natural light to detect the flame positions with short exposure times. Muard [2006] has shown little difference in flame front images generated in simultaneous high speed schlieren and natural light photography in an engine.

These techniques are useful for understanding the dynamic behaviour of flames, but they yielded only little insight into the structure of the turbulent flames, because these methods averaged the flame over the line of sight. One of the developments in the laser diagnostics was Mie scattered light images (laser sheet visualization) of flames, which will be introduced in the following Section 4.2.2; this method essentially produce images of "slice" sections of a flame, allowing more detailed characterization of the flame front structure (Cairns [2001]). It is also possible to reconstruct a 3D flame with a number of images taken in a range of planar sheets at a short time (Hattrell [2007]).

Another two-dimensional planar measurement method to trace the flame front is Planar Laser Induced Fluorescence (PLIF). The principle of PLIF is to collect the spontaneous emission of photons when a molecule state moving from an excited electronic level to a ground level. There is an energy loss associated with this process. Therefore, detected emission light should be at a longer wavelength than the excitation laser source ((Eckbreth [1996])). This technique also can be used to detect the flame reaction zone when the excited species are CH*, C_2*. Planar Laser Induced Fluorescence (PLIF)

has been successfully used in the internal combustion engine to mark the flame front by imaging the OH* or CH* radical (Hult et al. [2002]), or to mark air and fuel mixture with acetaldehyde seeds (Neij et al. [1994]). More details would not be presented here, as a comprehensive description of PLIF can be found in Zhao and Ladommatos [2001]. In this study, CH* chemiluminescence method was adopted to observe the flame development process, while a laser sheet technique using Mie scattered light was employed for investigation of the flame front structure.

4.2.1 CH* chemiluminescence imaging

Chemiluminescence occurs in flames due to the high temperature in the reaction zone leading to a spontaneous emission of light, this signal can be used as a marker of the flame front. In the previous engine combustion experiments with the LUPOE engine, a high speed CMOS (complementary metal oxide semiconductor) camera Photron Ultima APX-RS with 10 bit grey scale was applied to capture luminescence light flame images (Dawood [2010]; Hussin [2012]). A CMOS camera has faster frame rates and a lower cost than a CCD camera. A PC with the Photron's PFV software package installed was used to control and save images from the camera via an IEEE1394 interface.

However, it was found that the luminescence signal from the flame front was strongly interfered with by the light generated in the high temperature burnt gas, and the flame reaction zone was hard to detect. Therefore, a band pass filter is used to isolate the collected light in a certain wavelength region, in order to acquire an clear flame front and resolve the flame reaction zone. Nevertheless, the sensitivity of the CMOS camera is low and the emission intensity from the flame front is relatively weak. After the reduction of the light intensity by filters, the COMS camera could not record any bright flame image. For this reason, a high speed intensifier has to be used to enhance the intensity of light. The new configuration of flame imaging system established in this study is shown in Figure 4.3. It consists of a 430 nm interference spectral filter, intensifier, high speed digital camera, controller and computer.

An HS-IRO (high speed IRO) image intensifier was employed, the structure of it is shown in Figure 4.4. When flame emission light passes the input window, photoelectrons are generated by a photocathode, then they are accelerated by high voltage gradient between the two sides of the micro-channel plate (MCP), and arrive on the phosphor screen, where it produces an intensified image. A micro-channel plate (MCP) consists of a thin glass plate (0.5 mm) with a large number of parallel channels. Each channel has 6 μm diameter (Lavision [2012]). An extremely short exposure time of 100 ns can be achieved by

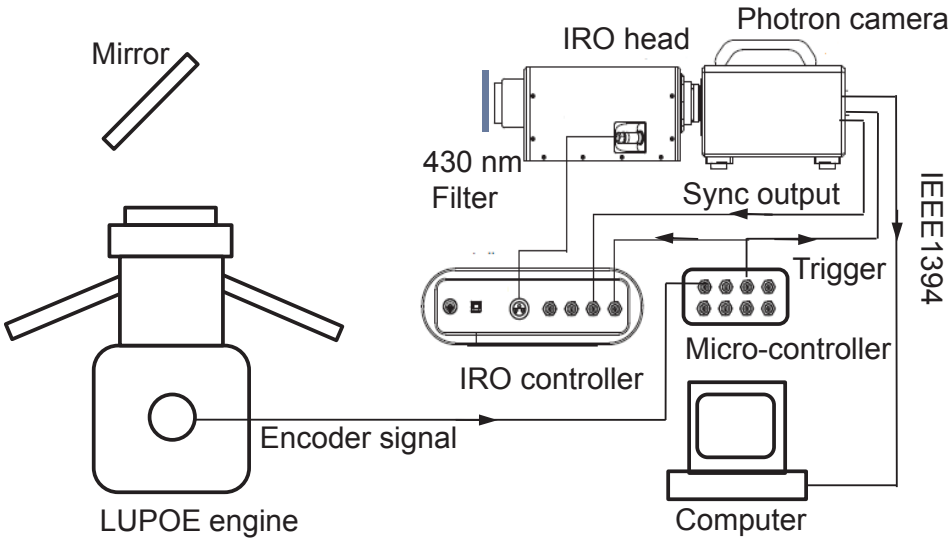

Figure 4.3: Experiment set up of high speed flame imaging acquisition system.

this image intensifier. Therefore, it also can act as a fast shutter. The lens coupled method was used in this study to transfer the image on the phosphor screen to CMOS arrays. Special attention has to be paid for the correct synchronization of the image intensifier gate and the CMOS exposure time. The synchronization of the intensifier and camera is achieved by setting the camera as a master device, and using the "sync-out" signal as the intensifier clock input. The start recording signals are generated by the micro-controller according to desired crank angle signal.

During the experiment, the Photron Ultima APX-RS camera was set at $10,000 fps$ with an image resolution of 512×512 pixels. The camera was operated under the random recording mode, which means that the camera only records the desired number of frames on each firing cycle, once it received a trigger signal. An Auto Focus 100 mm lens set at its maximum aperture of 2.4 was used, which was essential to detect the maximum possible amount of light. The gate time and intensity scale setting of the IRO intensifier are highly dependent on the experimental setup and conditions. i.e. the gate time was set as 60 μm, 75% gain was used at engine speed of 750 rpm with a 430 nm filter to capture a stoichiometric moderately turbulent iso-octane flame. It should be noted that a too strong light input with a short gate setting may produce a local photocathode etching or even destroy the whole device (Lavision [2012]). A silver surfaced high-reflective planar mirror was fitted above the engine with an angle at 45^o to divert the light emission from engine top window to imaging acquisition system set up with a horizontal optical axis, see Figure 4.3. In order to avoid pixel distortion in the image, the position of the mirror

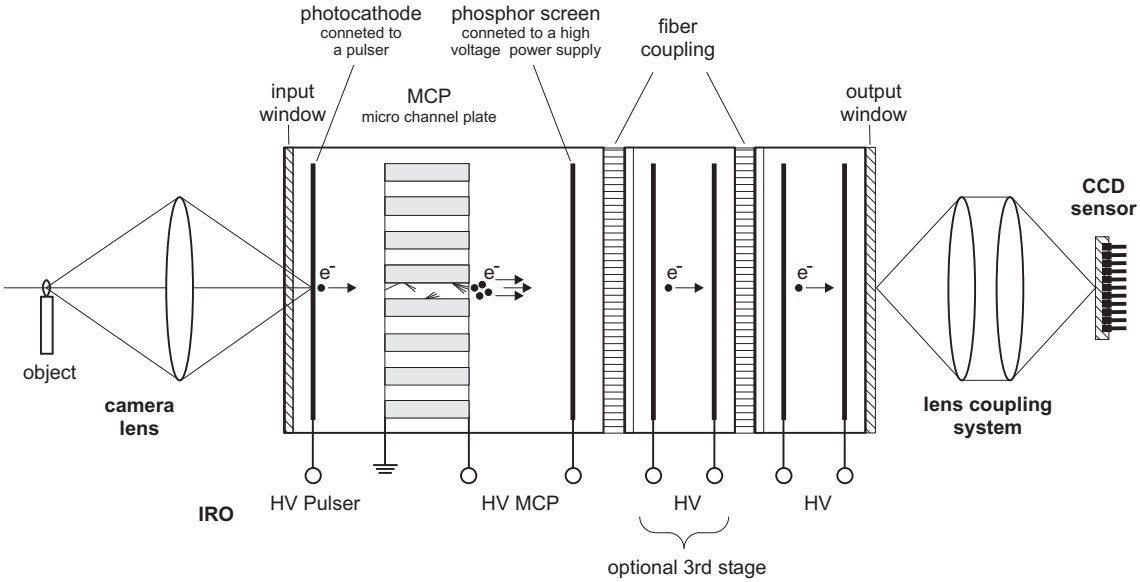

Figure 4.4: Structure of IRO intensifier adopted from Lavision [2012], CMOS sensor camera was used in this study.

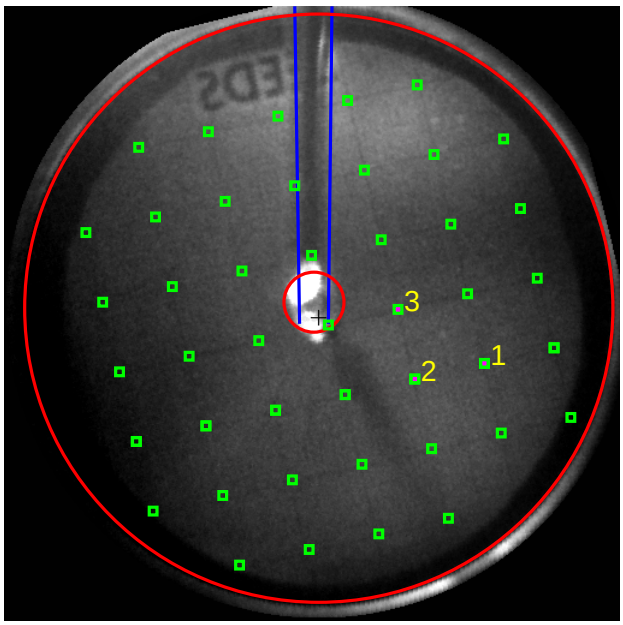

Figure 4.5: Calibration grid plate imposed by a generated uniform grid plate (green square points) based on three selected points.

and imaging system needs to be adjusted carefully. This can be checked by the following calibration method.

A calibration grid plate was used before the experiment, to evaluate the image distortion, as well as the magnification ratio of the image acquisition system. Figure 4.5 is a snapshot image of the calibration grid plate put on the piston surface and covered with the optical head. Three points in the corners of one grid are randomly and manually selected. Based on these three points, a uniform grid plate shown in green square points was generated by the computer. Comparing new grid positions to that on the original calibration grid plate, the image distortion can be evaluated. The pixel resolution also can be estimated by dividing the distance between two points on the calibration grid plate to the number of pixels of the recorded image. Errors exist when a large difference between the calibration grid plate and the uniform grid plate is found. These errors usually are caused by a shift of the optical path or refraction of light though a concave or convex window. The error of optical path can be reduced to a negligible value by adjusting the position of the mirror and camera acquisition system. However, to correct the optical distortion induced by a non-planar window or imaging acquisition system, the image registration method needs to be applied. This method calculates a spatial transformation map, which can be used to correct distorted images. By looking at the Figure 4.5, it can be considered that the distortion of the recorded image is negligible, after a careful adjustment of the light path. Low distortion also comes from the fact that the top of the engine head is a flat high-transparency quartz window. Furthermore, the acquisition system has a high image recording performance. Therefore, the image registration method was not engaged here. The accurate magnification ratio was obtained by using grid plate calibration before each set of experiment. The resolution of each pixel is approximately 156 μm, which is lower than the CCD camera used in the PIV system.

During the experiment, black spots were found on the inner surface of the top window; there might be associated with soot particles or unburnt oil droplets left from previous or current firing cycles. Hence, the engine top window was cleaned before each engine running set, about 15 firing cycles. The amount of lubrication oil used in the engine also was carefully controlled to minimize their effects on the image quality. Moreover, the laboratory has no windows; therefore it guarantees a condition of nearly complete darkness for the tests once the light is turned off. Thus, errors arising from scattering, and interference from other light sources could be neglected.

A series of flame images were taken in the LUPOE 2D boosted engine running at a speed of 750 rpm and a spark timing 2^o bTDC, with stoichiometric iso-octane fuel, except the image taken from Mandilas [2008] which used a different imaging method. Typical

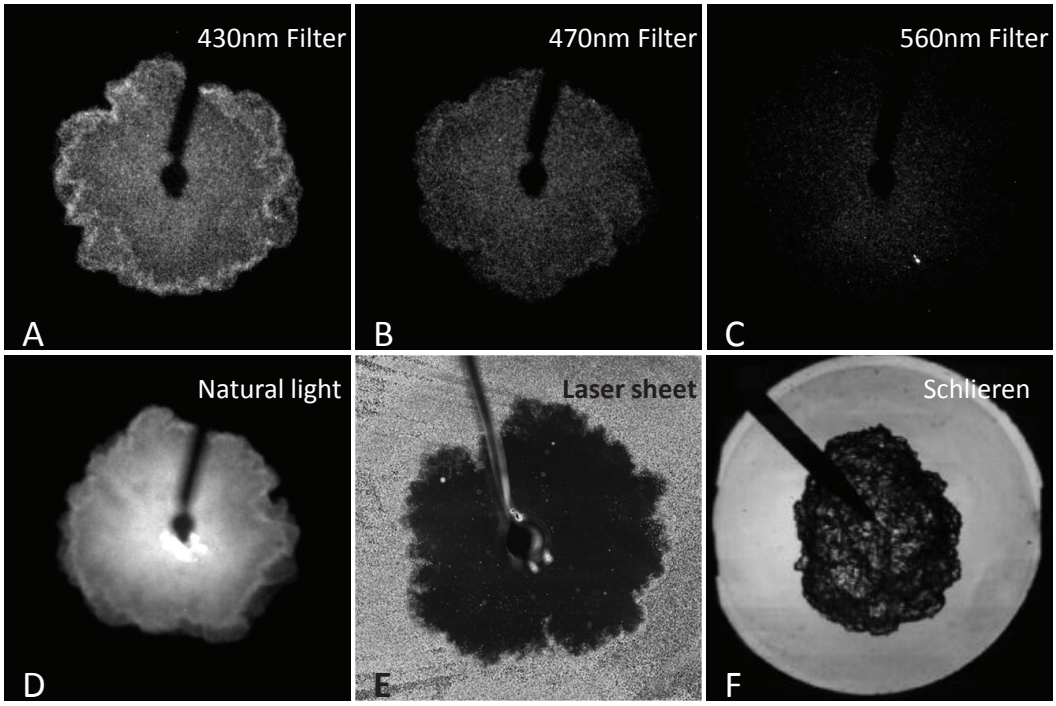

Figure 4.6: Typical images of different flame imaging methods: (A) 430 nm filter, (B) 470 nm filter, (C) 560 nm filter, (D) Natural light (E) Laser sheet method (F) Schlieren: the images of (A-F) are from LUPOE 2D boosted engine running at a speed of 750 rpm and spark timing 2^o bTDC, stoichiometric iso-octane fuel, (F) is taken from Mandilas [2008].

images given by these methods are compared in Figure 4.6. From the flame spectrum shown in Section 2.2.2.5, the 430 nm filter is related to CH* emission, both the 470 nm and 560 nm filters correspond to C_2*. It can be seen that the 430 nm has the strongest emission intensity among the three filter methods, while by comparing it to a natural light image, it shows a sharper flame front, and the flame thickness also may be deduced from the higher bright edge zone. At the same condition, the laser sheet method which will be introduced in the next section, shows a more wrinkled flame, because it is a kind of slice view of the flame. The details of frame wrinkle and curvature information can be calculated from this kind of images. The last schlieren flame image was taken from a constant combustion vessel (Mandilas [2008]). The schlieren method has been introduced before. It was not used in this study because the engine configuration could not allow two optical paths going along the cylinder axis. In this study, CH* chemiluminescence at 430 nm was adopted for flame development study, and laser sheet method was employed for flame structure investigation.

4.2.1.1 Luminescent flame image processing

The first step of CH* chemiluminescence image processing is to chop and separate continued recorded flame image sequences into each cycle's file folder. Each digital image is stored in the form of a two-dimensional matrix, where each element of the array corresponds to a single pixel. In this study, an image in the form of an 8-bit bitmap stored as a 512 by 512 matrix.

Each image was rotated so as to position the spark plug image at the top of the picture as shown in Figure 4.5. The spark plug with its connection line was masked by a ring with two lines for simplifying the image analysis. The pixels inside the mask regions were set as complete black. Therefore, the early flame propagation, where the flame diameter was less than 5 mm could not be recorded. When the flame approaches the cylinder wall, light reflections occur from the wall surface. A circular mask with cylinder diameter was used to eliminate the bright pixels out of the cylinder boundary.

The following step consisted of converting the original grey-scale images into binary black and white, to determine the actual flame shape. The black pixels represent the unburnt mixture, and the area of white pixels is the projected flame shape. This process is known as the image binarisation. It is achieved with Otsu's thresholding method (Otsu [1975]). The principle of this method is to determine a global threshold value by comparing local grey level variations over whole image, then all pixels are set to be zero or one. The number of white pixels can be converted to flame area and a mean flame radius. The mask for the plug connection wire covered part of the flame area, and this caused the flame front discontinuity. A straight line was plotted to complete this thin strip gap, and the gap was filled up to eliminate any false reading of the flame projected area, see in the left side of Figure 4.8.

A mean flame radius derived from the flame projected image, it was calculated as that of a circle having identical area to the enflamed cross-sectional area (Cairns [2001]). This mean flame radius was considered to be the turbulent entrainment radius R_e, where fresh unburned gas was entrained into the flame front. The entrainment burning velocity U_e can then be calculated as follows:

$$U_e = \frac{\rho_b}{\rho_u} \frac{dR_e}{dt} \tag{4.16}$$

where ρ_b, ρ_u are burned and unburned gas density, respectively.

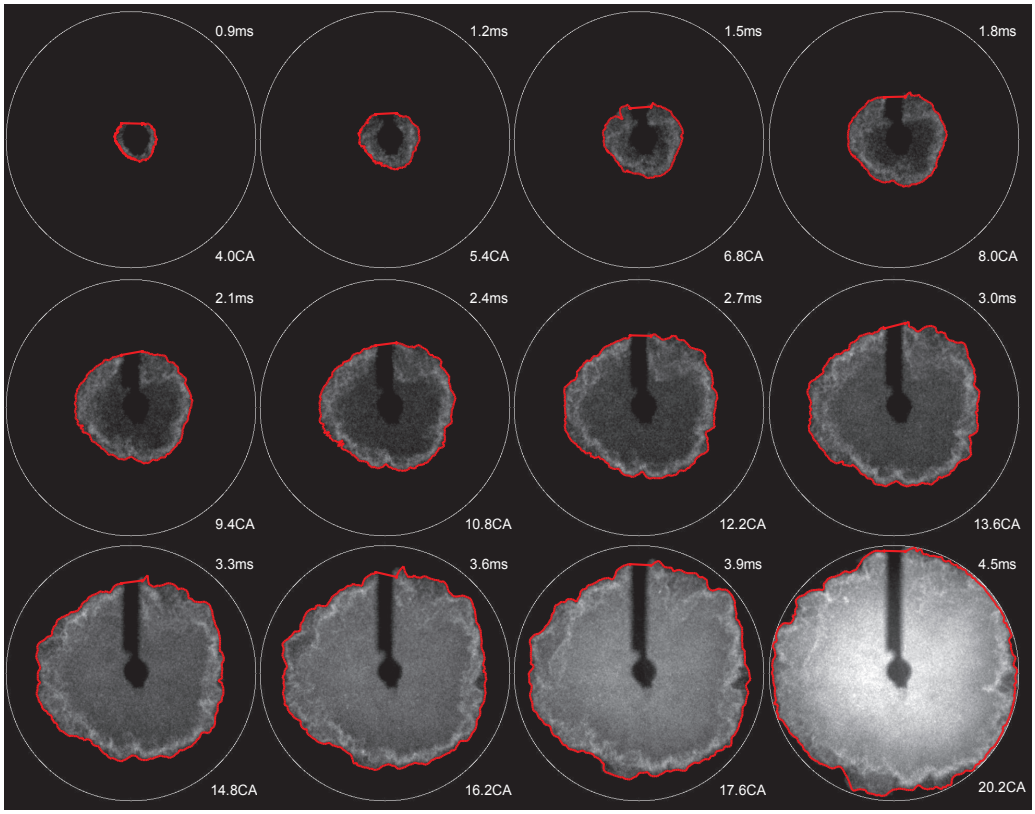

Figure 4.7: A developing flame captured in the optical LUPOE 2D boosted engine via CH* chemiluminescence technique. The engine was run at a speed of 750 rpm and spark timing 2^o bTDC, with stoichiometric iso-octane fuel. Initial pressure was 2.0 bar.

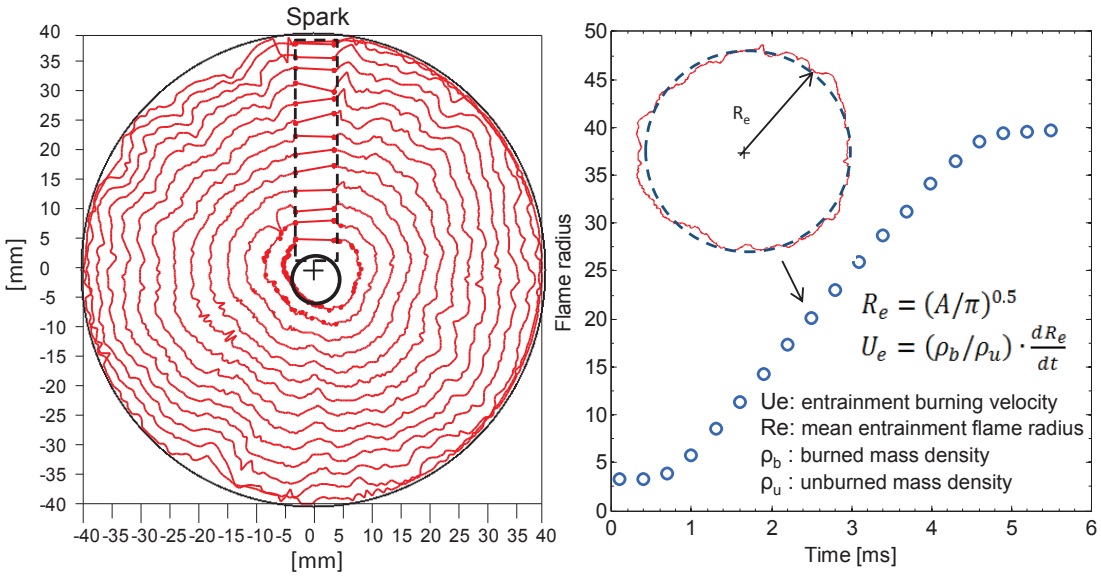

Figure 4.8: Flame front propagation trace derived from Figure 4.7 (left), definition of mean flame radius and entrainment burning velocity calculation (right).

A sequence of flame propagation images with their derived flame fronts is shown in Figure 4.7, the corresponding flame radius is shown in Figure 4.8, the mean flame radius calculation method is also illustrated. It can be seen that the flame front is the maximum radius along the projected sight line, especially at the end of flame propagation stage. Hence, these images could not provide reliable information on flame front wrinkling; however, it is still a good method to investigate the flame development process by using mean turbulent entrainment flame burning velocity.

It is also well considered that high CH* exists only in the main reaction zone (Gaydon [1957]), thus the resulting images provide a good indication of the instantaneous flame reaction zone location. Flame brush thickness may be derived from the intensities of the pixels in the flame image. However, the convolutions of the flame front existing in a highly turbulent flow may make it difficult to interpret the flame properties. This is because the signal is an integral value equal to the depth of field of the collection optics. In this study, the flame is weakly wrinkled, so that the errors caused by the line-of-sight technique are hopefully small.

Images of local CH* chemiluminescence collected in laminar and moderate turbulent iso-octane flames are plotted with pseudo-colour in the left side of Figures 4.9 and 4.10, and the global flame shape with chopped region position are shown in the right bottom corner in the each image. A significant difference between these two kinds of flames can be observed. Strong light emission zones can be found in both flame front regions. These high intensity pixels can be used as an indication of the flame reaction zone. In order to characterize the flame thickness, a line along the flame radius, across the flame front versus normalized luminous intensity, are plotted and shown in the right sides of Figures 4.9 and 4.10. As observed in the spatial space, the flame luminous intensity has a peak value close to the flame front. The radius position, with 10% luminous intensity, was defined as the flame front. Usually, the flame thickness can be defined as $1/|\frac{dw}{dx}|$, a straight line between peak position and the flame front can be fitted very well. In order to simplify the data processing. In this study, the distance between flame front and 90% luminous intensity inside the flame was considered as the flame brush thickness.

It has been mentioned that flame chemiluminescence as a line-of-sight technique is not an ideal way to investigate flame structure because the flame front derived from the image is a projected shape. A detailed cross-section of flame front structure can be acquired by cutting the flame into slices. This can be achieved by applying laser sheet visualization technique in the following Section.

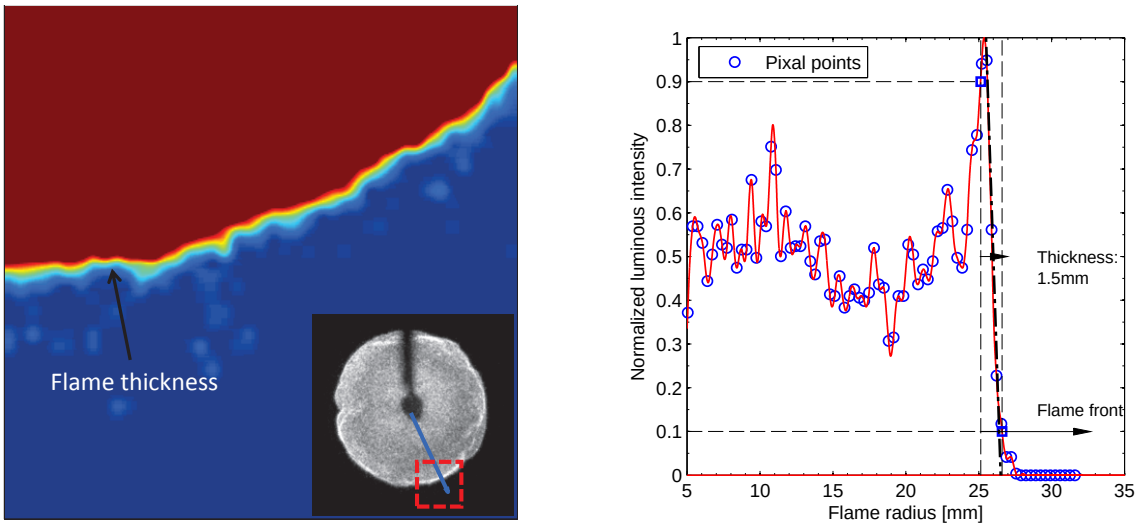

Figure 4.9: Left: Pseudo-colour image of local CH* chemiluminescence flame taken from square region of a weakly wrinkled flame from the LUPOE 2D boosted engine running at a speed of 100 rpm and spark timing 10^obTDC, stoichiometric iso-octane fuel. Right: Normalized luminous intensity distribution along the flame radius direction indicated as a line in the left image.

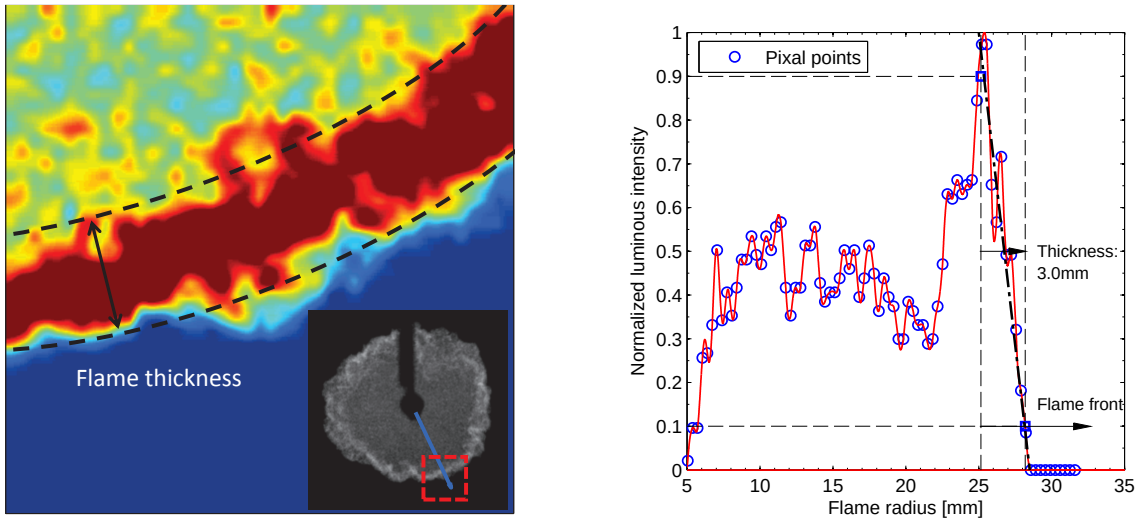

Figure 4.10: Left: Pseudo-colour image of local CH* chemiluminescence flame taken from square region of a moderate turbulent flame in the LUPOE 2D boosted engine running at a speed of 750 rpm and spark timing 2^o bTDC, stoichiometric iso-octane fuel. Right: Normalized luminous intensity distribution along the flame radius direction indicated as a line in the left image.

4.2.2 Two-dimensional laser sheet visualization

The ”laser sheet visualization” technique makes use of the Mie-scattering light from seed particles to discriminate burnt from unburnt mixture. The seeding, such as oil droplets, would vaporise in the high temperature burnt gas and not reflect light into the image. The seeds in front of the flame could scatter the bright light when the diameter of the seeds is equal or greater than the wavelength of the incident laser. This process has no energy exchange between the light and incident medium, therefore the incident and scattered light frequencies are equal. The flame front can be well defined between the bright and dark areas.

Comparing laser sheet method to the Planar laser Induced Fluorescence (PLIF), the PLIF technique requires that the excitation laser source has the same wavelength as the desired excited species; usually this is achieved by using tunable dye laser. On the other hand, the fluorescence signal can be linearly proportional to the input laser irradiance before it reaches saturation, and a powerful laser pulse is necessary (Eckbreth [1996]). Therefore, the laser source in the PLIF experiment must be carefully selected to fulfill the requirements of both high power output and appropriate wavelength. Moreover, the quenching effect will occur with the pressure increasing, so it is difficult to achieve complete PLIF measurement in a high pressure engine (Zhao and Ladommatos [2001]). ”Laser sheet” method has much less stringent critical requirements to the laser source, and the application is almost not affected by pressure.

In this study, the laser sheet method has been adopted. The experiment setup is similar to the PIV experiment and is shown in Figure 4.11. The mixture is seeded with submicron sized oil droplet particles. A thin planar sheet of laser is generated by Nd:Yag laser, the light passes through the cylinder. A CCD camera was used to record the images from the top window of engine. A PTU (Programmable Timing Unit) was used to synchronize the CCD camera and the laser, the experimental procedure and calibration method are similar to the CH* chemiluminescence experiment.

4.2.2.1 Flame front detection

A snap shot of the raw laser sheet image is shown in the left side of Figure 4.12. A more wrinkled flame front can be observed by comparing with the CH* chemiluminescence image. The image on the right side of Figure 4.12 is a magnified image of a small part of a flame with grey levels changed into pseudo-colour. Comparing it to the flame image captured at the same condition using the CH* chemiluminescence technique in Figure

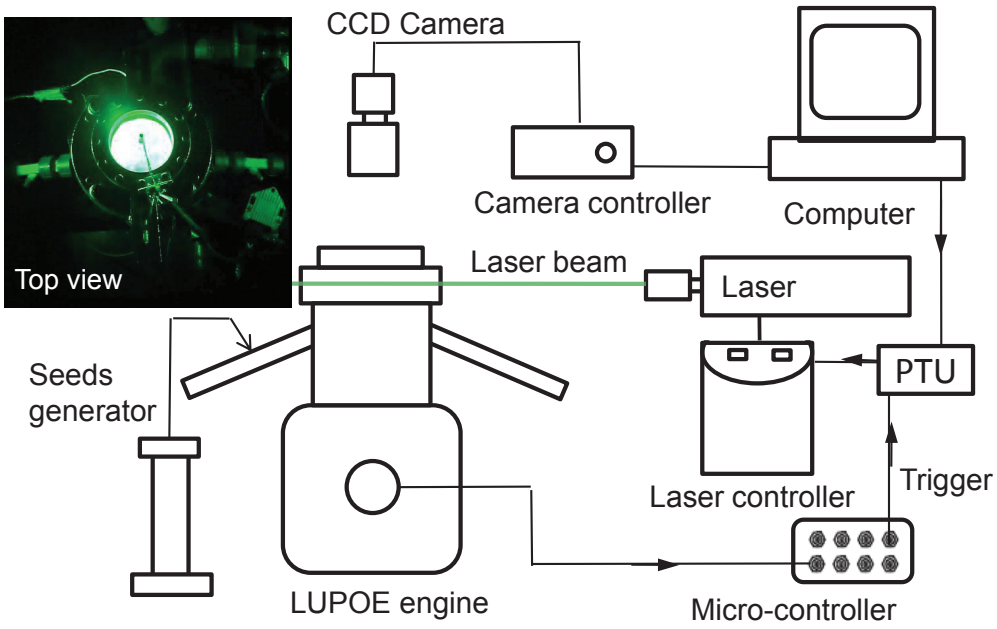

Figure 4.11: Experimental setup of laser sheet method with a snapshot image from top view of the engine head .

4.10, large pixel noise in both unburnt and burnt mixture can be found in this image. These spots are generated by non-uniform light scatter and seeding mixture, some spots may come from the window speckles during the experiment. The image binarisation using Otsu's threshold method failed in this situation, because a single threshold could not be found to distinguish occasional bright spots appearing in the burnt region, as well as dark spots in the unburnt region. In the previous study, the majority of this kind of image processing was operated manually (Cairns [2001]).

This problem can be also clearly observed form the luminous intensity distribution along the flame radius direction as shown in Figure 4.13. It can be seen that a strong fluctuation of pixels intensities existed in the unburnt gas side, which makes it hard to set a threshold to binarise the image directly. However, the gap between unburnt and burnt mixture is still clear.

This finding has inspired development of a new image processing method to derive the flame front from laser sheet images. A polar coordinate based method was used to search for the flame front position along the flame radius at each constant angle. Then, an interpolating line is generated using raw pixel's intensities. The peaks of derivation of this line represent the large gradients in the raw data. A mean luminous intensity value and its first standard deviation are calculated. The flame front point was defined at one of the peak points of the derivation line, and its right point in the interpolate line

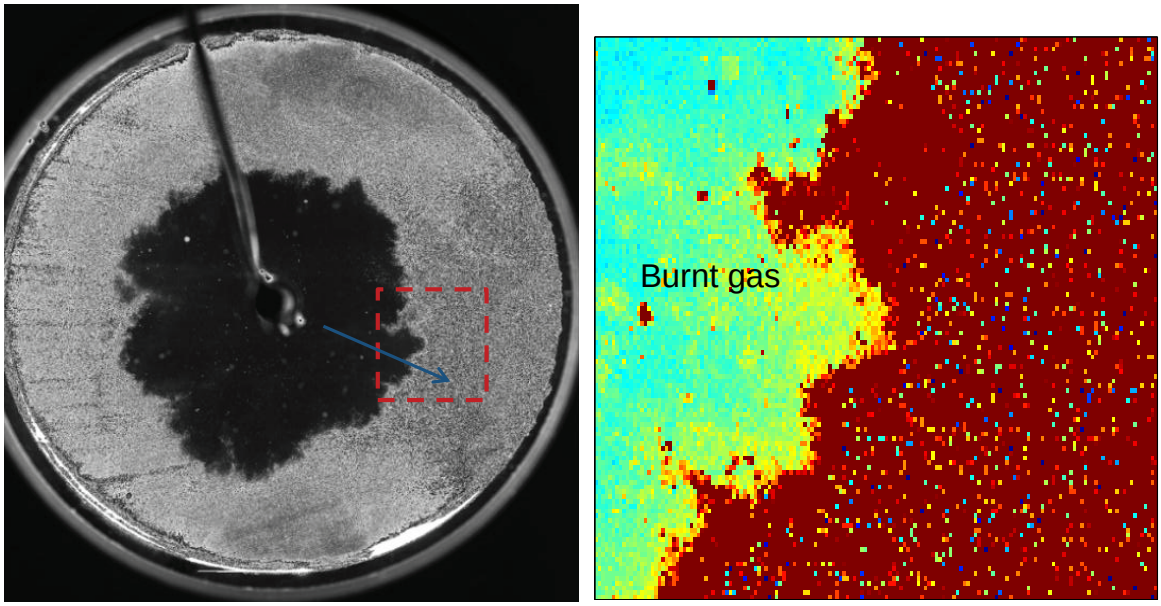

Figure 4.12: Right: Pseudo-colour image of the laser sheet method taken from square region of a turbulent flame (Left) from LUPOE 2D boosted engine running at a speed of 750 rpm and spark timing 2^o bTDC, stoichiometric iso-octane fuel.

is larger than mean value, while its left point in the interpolate line is lower than mean value minus first standard deviation. Finally, an approximate flame possible front can be distinguished, an example is shown in Figure 4.14, the blue line is the flame front searched by using this method. However, this method still has two issues. First, the defined flame front is not in the burnt gas side, where the luminous intensity of pixels should tend to zero due to the high temperature. Second, it could not recognize the more than one flame front point in the one direction of flame radius, which was caused by strong flame front wrinkling.

Therefore, a second step of local flame front searching was designed. Firstly, a small square region was acquired with a 10^o angle step along the flame front defined in the first step. Image binarisation using Otsu's thresholding method was used, this makes use of the intensity information from a local region, the light emissions in a small area are assumed to be more uniform than that from a whole image. Secondly, a 3×3 spatial Gaussian filter was applied to smooth and further enhance each image. A low threshold was set at 20%, where seeds are vaporised by the high temperature in the burnt gas, to achieve the edge detection. The final flame contour was detected using a search algorithm by checking each pixel; the pixel on the flame edge is the one whose neighbour's have the reverse colour. The processing of laser sheet image is illustrated in Figure 4.14. The final detected flame front was shown in red colour. This method can solve the difficulty of direct binarisation of raw images, caused by non-uniform of seeding and laser light

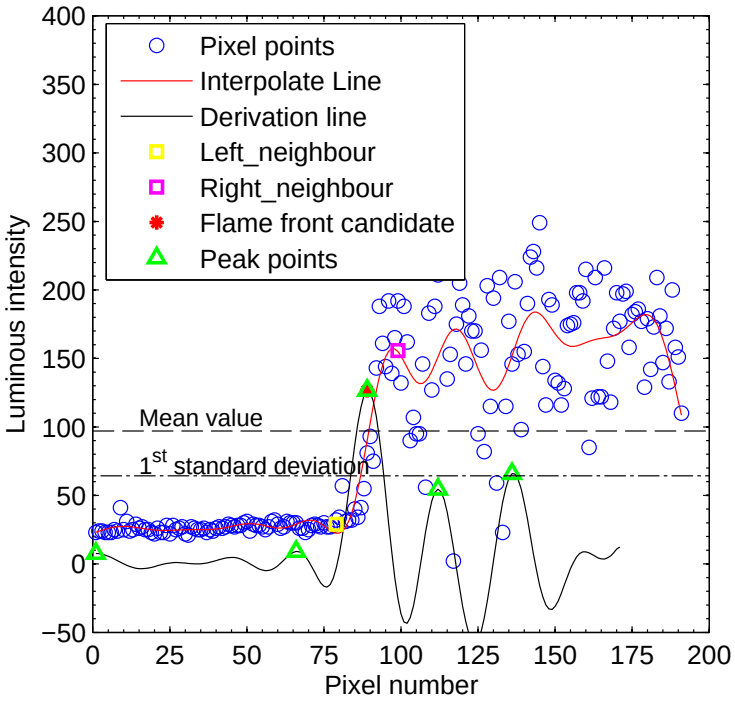

Figure 4.13: Luminous intensity along the flame radius direction taken as a line in the Figure 4.12.

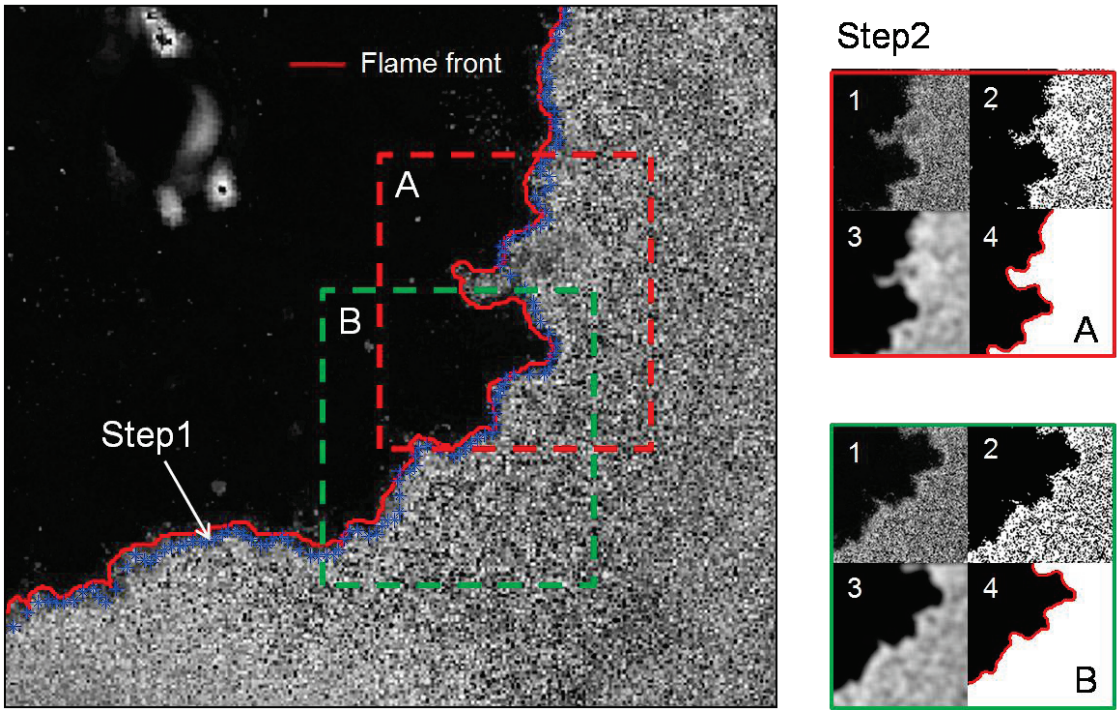

Figure 4.14: Laser sheet image processing: Step 1 is to find approximate flame front position, Step 2: local image process including: (1) Chop image; (2) Binarization; (3) Image expansion; (4) Binarization and flame front detection.

intensity. Furthermore, based on this local image processing strategy, more sophisticated filter algorithms and edge detection methods can be applied to obtain higher resolution edge detection results. Since this image processing method can deal with the image with large pixel noise. The PIV images with low seeding density also could be processed as a laser sheet image, this provides a way to investigate the interaction between flame and flow using the same experimental setup.

4.2.2.2 Flame contour processing

The flame contour data derived from the laser sheet images are stored in a series orthogonal coordinates (x,y). In order to characterize the flame wrinkle level, a mean flame radius $\bar{r}$ is calculated using minimum least square algorithm to acquire an "equivalent" flame radius. Therefore, the wrinkled flame structure induced by the eddies, which are larger than the flame itself, could be cut off. The deviation of the flame contour $d(s)$ from the mean radius at the length s along the contour could be calculated as:

$$d(s) = r(s) - \bar{r} \tag{4.17}$$

where $r(s)$ is the instantaneous flame radius at s length along the flame contour. The mean $d\bar{(s)}$ and the root mean square $d(s)'$ values of the flame edge fluctuation can be defined as:

$$d\bar{(s)} = \frac{1}{L_{tot}} \int_0^{L_{tot}} d(s)ds \tag{4.18}$$

$$d(s)'^2 = \frac{1}{L_{tot}} \int_0^{L_{tot}} (d(s) - d\bar{(s)})^2 ds \tag{4.19}$$

where L_{tot} is the total length of flame contour. This value can be considered a parameter to characterize the flame wrinkle level.

For the calculation of the flame front curvature, firstly, the flame front was sampled using a cumulative angle approximating 2^o between two digitized points (Hicks et al. [1994]), see Figure 4.15. Secondly, third order polynomials were fitted to represent local flame contours as two functions x(s) and y(s) using 2 neighboring points. Then the local

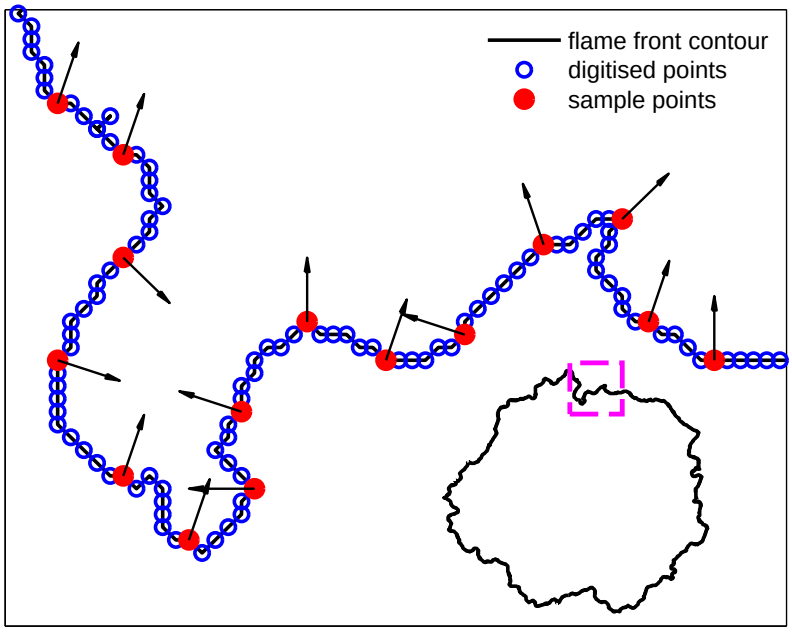

Figure 4.15: Illustration of flame contour sampling using a cumulative angle. The global flame shape with chopped region position is shown in this figure, the arrows are normal directions of local fitted curves using third order polynomials.

curvature κ was calculated at each pixel point along the flame contour, using the first and second derivatives with respect to s as follow:

$$\kappa = \frac{\dot{x}\ddot{y} - \dot{y}\ddot{x}}{(\dot{x}^2 + \dot{y}^2)^{3/2}} \tag{4.20}$$

Flame spectral analysis is also employed, this method requires that the length of the line segments δs along the flame contour is uniform. However, the flame contour extracted from the laser sheet image was stored in a series orthogonal coordinates connected by line segments, the length between two pixels may be different. Therefore, the digitized points need to be re-sampled along the flame contour at constant intervals s' using an interpolation method. This process enables the obtained data as a function of a stationary independent coordinate. Following this step, a spatial autocorrelation $\xi(s')$ of a function of s' can be expressed as:

$$\xi(s') = \langle d(s) \cdot d(s+s') \rangle_{cont} = \frac{2}{L_{tot}} \int_0^{L_{tot}/2} d(s) \cdot d(s+s') ds' \tag{4.21}$$

An integral length of flame wrinkle L_a could be defined as follow:

$$L_a = \int_0^{\xi=0} \xi(s')ds' \tag{4.22}$$

The Fourier analysis of the $\xi(s')$ can then be solved as:

$$\Phi_\xi(k) = \int_0^{L_{tot}/2} cos(k \cdot s')\xi(s')ds' \tag{4.23}$$

The laser sheet imaging and data processing method presented here will be applied to investigate the pressure influences on the turbulent flame structure in the boosted LUPOE 2D engine in Chapter 6.

Chapter 5

Iso-octane burning velocity in SI engine

The LUPOE 2D engine can be considered as a reciprocating combustion rig, when it runs at extremely low speed, less than 100 rpm. It can be employed to study characteristics of laminar flame propagation at high pressures and temperatures, which are hardly achievable with other combustion rigs, e.g. constant volume vessel, owing to safety restrictions. Moreover, a direct measurement in an engine chamber enables the measured laminar flame to ”carry” more engine combustion information, such as the effects of flame geometry, confined volume, and flame instability. This kind of ”quasi-laminar” flame measured under engine relevant condition might be useful for engine turbulent combustion modelling (Gerke et al. [2010]).

This Chapter presents the flow velocities which were measured near the TDC (Top Dead Centre) at slow engine speeds. The purpose was to confirm that the flow velocity was slow enough to assume it a laminar flow condition. Subsequently, direct measurements of flame speed at engine speed of 100 rpm was conducted. An extrapolation method, using flame speed at different low engine speeds region (150-300 rpm), was developed to derive the burning velocities at zero rpm. The published experimental data and correlation equations for the laminar burning velocity of iso-octane were reviewed and calculated at the engine conditions. The best performance correlation equations and chemical mechanisms were used to calculate the laminar burning velocity at the current experimental condition to compare with the measured results.

5.1 Effects of engine speeds on turbulence

Laminar flame measurement requires a turbulence-free environment. It is well known that the turbulent Root Mean Square velocities change in an engine scales nearly linearly with the engine speeds (Hall and Bracco [1987]). Figure 5.1 illustrated a snapshot of the velocity field at the mid-plane of the LUPOE 2D clearance volume in form of vector and scalar maps. This flow field was captured using a PIV system at 2^o bTDC when the engine was run at a speed of 100 rpm. The use of the PIV system has been described in Chapter 4. The corresponding velocity probability density functions (pdf) of this flow velocity field was shown in Figure 5.2. The inlet and exhaust port positions and their coordinates were also plotted in the corner of this Figure. The maximum value in the individual velocity field was lower than 0.5 m/s, and no bulk air flow structure can be discerned.

At the same measurement position and moment, approximately 100 cycles flow velocity fields have been collected at different engine speeds ranged from 100 rpm to 300 rpm. The ensemble mean velocity fields have been calculated and shown in Figure 5.3. In general, mean velocities at the TDC position become quite small with engine speed decreasing. At a higher engine speed, the velocities at the centre of the combustion chamber are lower than that at the cylinder wall. The existence of spark plug, and its connecting line in the right side, may obscure some measurement areas, so that some erroneous and missing vectors may be generated. In the vicinity of the spark, the spots of high velocity seen at 10 o'clock are most likely a consequence of the reflection of the laser sheet from the edge of the side quartz window. Furthermore, the mean velocity at each point in the mean velocity field was averaged, and the mean and standard deviation values were plotted in Figure 5.5. At the engine speed of 100 rpm, the mean gas velocity in the chamber is lower than 0.1 m/s.

The Root Mean Square velocity fields also have been calculated from 100 cycles under each condition. It can be observed that turbulence exists at the centre of the cylinder and decreases when approaching the wall at an engine speed of 300 rpm, see Figure 5.4. With the engine speed decreasing, the turbulence disappears and the flow field becomes more isotropic and homogeneous. At the engine speed of 100 rpm, the maximum RMS velocity is smaller than 0.2 m/s, which is much lower than the one at the engine speed of 300 rpm, where the maximum RMS velocity can reach 0.6 m/s. Mean and standard deviation values of these RMS velocity maps were calculated and are shown in Figure 5.6. It can be seen that the mean turbulence intensity at the engine speed of 100 rpm is lower than 0.1 m/s, which is negligible.

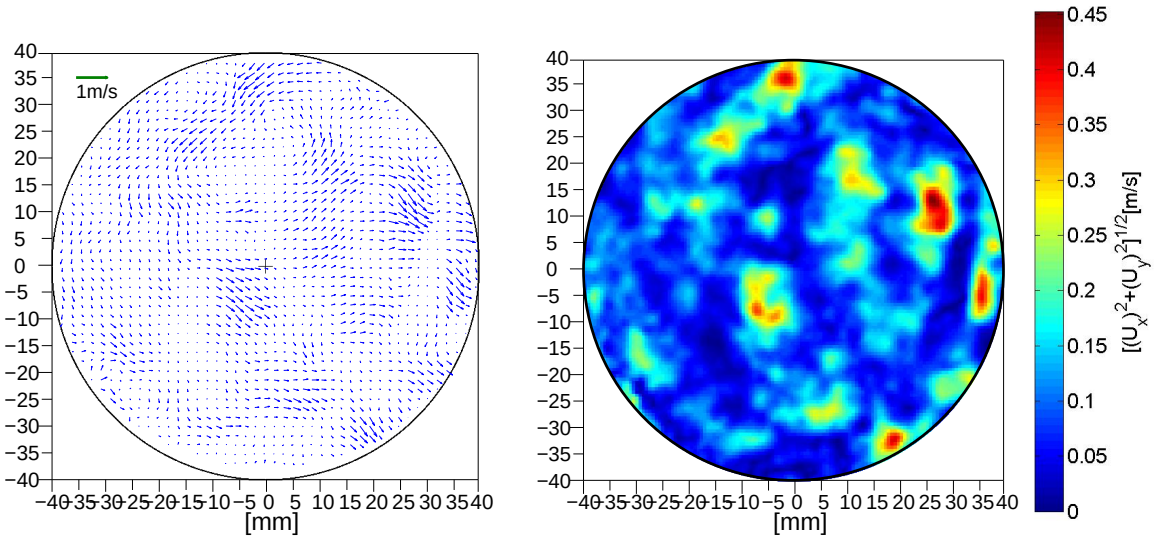

Figure 5.1: A snapshot of the flow velocity field captured by PIV at 2^o bTDC position at an engine speed of 100 rpm, illustrated in the form of vector (left) and scalar (right) maps.

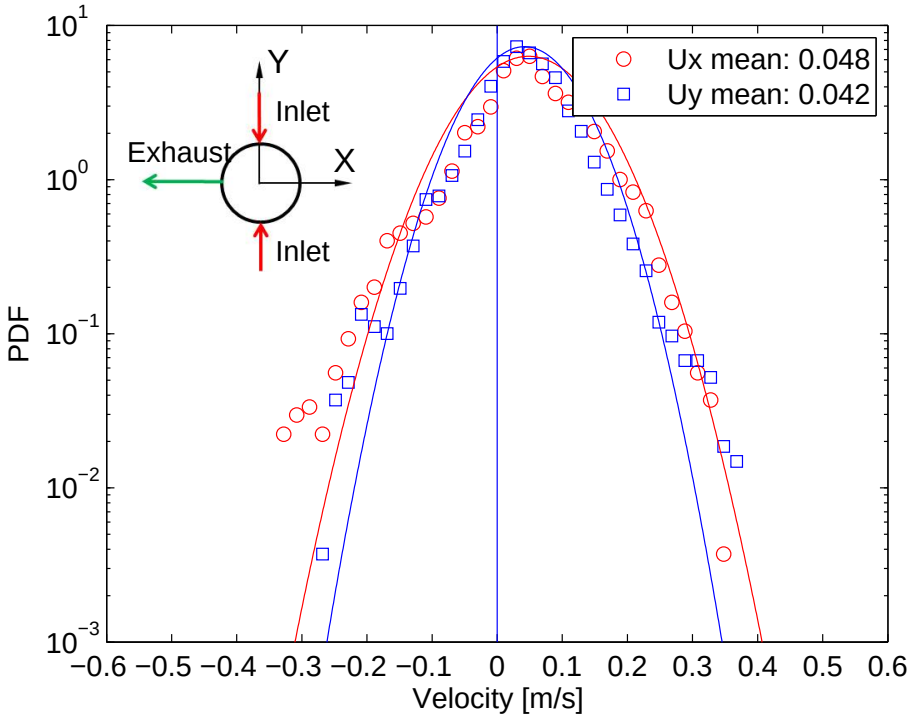

Figure 5.2: The velocity probability density functions (pdf) of the flow velocity field shown in Figure 5.1. The inlet and exhaust pipe positions and their coordinates were plotted in the corner.

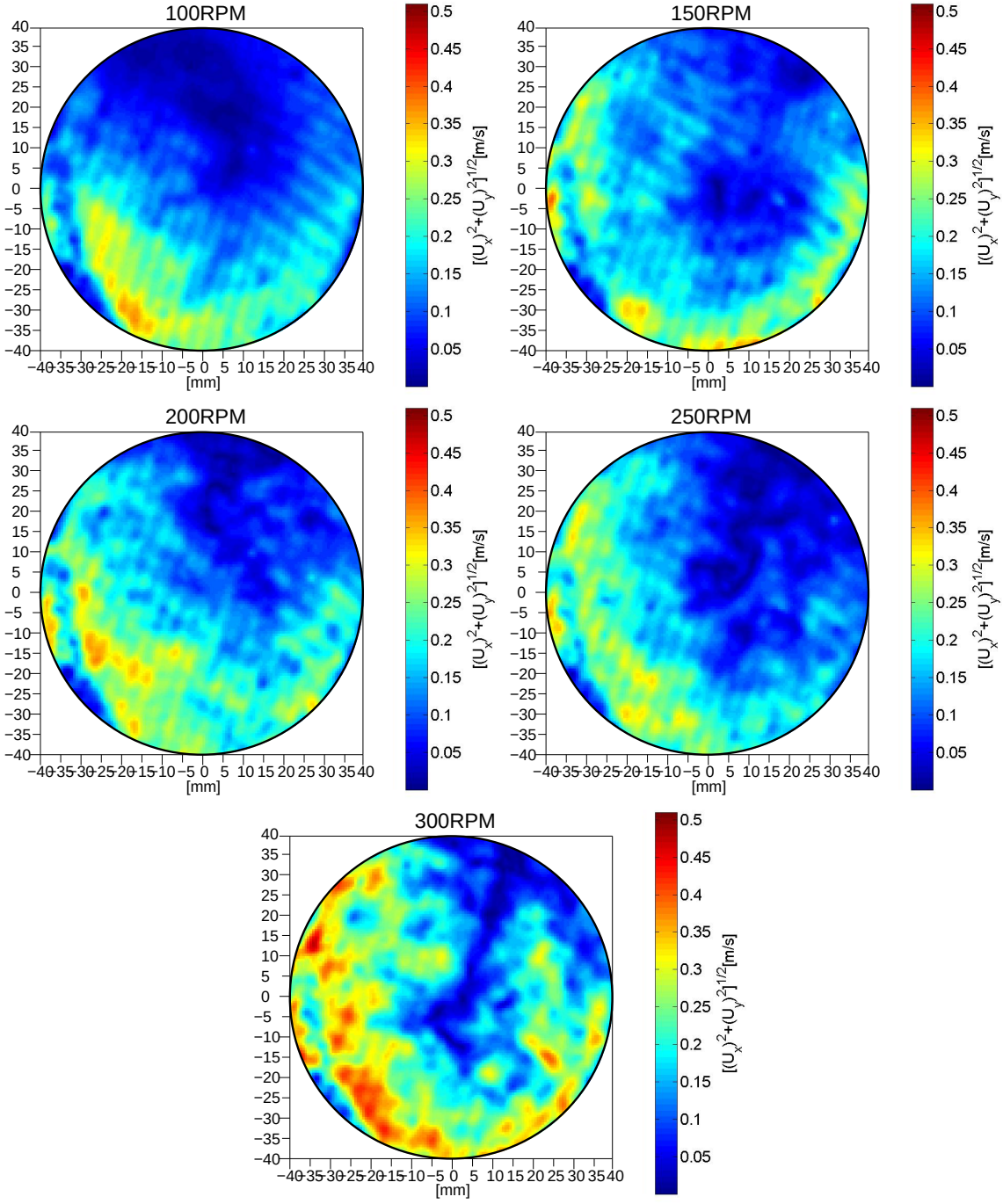

Figure 5.3: Flow fields of the mean velocity magnitude from PIV measurements at 2^o bTDC for different engine speeds from 100 rpm to 300 rpm.

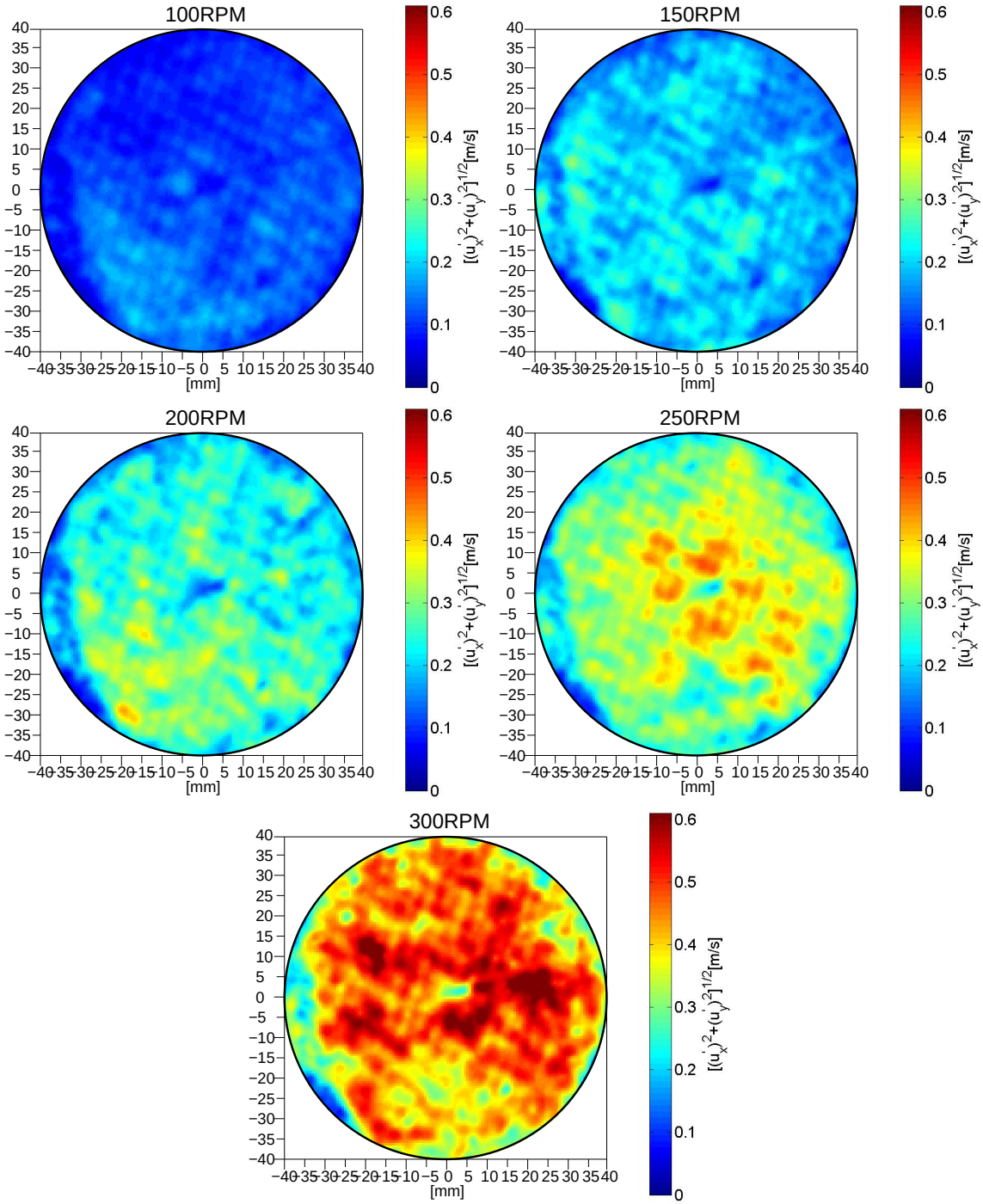

Figure 5.4: Flow fields of the RMS velocity from PIV measurement at 2^o bTDC for different engine speeds from 100 rpm to 300 rpm.

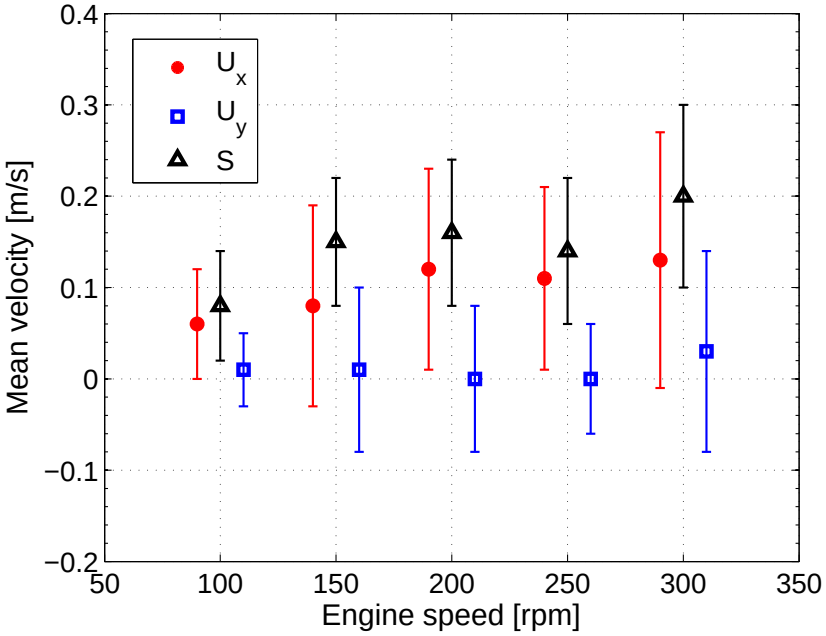

Figure 5.5: Mean and standard deviation (represented as error bar) of the mean velocity fields shown in Figure 5.3. U_x: mean velocity in X direction, U_y: mean velocity in Y direction, S: velocity magnitude. U_x and U_y are at the same speed, shifted for illustration only.

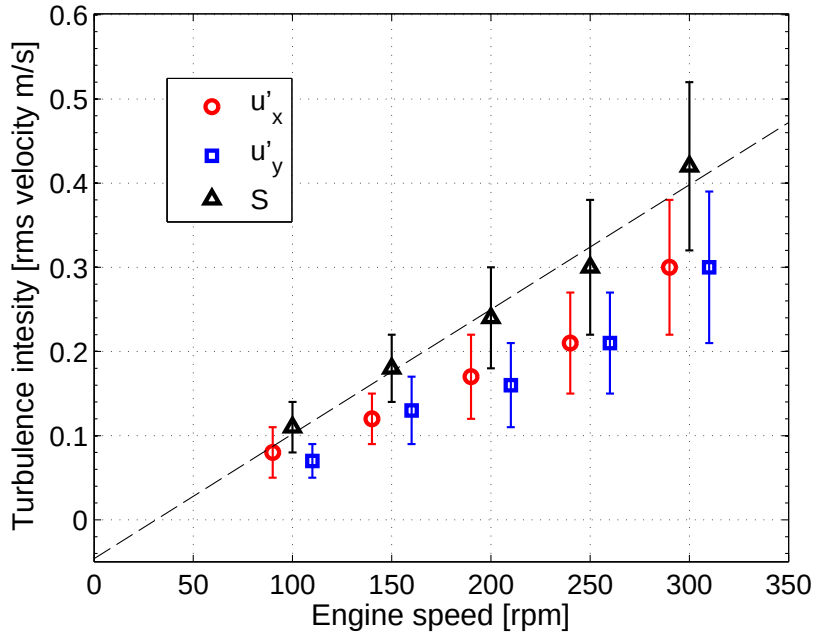

Figure 5.6: Mean and standard deviation (represented as error bar) of the RMS velocity fields shown in Figure 5.4. u'_x: RMS velocity in X direction, u'_y: RMS velocity in Y direction, S: RMS velocity magnitude. u'_x and u'_y are at the same speed, shifted for illustration only.

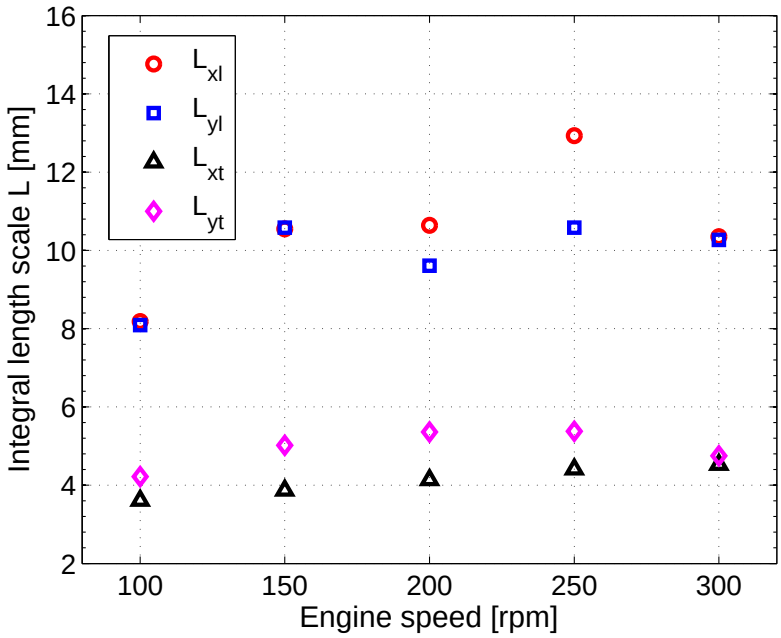

Figure 5.7: Longitudinal and transverse integral length scales based on spatial analysis at 2^o bTDC with engine speed increasing.

The RMS velocity has a significant change with the engine speed compared to mean velocity. Both velocities at X axis and Y axis have the similar magnitude and they increase almost linearly with the engine speed. A linear extrapolation line between the engine speeds and the turbulent intensities was plotted in Figure 5.6, it was extended to the engine speed of zero, where the turbulence intensity was almost 0 m/s.

The integral length scales were calculated for the X axis and Y axis from the mean PIV vector fields at the 2^o TDC, as shown in Figure 5.7. The calculation process has been described in Section 4.1.3. It can be observed that, in general, average values of the longitudinal integral length (L_{xl},L_{yl}) scales were approximately twice that of the transverse (L_{xt},L_{yt}) scales, as it is the case with isotropic turbulence. Both longitudinal and transverse integral lengths decrease slightly with engine speed decreasing. The difference along the longitudinal direction between RPM 100 and RPM 300 is about 2 mm, which is less than 1 mm along the transverse direction. This is a further indication that the in-cylinder turbulence at around TDC could be considered locally isotropic.

The measurement of turbulence proved that the employed single-cylinder LUPOE 2D engine could be considered as an almost laminar flow condition at extremely low engine speed, i.e. lower than 100 rpm, and it can be used as a suitable device for the "quasi-laminar" flame investigations near the Top Dead Centre.

5.2 Direct measurement of burning velocities

As shown in PIV results, both averaged mean and RMS flow velocities at the engine speed of 100 rpm are lower than 0.1 m/s. Under this condition, the flame propagation in the cylinder might be considered as a laminar flame. Pressure and imaging measurement methods have been applied in this Section to measure the stretched laminar flame at elevated pressure. The measurement was conducted near TDC to reduce further influence of the flow velocities on the flame propagation.

5.2.1 Pressure results

For all the tests presented below, the engine speed was set at 100 rev/min, intakes and wall temperature were kept at 323 K, the same as for the high speed engine experiment in Chapter 6. The spark timing was 10^o bTDC (before Top Dead Centre). The temperature at spark timing can reach about 600 K, calculated from LUSIEDA. The spark energy was adjusted to be at a minimum, at such that a stable ignition can be achieved in order to avoid a high energy spark discharge disturbing the initial flame development. Each firing cycle was followed by 10 motoring cycles with skipped ignition. Only 6 cycles could have been recorded during each engine run with a data scan rate of 50 kHz. Figure 5.8 shows the 5 pressure cycles collected for varied equivalence ratios from 0.6 to 1.2. Both the pressure rise rate and the peak pressure increase with the equivalence ratios increasing. The cycle variability becomes significant with equivalence ratio decreasing, and the engine operation at equivalence ratio 1.2 has the lowest cycle variability. These tests proved that the experimental results were repeatable, and the effect of turbulence on flame propagation was negligible at this low engine speed. The pressure at spark timing for all cases was approximately 12 bar.

5.2.2 Laser sheet visualization results

The laser sheet visualization method was applied in order to investigate the detailed flame shape and its variability. The flame contour is determined from an image created by a laser sheet passing through a seeded medium, see Section 4.2.2. About 30 flame contours were collected at 2^o CA after ignition at the engine speed of 100 rpm, and at 10^o CA after ignition at the engine speed of 750 rpm, respectively, approximate 1.2 ms elapsed since the spark timing for stochiometric charge. Figure 5.9 shows the flame front of each firing cycle at two engine speeds with the cylinder wall. Although a slightly wrinkled

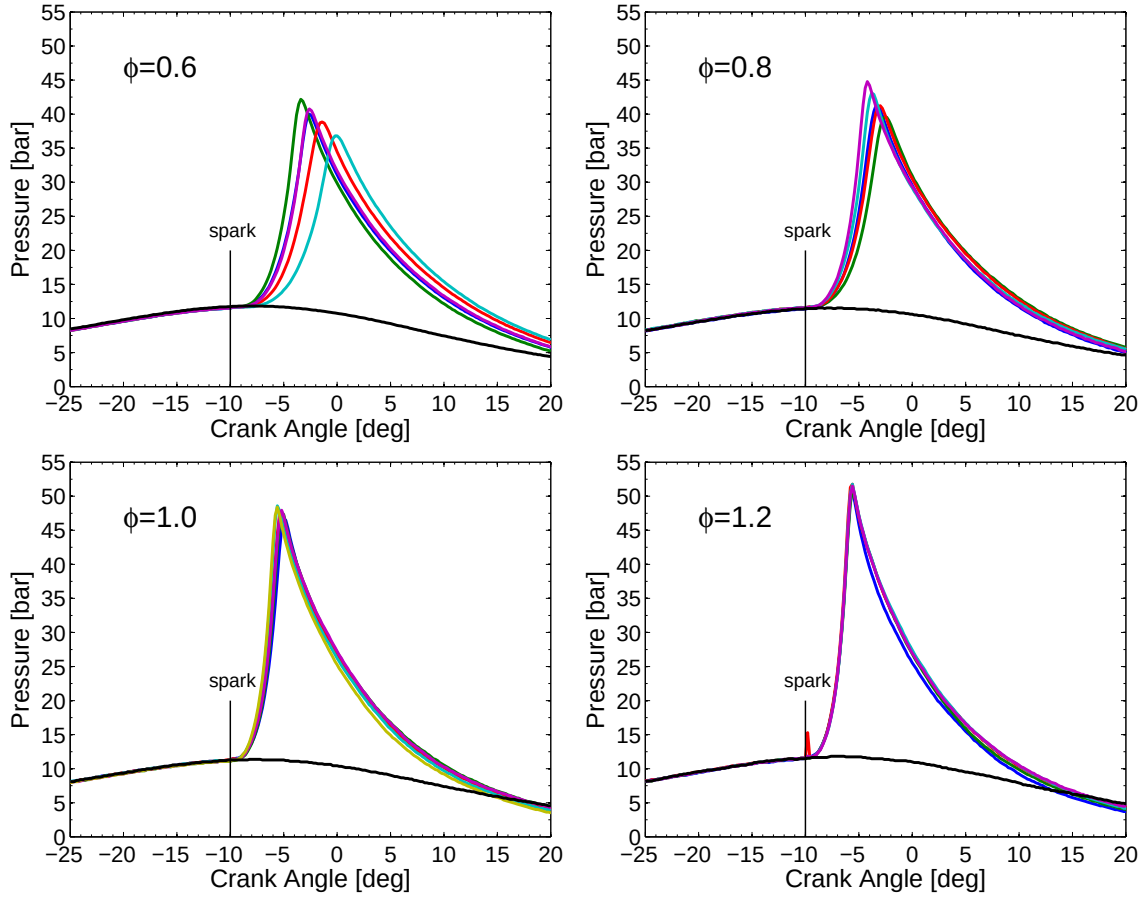

Figure 5.8: Pressure cycles from one engine run at a speed of 100 rpm for different equivalence ratios.

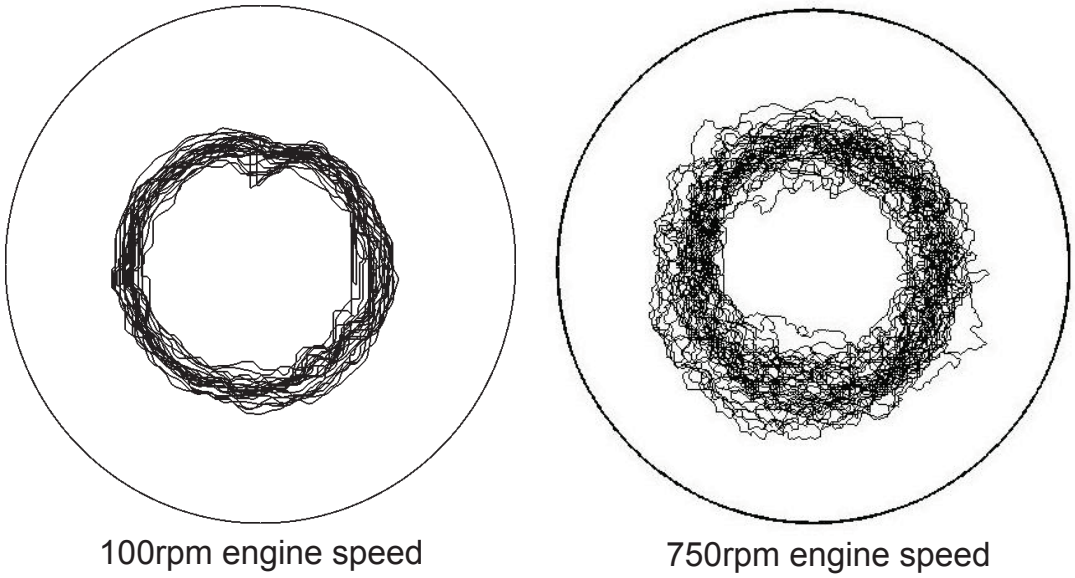

Figure 5.9: Comparison of flame contours at engine speeds of 100 rpm and 750 rpm, these flame contours were derived from laser sheet images at the 2^{o}CA and 10^{o}CA after ignition, respectively, with stoichiometric iso-octane fuel.

flame front still can be observed at the engine speed of 100 rpm, they are relatively small compared to the turbulent flame at the engine speed of 750 rpm, and the differences of flame radius between each firing cycle at the low engine speed are also much lower than that of a turbulent flame at the high engine speed.

5.2.3 CH* chemiluminescence image results

The CH* chemiluminescence image method, i.e. flame photographs taken with an interference filter for 470 nm, see Section 4.2.1, was used to obtain the flame development information. Shown in Figure 5.10 are 4 typical examples of sequential CH* imaging of developing iso-octane flames for lean, ϕ = 0.6 and 0.8, stoichiometric, ϕ = 1.0, and rich mixtures ϕ=1.2. Intakes and wall temperature were kept at 323 K, and the spark timing was set at 10^o bTDC. The pressure and temperature at the spark discharge are 12 bar and 600 K, as derived from LUSIEDA simulation. The dotted circle, which has the same area as the flame, is also shown in each flame image to compare with the instantaneous flame front shape.

The moments of nearly equal flame areas were selected in each row to compare the effect of equivalence ratio on the flame front. The time and crank angle of each flame were listed on the top left corner and bottom left corner. There was a large difference in the time that flame radius took to reach a similar size, between 0.6, 0.8, and 1.0, while the stoichiometric and rich flames look more similar. This observation agrees with the pressure traces shown in Figure 5.8.

The high ignition energy from spark disturbed the initial flame shape. The lean flame retained the ”cracks” caused by the spark and growing, became more wrinkled. However, the flame surface still attained an almost spherical shape with large scale distortions. Stoichiometric and rich flame spread more uniformly during the initial stage and had an ability to ”recover” from the spark-induced ”cracks”. The flame kept a spherical shape until the flame developed to a radius of approximately half of the engine cylinder diameter (20 mm). Small scale wrinkles started to appear, and quickly covered the whole flame surface. It was the same for the lean flame.

These regular curved small shapes are similar to the cellularity structure caused by a hydrodynamic instability. Although the detailed structure observation is limited by the 2D measurement method, the observed structures were significantly different from those observed at high turbulent flow conditions, where flame showed very irregular wrinkled shapes that occurred quickly after ignition. Flame deceleration happens when

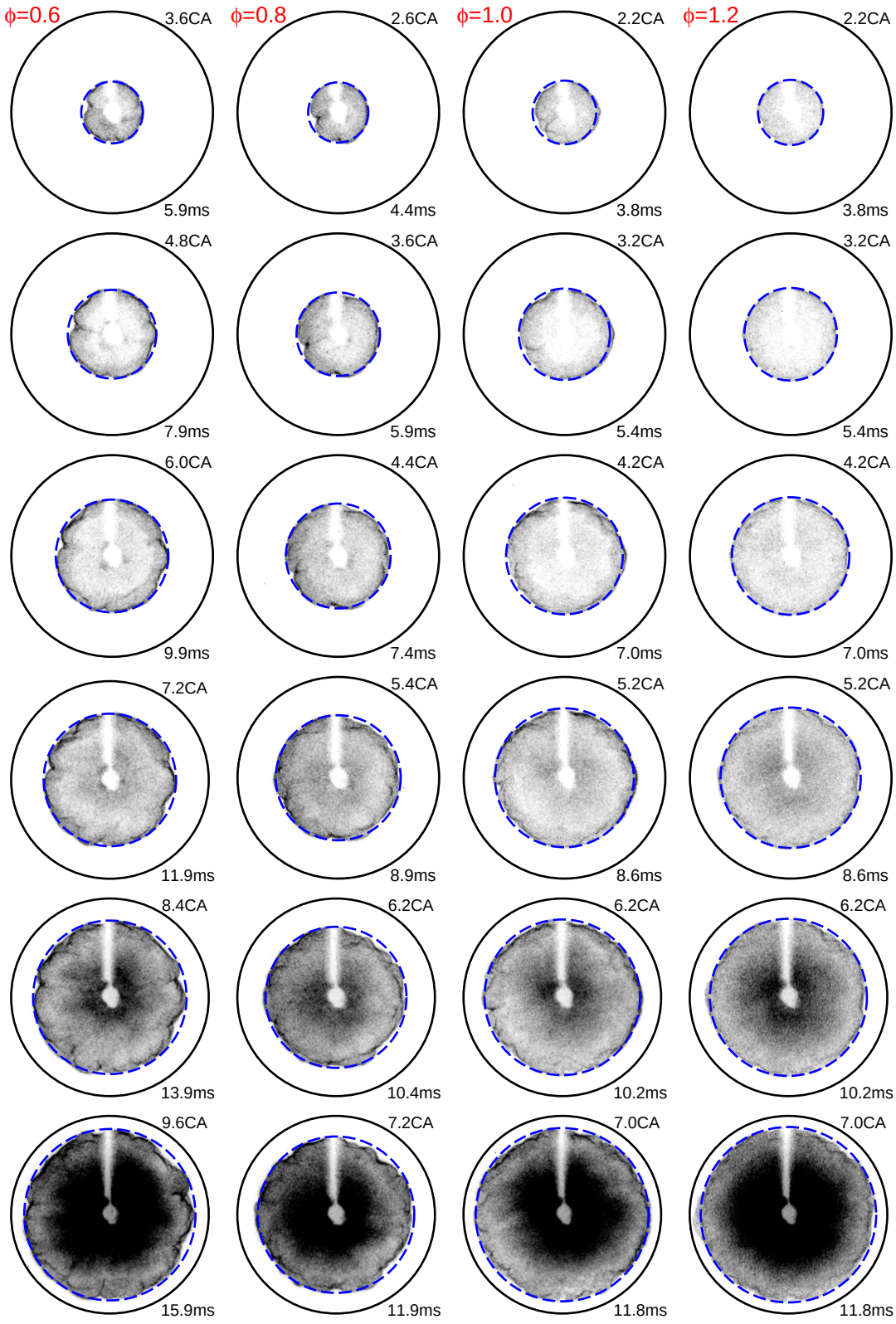

Figure 5.10: Typical CH* chemiluminescence images (colour inverse) at different equivalence ratios at the engine speed of 100 rpm, pressure is 12 bar and the temperature was estimated 600 K at the spark timing. The dotted circle has the same area as the flame.

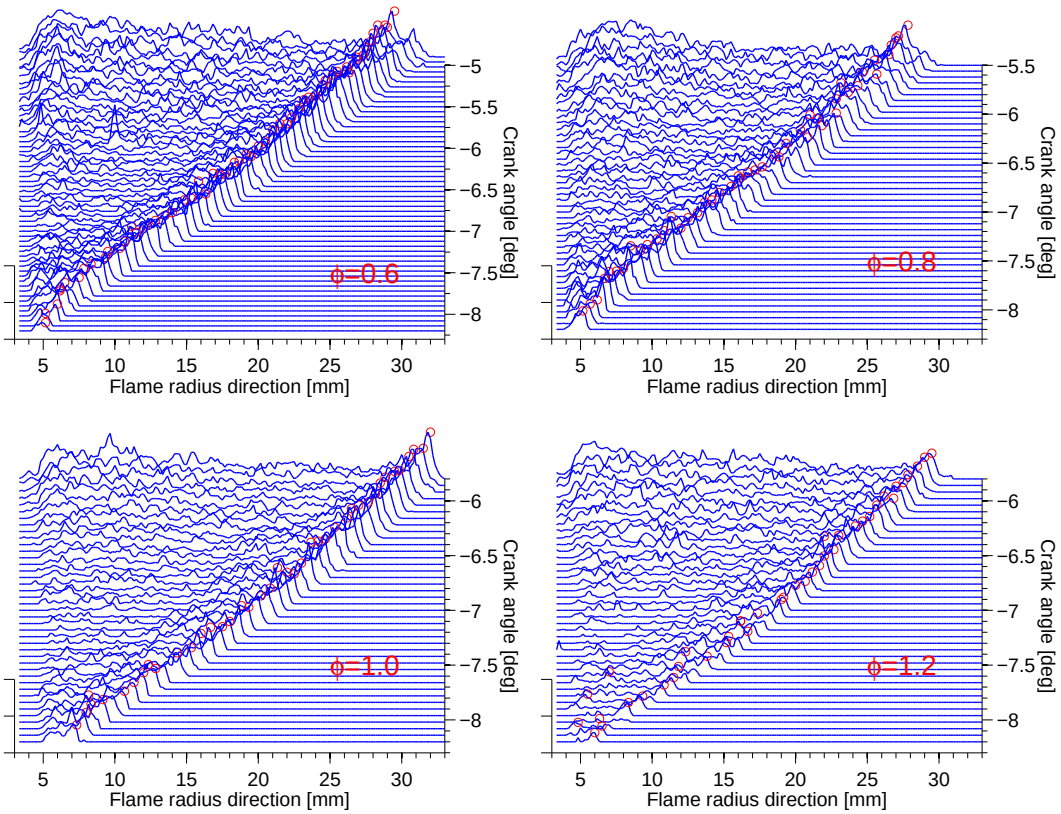

Figure 5.11: Local flame propagation with image intensities as magnitude derived from Figure 5.10 at the third direction in Figure 5.12.

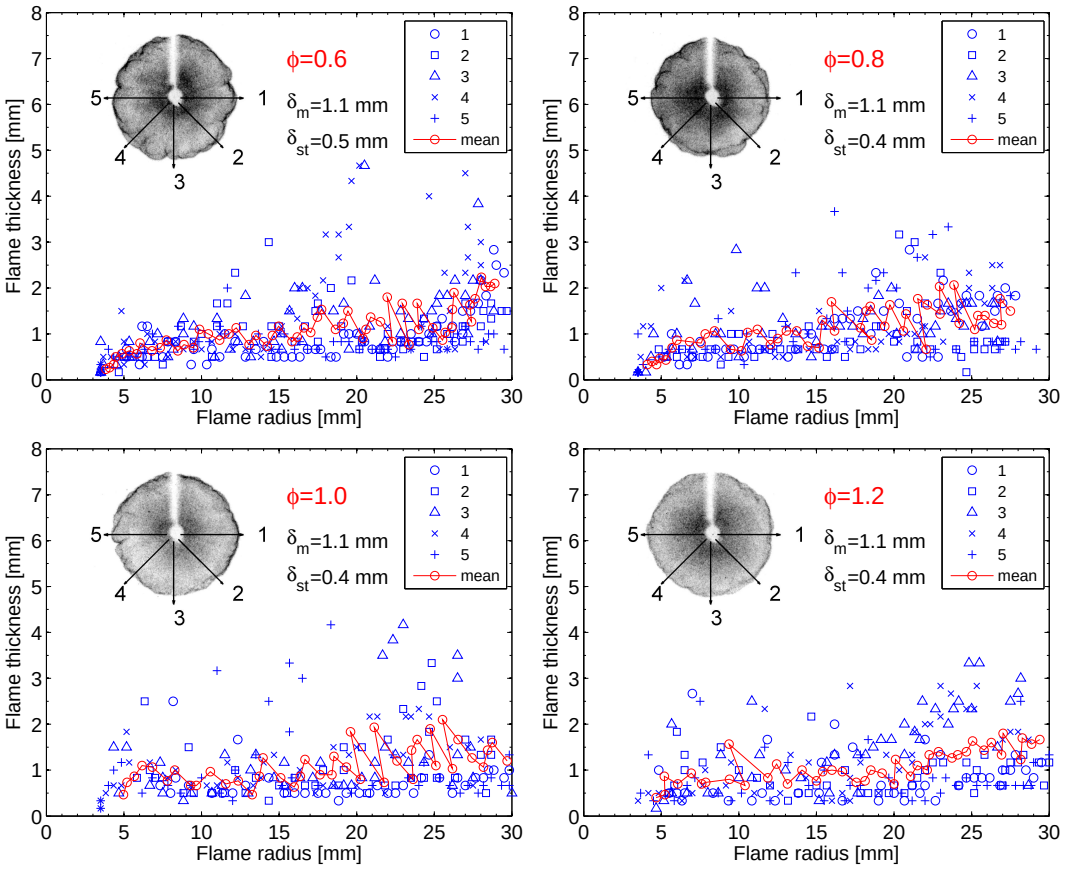

Figure 5.12: Local flame thickness development at 5 directions along the flame radius derived from 5.10 at different equivalence ratios.

the flame is approaching solid walls; the walls also significantly reduce the visible flame speed because they suffuse the flame thermal expansion.

The flame brush thickness might be characterized using the pixel intensity of the CH* chemiluminescence images, this method has been demonstrated in Section 4.2.1. The sliced profiles of luminescence signals from four different equivalence ratios flames along the radial direction were shown in Figure 5.11 with crank angle. The positions of these sliced profiles were in the third direction drawn in Figure 5.12. The sharp gradient of the flame luminescence signal can be observed in the front, the peak positions have been denoted by red circles. The distance between this peak position and the flame front was defined as the flame brush thickness. Due to the noise existing on the flame image caused by soot or droplets on the top window, the detected peak position of the flame front would be interfered with, see the left bottom corner of the fourth sub-figure in Figure 5.11, however, this method should still be able to derive the main feature of the flame front.

The calculated flame brush thicknesses from five directions with 45^o angle interval have been plotted in Figure 5.12. These four sub-images represent the four flames given in 5.10 with different equivalence ratios. It can be seen that the flame thickness becomes thick with the flame propagating; this value is about 1-2 mm. The mean flame brush thicknesses calculated from five directions were also plotted in Figure 5.12. The mean flame brush thickness was further averaged with the time, the averaged mean thickness with its standard deviation was shown in Figure 5.12. Four cycles show the same mean value of 1.1 mm and standard deviation of 0.4 mm, only the lean case $\phi = 0.6$ show a slightly larger value than others in the standard deviation value, since the camera has only about 0.1 mm resolution, so the difference below this value could not be distinguished. The small value of flame thickness confirmed that the flame tended to be laminar flames at a slow engine speed.

5.2.4 Experimental conditions

Pressure history with crank angle and flame radius between 10 to 20 mm are shown in Figure 5.13, at an engine speed of 100 rpm for lean, ϕ = 0.6 and 0.8, stoichiometric, ϕ = 1.0, and rich mixtures, ϕ = 1.2. Intakes and wall temperature were kept at 323 K, and the spark timing was set at 10^o bTDC. From the Figure 5.13, the minimum pressure change happens at equivalence ratio 0.8, the value was about 4 bar, the maximum pressure change was 10 bar at equivalence ratio 1.2 and 0.6. The volume change is illustrated in Figure 5.14, the clearance height of the LUPOE 2D engine is 8 mm, the spark plug has 4 mm height. After

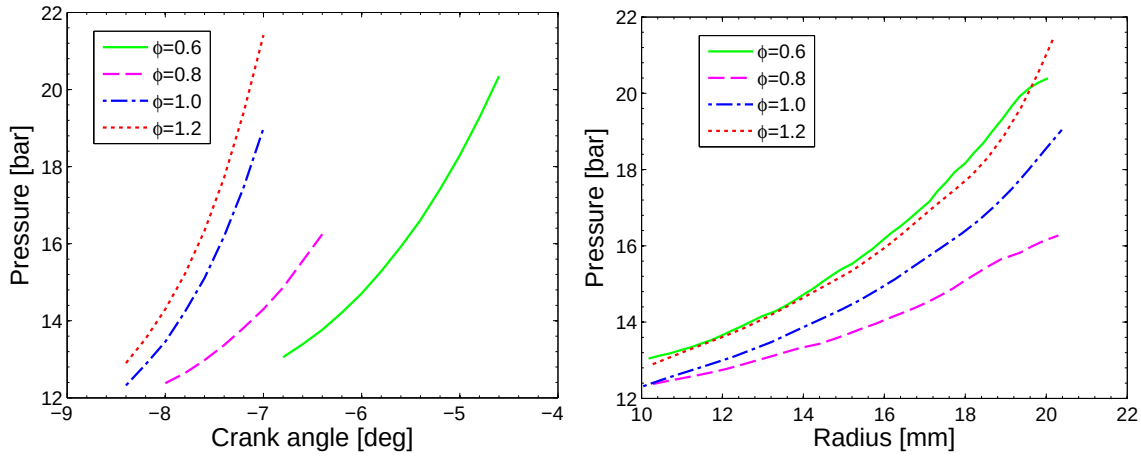

Figure 5.13: Pressure change with crank angle (left) and flame radius (right) at spark timing 10^o bTDC and an engine speed of 100 rpm with different equivalence ratios.

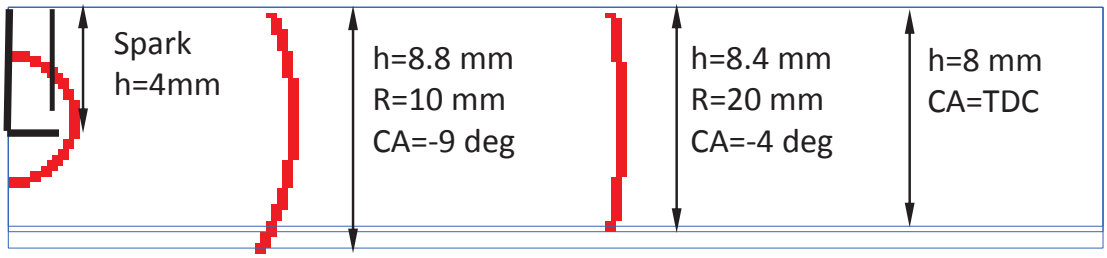

Figure 5.14: Engine volume change with crank angle and flame radius.

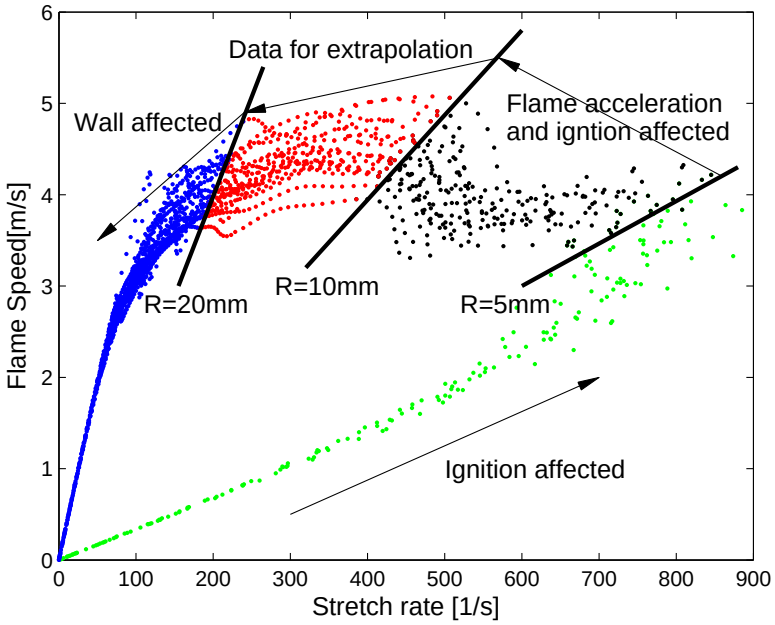

Figure 5.15: The flame speed as a function of stretch rate for a stoichiometric flame at an engine speed of 100 rpm.

expansion, the spherical flame contacted the cylinder head wall and piston surface, the curvature of flame front became flat, thus the flame could be considered as a cylindrical flame. During flame propagation from 10 to 20 mm, the volume height changed only about 0.4 mm, which is equal to 5% of the total volume. This combustion process can be considered to be a constant volume process.

The flame speed as a function of stretch rate for stoichiometric flame at the engine speed 100 rpm was calculated using equation 2.28, and shown in Figure 5.15. It can be seen that there was an acceleration of flame speed during flame radius was 5 mm to 10 mm, and a deceleration near the wall. Therefore, the experiment data influenced by ignition, and wall confinement region should be excluded.

5.2.5 Burning velocities

The development of the flame radius was determined from CH* chemiluminescence photographs collected in Section 5.2.3. The method has been described in Section 4.2.1. Different equivalence ratios flame radius histories were grouped and shown in Figure 5.16. The effects of mixture stoichiometry on the cycle variability are identical to those observed from the pressure traces.

The flame radius is close to a linear function of time in the middle of flame development. The initial flame development is influenced by the spark until the flame developed to a radius of approximately 8 to 10 mm, while the flame radius decelerated near the wall. Thus, the initial and final stages were excluded from the burning velocity calculation. The mean value of stretched flame speed S_n of each firing cycle was determined as a value equal to the slope of the linear-fit line for the flame radius between 10 mm and 20 mm.

The burning velocity was further derived as $U = (\rho_b/\rho_u)S_n$, and the value of the thermal expansion ratio was calculated for the converted values of pressure using LUSIEDA software. This burning velocity is affected by stretch and instability. The mean and first standard deviation values of burning velocities at different equivalence ratios were shown in Figure 5.17. The lean mixture has lower burning velocities of 0.6 m/s and 0.8 m/s, while rich and stoichiometric mixture exhibit almost the same burning velocities of 1.1 m/s. These values will be compared to the other measurements in the following Sections.

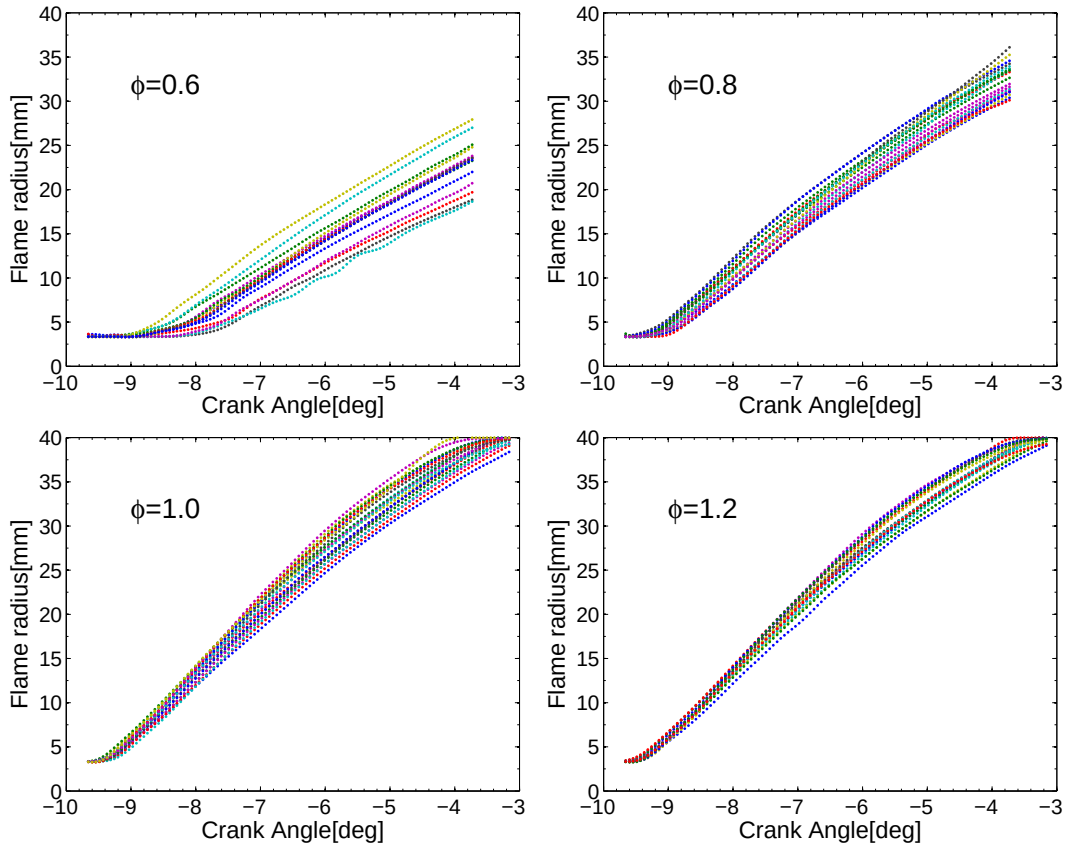

Figure 5.16: Flame radii development at different equivalence ratios at an engine speed of 100 rpm.

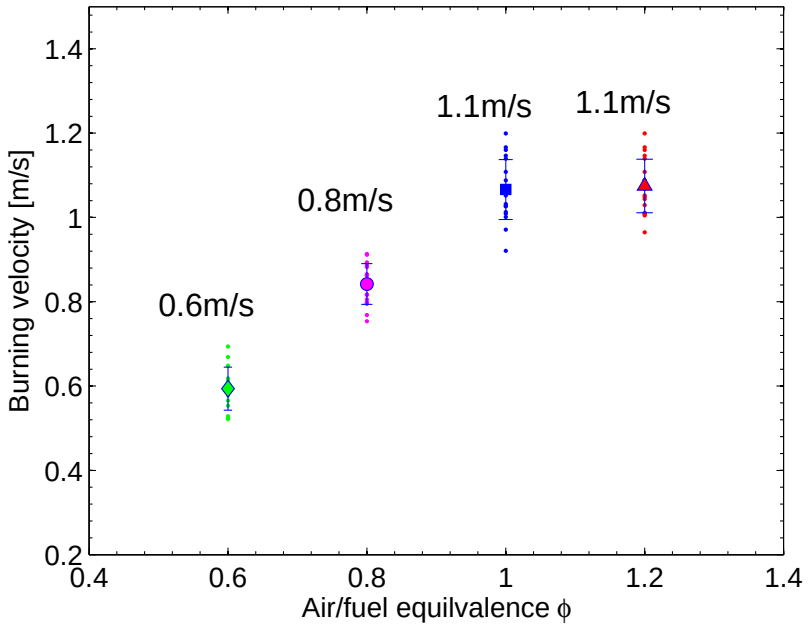

Figure 5.17: Mean burning velocities of iso-octane-air mixture at an engine speed of 100 rpm, the initial pressure is 12 bar and temperature is 600 K at the spark moment.

5.3 On a turbulence free burning velocity in engines

It has been shown in Section 5.1 that there exists an almost linear relationship between the engine speed and RMS flow velocities in the cylinder. Turbulence-free flow can be assumed at a zero engine speed. Here, we explore a new method of measuring a laminar burning velocity at turbulence-free conditions, the method is based on extrapolating the burning velocities from different engine speeds. In order to maintain the same initial pressure and temperature conditions, the spark ignition timing has to be adjusted.

Because of knock occurrence at early advanced spark timing, for this new method, the spark timing was generally set after the Top Dead Centre. The spark timing, at which in-cylinder pressure attains 15 bar, was chosen. With increasing the engine speed, the in-cylinder peak motoring pressure also increases, thus the spark timing has to be retarded into the expansion stroke. Four engine speeds have been selected: 150 rpm, 200 rpm, 250 rpm, and 300 rpm. The peak pressure at 100 rpm was lower than 15 bar, so this speed was excluded from the extrapolation and used only for comparison analysis.

The pressure selected for ignition, P_0=15 bar, was slightly below the peak motoring pressure and it could have been achieved at either 6^oCA bTDC or at slightly differing times after TDC, see the annotated lines in Figure 5.18. Obviously, the peak pressure is very sensitive to the spark timing around the TDC. In order to match not only the pressure but also the temperature for different engine speeds, a set of calculations was undertaken using LUSIEDA, and the resulting pressure-temperature history is shown in Figure 5.18 (d), together with the indication of the in-cylinder charge state at the spark timing. Although the difference of temperature exists at TDC, the temperatures of the 4 conditions are similar at the spark timing with a high value 606 K.

Shown in Figure 5.19 are CH* images of growing flame at stoichiometric equivalence ratio at engine speeds from 150 rpm to 300 rpm. With increasing the engine speed, the mean and RMS flow velocities increase, shown in the Section 5.1. Although the flame kernels for 4 engine speeds look similar for a short while after ignition, the flame quickly becomes wrinkled, presumably because of turbulence at higher engine speed. Meanwhile, the flame also travels at a faster speed. This can be seen from Figure 5.19 which shows the flame shape taken at approximately the same flame size while the time required to reach this stage is shown in the annotations. It is appropriate to notice that, even though a higher engine speed means faster flame, the increase is not linear. At a low engine speed, the flames show a small regular curved flame structure during the flame propagation, while with stronger turbulence they have irregularly and strongly

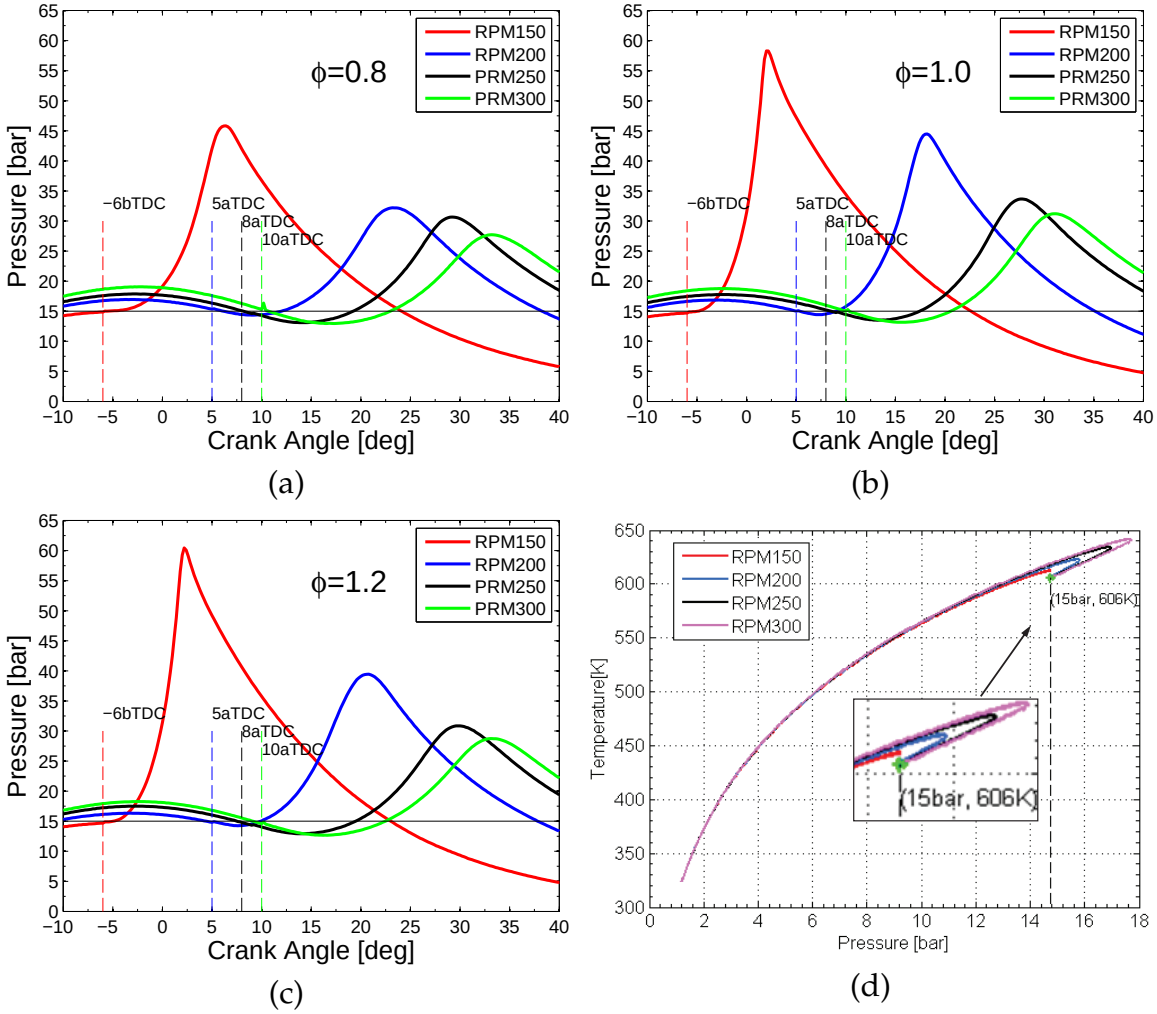

Figure 5.18: Mean pressure trace at different engine speeds and equivalence ratios with the same pressure at spark timing. The histories of pressure and temperature at these engine conditions are shown in (d).

curved fronts. A similar set of CH* flame images for rich flame at equivalence ratio of 1.2 are shown in Figure 5.20.

The method employed to derive the burning velocity from each firing cycle is the same one described in the Section 5.2.5. There were 30 cycles captured at each condition, and the mean value and the first standard deviation of burning velocities were plotted in Figure 5.21. The extrapolation method was applied using mean values at each engine speed, and the values at zero rpm were presented in the same Figure. As expected, the burning velocity decreases with the reduction of engine speed at equivalence ratio 0.8 and 1.0. The burning velocities are estimated as 0.78 m/s at equivalence 0.8, and 0.94 m/s at equivalence 1.0. Nevertheless, it is surprising that the burning velocity increases with the engine speed decreasing at the equivalence ratio 1.2 case.

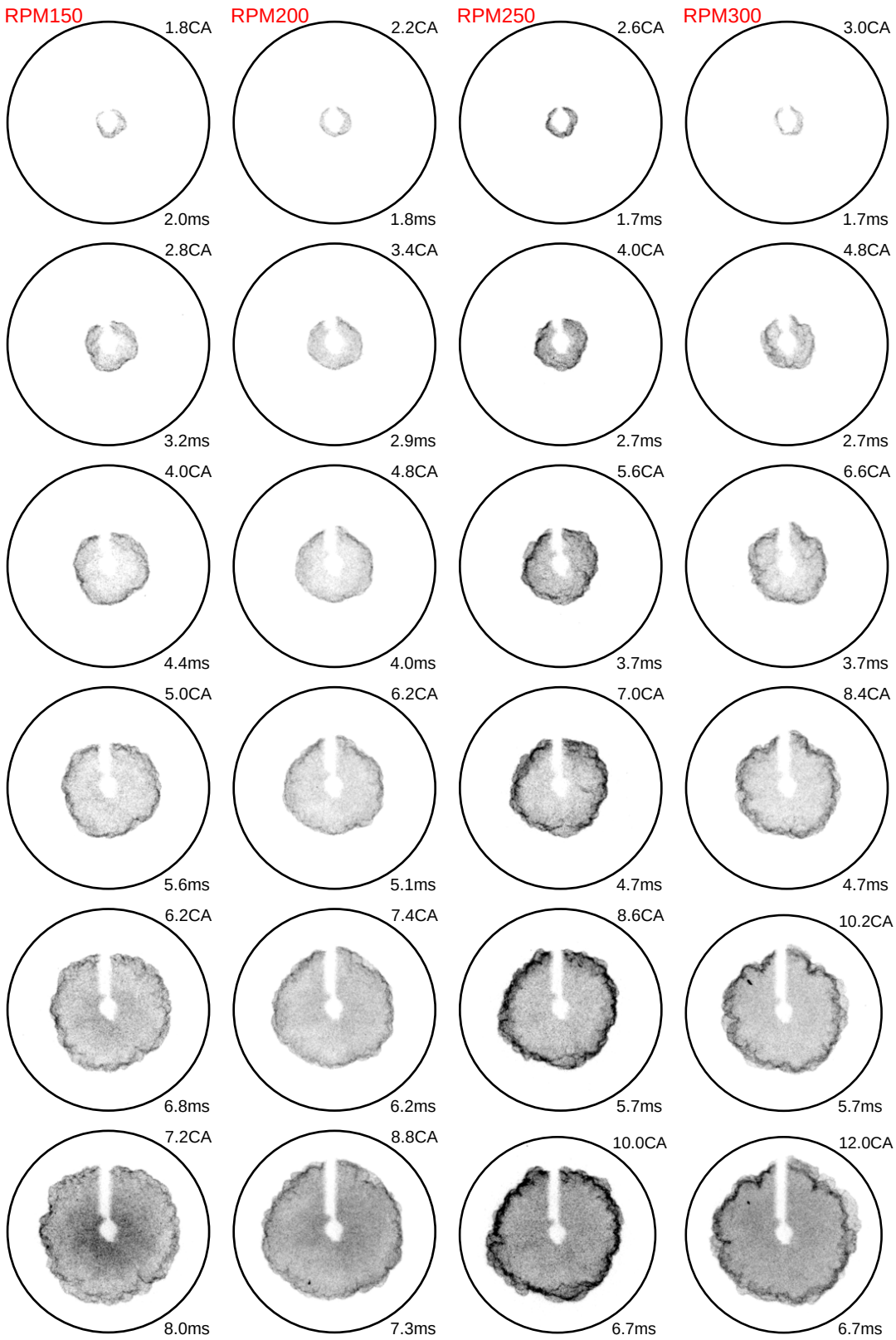

Figure 5.19: Typical CH* chemiluminescence images (colour inverse) captured at stoichiometric equivalence ratio at different engine speeds.

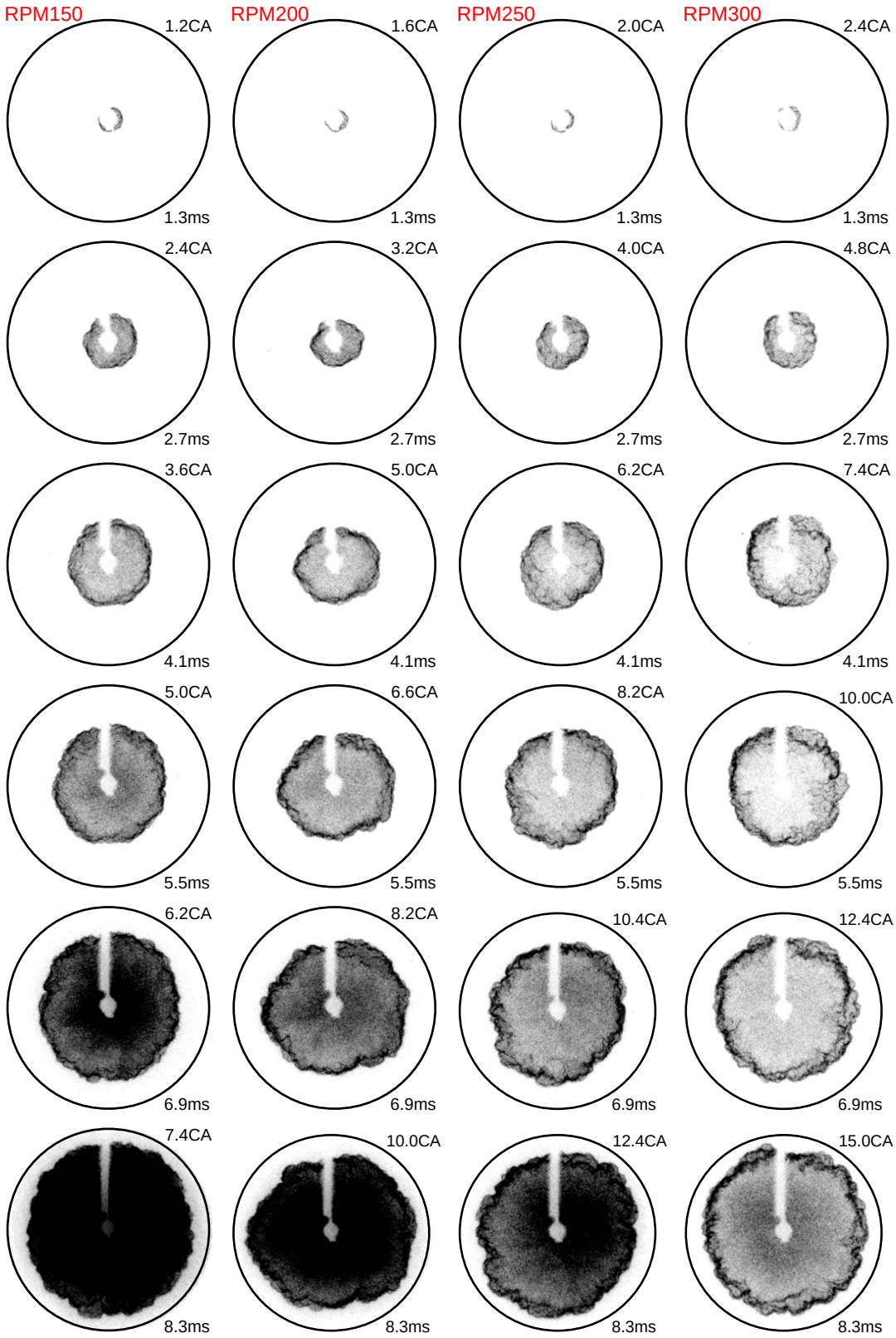

Figure 5.20: Typical CH* chemiluminescence images (colour inverse) captured at equivalence ratio 1.2 at different engine speeds.

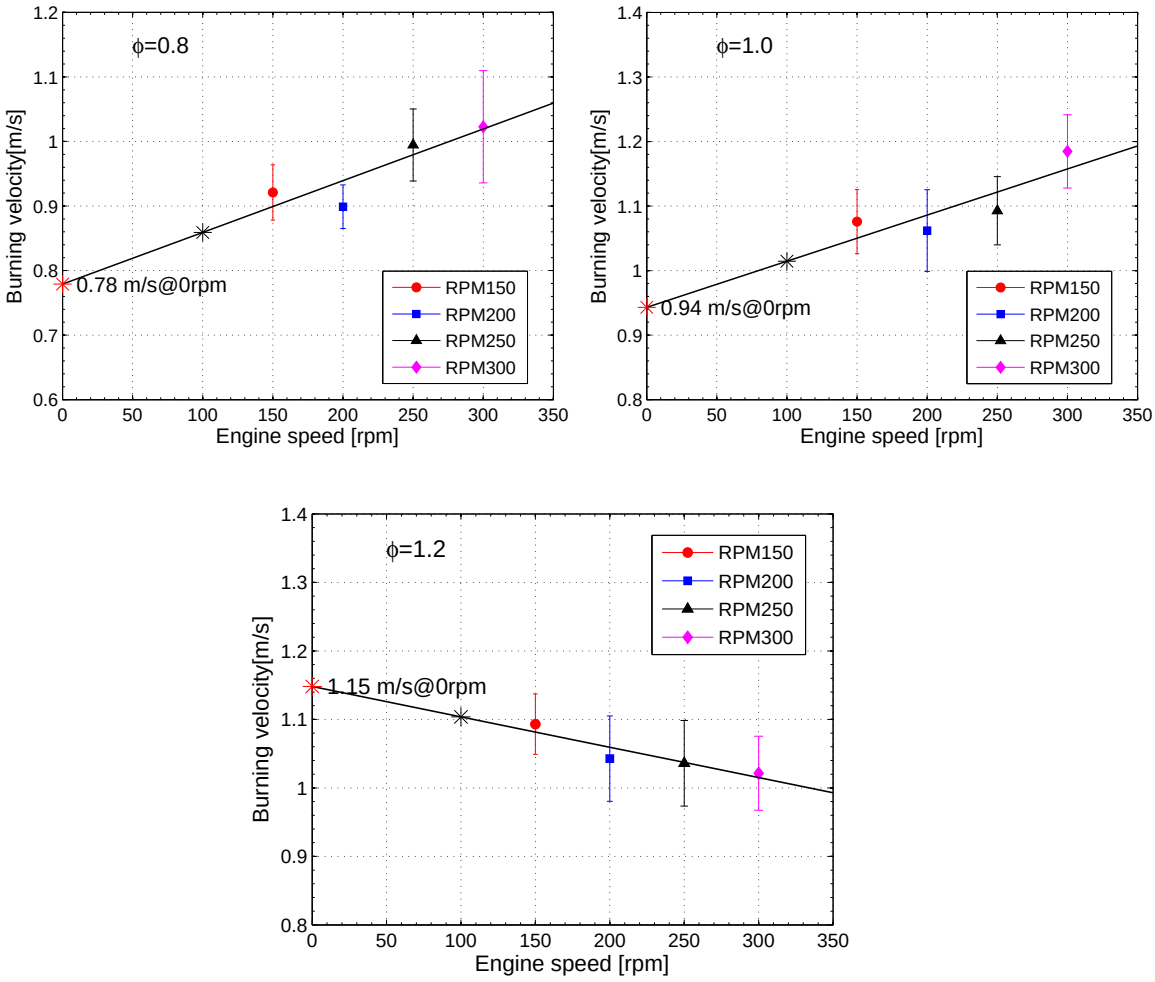

Figure 5.21: Extrapolation of flame speeds using mean burning velocities from different engine speeds at equivalence ratios 0.8, 1.0 and 1.2. The error bar is the standard deviation of burning velocities at each condition.

By applying a similar method to that described in Section 5.2.3, the flame brush thickness during the flame propagation was characterized. The flame thickness was derived from the gradient of the image pixel intensity along the flame radius. The directions of a sliced sections have been shown in Figure 5.22. Comparing the values of flame thickness at equivalence ratio of 1.0 and 1.2 with different engine speeds, it can be seen that there is a significant increasing of flame thickness at the stoichiometric case from δ_m = 1.3 to 2.0 mm, while this tendency is not obvious for the equivalence ratio 1.2. The flame instability may compensate the turbulence influence at rich mixture. This finding needs more data to be validated. However, this phenomena would not bring a large error in the measured burning velocity, since the slope of extrapolation at equivalence ratio 1.2 is very small.

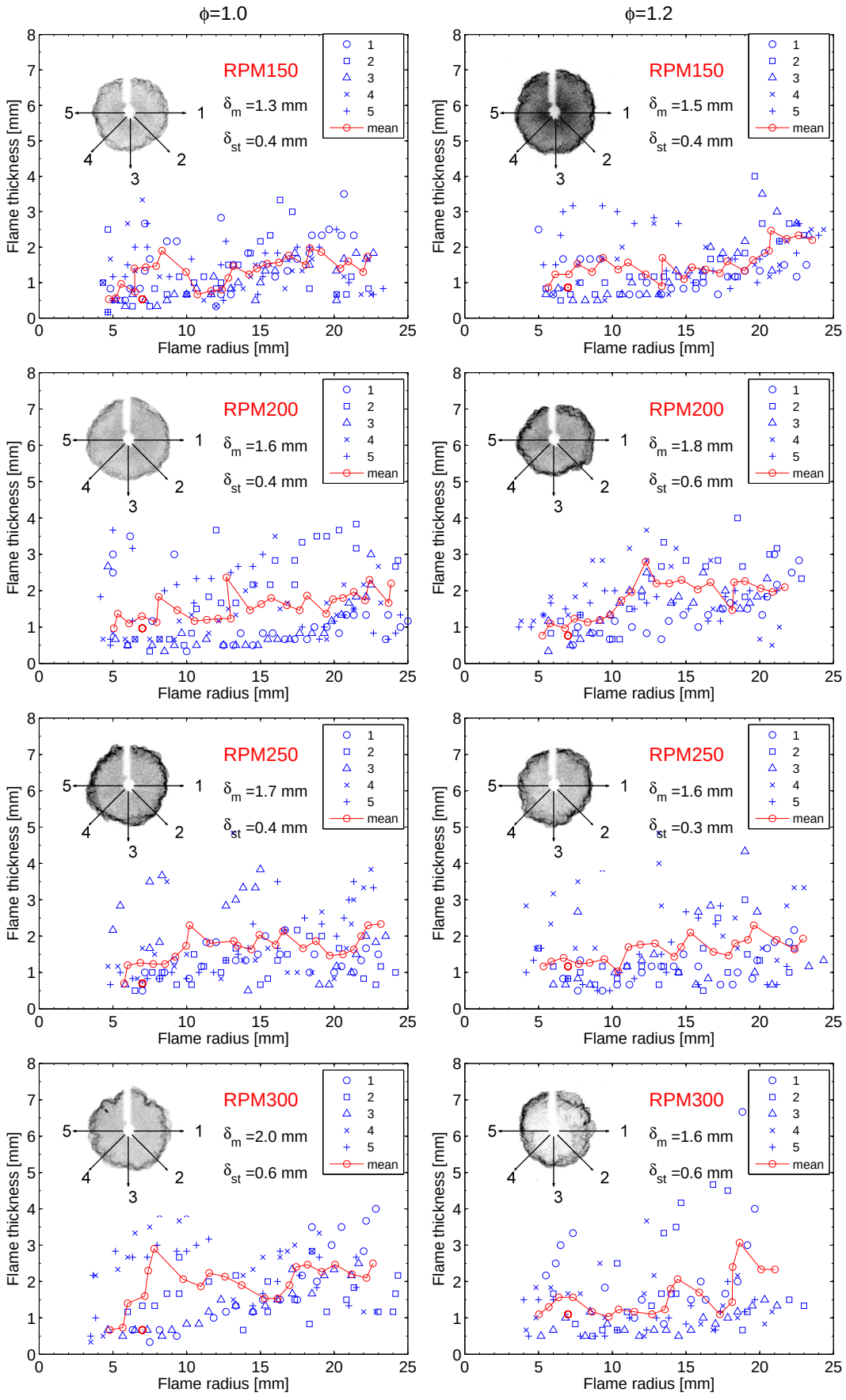

Figure 5.22: Comparison of flame brush thickness derived from Figure 5.19 for stoichiometric $\phi = 1.0$ and Figure 5.20 for rich mixture $\phi = 1.2$.

5.4 Laminar flame speed correlations and simulation

The laminar burning velocity of iso-octane fuel has been widely measured in constant volume combustion vessels (Bradley et al. [1998]; Galmiche et al. [2012]; Jerzembeck et al. [2009]; Metghalchi and Keck [1982]. Nevertheless, the current measurement pressure and temperature conditions are outside the range that can be obtained in these bomb experiments as shown in Figure 5.23. The available experiment data from the literature also could not cover the real boosted engine operation region, used in this work. In order to validate the measurement results, correlation equations and computer modelling method were used. First, various correlation equations for laminar flame speed and a chemical reaction mechanism were evaluated by the experimental data from bomb at the low pressure and temperature range in this Section. Then the calculated data were extended to the current high pressure and temperature experimental conditions to compare the measured data in the next Section.

5.4.1 Experimental data review

Outwardly propagating flame configuration has been proven to be the most suitable for high pressure flame speed measurements. Iso-octane burning velocities of laminar flame at elevated pressures are often measured in a constant volume vessel. Early works include those of Metghalchi and Keck [1982], and Ryan and Lestz [1980]. They derived the burning velocities from thermodynamic analysis of the pressure rise in a bomb. Even though effects of flame stretch and hydrodynamic instabilities might be included in these measurements, they were neglected for a long time. Recent works, e.g. Bradley et al. [1998], and Jerzembeck et al. [2009], applied optical methods to record the flame propagation process, hence it can be considered to be the direct measurement of the stretched laminar flame propagation speed. Here, four sets of experimental data for iso-octane laminar burning velocities were used to validate the correlation equations and chemical reaction simulation at the low pressure, these experimental data are from four research groups, and they are listed in Table 5.1.

All reviewed experiments were conducted in constant volume combustion vessels or bombs, of different sizes and shapes. The spherical stainless steel bomb in Leeds (Bradley et al. [1998]) has the large inner diameter of 380 mm and optical windows of 150 mm diameter, and it is capable of withstanding initial pressures of up to 15 bar and initial temperatures of up to 500 K. The air and fuel were mixed using four fans driven by electric motors. Galmiche et al. [2012], carried out experiment in a similar spherical

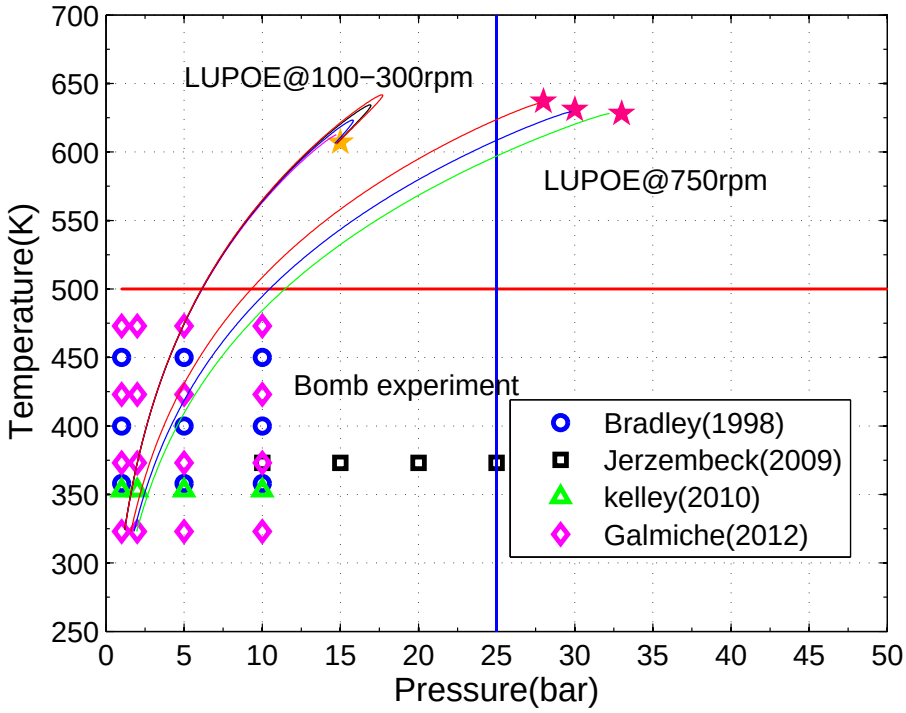

Figure 5.23: Comparison of experimental conditions in this study with available experiment data of iso-octane laminar burning velocity from bomb experiments in the literature (Bradley et al. [1998]; Galmiche et al. [2012]; Jerzembeck et al. [2009]; Kelley et al. [2011]).

Table 5.1: Previous high pressure iso-octane air laminar burning velocity studies.

Investigators	Equivalence ratio	Pressure [bar]	Temperature [K]	Closed vessel size
Bradley et al. [1998]	0.8,1.0	1-10	358-450	380mm spherical
Jerzembeck et al. [2009]	0.7-1.2	10-25	373	100mm spherical
Kelley et al. [2011]	0.7-1.7	1-10	353	82.55mm cylindrical
Galmiche et al. [2012]	0.8-1.1	1-10	323-473	200mm spherical

combustion bomb relying on molecular diffusion for mixture preparation. The inner diameter of the bomb used in his experiment was 200 mm, and the initial pressure inside the combustion chamber was limited to 10 bar. Jerzembeck et al. [2009], used a small bomb with inner diameter 100 mm, and optical windows 50 mm. The maximum initial pressure achieved in his experiment was up to 25 bar. Kelley et al. [2011], developed a dual-chamber cylindrical vessel. The outer chamber has 273 mm inner diameter and 304.8 mm length, the inner chamber was 82 mm inner diameter and 127 mm length. Two quartz windows (114 mm diameter) were installed at the both end sides. The maximum pressure was claimed to achieve 60 bar, however the data for iso-octane presented in their published work was at 10 bar.

During experiments at the constant volume vessel, fuel and air mixture were ignited at the centre, and schlieren photography was applied to record the progress of flame development. The mean flame radius was derived from each schlieren image. The laminar flame speed could be calculated as the rate of change of flame radius with time. Only images of laminar flame propagation without ignition effect and captured before the onset of flame instability were used (Bradley et al. [1998]). Bradley et al. [1998] applied a first order least-squares fit through four adjacent radii to obtain a flame speed, then derived an unstretched laminar burning velocity using a first-order fitted Markstein length as described in Section 2.2.1.2. Jerzembeck et al. [2009] adopted the similar way to process the data. Both Kelley et al. [2011] and Galmiche et al. [2012] used a nonlinear extrapolation method to obtain the unstretched laminar burning velocities.

5.4.2 Evaluation of modelling methods

A widely used laminar flame speed correlation expression has been proposed by Metghalchi and Keck [1982], which is a simple power law equation with reference temperature T_0 and pressure P_0 with two exponents α and β. these parameters were obtained using pressure traces recorded in a bomb.

$$u_l = (B_m + B_2(\phi - \phi_m)^2) \left(\frac{T_u}{T_0}\right)^{\alpha} \left(\frac{P}{P_0}\right)^{\beta} \tag{5.1}$$

where u_l is the laminar burning velocity, T_u is the unburnt gas temperature (K) and P is the pressure (bar). ϕ is the equivalence ratio. Similar expression was proposed by Al-Shahrany et al. [2005] using schlieren images recorded from two opposite propagating flames in a constant volume bomb. For an iso-octane-air mixture, the input parameters

Table 5.2: The range of applicability and data resource of different correlations.

Investigators	Equivalence ratio	Pressure [bar]	Temperature [K]	Data source
Metghalchi and Keck [1982]	0.8-1.5	0.4-50	298-700	Experiment
Al-Shahrany et al. [2005]	0.8-1.4	5-30	358-470	Experiment
Martz et al. [2011]	0.1-1.0	1-250	298-1000	Simulation

Table 5.3: Constants for Equation 5.1 for iso-octane-air mixtures.

Item	Metghalchi and Keck [1982]	Al-Shahrany et al. [2005]
α	2.18-0.8(ϕ-1)	1.16-3.33(ϕ-1)
β	-0.16+0.22(ϕ-1)	-0.30+0.42(ϕ-1)
P_0 [bar]	1bar	5bar
T_0 [K]	298 K	360 K
B_m [m/s]	2.632	0.32
B_2 [m/s]	-8.472	-1.07
ϕ_m	1.13	1.11

calculation are listed in Table 5.3. Another kind of laminar burning velocity correlation is based on an asymptotic analysis of flame structure, and the coefficients of equations are derived by fitting some approximate formulas with the data from numerical simulation. This type of correlation was proposed by Muller et al. [1997], and further developed by Martz et al. [2011] using a 215 species chemical kinetic mechanism to simulate steady laminar burning velocity in a wider range of equivalence ratios, unburnt gas temperatures, and pressures compared to the experiment, see Table 5.2. These data set were fitted depending on following Equations (Martz et al. [2011]), with the fit parameters listed in Table 5.4.

$$S_l = F(Y_f^u)^M exp(-G/T^0) \left(\frac{T_u}{T^0}\right) \left(\frac{T_b - T^0}{T_b - T_u}\right)^n \tag{5.2}$$

where Y_f^u represents the fuel mass fraction of the unburnt gas, T_b and T_u are burnt and unburnt gas temperatures. The inner layer temperature T^0 is calculated:

$$T^0 = \left(\frac{-E}{\ln(p/B)}\right) \left(Y_f^u + C_7\right)^{C_8} + C_9 T_u + a_1 p^{a_3} \left((Y_f^u)^{a_2} - Y_{f,stoich}^{a_2}\right) \tag{5.3}$$

Table 5.4: Constants for Equations 5.2, 5.3 and 5.4 for iso-octane-air mixtures.

F[cm/s]	M	G[K]	n	B[bar]	E[K]
280583	2.0837	-1375.3	4.9991	2.52E+10	81006
C_7	C_8	C_9	a_1	a_2	a_3
0.01599	0.4539	0.3218	0.72	-1.1	0.1
c	d	e	f	g	
2638.1	194.6	-773.045	-0.34968	0.3432	

Burnt adiabatic flame temperature, T_b, is calculated from the Equation:

$$T_b = T_u + \phi(c + d\phi + e\phi^2 + fT_u + gp) \tag{5.4}$$

Unstretched laminar burning velocity also can be calculated by using one dimensional adiabatic planar premixed flame simulation codes, such as the PREMIX in the CHEMKIN II package (Robert [1989]) with a number of elementary reaction mechanisms. In this study, a 99 species reduced mechanism for iso-octane/air mixture created by Yoo et al. [2013] was employed, and PREMIX code was used to simulate the laminar flame burning velocities. This mechanism was reduced from a detailed kinetic mechanism and has been applied to characterize the ignition process under HCCI and SACI engine conditions. The reaction mechanism should be carefully validated before applying them to laminar flame speed calculations. Furthermore, the effects of flame stretch and instabilities, which would typically be present at the elevated temperatures and pressures, were not included in these calculated burning velocities. It is not clear what the relationship of the idealised flame speed from such simulations to engine conditions where flamelets are subjected to curvature and instabilities. In the following content, the laminar flame correlation equations and adopted chemical kinetic mechanism are compared with the reviewed experimental data, to evaluate the performance of these modelling methods.

First, the two published iso-octane experimental data and four laminar burning velocity correlation expressions were compared at 358 K, 1 bar over a range of equivalence ratios as shown in Figure 5.24. These results represented the unstretched and stable laminar burning velocities, except the ones from Metghalchi and Keck [1982]. In their experiment, the effects of stretch and instability on the flame front were not corrected. However, their correlation gives slightly lower values at atmospheric conditions. The maximum difference predicted from the burning velocity correlation equations at stoichiometric was about 20 cm/s. For lean and rich flames, the divergences decreased moderately. By comparing the two sets of experiment data they have close values at

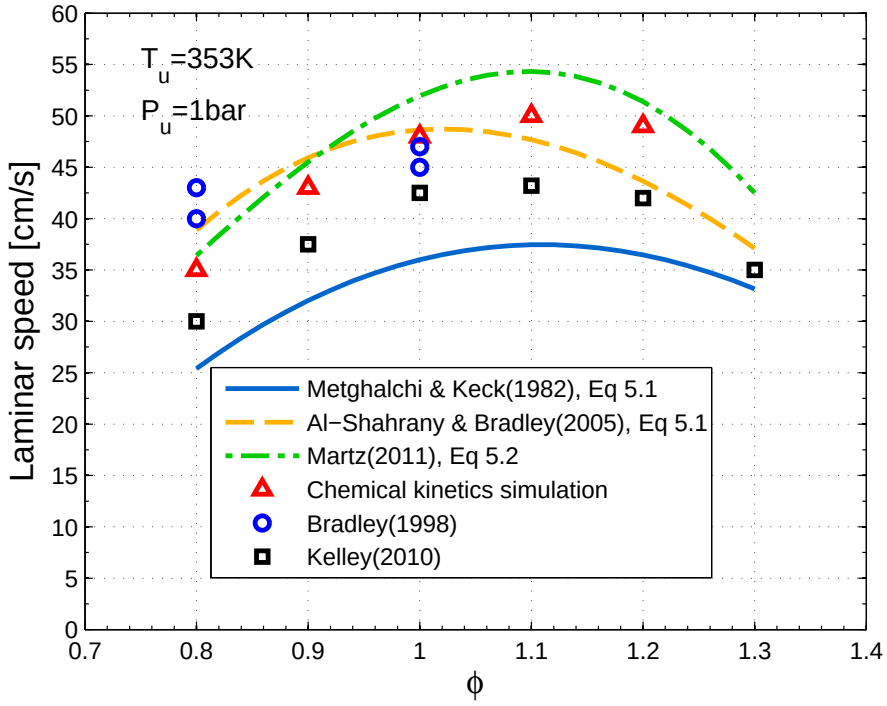

Figure 5.24: Laminar burning velocity correlations and experimental data compared at 1 bar and 353 K across a range of equivalence ratios.

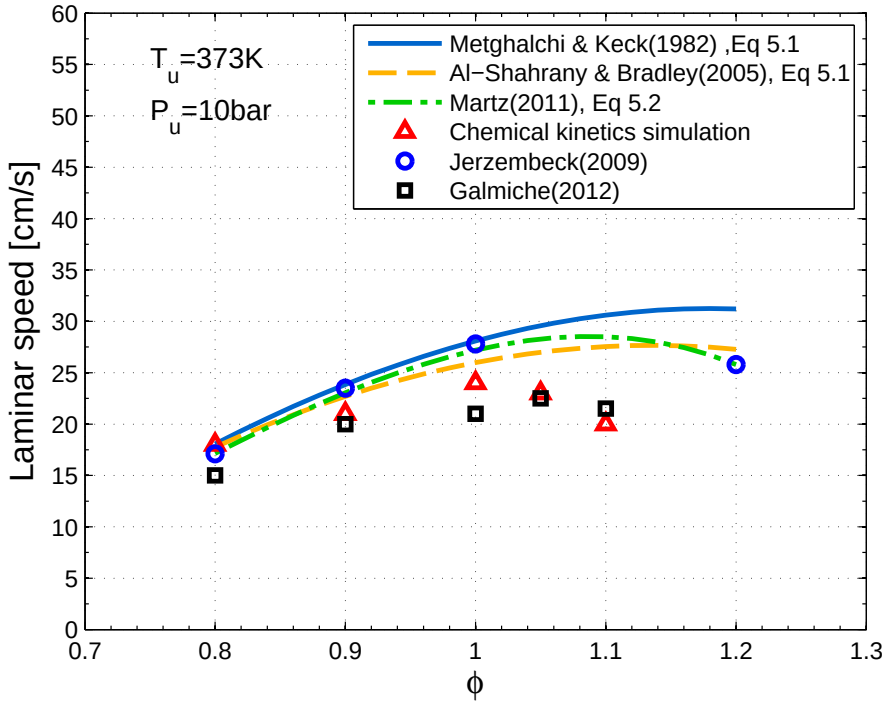

Figure 5.25: Laminar burning velocity correlations and experimental data compared at 10 bar and 353 K across a range of equivalence ratios.

stoichiometric, but about 10 cm/s difference at the lean condition (0.8). The values of burning velocity using the chemical kinetic mechanisms are located between two sets of experiment data. By increasing pressure to 10 bar with temperature at 353 K, as shown in Figure 5.25, the divergences between all the results became smaller at lean and stoichiometric sides. Martz's correlation corresponds well with the measurements of Jerzembeck's experiment, while chemical kinetic mechanisms results are closer to Galmiche's experiment.

Shown in Figures 5.26 is a comparison of the different laminar burning velocity expressions and experimental data over a wide temperature range. All the expressions exhibit an increasing tendency when the temperature increases. Laminar burning velocities of iso-octane in a wide range of temperature were only found in Galmiche's experiment. The differences between the results are not significant for low to intermediate temperatures compared to their values at high temperature (above 500K). Correlation equations show a large scatter at high temperature. The correlation equation of AI Shahrany predicts significantly lower values than the other correlation equations. The steepest temperature gradient was shown in Metghalchi and Keck's equation. The temperature evolution predicted by Martz's equations, and the chemical kinetic mechanisms, are very similar. It is hard to draw a conclusion on high temperature effects on flame because of the lack of experimental data.

The burning velocities are displayed on a logarithmic coordinate system with pressure change at temperatures around 373 K in Figure 5.27. All expressions show similar drop slops in the burning velocity with pressure increasing, with the exception of the correlation of Metghalchi and Keck, which showed a slowly burning velocity decreasing compared to the others at high pressure. Higher burning velocity was predicted by Metghalchi and Keck's equation, possibly due to the inclusion of cellular flames. The values of other correlations are higher than the data from Kelley and Galmiche's experiment, but have the best match with the data from Jerzembeck's experiment at high pressure. Jerzembeck and Galmiche's data have shown about a 10 cm/s difference at a pressure of 10 bar. This difference could be attributed to the effects of confined volume and extrapolation method. Even using the same extrapolated method, Kelley's results are still higher than Galmiche's, therefore the size of vessel volume has an effect on measurement of laminar flame burning velocity.

It can be concluded that these correlations can predict the tendency of laminar flame behavior with temperature and pressure. Martz's equations have a good prediction at low pressure for unstretched and stable flames. Metghalchi and Keck's correlation equation over predict the burning velocity at high temperature and pressure, it is prob-

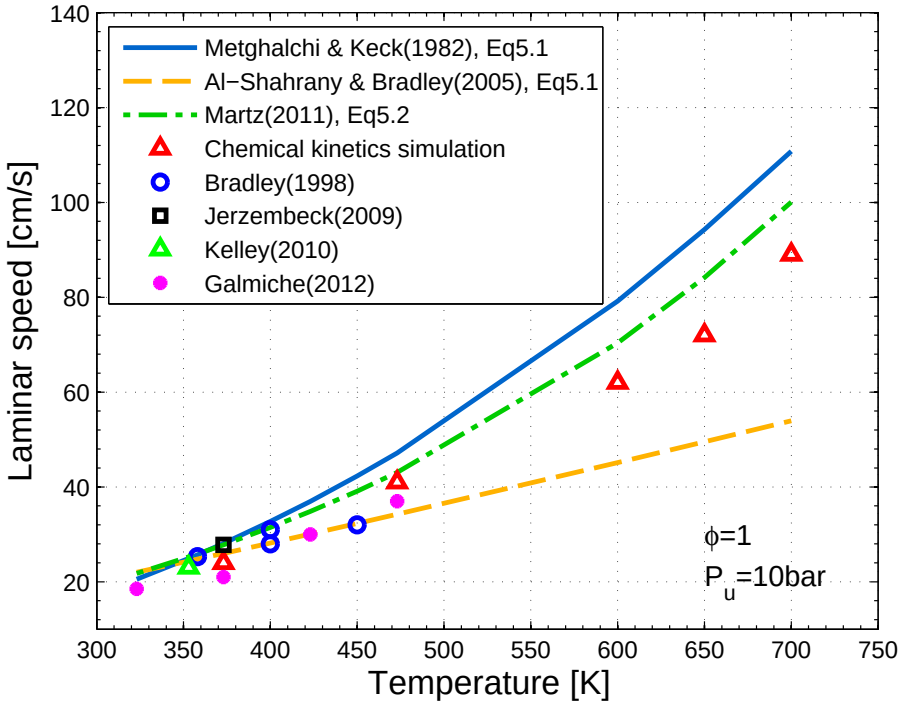

Figure 5.26: Laminar burning velocity correlations and experimental data compared at 10 bar and equivalence ratio 1 across a range of temperatures.

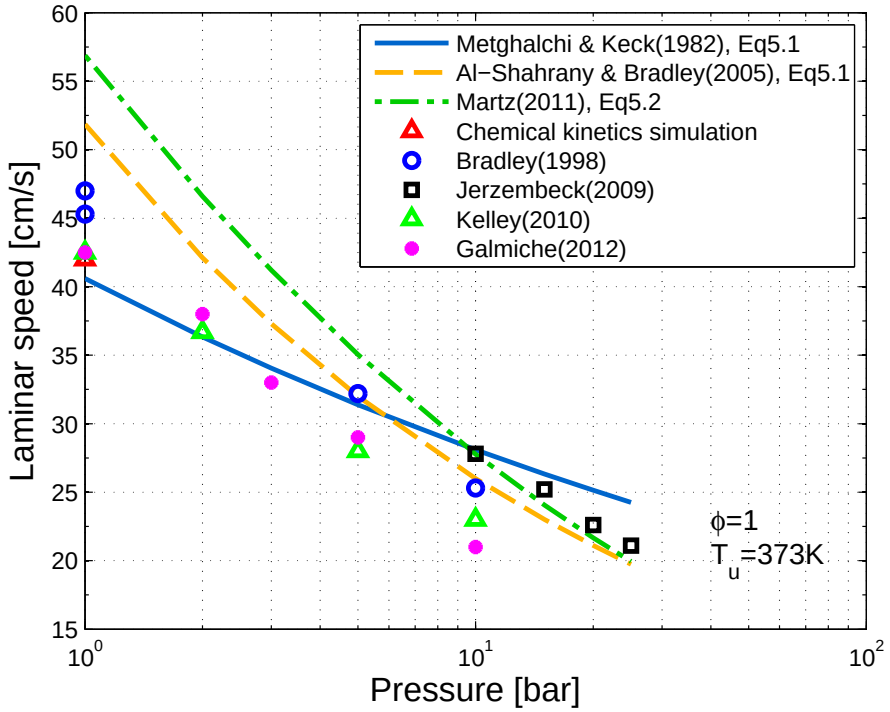

Figure 5.27: Laminar burning velocity correlations and experimental data compared at 373 K and equivalence ratio 1 across a range of pressures.

ably due to existence of stretch and instability in the measured flame. AI Shahrany's correlation equation might not be accurate at high temperature. When comparing the calculation results using the chemical kinetic mechanisms to the experimental burning velocity values, it can be seen that it has similar prediction as Martz's correlation equations. Because Martz's equations was derived from massive data using chemical kinetic mechanisms calculation, essentially, they employed the same method.

5.5 Comparison of experimental and numerical results

Comparing current measured burning velocities to predicted values from correlation equations at high temperature (600 K) and pressure (15 bar) in Figure 5.28, it was seen that the measurements in this study were higher than all calculation results at different equivalence ratios. The values extrapolated from different engine speeds have lower values than the ones directly measured from 100 rpm except for the rich mixture case. The difference between direct measurement and extrapolation at 100 rpm can be negligible.

Although the values derived from extrapolation method are lower than that from direct measurement, they are almost twice higher than the predicted values from Martz's correlation equations and chemical kinetics simulation. This means that turbulence-free environment is just one of pre-requisitions for accurate measurement of laminar flame speed. Flame speed are strongly affected by flame stretch, instability or other factors. For iso-octane-air mixtures at high temperatures and pressures, the Markstein number is low (Bradley et al. [1998]), hence neglecting the stretch effect on laminar burning velocity may not be too serious. Gerke et al. [2010] measured the hydrogen burning velocities in a single-cylinder compression machine at high pressure, and estimated an approximate speed ratio of 2, between the unstable laminar flame speed acquired from experiments and the simulated stable laminar flame speed for stoichiometric mixtures. This agrees well with the results presented here. Instabilities which arise at increasing pressure, may play an important role on flame speed, and it results in an acceleration of the flame speed.

It should also be noted that the measured values are higher than those predicted from Metghalchi and Keck's correlation equation, which may have included instability and stretch effects. Burke et al. [2009] reported that flame speed could be changed through more wrinkled flame surface induced by the thermal expansion near the wall. The size of combustion vessel has a great effect on determination of the laminar flame speeds. This effect can be observed on flame measurement by comparing the experimental data from different size bombs at the same pressure and temperature condition.

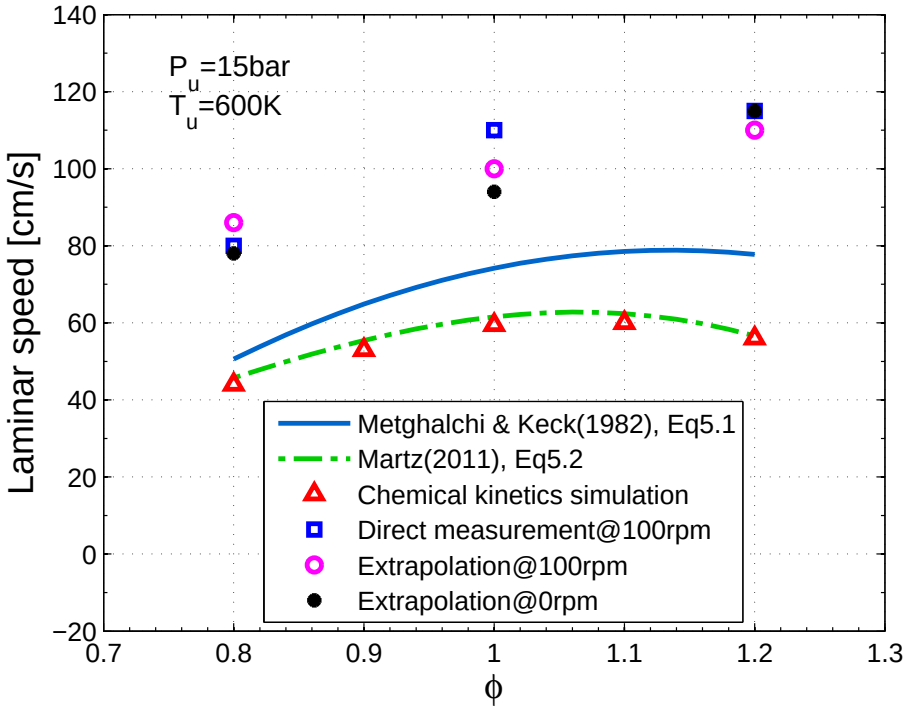

Figure 5.28: Laminar burning velocity expressions and experimental data compared at 15 bar and 600 K across a range of equivalence ratios.

This difference could reach 10 mm at high pressure of 10 bar when the cylinder size was halved in Galmiche's and Jerzembeck's experiment, see Figure 5.27. This might explain the difference between the measured value and that predicted one of Metgakhatchi and Keck's correlation equation. Their original data were from a spherical bomb with inner diameter 152.4 mm, while the bore size of the LUPOE engine is only 80 mm, height is about 8 mm.

In the combustion literature, a successful measurement of laminar flame usually is defined at these conditions (Kelley et al. [2011]): the experiment must be conducted at a nearly constant pressure and turbulence-free condition, must ensure that no cellular structure on the flame surface, and the effects of stretch need to be processed properly. Therefore, the flame radii are measured only before the onset of instability, or applying correction method to derive a stable flame speed (Al-Shahrany et al. [2005]). The measured stretched cylindrical laminar burning velocities also need to be corrected by using the Markstein length. However, it might be hard to apply these corrections in this study.

First, the small volume of the engine chamber could not be seen as a constant pressure process. At this condition, the confined small volume would have a significant effect on flame propagation. Second, the flame instability may occur immediately after ignition,

which can accelerate the flame speed. At the same time, ignition had similar influence on the flame speed. Therefore, it was hard to determine if the flame speed was accelerated by the flame instability or ignition in the initial stage, see Figure 5.15. Lastly, the cylindrical flame would have a large area contacting with the cylinder head and piston surface during flame propagation. The expansion gas in front of the flame front may push the air-fuel mixture, and the viscous boundary conditions can lead to velocity variations between flame front in the middle plane of chamber and the walls. The flame front may be bent in the contact places under these effects. This can accelerate the flame speed. How large the effects will be induced by this phenomenon has not been studied for the engine condition.

In conclusion, it has been shown that the flame speed, measured at a turbulence-free engine environment, can reach high values compared to that measured from constant volume combustion vessels. This is mainly due to flame instability and small confined volume. It is unreliable to apply the correction methods to correct the current measured "quasi-laminar" burning velocity to unstretched and stable burning velocity directly. However, since there existed a large difference of burning velocity between stable and unstable flames at engine relevant pressure and temperature conditions, it worth considering whether the influence of flame front instabilities should be included in laminar burning velocity, before putting it into a turbulent combustion model. This requires further investigation with the turbulent flame studies.

Chapter 6

Flame development in a boosted engine

Understanding the influences of high pressure on the flame dynamics and structure are crucial for designing new efficient ”Downsizing” spark ignition engines. The effects of highly boosted initial pressure on unsteady flame development, turbulent burning velocity and flame structure at the same condition of turbulence intensity have been investigated experimentally in this Chapter. The measurements were performed in the boosted optical engine LUPOE 2D with an independently controlled exhaust system valve detailed in Chapter 3. The turbulent intensity and the integral length scale were characterized by two-dimensional Particle Image Velocimetry (PIV). High speed CH* chemiluminescence imaging method was applied to record the flame front position, combined with a ”reverse” thermodynamic analysis engine model, burning rate and flame brush thickness can be obtained. The structure of the flame front at high pressure and its response to pressure effects have been further investigated using a laser sheet visualization method. The detailed cross section flame front topology was observed. Wrinkle and curvature of the flame front were characterized to compare the flame shapes under different boosted initial pressures.

6.1 Engine operation condition

The LUPOE 2D boosted engine can be boosted by two methods. The first method is to increase the inlet flow mass rate. It is widely used in most boosted engine experiments (Landry et al. [2008]; Merola et al. [2007]). Compared with the lifted valves engine, the turbulence generated by the jet-type intake of LUPOE 2D engine shall be more sensitive to the inlet flow velocity. Increasing the inlet flow velocity may result in the turbulence intensity increasing. The second method is to use the exhaust valve described in the previous Chapter 3; the LUPOE 2D engine can gain the higher initial pressure at the same flow rate setting through extending the time during which the exhaust valve closed before a firing cycle.

An initial inlet pressure map for the boosted LUPOE 2D engine has been developed and it is shown in Figure 6.1 for different combinations of inlet flow rate and exhaust valve closing time. The engine was fired at a speed of 750 rpm. At this speed, each cycle lasts 80 ms. It can be seen that the initial pressure does not change significantly when the exhaust valve closes one cycle before firing. This is because of the small flow rate and delay time of exhaust valve, about 15 ms. Due to the skip firing cycles, the the exhaust valves closing time can be advanced further before the firing cycles. Under the same condition of valve closing time, the initial pressure increases rapidly with the flow rate. However, the flow rate has to be increased up to 50% in order to increase the initial pressure 1.6 to 2.0 bar. Such a change might affect the turbulence intensity at the same time.

The maximum initial pressure shown in the map is approximately 4 bar, see Figure 6.1. Analysis of this Figure shows that when the mass flow rate is changed at a constant number of cycles before the firing one during which the exhaust valve is closed, it will change at the same time the turbulence and the initial pressure. However, by a simultaneous variation of the time of the exhaust valve closure and the flow rate, one may achieve the same inlet pressure at different turbulence strengths. This has been attempted in the present work. These assumptions are confirmed by using Particle Image Velocimetry (PIV) in the following Section.

Most experiments in this work have been done with conditions shown in the first column of the map, the initial pressures of these points are 1.6 bar, 1.8 bar and 2.0 bar, respectively, these cases are denoted as Pi16, Pi18, Pi20. In order to test the flow rate effects, other two conditions were also used, which have almost same initial pressure, but higher inlet flow rates, these are denoted as Pi18ref, Pi20ref. These five conditions are listed in Table 6.1.

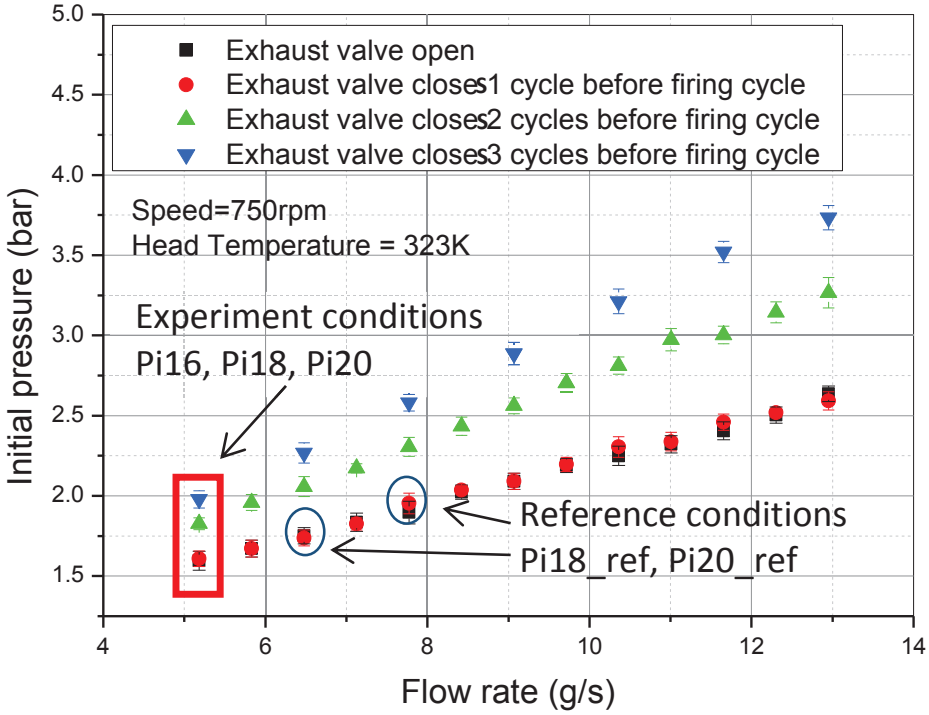

Figure 6.1: Initial inlet pressure map with different inlet flow rates and exhaust valve operation times.

Table 6.1: Selected LUPOE 2D engine operation conditions.

Item	value
Baseline	Pi16
Initial pressure (Pi)	1.6 bar
Flow rate each inlet (FR)	5.2 g/s
Exhaust valve (EV)	open
Spark timing	2^o bTDC
Equivalence ratio	1
Engine speed	750 rpm
Fuel	Iso-octane
Method 1	Increasing air charging time
Pi18	Pi=1.8 bar, EV closes 2 cycles before firing
Pi20	Pi=2.0 bar, EV closes 3 cycles before firing
Method 2	Increasing inlet flow rate
Pi18ref	Pi=1.8 bar, EV open, FR 25% increase
Pi20ref	Pi=2.0 bar, EV open, FR 50% increase

The LUPOE 2D engine was set to run at the following reference conditions: equivalence ratio was 1, engine speed was 750 rev/min, sparking timing was 2^o bTDC (before Top Dead Centre). The tested fuel was 100% iso-octance. All conditions were selected in the non-knocking region, in order to avoid the abnormal combustion affecting on the flame propagation. Pi20ref is the condition which is the closest to the knock boundary. The knock boundary map of the LUPOE 2D boosted engine is presented in Chapter 7. 100 cycles have been recorded in each experimental condition for statistical analysis. The number of cycles required to compare the variance of engine pressure cycles has been investigated by Hussin [2012]. He found there was not a significant change of statistical results when more than N/7.5 cycles were used for the LUPOE 2D engine, N is the engine speed. Intake and cylinder head temperature were all kept at 323 K. When the temperatures were set below 40^oC, an unsteady air fuel mixture strength would happen due to condensation of fuel on the wall surface of the intake pips (Dawood [2010]), while these temperatures were set above 60^oC, high initial temperature would cause occurrence of knock and increase the risk of the optical window damage. For all engine experiments, its skip-fire ratio was set at 20, sufficient for effective exhaust scavenging with no occurrence of the run-on phenomenon.

6.2 Flow characteristics in boosted LUPOE 2D engine

This Section examines whether the installed exhaust valve has the ability to boost the initial pressure and control the turbulence at the same time. Increasing the pressure by flow rate was also tested to validate the assumption that the inlet flow rate might change the turbulent flow significantly in the LUPOE 2D boosted engine.

6.2.1 Individual cycle

A snapshot of the flow velocity field captured using PIV system at the condition Pi20 is shown in Figure 6.2 in the form of vector and scalar maps. The measurement was taken at 2^o bTDC in the mid plane of the clearance volume. The flow structure changes from cycle to cycle, as mentioned in Chapter 3, the engine was designed to eliminate the strong bulk flow and make the flow uniform. It is clearly shown in this Figure that there does not exist a swirl structure, and no significant flow direction could be observed. The large and small vortices distribute all over the field homogeneously. These vortices have a spatial dimension of order of 5-10 mm. The flow velocity decreases near the wall. The accuracy

of velocity values near the image edges may be degraded by the laser light reflections from the curved side windows and cylinder wall.

The velocity probability density functions (pdf), over the entire flow field of Figure 6.2, is shown in Figure 6.3. This Figure also shows the inlet and exhaust port positions and their coordinates. This coordinate definition was used in the following sections for the PIV measurements. The mean velocity along the Y direction is close to zero, while the velocity along the X direction is slightly skewed towards positive values. The probability of large velocity fluctuations is low, as is the frequency of their occurrence, e.g. the probability of the instantaneous velocity attaining the value of 5 m/s is 1%.

The energy density spectrum of this individual turbulence flow field also was calculated and shown in Figure 6.4. The wave number distributes in the region of $10^{-2} - 10$ mm^{-1}. The -5/3 power law can be seen in the large length scale region of energy densities spectrum, which agrees with the energy density spectrum of flow fields measured from in the constant combustion vessel (Scott [1992]) and burner (Kobayashi et al. [2002]). The position of the engine bore size, the estimated integral length scale l_i of 10 mm and Taylor length scale l_t of 0.2 mm are also marked in this Figure. The measured eddies size are between the integral length scale and Taylor length scale, the eddies smaller than the Taylor length scale could not be resolved by the current PIV system.

6.2.2 Compression stroke process

In-cylinder flow was measured during the compression stroke before the spark at the engine speed of 750 rpm. The measurements were taken in the mid plane of the clearance volume. Ensemble averaging was adopted to calculate the mean and RMS (Root Mean Square) flow velocity at each grid point in the measurement plane from about 100 cycles. Such spatial ensemble evaluation was considered to be a suitable way to investigate the turbulence structure in the engine cycle experiments (Larsson [2009]). The detailed calculation process has been presented in Section 4.1.3.

Calculated fields of mean and RMS (Root Mean Square) velocities during the compression stroke are shown in Figure 6.5 for the initial pressure of 1.6 bar case. From the top to bottom of this Figure, illustrated are times 40^o bTDC, 20^o bTDC, 10^o bTDC and 2^o bTDC, suitable for spark timing. Turbulence in this time period range has a strong effect on subsequent combustion. In general, as the piston approached the TDC position, the mean and RMS turbulent velocity decreased. A strong turbulence intensity of 2 m/s was

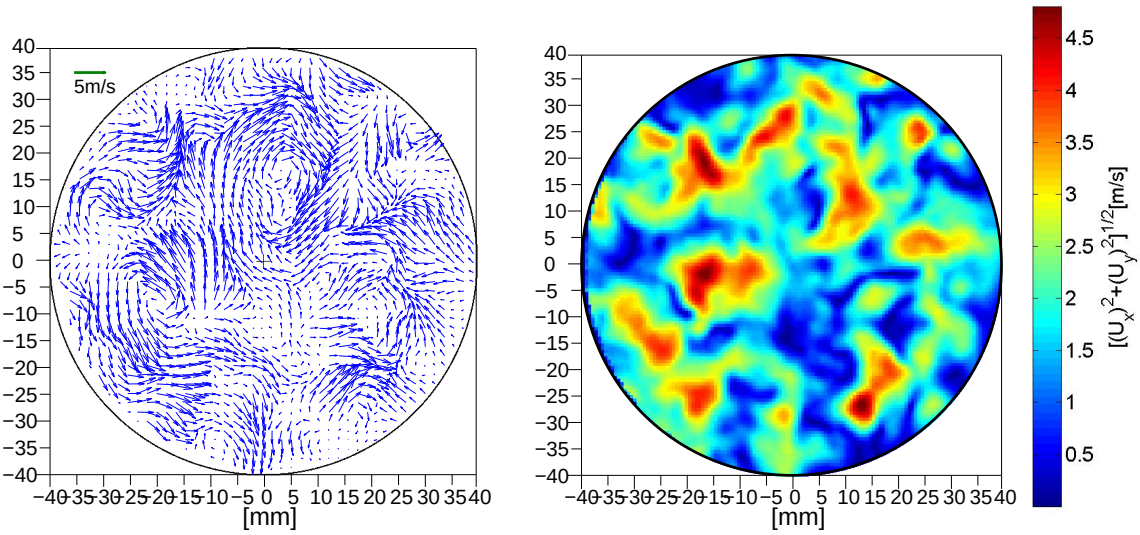

Figure 6.2: A snapshot of flow velocity field captured by PIV for the condition Pi20, illustrated in the form of vector (left) and scalar (right) maps.

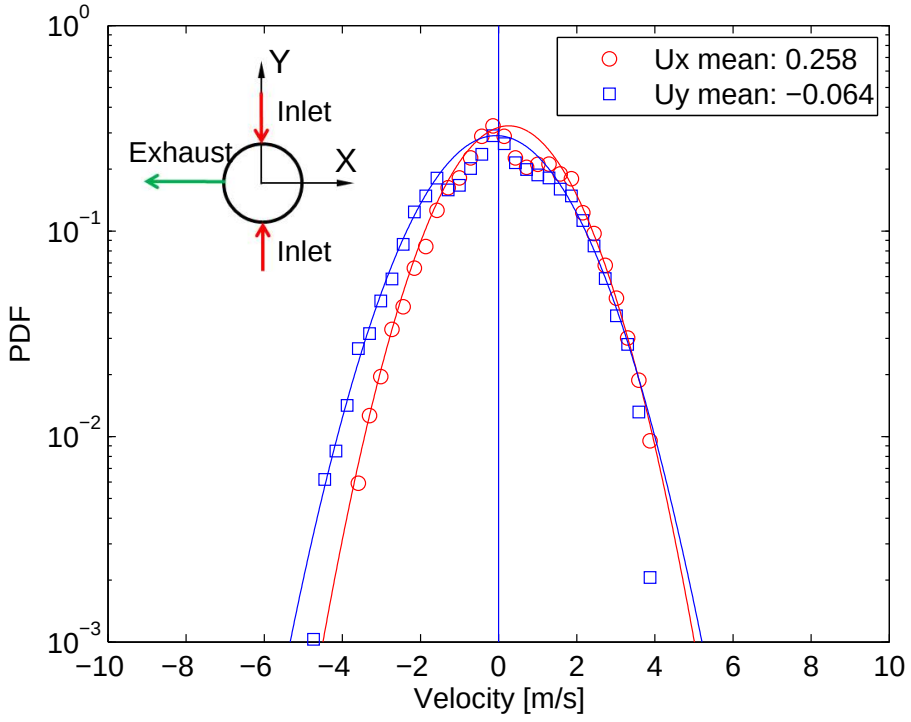

Figure 6.3: The velocity probability density functions (pdf) of the flow velocity field shown in Figure 6.2. The inlet and exhaust pipe positions and their coordinates are plotted in the corner.

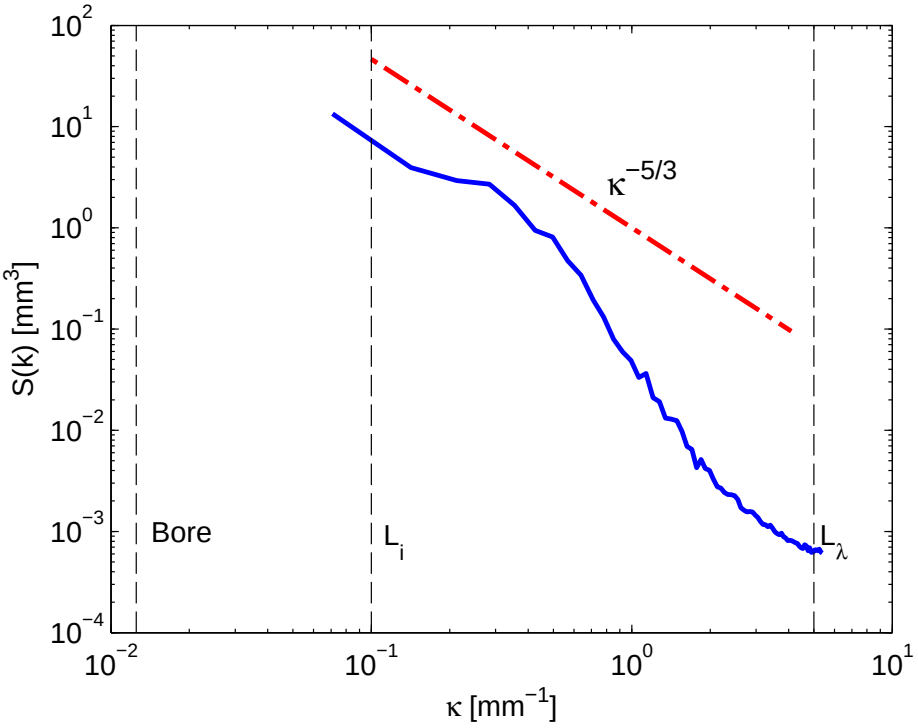

Figure 6.4: The energy density spectrum of turbulent flow shown in Figure 6.2 with the position of engine bore size, integral length scale L_i, and Taylor length scale L_λ.

evident at the beginning of the compression stroke and reduced to approximate 1 m/s near the TDC position.

No significant swirl motion can be observed. Comparing to the individual flow field, one significant difference is that the patchy structures can be seen in the images, this might be caused by the ensemble data processing. From the mean flow field, the velocities near the exhaust pipe side have higher mean velocities than those on the other side. In the RMS flow field, there is clearly strong turbulence near the inlet (on the lower part of the picture), also, much smaller values at the exhaust. From a previous study (Cairns [2001]), the tumble motion may exist during engine charge in the LUPOE engine and it is dissipated during the compression stroke. Moreover, each inlet air flow rate has been separately and accurately controlled by mass flow meters, but the new seeding flow was controlled only by one flow meter and then separated into two channels to each inlet. This configuration may potentially lead to uneven flow rates between the intakes.

It also needs to be noted that the spark plug and reflections from it, may cover the centre and partially right side area, leading to some erroneous and missing velocity vectors near these areas. Nevertheless, there is no significant directional flow motion observed near the TDC, when the piston is very close to the cylinder head, and the tumble

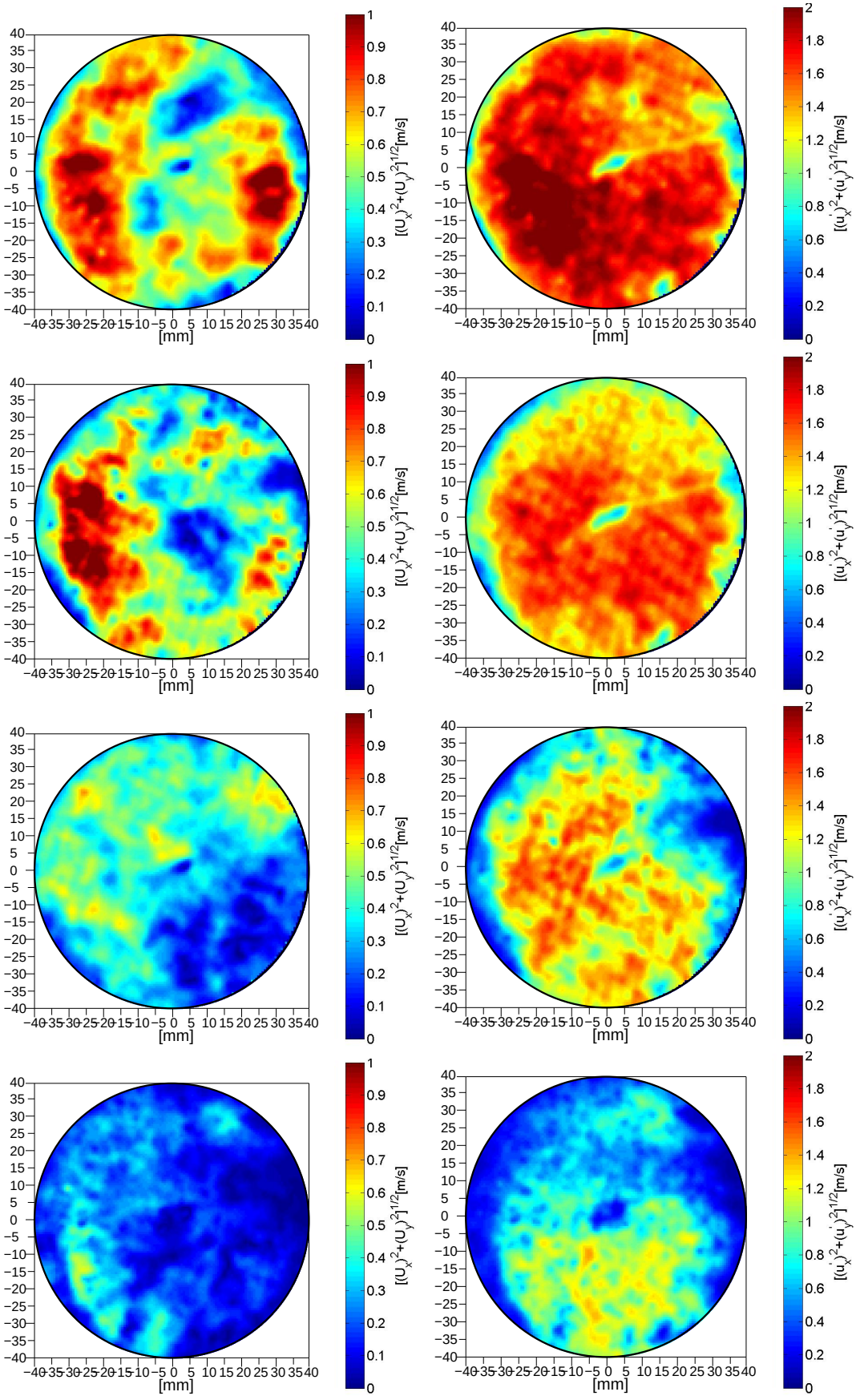

Figure 6.5: Flow fields of mean (left) and RMS (right) velocity during compression stroke at 40^o bTDC, 20^o bTDC, 10^o bTDC, 2^o bTDC (from top to bottom), in the LUPOE 2D boosted engine running at a speed of 750 rpm, the inlet initial pressure was 1.6 bar.

effects can be neglected. The spatial variation of the RMS velocity also was lower than 1.0 m/s, therefore, the turbulence in the LUPOE 2D boosted engine might be assumed as locally homogeneous and isotropic, especially in the proximity of the spark plug.

6.2.3 Effects of inlet flow rate and pressure

In order to compare the effects of the inlet flow rate on flow velocities, approximately 100 cycles of flow field measurement were collected at 2^o bTDC under 5 conditions listed in Table 6.1, where the initial pressure for the test cases Pi20, Pi20ref are 2.0 bar; Pi18, Pi18ref are 1.8 bar, Pi16 is 1.6 bar. Air mass flow rate for the three test cases Pi16, Pi18, Pi20 equals 5.2 g/s, for the case Pi18ref, it is 6.48 g/s, and Pi20ref equals 7.77 g/s. The clearance height is about 8 mm at the instant when the PIV image is taken.

Flow fields of the ensemble mean and RMS velocities for 5 conditions near the TDC position are shown in Figure 6.6 and Figure 6.7. The baseline condition is Pi16, at the same flow rate, the initial pressure can be increased to 1.8 bar (Pi18) and 2.0 bar (Pi20) by closing the exhaust valves 2 cycles and 3 cycles before a firing cycle. Effectively, this procedure pressurizes the volume between the liner and barrel, together with the exhaust pipe between the exhaust valves and the barrel.

Meanwhile, an increase of the flow rate by 25% and 50% in each inlet can boost the inlet pressure to 1.8 bar (Pi18ref) and 2.0 (Pi20ref) bar, respectively. The seeding flow rate also needs to be carefully adjusted in order to keep the total air mass flow rate constant. It can be seen from Figure 6.7 that all five conditions show similar flow structures. Distribution of the RMS values gradually decreases from the centre spark position towards the cylinder wall, especially for the right and left sides. The magnitude and distribution of turbulence intensity were very similar when using the exhaust valve. The flow structure tends to be more homogeneous under higher inlet flows.

Figure 6.8 and Figure 6.9 show the averaged mean and RMS flow velocities along X and Y axes from the flow fields in Figure 6.6 and Figure 6.7. The first standard deviation of these flow fields were also calculated and indicated as error bars. The definition of the X axis and Y axis is the same as the one used in Figure 6.3. It can be seen that velocity components along the X axis have near zero mean velocity, which indicate a balance of flow between the opposite inlets. Velocity components along the Y axis seem to be higher on the side opposite to the exhaust port; they increase with the inlet flow rate. The standard deviation of the mean flow value also increased with the increasing inlet flow. The mean flow velocity at baseline Pi16 was the lowest.

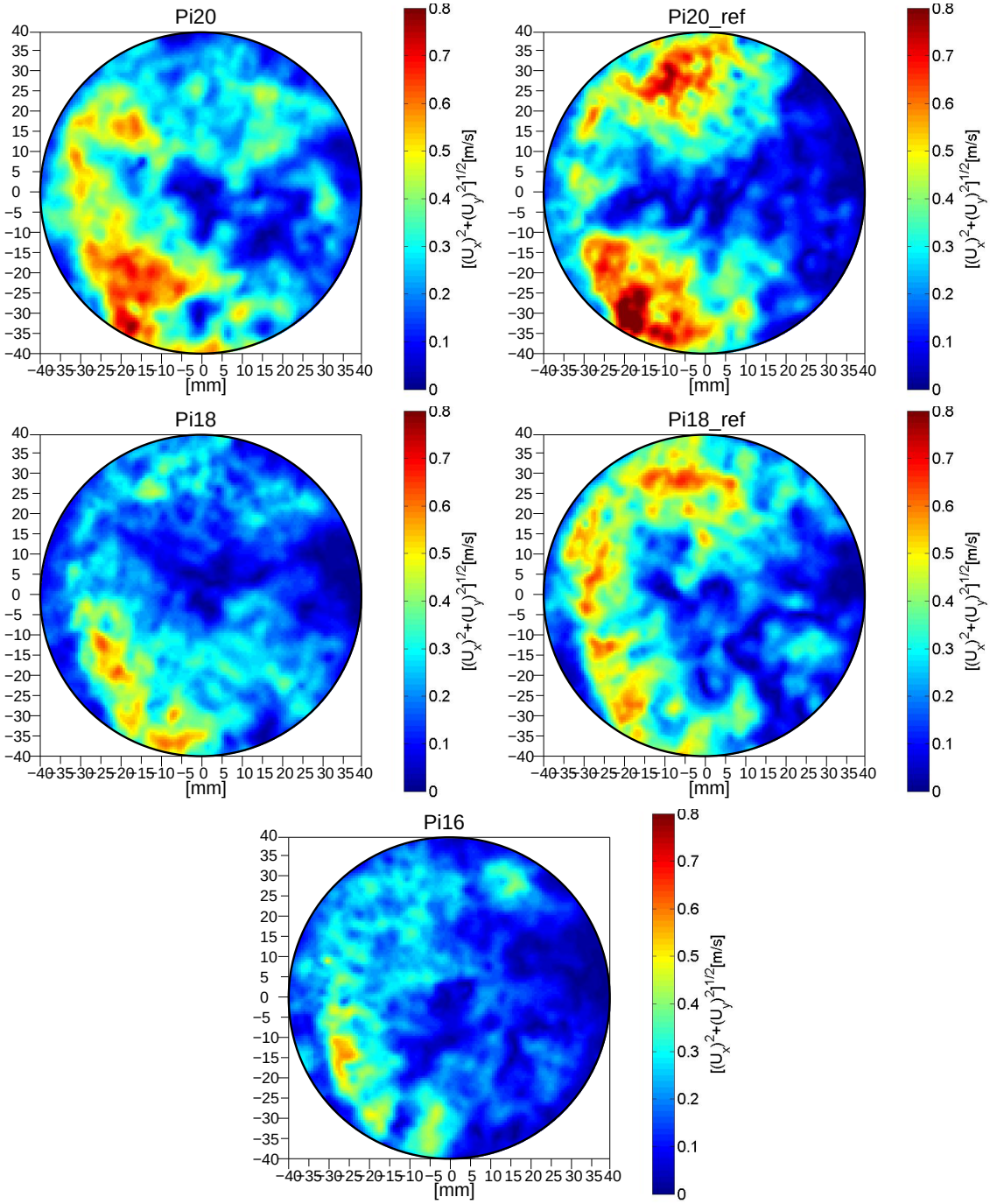

Figure 6.6: Flow fields of mean velocity at 2^o bTDC in the LUPOE 2D boosted engine running at a speed of 750 rpm, the initial pressure for the test cases Pi20, Pi20ref are 2.0 bar; Pi18, Pi18ref are 1.8 bar, Pi16 is 1.6 bar. Air mass flow rate for the three cases Pi16, Pi18, Pi20 equals 5.2 g/s, for the case Pi18ref, it is 6.48 g/s, and Pi20ref equals 7.77 g/s.

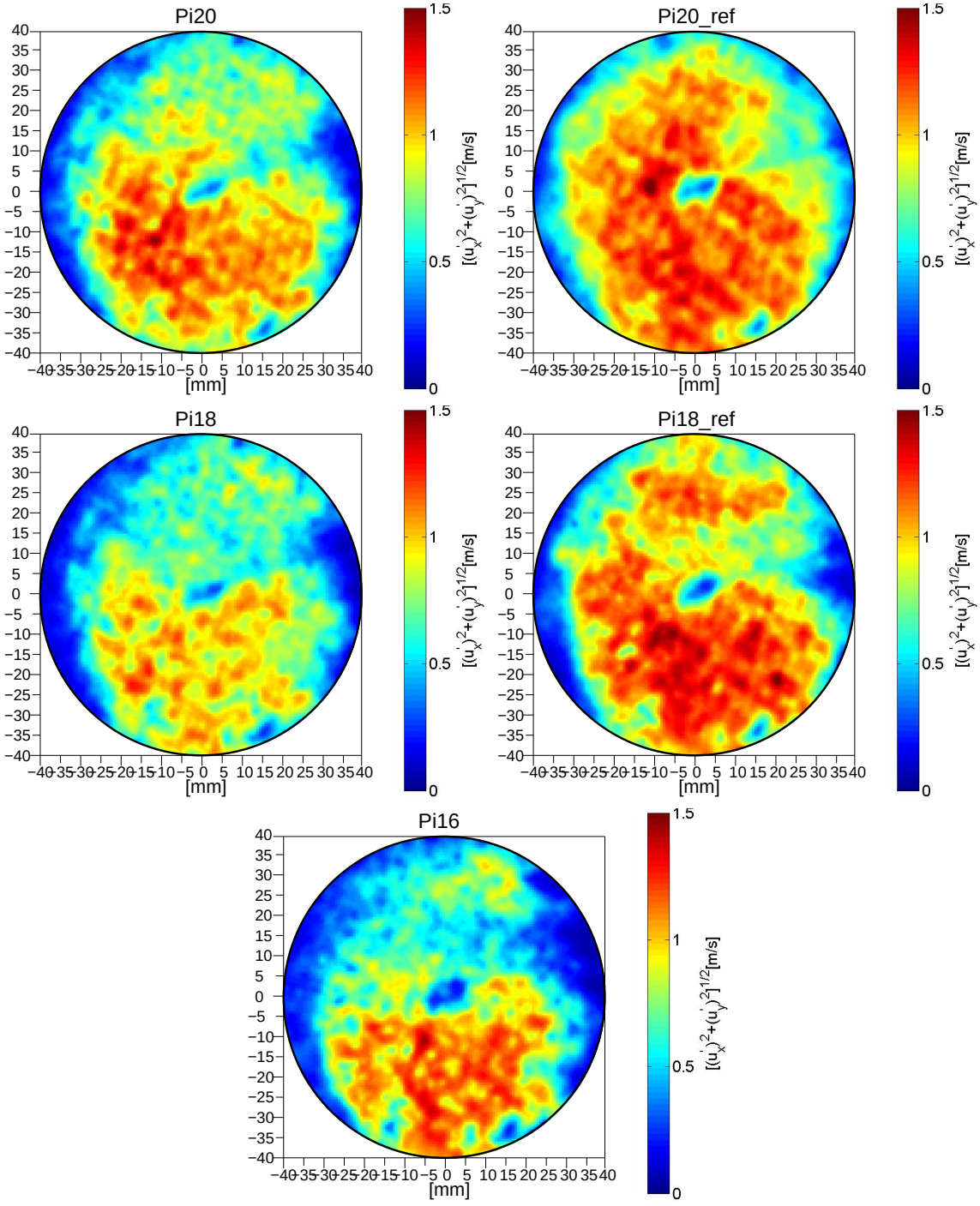

Figure 6.7: Flow fields of RMS velocity at 2^o bTDC in the LUPOE 2D boosted engine running at a speed of 750 rpm, the initial pressure for the test cases Pi20, Pi20ref are 2.0 bar; Pi18, Pi18ref are 1.8 bar, Pi16 is 1.6 bar. Air mass flow rate for the three cases Pi16, Pi18, Pi20 equals 5.2 g/s, for the case Pi18ref, it is 6.48 g/s, and Pi20ref equals 7.77 g/s.

A similar tendency also was observed in the RMS velocities in Figure 6.9. Increasing the inlet flow rate can cause a stronger turbulence intensity. The averaged RMS velocity at Pi16 was 0.65 m/s, then it changed to 0.9 m/s at the Pi20ref case after the intake flow rate was increased by 50%. While the exhaust valve can keep the RMS velocity at the almost same level. For the highest and lowest levels of tested mass flow rate, both the X axis and Y axis have the similar mean and standard deviation values. These observations were in agreement with the flow field map results.

The turbulence intensity changes during the compression process at different engine inlet air mass flow rates with different exhaust valve closing timing, as shown in Figure 6.10. It can be observed that the effect of inlet mass flow rate on the RMS in-cylinder flow velocity is very significant in the early stage of the compression stroke, but reduces towards TDC. Increasing each inlet flow rate 25-50% can raise the turbulence intensity by 20-40% near the TDC position, while the exhaust valve can keep the difference of RMS velocity in a minimum range when the initial pressure was increased. These observations confirmed that the new boosting configuration using the exhaust valve enabled the intake mass flow rate and the initial pressure to be independently varied. The turbulence quantities, which were heavily influenced by the inlet flow velocities in the ported engine, can be controlled to the greatest extent.

Dawood [2010] performed PIV measurement in the aspirated naturally LUPOE engine with a liner having four rows of exhaust orifice at 750 rpm. The measured mean velocity magnitude was about 0.2 m/s and the RMS velocity was 1.5 m/s at TDC. In this study, the exhaust gas leaving the cylinder chamber might be blocked to a certain extent due to the small orifice section of the installed exhaust valves. This resulted in a lower flow velocity compared to the value measured in the naturally aspirated LUPOE engine. Landry et al. [2008] investigated the turbulence in a four stroke boosted optical engine, and the turbulence intensity was measured as 1.15 m/s at 10^o bTDC at the engine speed of 1200 rpm. Since the turbulence intensity decreases with engine speed decreasing, mean velocity magnitude was 0.1 m/s and RMS velocity was 0.65 m/s at the LUPOE 2D engine baseline condition Pi16, which can provide a good approximation to conditions in real commercial lifted valves engines at a low engine speed.

The longitudinal integral length scales along the X axis L_{xl}, along the Y axis L_{yl}, and transverse length scales along the X axis L_{xt}, along the Y axis L_{yt} were calculated following the procedure described in Section 4.1.3 using the mean PIV vector fields and have shown in Figure 6.11. It can be observed that, in general, average values of the longitudinal integral length scales are between 8-10 mm, which was approximately twice that of the transverse integral length scales 4 mm. This is a further indication that the

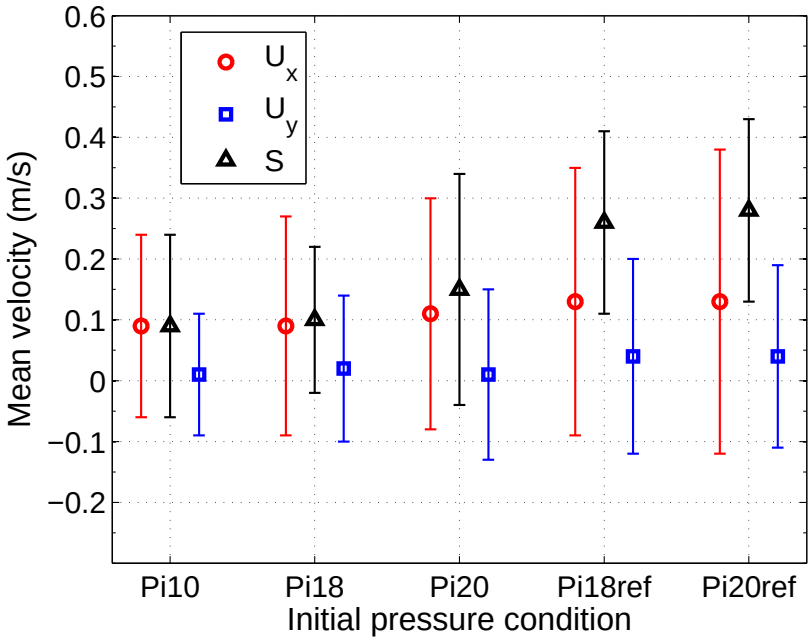

Figure 6.8: Mean and standard deviation (represented as error bar) of mean velocity fields shown in Figure 6.6. U_x: mean velocity in X direction, U_y: mean velocity in Y direction, S: velocity magnitude. U_x and U_y are at the same speed, shifted for illustration only.

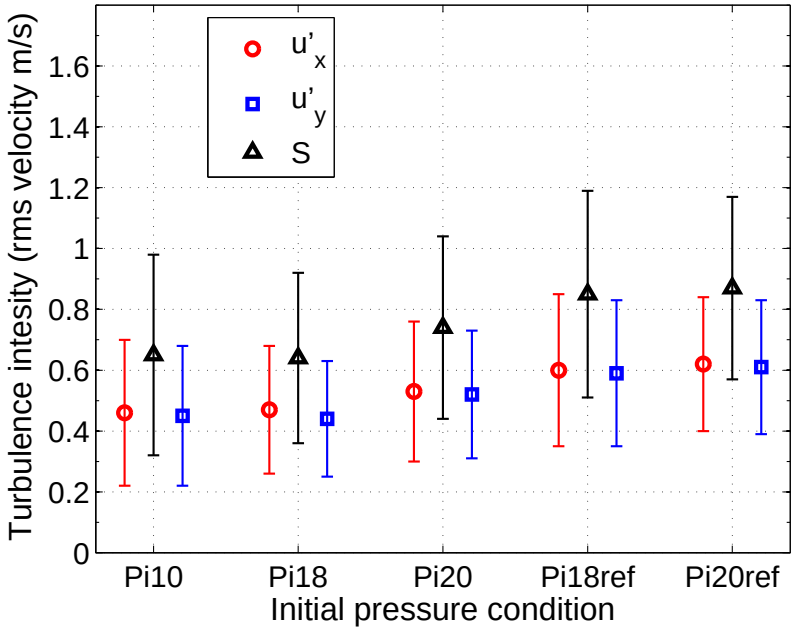

Figure 6.9: Mean and standard deviation (represented as error bar) of RMS velocity fields shown in Figure 6.7. u′$_x$: RMS velocity in X direction, u′$_y$: RMS velocity in Y direction, S: RMS velocity magnitude. u′$_x$ and u′$_y$ are at the same speed, shifted for illustration only.

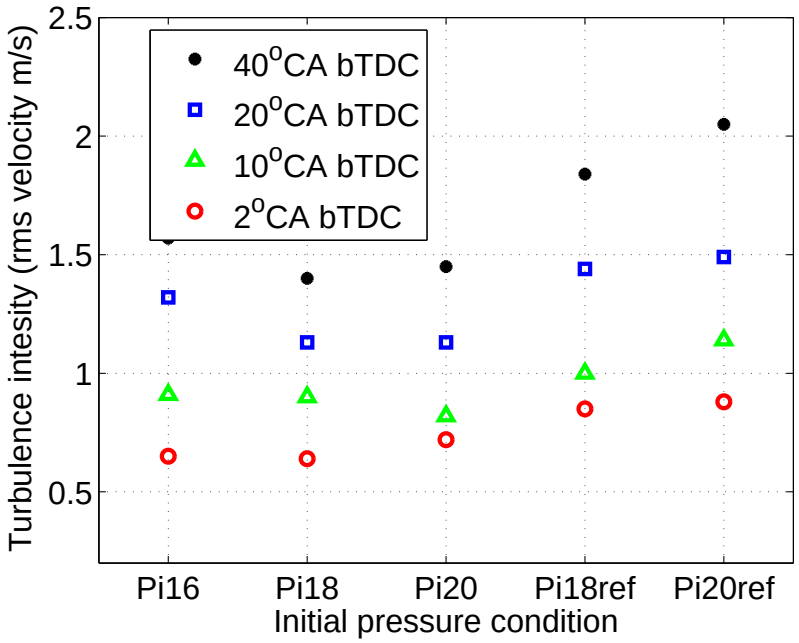

Figure 6.10: Influence of intake air mass flow rate on the averaged RMS (root mean square) velocity during the compression stroke measured at 2^o bTDC, in the LUPOE 2D boosted engine running at a speed of 750 rpm, the initial pressure for the test cases Pi20, Pi20ref are 2.0 bar; Pi18, Pi18ref are 1.8 bar, Pi16 is 1.6 bar. Air mass flow rate for the three test cases Pi16, Pi18, Pi20 equals 5.2 g/s, for the case Pi18ref, it is 6.48 g/s and Pi20ref equals 7.77 g/s.

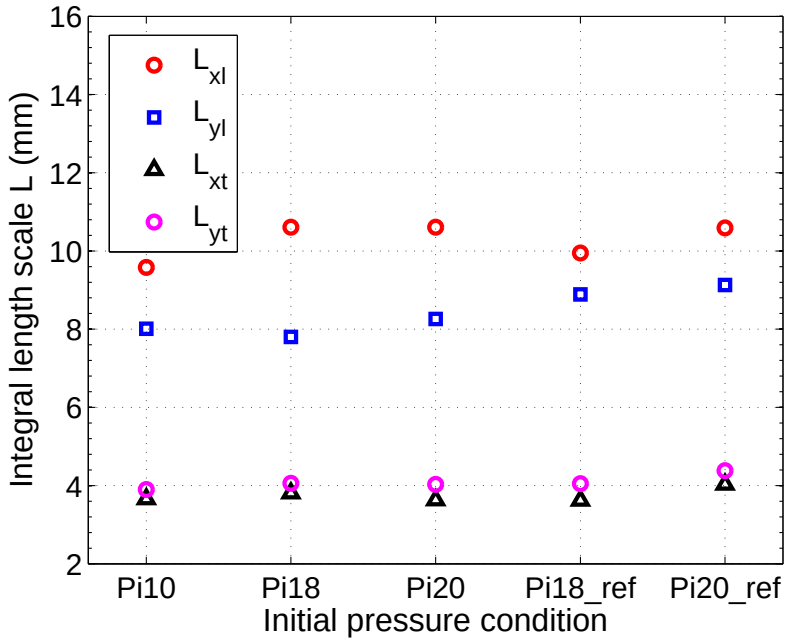

Figure 6.11: Longitudinal and transverse integral length scales based on spatial analysis at 2^o bTDC, in the LUPOE 2D boosted engine running at a speed of 750 rpm, the initial pressure for the test cases Pi20, Pi20ref are 2.0 bar; Pi18, Pi18ref are 1.8 bar, Pi16 is 1.6 bar. Air mass flow rate for the three test cases Pi16, Pi18, Pi20 equals 5.2 g/s, for the case Pi18ref, it is 6.48 g/s and Pi20ref equals 7.77 g/s.

in-cylinder turbulence at 2^o bTDC could be considered locally isotropic. There is a small difference in the mean values of the longitudinal scales for X and Y velocity components. Hussin [2012] measured the transverse length scale to be about 3.5 and 7 mm at TDC with turbulence intensity at about 1.5 m/s at a speed of 750 rpm in the natural aspirated LUPOE engine, thus the length scales decreased slightly with the decreasing of the turbulence intensity.

6.3 Engine combustion experimental results

Following the investigation of the engine flow, combustion experiments were conducted and the results are presented in this Section.

6.3.1 Observations of turbulent flame propagation

Before studying the pressure effects on flame propagation, several images of flame development with different equivalence ratios and engine speeds were obtained, and they are shown in Figure 6.12, to provide a general observation of the turbulent flame characteristics. These images were captured from the LUPOE 2D boosted engine using a CH* chemiluminescence imaging method, and the main experimental operation parameters were listed on the left-up insert. The head and intake temperature were kept at 323K, and the spark timing was fixed at 2^o bTDC for all cycles. The second cycle was the Pi16, which has the initial pressure of 1.6 bar. On the left of Pi16 was the case which had the similar operation conditions as Pi16, except that the equivalence ratio was reduced to 0.8. The third column was cycle Pi20ref, which had a higher initial pressure of 2.0 bar and turbulence than Pi16. The last cycle had almost the same operational conditions as cycle 3, except that the engine speed was increased to 1500 rpm.

From these images, it was clearly shown that the flame speed of lean cycle 1 had the slowest flame propagation speed compared to the stoichiomtric one (cycle 2), when the other operational parameters were kept the same. There was not significant difference between cycle 2 and cycle 3 from image observation for the flame speed. Under the same initial pressure of 2.0 bar, the flame speed at the high engine speed achieved a faster burning velocity and more wrinkled flame front, see last column in Figure 6.12.

These flame images were analyzed using the method described in Section 4.2.1, the flame thickness values were estimated from the gradient of image intensity along the flame radius at several angles. The positions of the sliced section of the flame are

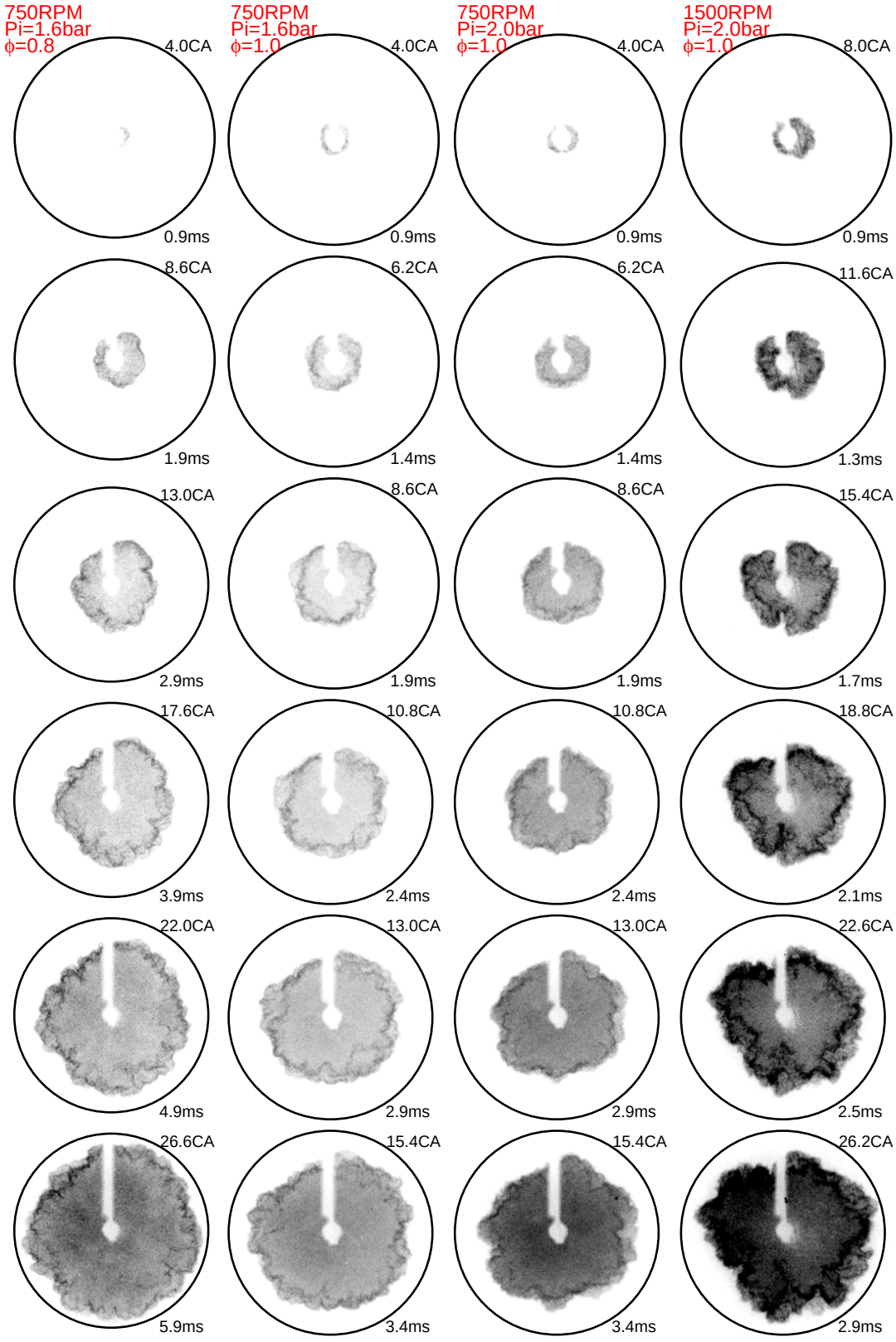

Figure 6.12: Development of turbulent flame at different conditions from CH* chemiluminescence imaging (colour-reverse), in the LUPOE 2D boosted engine, the intake and head temperature were kept at 323 K, the other main operation parameters are listed in the Figure.

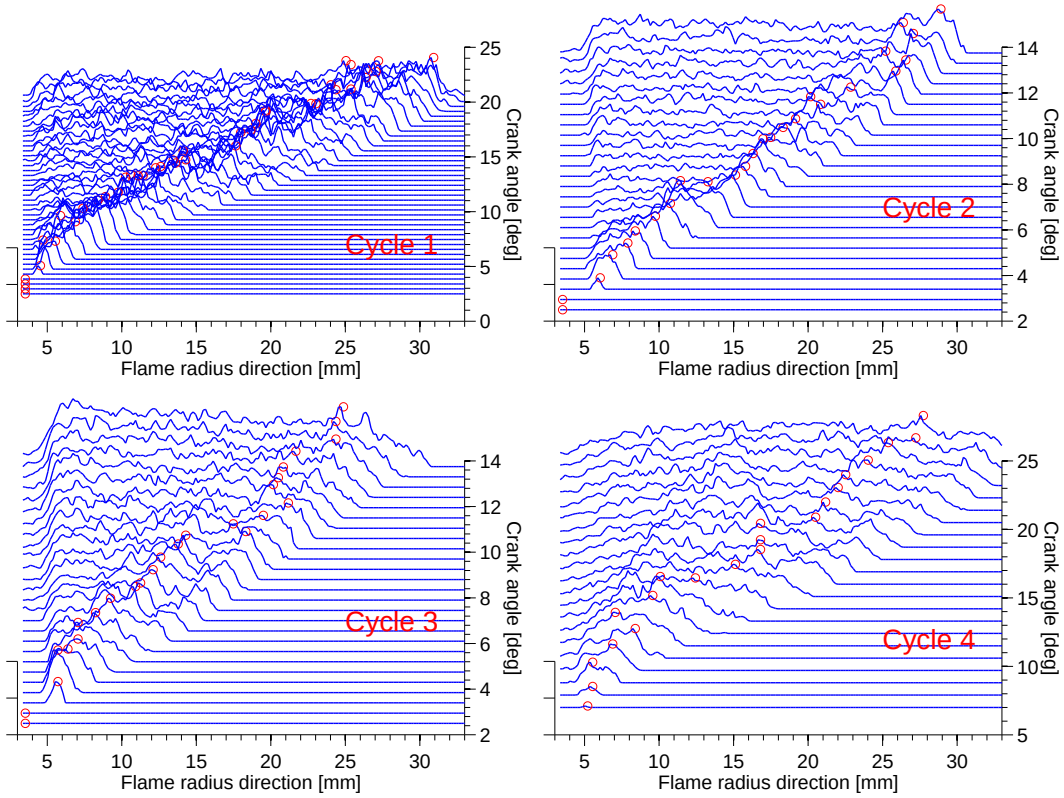

Figure 6.13: Local flame propagation with image intensities as magnitude derived from Figure 6.12 at the first direction in Figure 6.14.

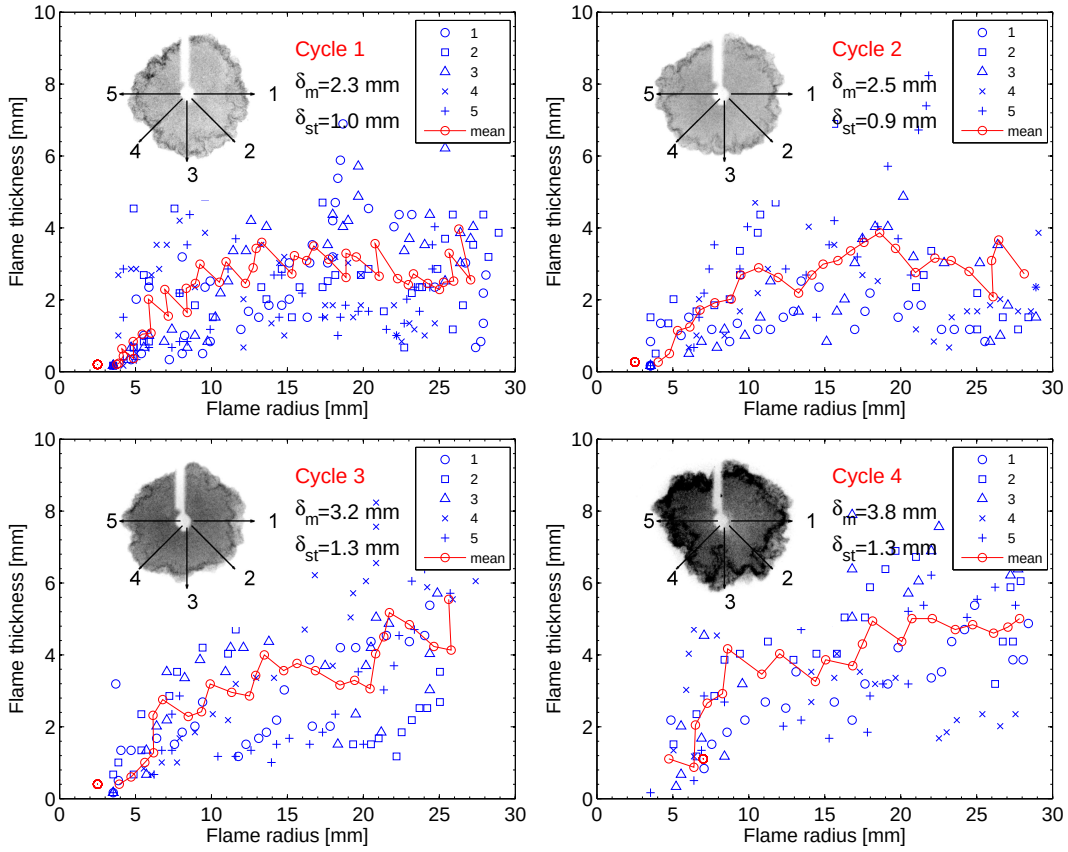

Figure 6.14: Local flame brush thickness development at 5 directions along flame radius with image intensity as magnitude, these data are derived from 6.13.

illustrated in Figure 6.13, and the third direction of each flame with crank angle was shown in Figure 6.14. It can be clearly seen that the sharp intensity gradient existed in the flame front position, and the peak position near the flame front was denoted by red circles.

The derived flame brush thicknesses along five directions at each flame radius position were plotted in Figure 6.13. There was a considerable scatter in each direction for all cycles, because the turbulence effect was non-uniform in the each flame propagation direction. Moreover, the bright spots associated with the optical window also would bring errors into the data analysis process. In order to further characterize the difference between four cycles, the mean flame brush thickness was averaged, this value with standard deviation were shown in the 6.14, it can be seen that these values were much larger than that observed at the engine speed of 100 rpm (δ_m= 1.1 mm, δ_m= 0.4 mm), see Figure 5.12. The lean flame (cycle 1) had the smallest value of flame brush thickness, and this value was not changed much when the equivalence ratio was increased to 1. Increasing engine speed can raise the turbulence intensity in the engine, resulting in a strongly wrinkled flame surface, this phenomena can be observed from cyele 4. There existed a large difference of flame brush thickness between cycle 2 (Pi16) and cycle 3 (Pi20ref), although they had similar flame speeds.

6.3.2 Pressure traces and mean flame radius

More experimental data have been collected under the experimental conditions discussed in Section 6.1. The conditions were kept unchanged except inlet flow rate and exhaust valve closing time, leading to the different initial pressures. For each tested condition, more than 150 pressure traces of firing cycles were recorded in approximately 12 engine runs, each run comprised of only 15 firing cycles to avoid any increase of engine inlet and wall temperatures. 20 skip firing cycles between each firing cycle were employed to scavenge the exhaust gas. Finally, only 100 firing cycles were accepted for further analysis with achieved images data. These data were collected at spark timing 2^o bTDC and engine speed 750 rpm, 100% iso-octane was used as fuel. Displayed in Figure 6.15 are plots of 100 cycles for individual supercharging conditions, with separation of fast, medium and slow cycles. The procedure of pressure data was presented in Section 3.5. These firing cycles were averaged based on crank angle and shown in Figure 6.16.

With the initial pressure increasing, the maximum pressure of the fast cycles was changed from 60-70 bar at initial pressure 1.6 bar to 80-90 bar at initial pressure 2.0 bar. Cycle variance also was increased with initial pressure. Paired comparisons of case Pi18

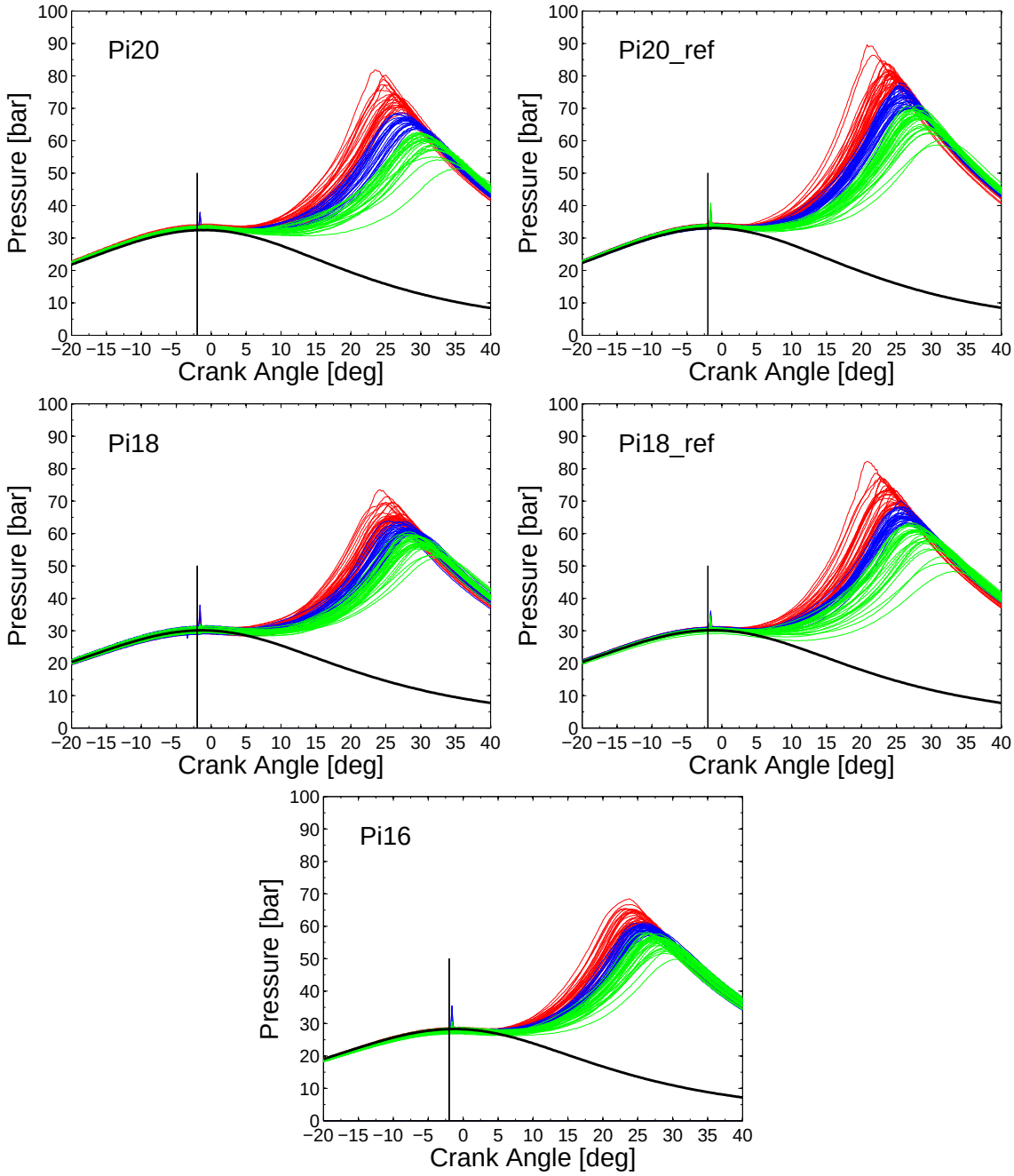

Figure 6.15: Pressure-crank angle diagrams of Pi16, Pi18, Pi20, Pi18ref and Pi20ref, collected in the LUPOE 2D boosted engine running at a speed of 750 rpm and a spark timing 2^o bTDC, stoichiometric iso-octane fuel. The cycles were split into three categories depending on their average rate of combustion; the fast cycles were shown in red, medium in blue and slow in green colors, respectively.

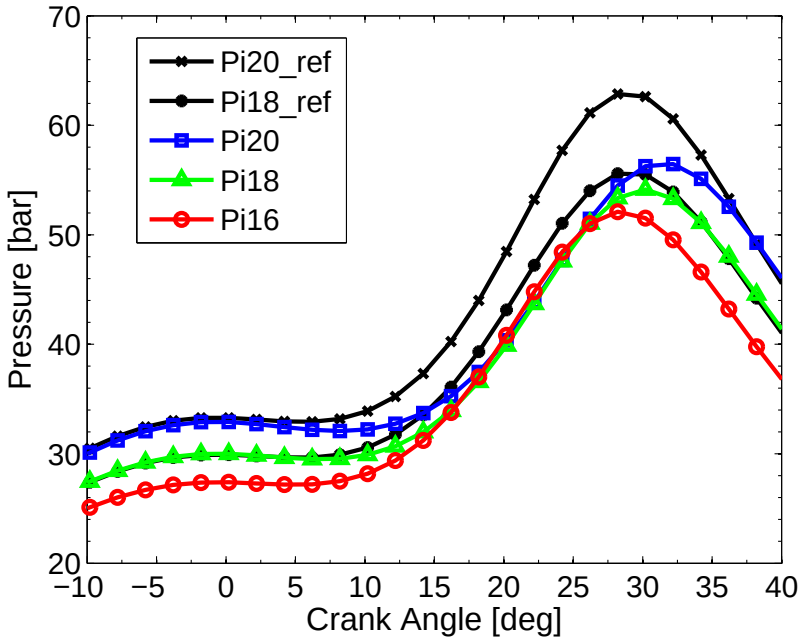

Figure 6.16: Crank-angle based ensemble average pressure for Pi16, Pi18, Pi20, Pi18ref and Pi20ref, in the LUPOE 2D boosted engine running at a speed of 750 rpm and a spark timing 2^obTDC, stoichiometric iso-octane fuel.

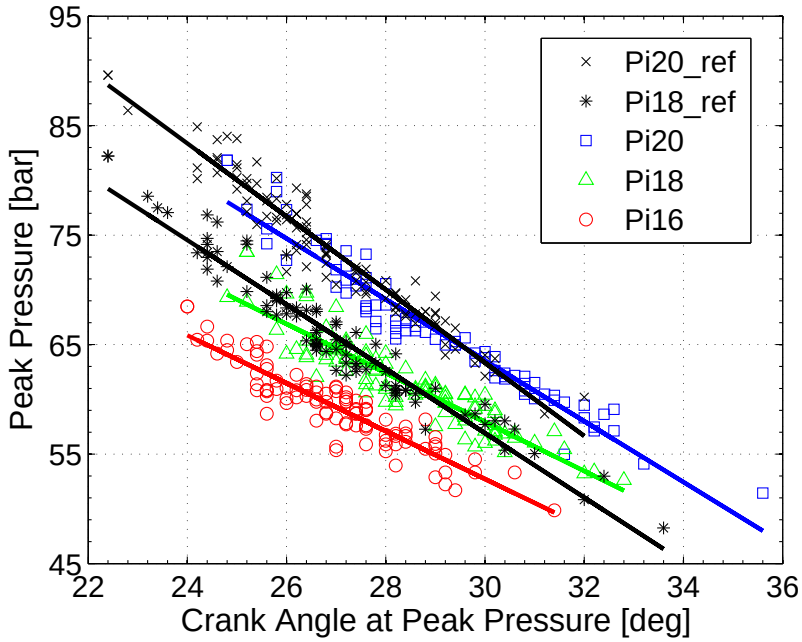

Figure 6.17: Peak pressure versus corresponding crank angle for its occurrence at experimental conditions: Pi16, Pi18, Pi20, Pi18ref and Pi20ref, in the LUPOE 2D boosted engine running at a speed of 750 rpm and a spark timing 2^o bTDC, stoichiometric iso-octane fuel.

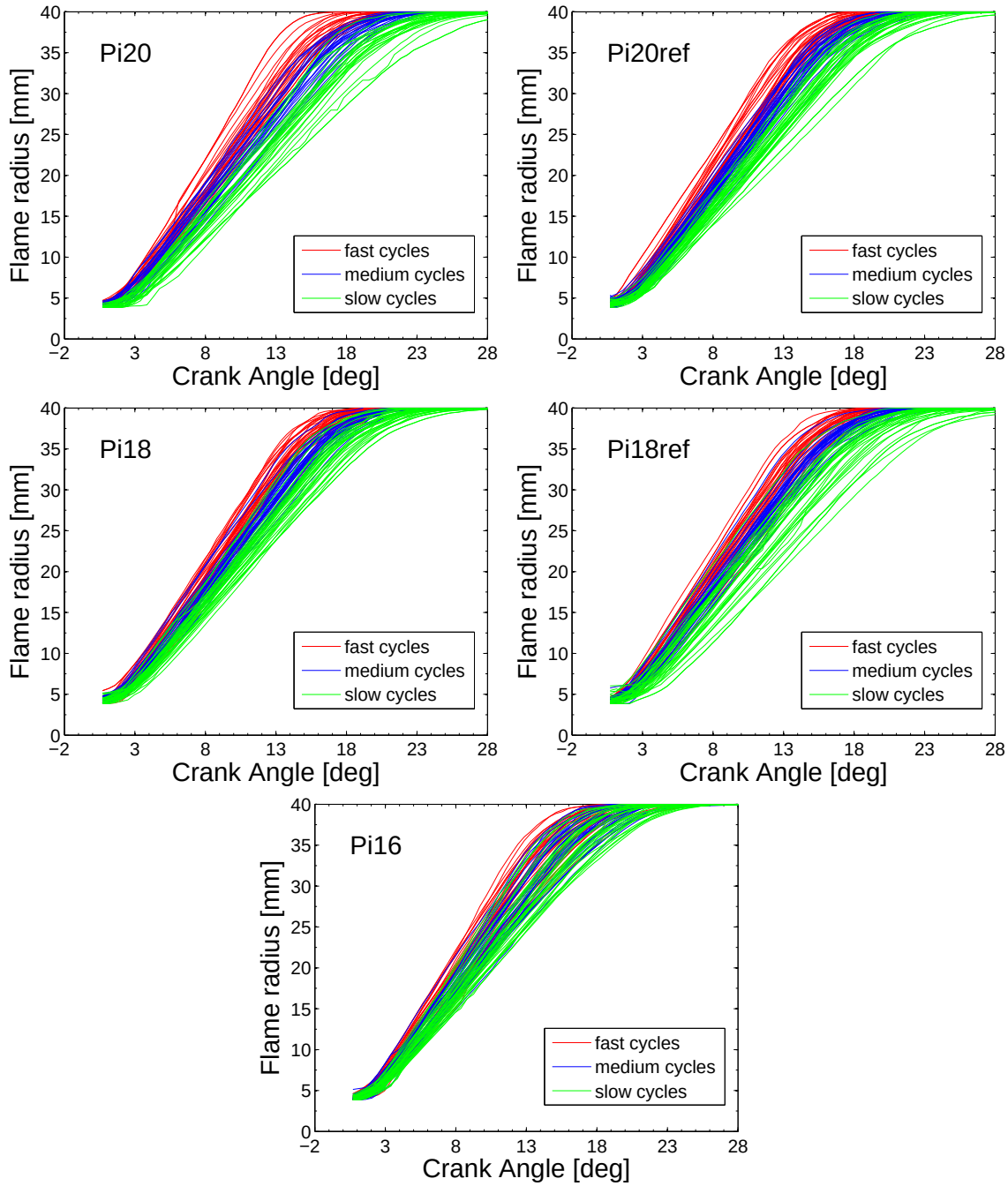

Figure 6.18: Mean flame radius versus crank angle for experimental conditions: Pi16, Pi18, Pi20, Pi18ref and Pi20ref, in the LUPOE 2D boosted engine running at a speed of 750 rpm and a spark timing 2^o bTDC, stoichiometric iso-octane fuel. The cycles are split into three categories depending on their pressure trace; the fast cycles are shown in red, medium in blue and slow in green colors, respectively.

and Pi8ref, Pi20 and Pi20ref show that the 20% increase of RMS turbulent velocity has a fairly strong effect on the burning velocity and the rate of combustion in the "ref" cases is noticeably faster. In case Pi16, Pi18 and Pi20 variations of turbulence are small. Figure 6.16 shows that higher pressure leads to slightly slower combustion. In these three cases the peak pressure is achieved between 24^o to 30^o aTDC.

Figure 6.17 shows an approximately linear relationship between the peak pressure and corresponding crank angle for its occurrence. The general trend is that the higher peak pressure is achieved at the earlier corresponding crank angle. Increased initial pressure shifts the linear relationship to the higher peak pressures at the same crank angle, but the slope remains almost same, whilst turbulence could increase the slope of fitting line, when Pi18 and Pi18ref or Pi20 and Pi20ref were compared.

Illustrated in Figure 6.18 are mean entrainment flame radii derived from the CH* chemiluminescence images for the all tested conditions. The cycles are split into three categories depending on their pressure trace. The entrainment flame radius is defined as the radius of a circle having the same area as the observed irregular flame boundary, see Section 4.2.1. There are some overlaps between adjacent categories at early and mid-stages of propagation. These entrainment flame radius will be used to calculate the entrainment burning velocity in the Section 6.5.

6.4 Combustion regime

In order to register the experimental conditions, described in the Section 6.1, on the Borghi regime diagram, both the parameters of turbulent flow and laminar flame properties are required for the calculation. The turbulent parameters include integral length scale and turbulent intensity, which have been measured and derived using the PIV system illustrated in Section 6.2. In order to obtain the laminar flame burning velocity and thickness values, the initial temperature needs to be estimated. This was achieved using the experimental pressure data as input for the LUSEIDA code. The histories of mean unburnt gas temperature for the three conditions Pi16, Pi18 and Pi20, after the spark ignition are shown in Figure 6.19. The temperatures did not change significantly with the inlet initial pressure increasing, and they have remained approximately 620-630K during the flame propagation at the initial stage.

According to the calculated temperature of 620-630K and the measured initial pressure of 28-34 bar, it was found that no experimental laminar burning velocity data were available at such high temperature and pressure. An attempt to measure "quasi" laminar

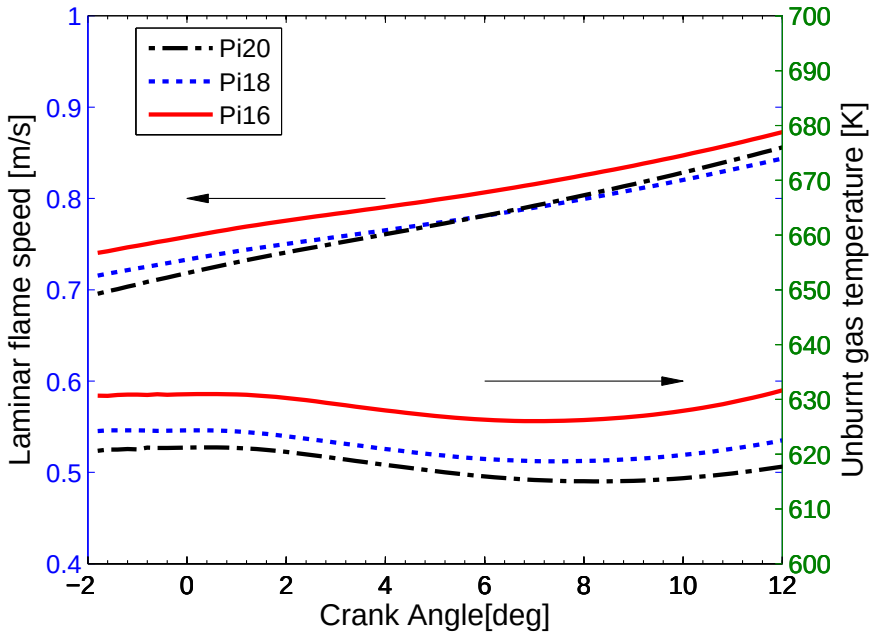

Figure 6.19: Calculated laminar flame speed and temperature after ignition at three initial pressure conditions: Pi16, Pi18 and Pi20, in the LUPOE 2D boosted engine running at a speed of 750 rpm and a spark timing 2^o bTDC, stoichiometric iso-octane fuel.

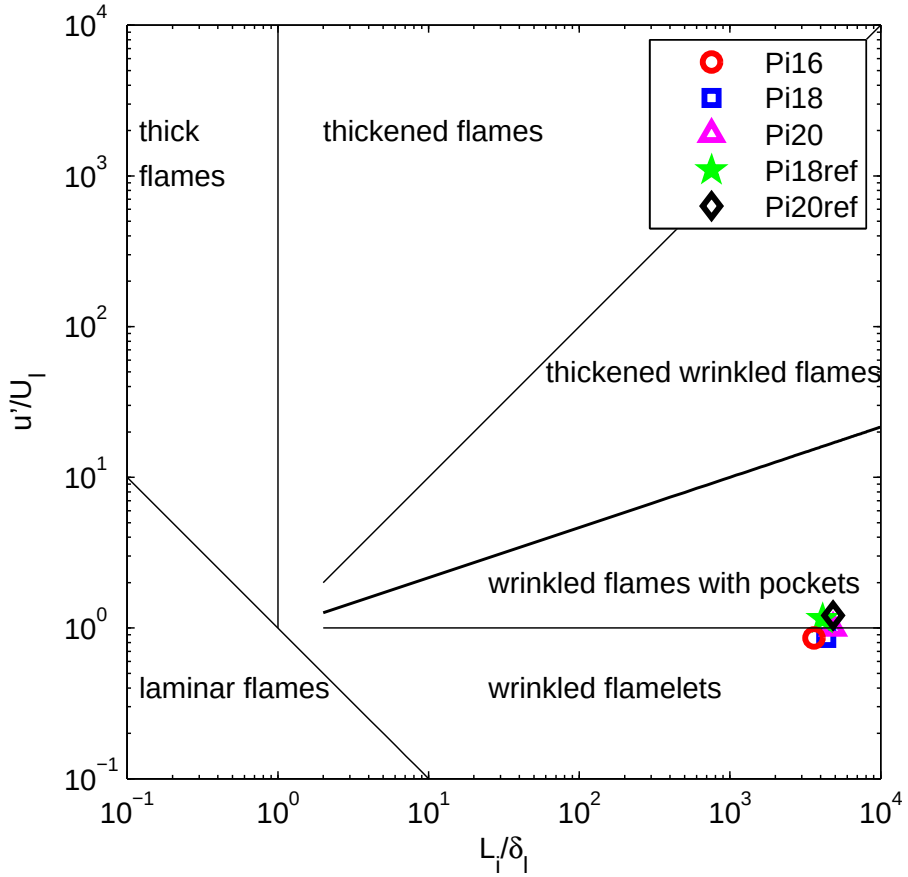

Figure 6.20: Borghi diagram for the turbulent flames for the conditions: Pi16, Pi18, Pi20, Pi18ref and Pi20ref, in the LUPOE 2D boosted engine running at a speed of 750 rpm and a spark timing 2 deg bTDC, stoichiometric iso-octane fuel.

iso-octane flame has been described in Chapter 5. Nevertheless, the peak pressure of 15 bar, achieved at the slow engine speed of 100 rpm, was still lower than 30 bar at the high engine speed of 750 rpm, owing to the strong blow-by effect. The results in Chapter 5 have shown the "power law" equation proposed by Metghalchi and Keck [1982] has a predicted value between the measured "quasi" stretched laminar burning velocity and the one dimensional unstretched flame simulation. Flame stretch and instability effects were not excluded in this equation. Therefore, this equation was adopted to calculate the laminar burning velocity, which has been inserted into the LUSEIDA code. The calculated laminar burning velocities after the spark ignition for the three conditions have been plotted in Figure 6.19. Pi16 condition has the highest laminar burning velocity at around 0.75 m/s, while the Pi20 has the lowest value of 0.7 m/s. This tendency did not change at the initial flame propagation stage. The laminar flame thickness was calculated from the Equation 2.19, the kinematic viscosity was acquired using the Gaseq chemical equilibrium code developed by Morley [2005]. The estimated experimental conditions on the Borghi regime diagram are plotted in Figure 6.20. Five selected conditions in Section 6.1 are located across the wrinkled flamelets and wrinkled flames with pockets, since the turbulence intensity is very close to the value of the laminar flame speed. Under the similar turbulent intensity conditions, the calculated laminar flame thicknesses become thinner, resulting in the operation regime horizontal shift to the right hand side, see conditions Pi16, Pi18 and Pi20. At the wrinkle flamelet regime, moderate turbulent flow wrinkled the flame front weakly, thus the effects of flame instability induced by high pressure might become significant. At the same initial pressure, stronger turbulence intensity leads the operation regime to enter into the wrinkled flame with pockets regime, see Pi18ref and Pi20ref, where the flame front could be strongly wrinkled by the turbulent eddies, and flame pockets or islands will appear in the flame front.

6.5 Effect of initial pressure on flame development

This Section presents the investigation of the degree of supercharging on flame development, and emphasizes the pressure effects on different flame development phases i.e. initiation, main phase, and termination phase. These analysis and discussions are based on the image and pressure data collected in Section 6.3. The experimental conditions have been presented in Section 6.1.

6.5.1 Experimental observation on burning velocity

In an SI engine, flame propagation happens in a small confined volume, the pressure changes significantly during this process, and the chamber volume also changes with the piston moving, it is necessary to clarify the change in conditions during the flame development stages. One pressure trace and the corresponding entrainment flame radius of an individual firing cycle from Pi20 condition are plotted in Figure 6.21. From the flame radius development curve, it is clearly shown that the flame propagation process could be separated into three stages: flame acceleration, fully development flame and flame deceleration. In the left side of this Figure, the cross-section of disc-shape engine chamber was illustrated with the piston moving positions at different stages.

In the initial stage, because the spark timing is close to the TDC (Top Dead Centre), the piston speed is very slow, so the volume change is also very small, and the pressure is nearly constant. The flame radius developed fast due to flame acceleration. Following this stage, flame propagation is at a nearly constant speed, during which both the pressure and the volume change a large amount, e.g. volume is increased by almost 50%, pressure is increased between 3 and 8 bar. This change affects the thermal expansion and ratio between burning velocity and flame speed. In this stage, flame radius development is almost linear with crank angle. When the flame is approaching the wall, the flame deceleration effect decreases the rate of flame radius development. There is still 50% mass unburnt at this last stage, the change in volume is small, but pressure increases significantly; it is supposed that this is a constant volume and pressure increasing process. Here, for the following data analysis, we define the pressure at the transition point between flame acceleration and fully developed as P_0, between fully development and flame deceleration as P_1, the pressure at the moment of flame reaching the walls as P_2. Δp_1 is the pressure change during the flame fully development; Δp_2 is the pressure change during the last combustion stage.

Based on the entrainment flame radius recorded using the CH* chemiluminescence imaging method, the entrainment flame speed can be directly estimated from the time derivative of this radius. The expansion factor, the density ratio of unburnt to burnt gas, is used for the conversion between entrainment flame speed and entrainment burning velocity, which is the rate of the fresh mixture being consumed by the flame front. The expansion factor was calculated from thermodynamic equilibrium using LUSIEDA. One example of entrainment burning velocity was shown in Figure 6.22. Three flame development stages can be easily discerned. Traditionally, combustion duration in SI engine was subdivided in terms of the burnt mass fraction x_b into the initial: $x_b < 0.1$, main: 0.1

$\leq x_b \leq 0.9$, and final: $x_b \geq 0.9$ stages. Based on an analysis of flame development, the recent work of Liu et al. [2013] showed that a more physical division is in terms of the burning velocity: initial acceleration, more or less constant speed propagation, and the final deceleration by walls. The boundaries of the initial acceleration period correspond only to few percent of the burnt mass, while more than half of the mass is unburnt when the walls begin to slow the combustion down.

Following the ideas of Liu et al. [2013]. Figure 6.22 presents a sample illustrating variations of burning velocity during one cycle. The flame images obtained with CH* chemiluminescence images are shown for the three individual stages. In order to compare the pressure effect on the flame development at different stages, two turning points were defined. The turning point is the maximum curvature point of the velocity curve at the beginning and end of the flame development, and then a linear fit was used to get the value of the initial flame acceleration and final deceleration. At the fully developed flame stage, the velocity was linear fitted from the flame radius between two turning points directly. Based on the split of flame propagation into the three stages described above, the burning velocity of each individual cycle was calculated and separated into three stages by using the turning points. The initial flame acceleration, fully developed burning velocity and final deceleration of 100 cycles for each condition were shown in Figure 6.23 in the form of histograms. The red line shows the mean value. The pressure and temperature at spark timing are listed in the table on the margin of Figure 6.23. Pressure values were measured and temperatures were calculated with LUSIEDA using the experimental pressure trace. The turbulent intensities (RMS velocity) presented in Section 6.2 are listed in the second column.

It is seen that the influence of pressure does not appear to greatly alter the low turbulent burning velocity. At the initial stage, the flame acceleration was decreased with the rise of pressure, but the rate of decrease was not monotonic. Usually, turbulence has a great positive effect of flame development (Lipatnikov and Chomiak [2002]), this conclusion also can be confirmed by comparing Pi18 and Pi18ref, Pi20 and Pi20ref, both of them have higher flame acceleration under the higher turbulence intensity conditions. This can explain why the Pi20 is larger than Pi18, However it is still lower than Pi16. This implies that pressure has negative effect on the initial stage of the flame. The initial stage of the flame may stay in a laminar flame mode, which is usually reduced by pressure.

At the fully development stage, all conditions show similar burning velocities. The LUPOE 2D boosted engine's turbulence intensities are not strong, the fully development flame is in the weakly wrinkled region on the Borghi diagram. The turbulence still has a positive effect on the burning velocity, but this kind of effect becomes weaker compared

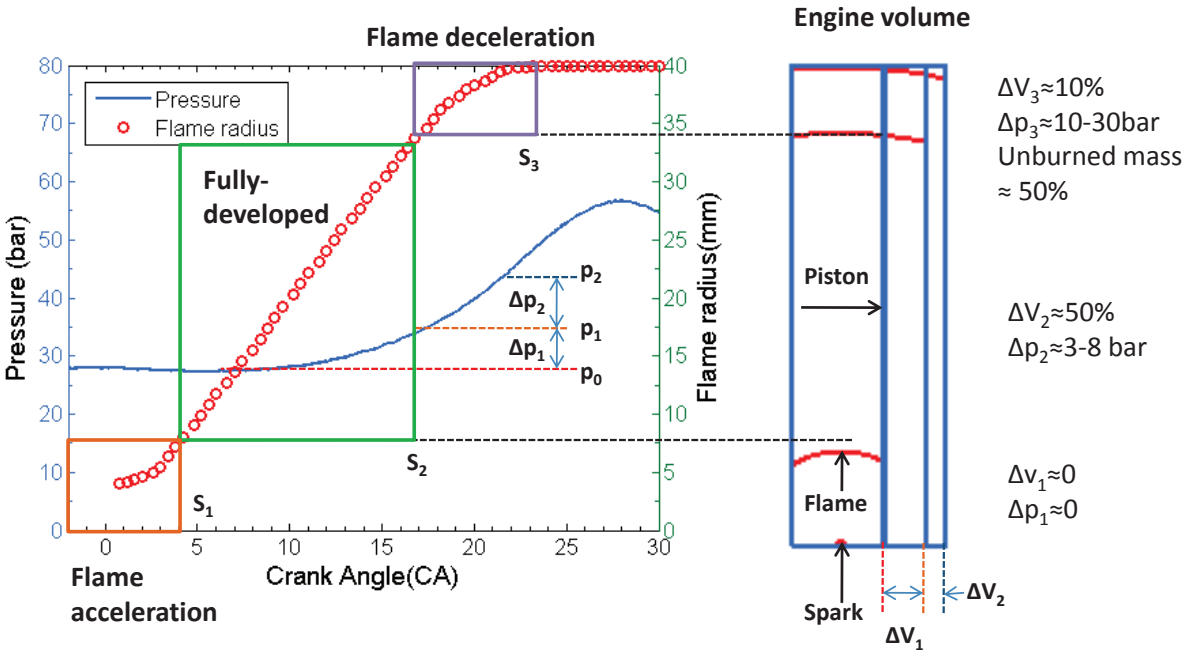

Figure 6.21: Conditions of in-cylinder pressure and engine volume change in three flame development stages: flame acceleration, fully developed and flame deceleration.

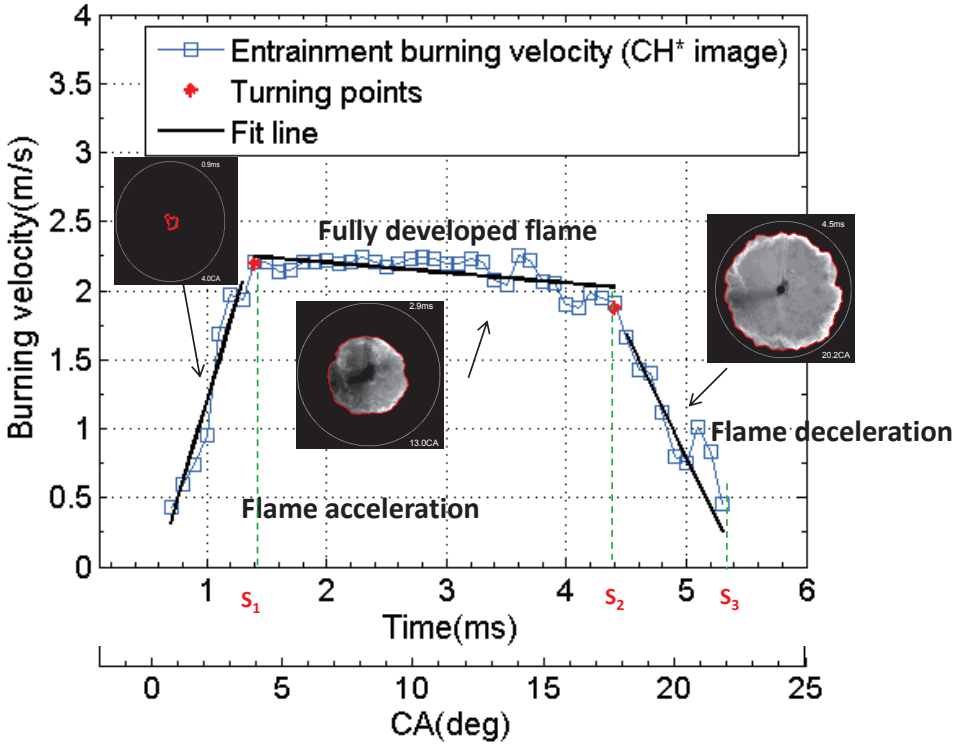

Figure 6.22: Illustration of burning velocity calculated from Figure 6.21 during flame development: flame acceleration, fully developed stage and flame deceleration.

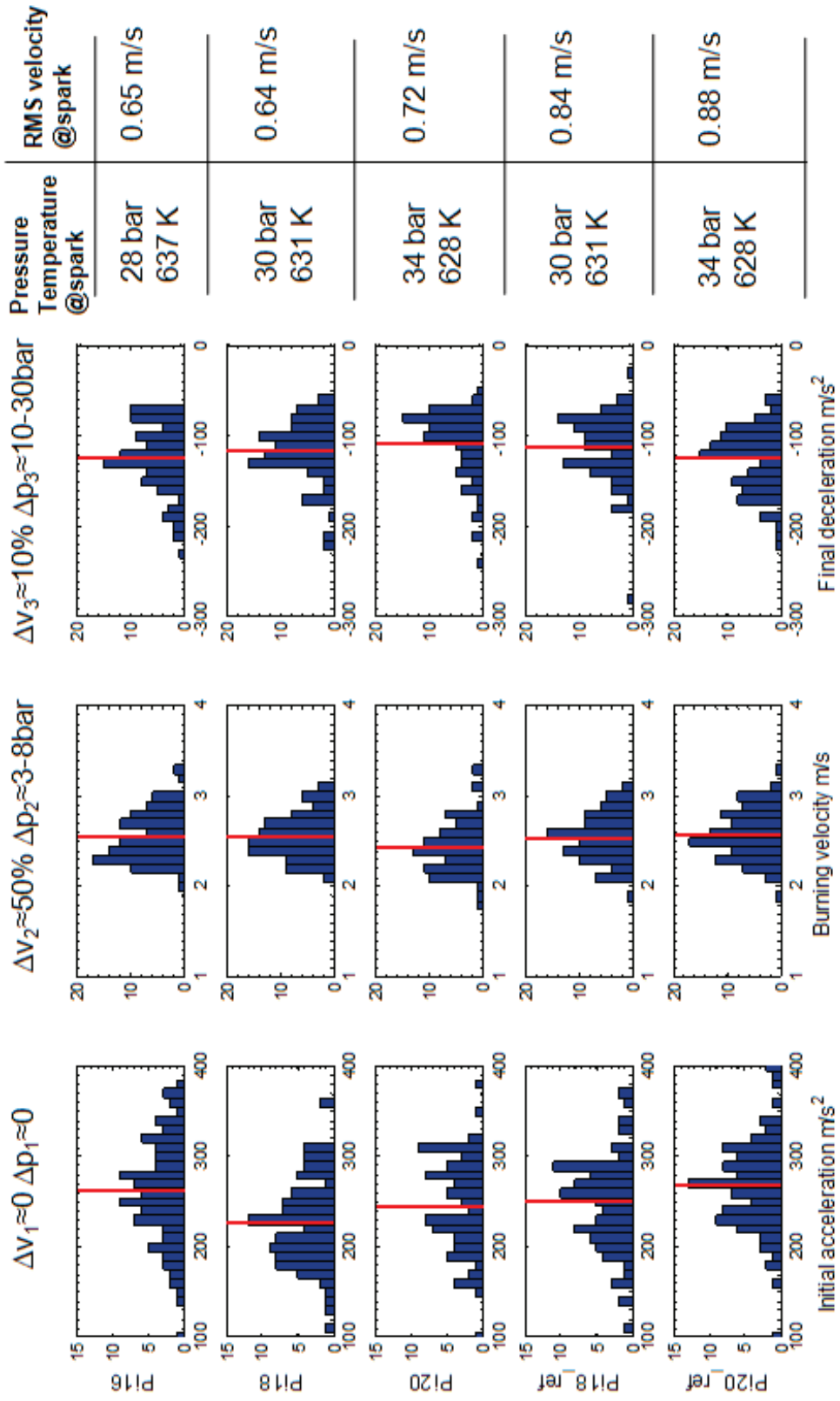

Figure 6.23: Histogram of flame development for the experimental conditions: Pi16, Pi18, Pi18ref, Pi20 and Pi20ref, in the LUPOE 2D boosted engine running at a speed of 750 rpm and a spark timing 2^o bTDC, stoichiometric iso-octane fuel. The red line shows the mean value.

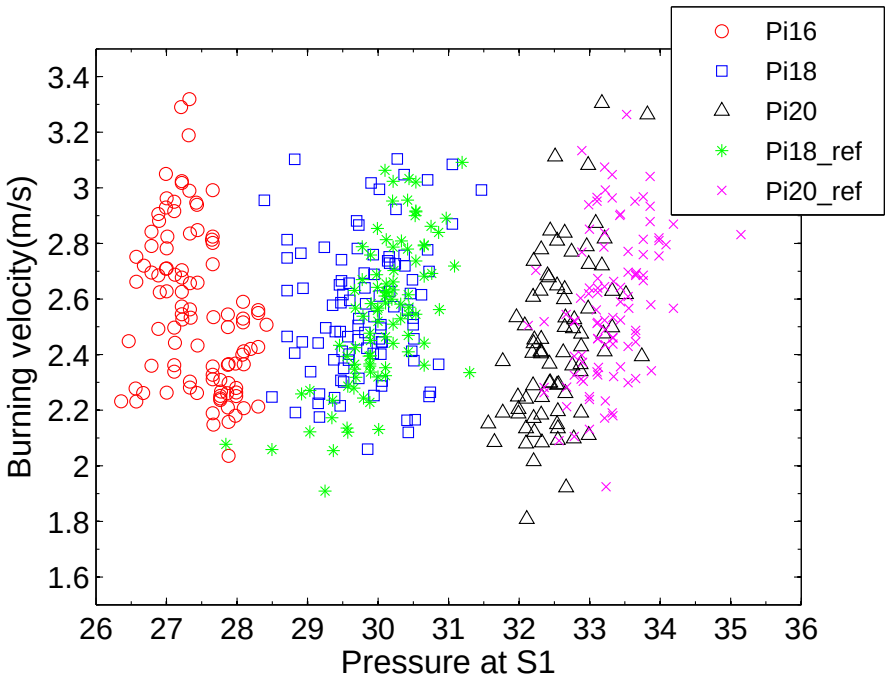

Figure 6.24: Correlation between pressure at the beginning of the fully developed stage and burning velocity for the experimental conditions: Pi16, Pi18, Pi18, Pi20 and Pi20ref, in the LUPOE 2D boosted engine running at a speed of 750 rpm and a spark timing 2^o bTDC, stoichiometric iso-octane fuel.

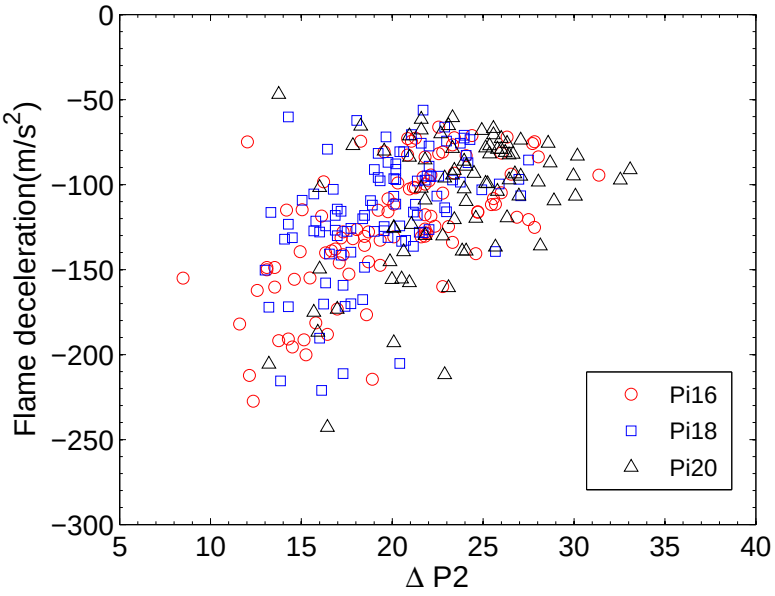

Figure 6.25: Correlation between pressure change at flame deceleration stage and burning velocity, for the three initial conditions: Pi16, Pi18 and Pi20, in the LUPOE 2D boosted engine running at a speed of 750 rpm and a spark timing 2^o bTDC, stoichiometric iso-octane fuel.

with the one in the initial stage. The higher pressure did not increase burning velocity, there is a slightly negative effect on it. However this could be caused by the low initial acceleration of the flame. The correlation between pressures at the beginning of fully developed stage (S1 shown in Figure 6.21) and burning velocities was made and shown in Figure 6.24. There does not exist relationship between burning velocities of each condition with initial pressures. The weakly relationship only can be observed at Pi20, where burning velocity increases with pressure, especially this effect is more significant under higher turbulent intensity. The measured turbulent burning velocities of iso-octane/air mixtures at high pressure of 26-35 bar, under the turbulent intensities that ranged from 0.65 m/s to 0.88 m/s, are 2-3.4 m/s. This value is very close to the one measured by Landry et al. [2008] in a 4 stroke boosted engine with a turbulent intensity of 1.15 m/s.

The turbulence in the near-wall region is always much smaller than in the bulk of the charge. Therefore, the role of the laminar burning velocity should become greater near the walls. It is well known that the laminar burning velocity decreases with the increased pressure; however the rate of burning velocity observed near the wall region is increased with the pressure increasing, therefore some other mechanisms such as flame instability or enhanced unburnt mass temperature by elevated pressure could play a role. These effects can make the flame speed decreasing rate slow. The correlation between the pressure change at the last combustion stage and the flame deceleration was shown in Figure 6.25. There is a strong relationship between them, a higher pressure change leads to a slower flame deceleration.

6.5.2 Burning rate and flame thickness

Pressure traces presented in Section 6.3.2 were used to calculate the mass burning rate in the LUSIEDA, which has been introduced in Section 3.5. The LUSIEDA code can calculate the burn rate by comparing the firing cycle pressure and a motoring cycle pressure within each 0.2 crank angle increment. The results are compared in the left side of Figure 6.26. Three conditions show a similar burn rate in the flame acceleration and fully developed stages. The burn rates increase with flame propagation until the flame approaches the walls. The burn rates have a slight decrease at the final stage. At this stage, the pressure has an effect on the burn rate, and a higher initial pressure results in a faster burn rate. These results match with the burning velocity observed from optical method. The cyclic variation has also increased with initial pressure, especially at the final stage.

By using the burn rate calculated from the cylinder pressure, the burnt gas radius could be calculated, and the mean flame brush thickness might be derived from

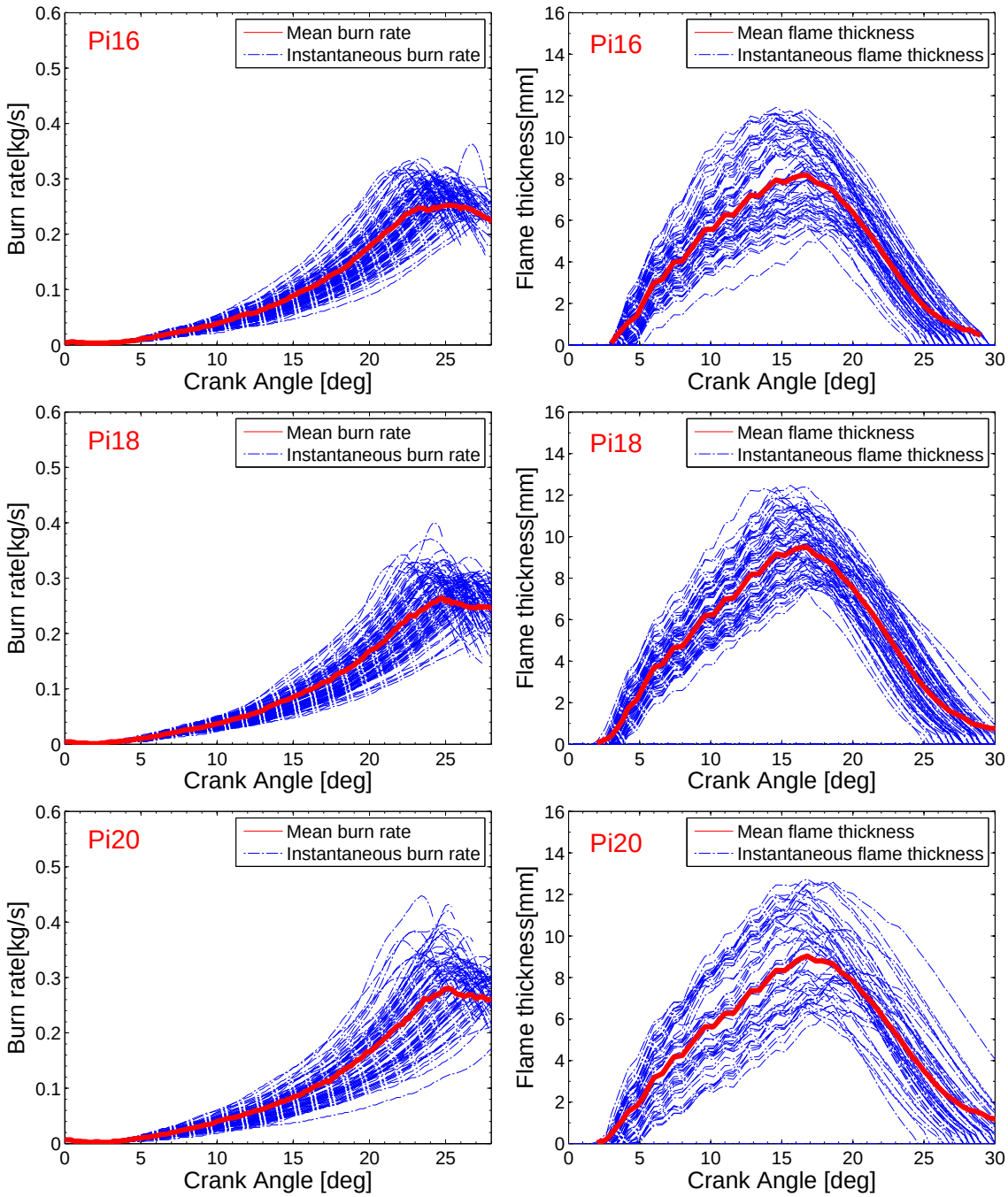

(a)Burning rate (b)Flame brush thickness

Figure 6.26: (a) The Burn rate of the mixture derived from LUSIEDA, (b) Flame brush thickness calculated from the difference between entrainment flame radius and burnt gas flame radius, for the three initial conditions: Pi16, Pi18 and Pi20, in the LUPOE 2D boosted engine running at a speed of 750 rpm and a spark timing 2^o bTDC, stoichiometric iso-octane fuel.

the difference between this burnt flame radius and the entrainment flame radius which are measured from the same cycle's CH* chemiluminescence images. The details of this method have been introduced in Section 3.5, and this method was applied to process each individual cycle for the three initial conditions. The instantaneous flame brush thickness at the different initial pressures were compared and they are shown in the right side of Figure 6.26. It can be observed that the flame brush thickness increases with the flame development. The peak values of flame brush thickness for the three initial pressure conditions are approximately 8-10 mm, which are achieved when the flame speed starts to decelerate after 15^o crank angles after ignition, about 10 mm far from the engine wall. This value agrees well with the one observed from the CH* chmeiluminescence images shown in Section 6.3.1. The flame brush thickness increases slightly with the rise of the initial pressure when the flame is near the walls, the variance of thickness is also amplified by the increased initial pressure.

6.5.3 Further discussion on flame development

Based on data from experiments, many models and correlations have been developed to express turbulent burning velocity. Abdi Aghdam [2003] investigated performance of three turbulent burning velocity correlation methods: the Leeds Ka and KaLe correlations (Abdel-Gayed et al. [1987]) and the Zimont model (Lipatnikov and Chomiak [2002]). It was found that the Zimont model was the most promising tool for engineering application. Here the Zimont model is validated by current data collected at high pressure, more details about Leeds Ka and KaLe correlations can be found in Abdi Aghdam [2003]. The turbulent combustion model developed by Zimont [1979] based on an assumption that the rate of the turbulent entrainment of fresh mixture into the flame brush is equal to the consumption of this mixture in the thickened reaction zone. The turbulent steady burning velocity is given by:

$$U_{t,0} = \mathrm{A}u'\mathrm{Da}^{1/4} = \mathrm{A}u'^{3/4}U_l k^{-1/4}L^{1/4} \tag{6.1}$$

Where $U_{t,0}$ is the developed turbulent burning velocity, A is a constant value of 0.5, u' is the root mean square (rms) turbulent velocity, U_l laminar burning velocity, Da is the Damkhöler number, Da = τ_l/τ_c where $\tau_l = L_i/u'$ is the integral time scale, and $\tau_c = U_l^2/k$ is the characteristic laminar chemical time, k is the characteristic laminar chemical time scale.

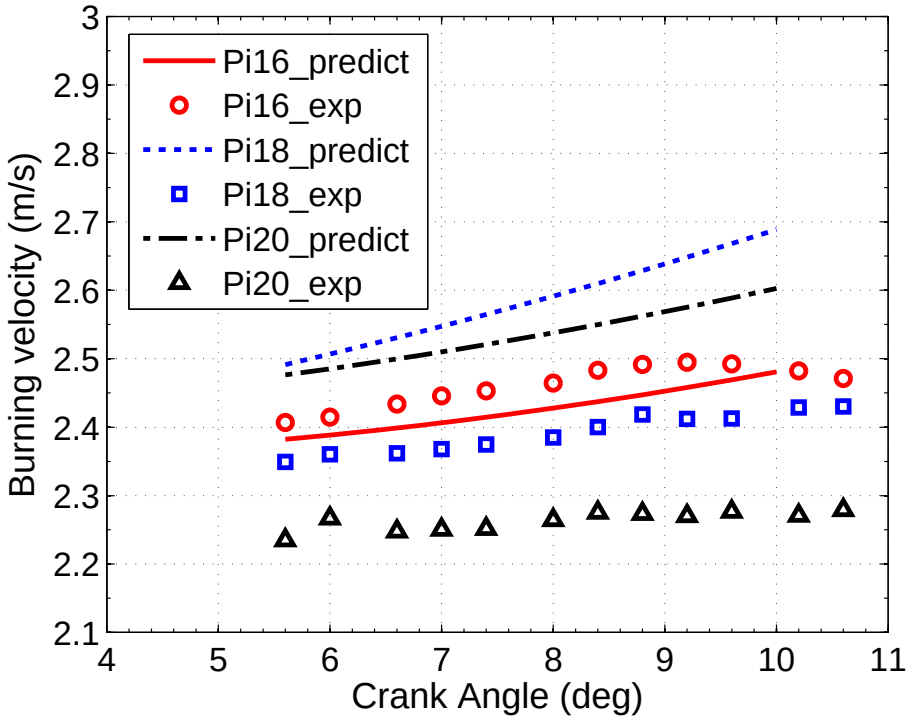

Figure 6.27: Comparison of modelling (Zimont model) and measured turbulent burning velocities for the three initial conditions: Pi16, Pi18 and Pi20, in the LUPOE 2D boosted engine running at a speed of 750 rpm and a spark timing 2^o bTDC, with stoichiometric iso-octane fuel.

The Zimont turbulent burning velocity model has been implanted into the LUSIEDA code. The thermodynamic conditions could be estimated from the input pressure trace. The laminar burning velocity and the temperature used to calculate the molecular transport coefficient have been shown in Section 6.4. The turbulent parameters were measured using the PIV system, then input into the code. The predicted mean turbulent burning velocities at the fully developed stage for the three initial pressure conditions are compared with the corresponding measured entrainment burning velocities derived from the CH* chemiluminescence images in Figure 6.27. The results show a good agreement in the values of burning velocities, the maximum error between the measured and predicted values is approximately less than 0.3 m/s, and it occurred at the strongest boosted condition Pi20. With the pressure rise, the predicted burning velocity increases. This tendency contrasts with the measured values. This may be attributed to the fact that the model does not include the effect of flame transient phenomenon.

There have been so far several models of flame acceleration proposed, e.g. an expression based fractal combustion models (Baratta et al. [2006]), integral of the dimensionless turbulence PSD by Abdel-Gayed et al. [1987]; and the one proposed by Lipat-

nikov and Chomiak [1997] based on Taylor diffusion theory. Rather than approximate the acceleration by a constant value in Section 6.5.1, it seems more physical to approximate it with one of the three functions proposed in the literature and derive from it with any turbulence-related parameters. Potential problem in doing so comes from variable thermal expansion and usual complicate application to engines. Here, the flame acceleration expression proposed by Lipatnikov and Chomiak [1997] was used to approximate the experimental data, the equation is as follow:

$$f_d = \left\{1 + \frac{\tau'}{t}\left[exp\left(-\frac{t}{\tau'}\right) - 1\right]\right\}^{1/2} \tag{6.2}$$

where τ' is a turbulent time scale. The fast, medium and slow burning velocity cycles derived from CH* chemiluminescence images from three initial conditions Pi16, Pi18 and Pi20 are plotted in the left side of Figure 6.28 according to the crank angle. The burning velocities were normalized by dividing by the maximum burning velocity. Pi16 has the fastest flame development rate in all fast, medium and slow cycles. Nevertheless, the difference between the three initial pressure conditions during the first 5^o crank angle after ignition is negligible in the fast and medium cycles, while only Pi20 has a lower burning velocity at the slow cycle. The curves calculated using Equation 6.2 are compared to the experimental data. The turbulent time scale was adjusted to achieve a minimum error between the predicted curve and the mean values of fast, medium and slow trace. From the left side of Figure 6.28, The predicted flame acceleration curve have a higher burning velocity value at the initial rate of flame acceleration, whilst it becomes smaller at the later stage of the flame acceleration. This trend is more evident at the slow cycles.

The same goes about deceleration by walls. Instead of quantifying the deceleration as a constant, it is much better to approximate the burning velocity at this stage in terms of an error function (Abdi Aghdam [2003]) and derive the best fit parameters from it. The original function used the flame thickness and radius position as two input variables. This study has found that the crank angle, instead of flame position, was the better value for fitting the error function:

$$f_w = \frac{1}{2}\text{erfc}\left(\frac{\theta_f - \theta_0}{\delta(\theta)}\right) \tag{6.3}$$

where θ_f is the crank angle with the flame radius development, $\delta(\theta)$ is the duration of flame deceleration, and θ_0 is the crank angle at the medium of flame deceleration duration. The fast, medium and slow cycles were selected from three initial conditions Pi16, Pi18 and Pi20. The burning velocities were obtained from CH* chemiluminescence

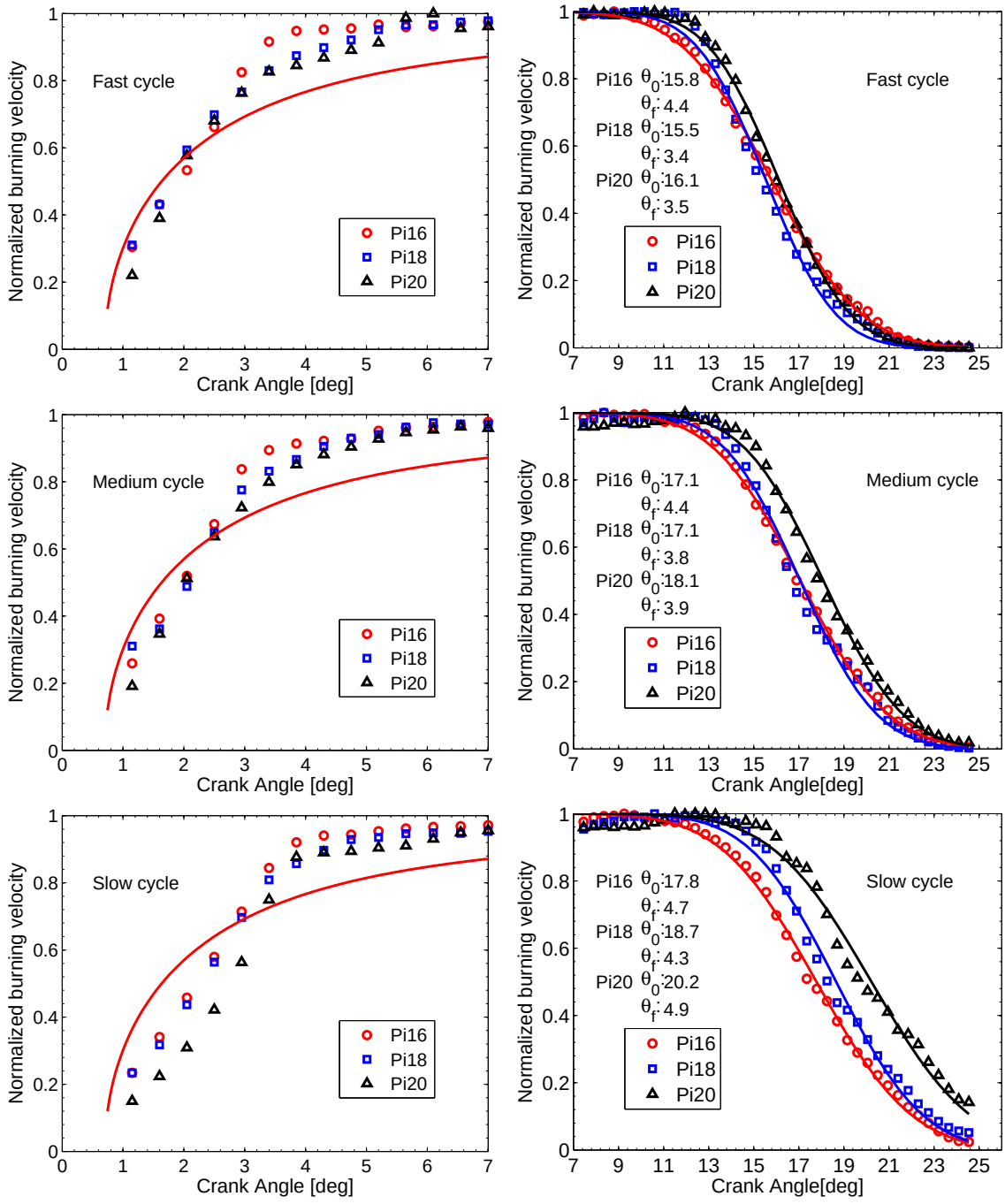

(a) Flame acceleration (b) Flame deceleration

Figure 6.28: (a) Fitted curves of flame acceleration and (b) deceleration compared against the experimental data (points) in terms of fast, medium and slow cycles, for Pi16, Pi18 and Pi20 in the LUPOE 2D boosted engine running at a speed of 750 rpm and a spark timing 2^o bTDC, stoichiometric iso-octane fuel.

images at the engine speed of 750 rpm and normalized using the maximum burning velocity. The differences between the three conditions are only obvious for the slow cycles, the higher pressure has the faster burning velocity than the lower one at the same crank angle. Since the fast, medium and slow cycles were mainly affected by the turbulent intensity (Hussin [2012]), this implied that the pressure effect might become significant at the low turbulent conditions. The least-squares method was applied to fit the non-linear flame deceleration curve using the error function Equation 6.3. The fitting curves are plotted in the left side of Figure 6.28. The calculated values of θ_0 and $\delta(\theta)$ were also presented. The duration of flame deceleration $\delta(\theta)$ does not seem to have a direct relationship with the time at the medium of flame deceleration duration θ_0. It is clear that the θ_0 will be short if the flame develops faster. Thus, all fast cycles show lower values of θ_0 than that of the slow cycles. In general, The θ_0 of Pi16 is smaller than the other two cases. Nevertheless, for the duration time of flame deceleration $\delta(\theta)$, Pi16 has the highest value. For the fast cycle, the flame deceleration crank angle $\delta(\theta)$ is the main value which is adjusted to fit the curve shape, whilst for the slow cycle, the θ_0 value becomes more important.

6.6 Effect of initial pressure on flame structure

In this section, the structure of flame at high pressure and its response to pressure effects were further investigated. The laser sheet visualization method was applied to observe the detailed cross section of the flame front topology. Wrinkle and curvature of the flame front were characterized to compare the flame shapes under different boosted initial pressure and turbulence. Flame spectral analysis also was applied.

Three conditions have been selected: Pi16, Pi20 and Pi20ref. The details of these condition operation have been presented in Table 6.1. Pi20 has a higher initial pressure than Pi16, while the rms velocities at spark timing are similar. The pressure effects can be seen by comparing these two conditions. Pi20 and Pi20ref have the same initial pressure, while the rms velocity of Pi20ref is higher than Pi20, turbulence effects may be obtained by comparing these two conditions. The other engine operation parameters were maintained the same for all the conditions: the engine speed was 750rpm, spark timing was 2^o bTDC, images were taken at 10 degrees after spark, and iso-octane was used as fuel.

6.6.1 Mean progress value and self-similar structure

A map of mean combustion reaction progress variable, which represents the probability of finding the burnt gas at a particular position, can be calculated on the amount of flame contour derived from laser sheet images. The mean progress variable $\bar{c_{ij}}$ at each pixel (i,j) is the average value of intensities of all binary images at the same position. This leads to the equation:

$$\bar{c_{ij}} = \frac{1}{n}\sum_{k=1}^{n} I_{i,j,k} \tag{6.4}$$

where n is the number of images. The calculated $\bar{c}$ contours become stable when the number of images tend to be infinite. Nevertheless, it is only possible to collect a finite number of images in the experiment. Hattrell [2007] found that the required number of images to obtain a stable contours of $\bar{c}$ was less than the estimated one from error analysis, there was little difference between the $\bar{c}$ values produced by averaging 50 and 100 images. In this study, about 40 to 50 laser sheet images have been collected for each conditions, some low quality images have been discarded during the image processing.

Limited by the low repetition laser (15 Hz), only one image could be captured during a firing cycle. The laser sheet also caused a strong light reflection near the engine wall region, thus only the flame structure at one crank angle during the flame fully-developed stage was studied here. The $\bar{c}$ field for the three initial pressure conditions Pi16, Pi18 and Pi20 are illustrated in the left side of Figure 6.29. These contours were obtained by averaging the binarised flames of 40-50 cycles for each condition at the crank angle 8^o bTDC (10^o CA after ignition). The lower limit of the scale (blue) represents 0% probability, whilst the upper (red) is 100%. The black circle represents the position of the engine cylinder walls. The three $\bar{c}$ fields show similar distributions. The largest flame size was observed in Pi16. Based on the map of progress variable $\bar{c}$ field, progress variable values along the flame radius direction could be sliced in each 10^o angle, and plotted in the right side of Figure 6.29. The measured profiles of the mean progress variable could be collapsed by a universal curve. This curve can be well approximated by complementary error function (Lipatnikov and Chomiak [2000]):

$$\bar{c}(x) = \frac{1}{2}\text{erfc}\left(\frac{x - x_0}{\delta_t(t)}\right) \tag{6.5}$$

where x_0 is the position of the value of $\bar{c}(x) = 0.5$. $\delta_t(t)$ is the flame brush thickness.

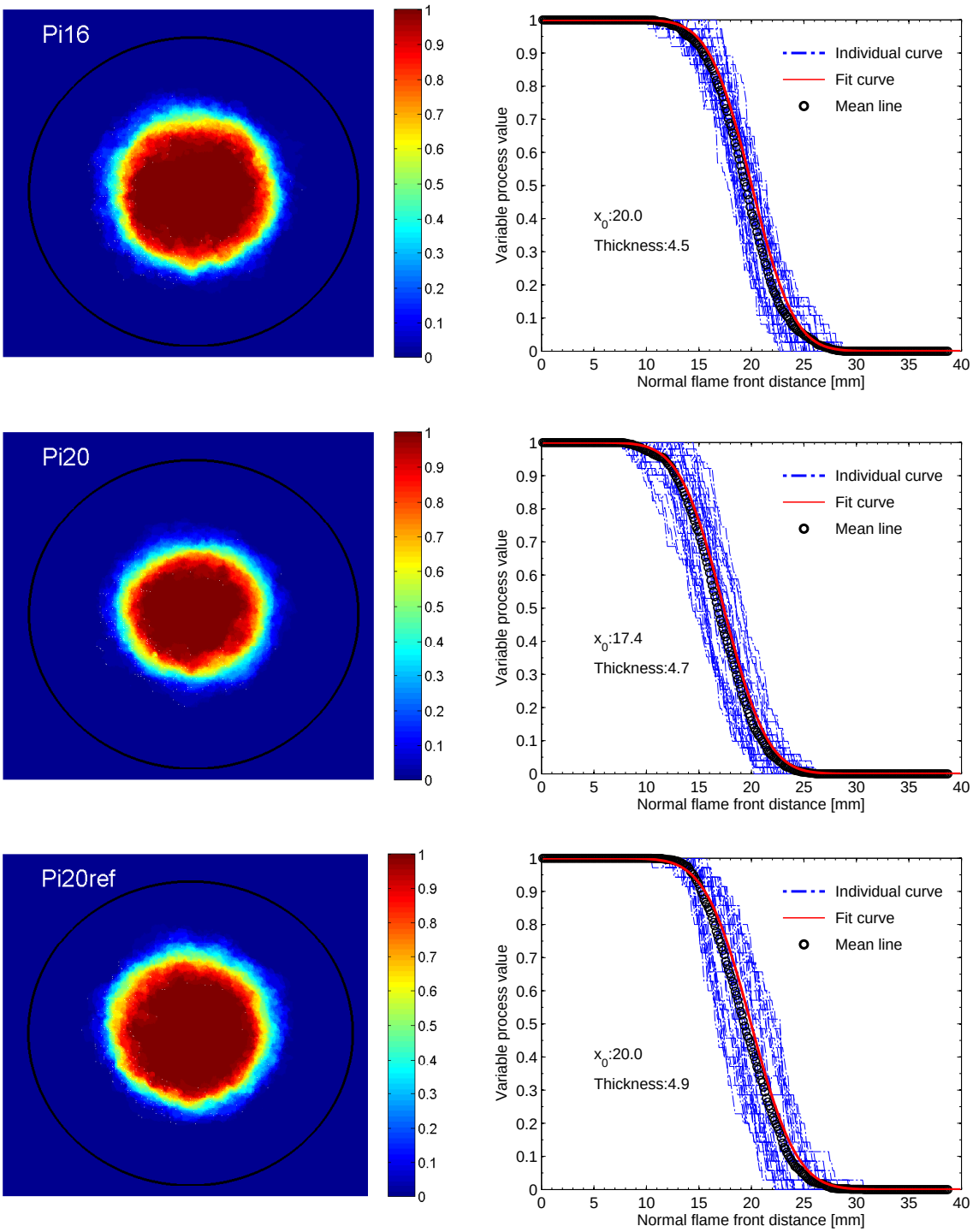

(a)Mean progress variable maps (b)Sliced mean progress variable profiles

Figure 6.29: (a) Mean progress variable maps, (b) corresponding sliced mean progress variable profiles along the flame radius direction with 10^o angle interval, for the three initial pressure conditions Pi16, Pi18 anf Pi20 in the LUPOE 2D boosted engine running at a speed of 750 rpm and a spark timing 2^o bTDC, stoichiometric iso-octane fuel.

The right side of Figure 6.29 shows the mean progress variables along the flame radius direction for the three initial pressure conditions derived from the left side $\bar{c}$ value maps with an angle interval of 10^o each. All the curves show a similar shape, the left side represents the burnt gas as value 1, and the fresh gas is in the right side as value 0. The mean profile curve is calculated according to crank angle, and is plotted in the right side of Figure 6.29. Based on Equation 6.5, the minimum least square method was applied to obtain the best values of position of flame x_0 and flame brush thickness $\delta_t(t)$ to fit this mean curve of the progress variable. The acquired two values are also listed in the Figures. From the results, it can be seen that the mean progress variable profiles can be well fitted by the complementary error function. This means that the flames at high pressure have the same self-similar properties of those observed at low pressure. From the positions of flame at the same crank angle, it can be observed that the case Pi16 has a faster speed than Pi18's and Pi20's. This result obtained using a laser sheet visualization method agrees with the one from the CH* chemiluminescence images. The thickness of the three conditions have similar values which range from 4.3 to 4.7 mm, and are close to the values of flame thickness of 6 mm acquired in Section 6.5.2.

6.6.2 Flame wrinkle and curvature

As shown in Section 6.3.2, the fast, medium and slow cycles classified using the peak pressure of each cycle have a relationship with the flame radius derived from the flame images. The fast cycles have significant larger mean flame radius values than the slow cycles' at each crank angle in the "fully developed flame" stage. Therefore, the cyclic variability also can be characterized using the mean flame radius below, within, or above one standard deviation from the ensemble average value. Figure 6.30 show the fast, medium and slow cycles selected from about 40-50 cycles at each experimental condition.

These individual cycles show the same tendency as observed from mean progress variable maps, that the Pi16 and Pi20ref have a larger radius than that of Pi20. The individual flame centre was calculated as the center of mass of the region covered by flame. It can be seen that the flame centres distribute uniformly around the spark plug (detonated as "+"). This is an evidence that the bulk air flow is homogeneous in the cylinder, which does not lead the flame to move in a certain direction.

It is arguable that the large eddies distort the overall flame shape; while those small eddies have wrinkled the flame locally. In order to study quantitatively these small eddy effects from images, filter methods could be applied to define a "mean flame contour" of the flame. The number of crossing points, and local distance between the instantaneous

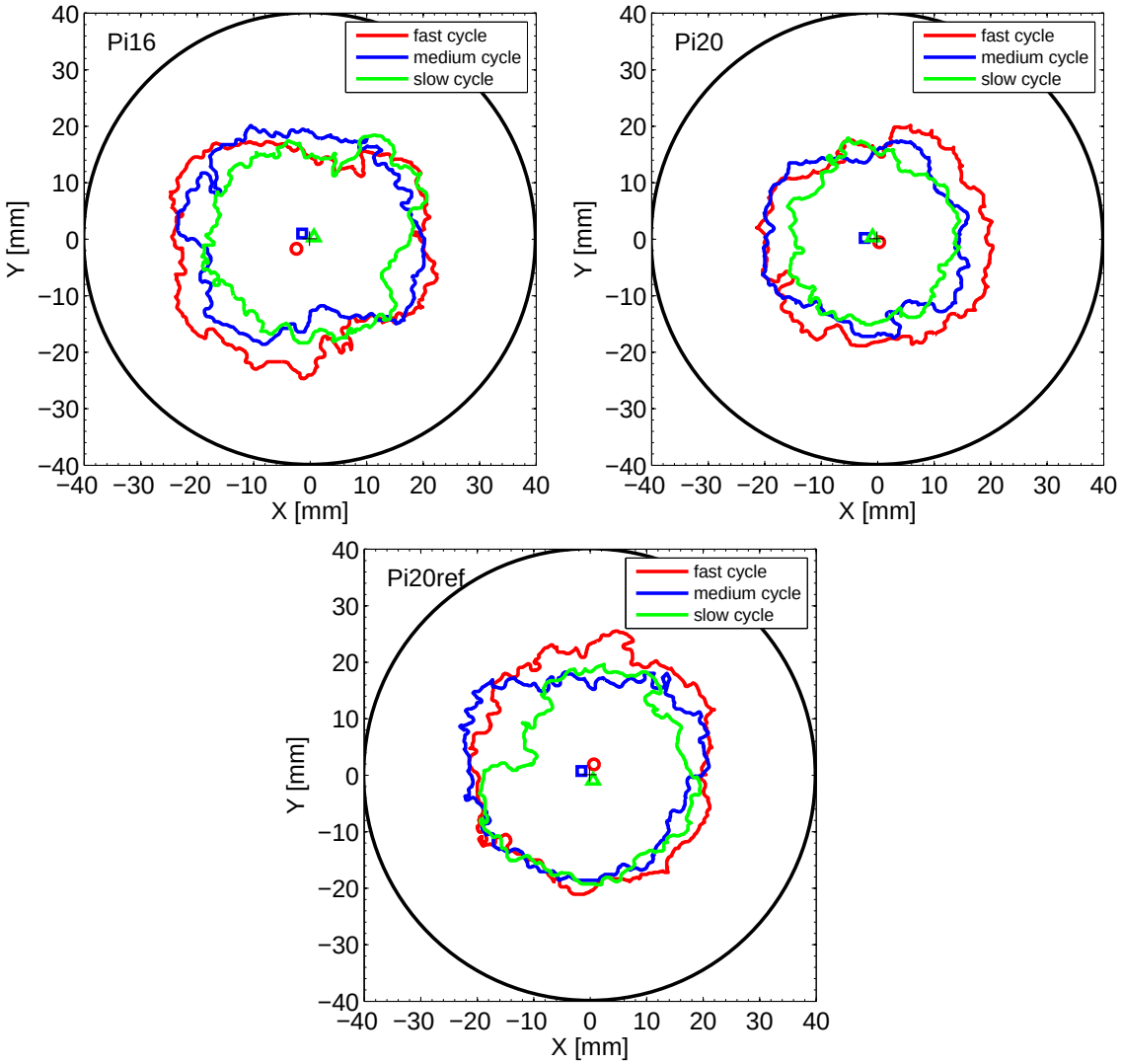

Figure 6.30: Flame contours of fast, medium and slow cycles selected from three conditions: Pi16, Pi20 and Pi20ref, in the LUPOE 2D boosted engine running at a speed of 750 rpm and a spark timing 2^o bTDC, stoichiometric iso-octane fuel.

and filtered contours could be further defined to qualify the flame wrinkle (Aleiferis et al. [2004]; Cairns [2001]). In this study, a "flame radius" was calculated using minimum least square algorithm. Thereafter, the wrinkle structure of a flame contour was characterized using the deviation between the flame contour and the mean radius at the sample points along the contour. The detailed calculation equation has been presented in Section 4.2.2.2.

The deviation values have been calculated for the three conditions: Pi16, Pi20 and Pi20ref, and the results are shown in Figure 6.31. The mean and standard deviation values are also listed in Figure 6.31. Generally, larger flame radius have longer flame contour lengths. By comparing Pi16 and Pi20, the wrinkle level of flame Pi16 is stronger than that of Pi20 at all fast, medium and slow cycles. These two conditions have the similar tur-

bulence intensities and different pressure above 6 bar, see Figure 6.24. This observation implies that the pressure decreases the wrinkle effect under moderate turbulence, which contrasts to the knowledge that flame front tends to be cellular under flame instability. The Le number was estimated approximate 2.0 in these conditions, thus, the diffusive-thermal effects may suppress the hydrodynamic instability, therefore, the flame surface retains a smooth shape. Stronger turbulence leads to severe flame front wrinkle, this can be observed when the Pi20 and Pi20ref were compared in medium and slow cycles, except that one in the fast cycle.

The mean flame curvature was also examined, because the geometry of the flame front also was influenced by the wrinkled flame structure. The calculation method has been introduced in Section 4.2.2.2. The curvature values of each individual flame front were combined together at each condition. The probability distribution curves for the three conditions are plotted in Figure 6.32. The curvature values are between -5 to 5 (1/m), similar to the measured values from a burner flame at 1 to 10 bar (Soika et al. [2003]). With the pressure increased by up 6 bar, no discernible systematic difference in either length-scales or shapes of the probability distribution can be observed.

Figure 6.33 show the normalized spatial autocorrelation curves of fast, medium and slow cycles at the three conditions: Pi16, Pi20 and Pi20ref. The L_a obtained from the Equation 4.21 are listed in the Figure 6.33. Pi20ref has the largest values of 6-8 mm in the medium and slow cycles, whilst, the values of Pi20 are smallest at the same group of Pi20ref. This means the turbulence effects on the flame contour happens in the large scales. By comparing the Pi16 and Pi20, it can be observed the decrease of L_a by increasing pressure, the value of Pi20 is about 1-3 mm, thus, the influence of pressure on flame wrinkle occurs in the small scales. In the fast cycle, the Pi20ref seems to have an abnormal small value if it was compared to the medium and slow ones. The same problem was also seen in the results shown in Figure 6.31. This may be due to the fact that using the flame radius to select the fast, medium and slow cycles is not the best way to choose a typical cycle. Ensemble averaging of all cycles' parameters may be better to represent a turbulent flame's characteristic.

Power spectral density (PSD) S(k) was estimated based on the Equation 4.22. The results of 9 flame contours are plotted in Figure 6.34 against the logarithms of the associated wavenumber,κ. No great difference can be distinguished, only a small spread in the values in the end of the spectrum. Thus, the shape of PSD is not affected by the pressure or turbulence increasing at the large scales. At the fully developed stage, the flame front experiences the full spectrum of wrinkle length scales. The PSD deceases with a almost constant slop as $\kappa^{-2.4}$, this value is steeper than that observed from the isotropic turbu-

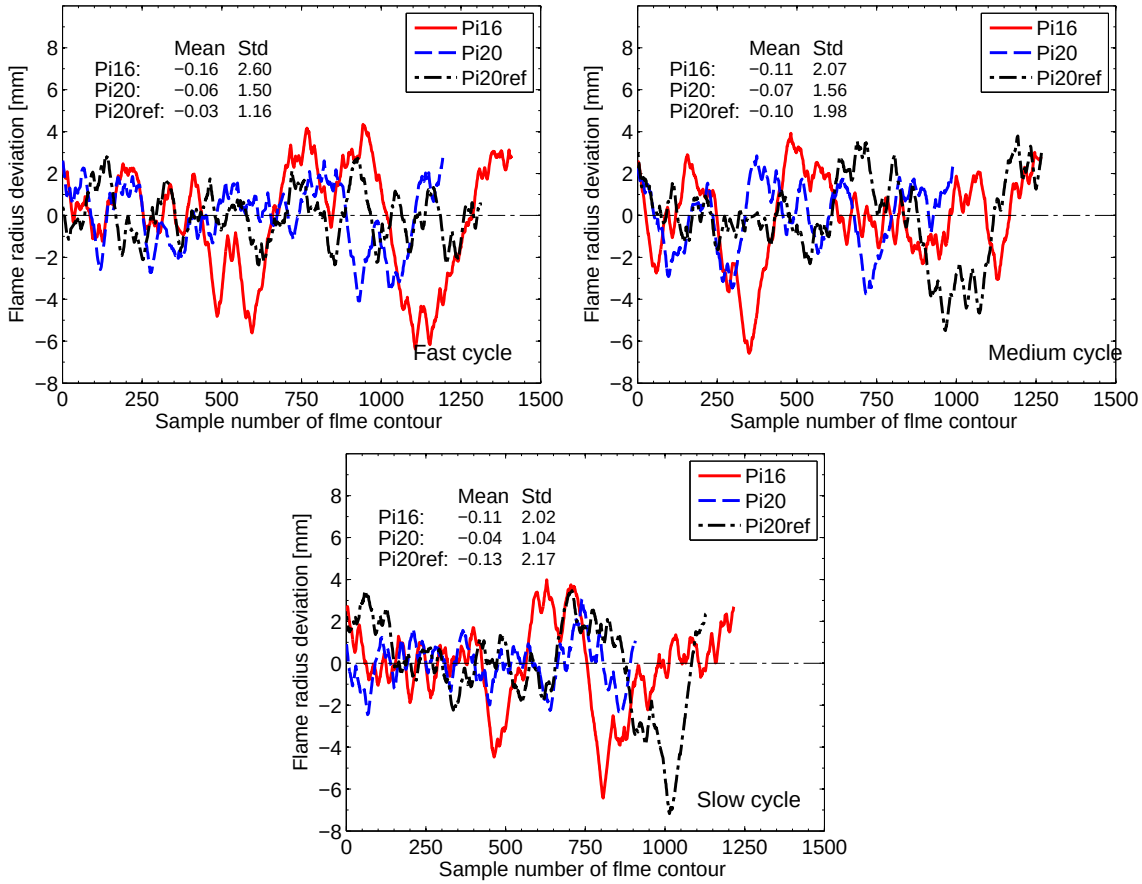

Figure 6.31: Comparison of flame radius deviation along the flame contour of fast, medium and slow cycles for three conditions: Pi16, Pi20 and Pi20ref, in the LUPOE 2D boosted engine running at 750 rpm, spark timing 2^{o}bTDC, stoichiometric iso-octane fuel.

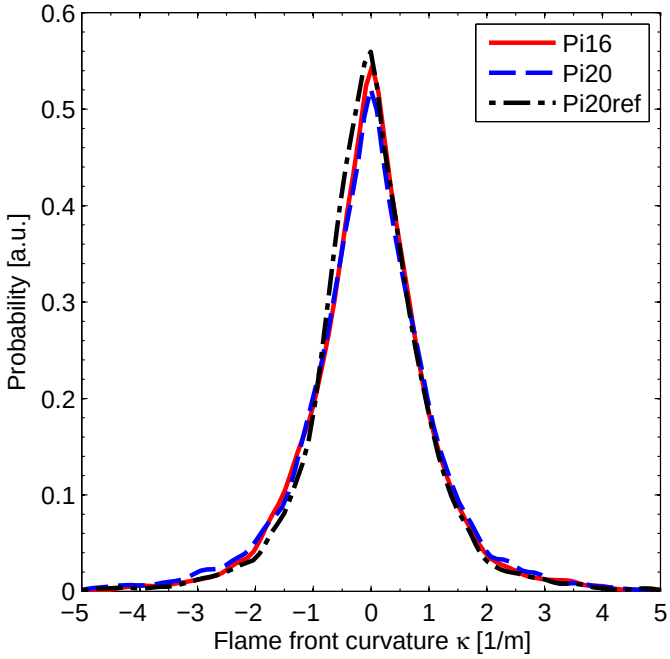

Figure 6.32: Mean curvature distribution of flames from the three conditions: Pi16, Pi20 and Pi20ref, in the LUPOE 2D boosted engine running at a speed of 750 rpm and a spark timing 2^o bTDC, stoichiometric iso-octane fuel.

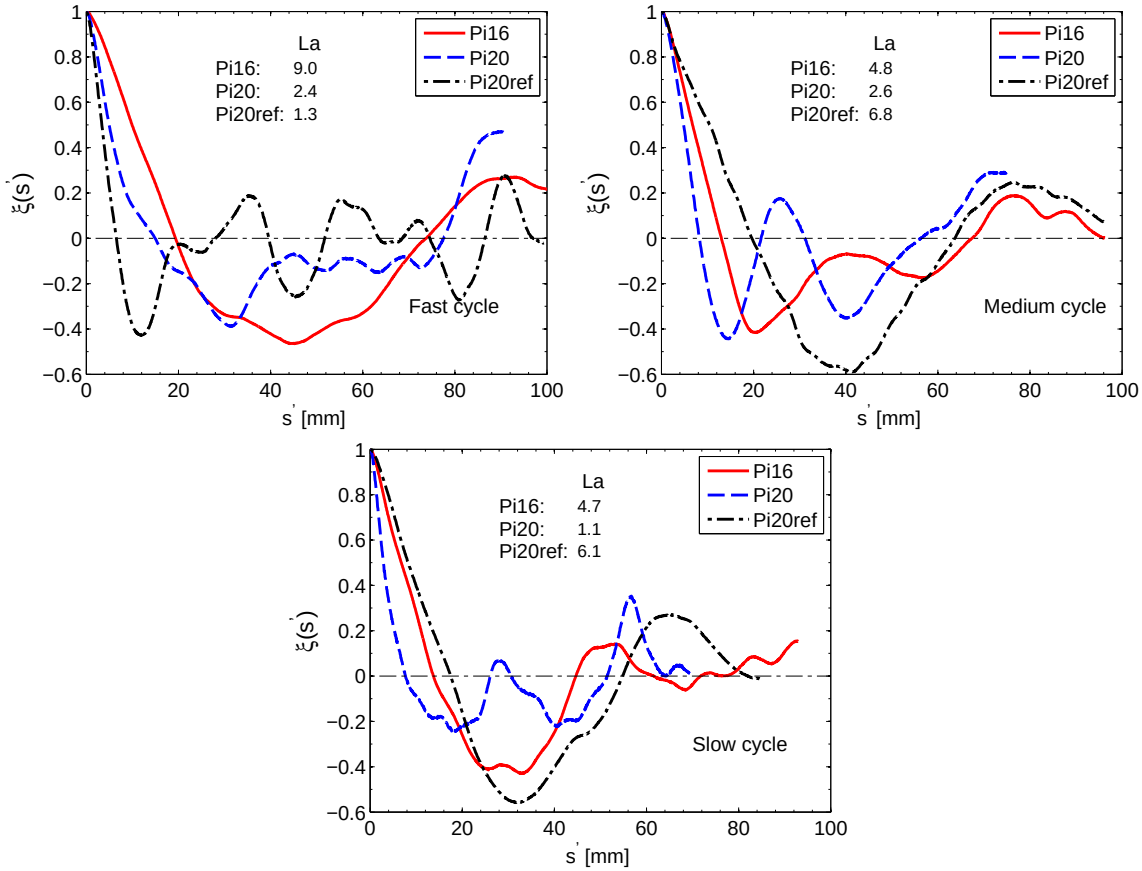

Figure 6.33: Comparison of autocorrelation along the flame contour of fast, medium and slow cycles for the three conditions: Pi16, Pi20 and Pi20ref, in the LUPOE 2D boosted engine running at a speed of 750 rpm and a spark timing 2^{o}bTDC, stoichiometric iso-octane fuel.

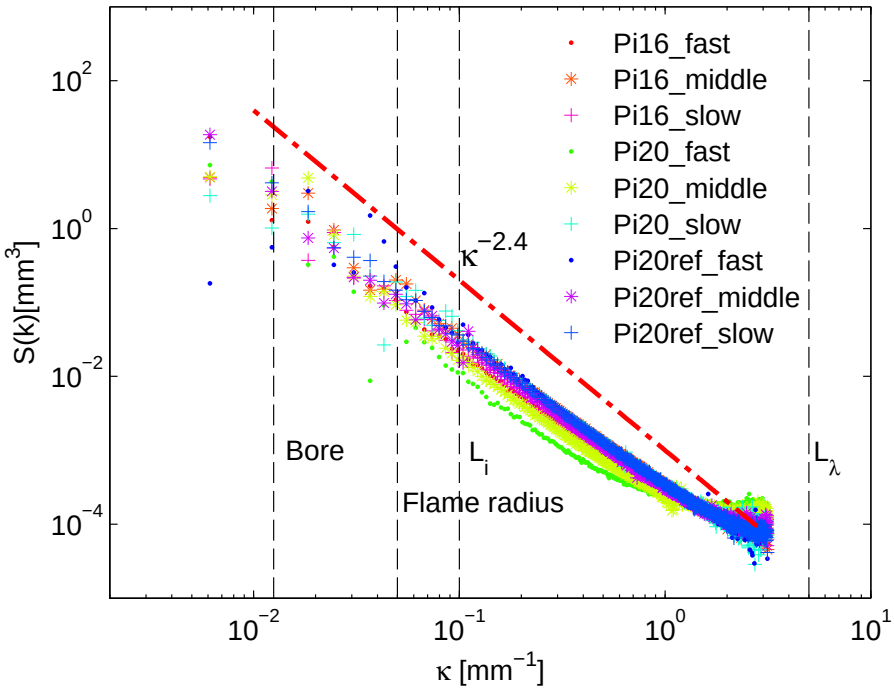

Figure 6.34: The energy density spectrum (PDS) of flame contour of fast, medium and slow cycles for the three conditions: Pi16, Pi20 and Pi20ref, in the LUPOE 2D boosted engine running at a speed of 750 rpm and a spark timing 2^o bTDC, stoichiometric iso-octane fuel.

lence flow $\kappa^{-5/3}$ in the LUPOE 2D engine shown in the Figure 6.4. This gradient of the PSD curve agrees with the measurement of Kheirkhah and Gülder [2013] and Hicks et al. [1994]. Several characteristic length scales also were labelled in Figure 6.34. The largest wavelength of PSD is close to the engine bore size, while the smallest wavelength is cut off above the estimated Taylor length scale (0.2mm), this is mainly caused by the restriction of the resolution of the images. The flame can be influenced by the eddies which are significantly larger (10 to 20 times) than the turbulence integral length scale L_i (10 mm).

Chapter 7

Autoignition in a boosted SI engine

This Chapter presents the effects of increased inlet pressure on knock characteristics studied in the strongly supercharged spark ignition engine, with a particular emphasis on understanding the occurrence of extreme knock. The knock images with different pressure oscillation amplitudes were obtained from the LUPOE 2D boosted engine. Based on these knock images and their corresponding pressure data, the development of autoignition sites and subsequently produced combustion waves were described, and the definitions of knock characteristic parameters, i.e. knock onset and knock intensity, were also evaluated. These defined knock parameters were used to understand the difference of cyclic variability and knock properties under naturally aspirated and strongly boosted engine running modes. Furthermore, several individual imaging knock cycles with gradually increased knock intensities from the same engine operation condition were selected. The effects of thermodynamics state of the end gas condition, unburnt gas mass fraction, and burning velocity on knock intensity were analyzed. The speed of the reaction front generated by autoignition site was calculated to check whether detonation exists in the extreme knock cycles.

7.1 Knock map of LUPOE 2D boosted engine

As a starting point, a series of experiments with different inlet initial pressure and spark timing at engine speed of 750 rpm have been conducted in the LUPOE 2D boosted engine to discriminate between knock and "no knock" regions of operation regimes. The knock

boundary was defined at the regime the number of knocking cycles is above 90% of all firing cycles [1]. An example of knock boundary is illustrated in Figures 7.1, which shows pressure traces of firing cycles around knocking borderline at the inlet initial pressure 1.6 bar. The spark timings were retarded and advanced by 2^o in such a way that the engine exhibits (a) slight knock, (b) "average" knock, and (c) severe knock. These data were obtained from the engine running at 750 rpm with ignition timing set at 5^o bTDC, 7^o bTDC, 9^o bTDC, respectively. The LUPOE 2D engine run with a stoichiometric iso-octane-air mixture. With an advanced spark timing, the flame propagation happens in a progressively decreasing volume as the piston is moving to the Top Dead Centre (TDC) position, thus a higher in-cylinder pressure could be achieved. This potentially results in the unburnt mixture self-ignition, and followed a rapidly pressure rise with pressure oscillation. The peak pressure and the magnitude of pressure oscillation of knock cycles were increased by an earlier spark timing and higher initial pressure in the manifold. The regime of knocking cycles (b) was selected as the knock boundary; a metal engine head was used and only pressure data were recorded, while the imaging data were obtained by using the optical head at the condition where the spark timing or initial pressure was retarded or decreased from knock boundary, e.g. the slight knocking in Figure 7.1.

During these knock mapping experiments, the metal engine head was used, and the knock was detected from the pressure trace and by ear. The knock map at an engine speed of 750 rpm, and the temperature of engine intake and head of 323 K is shown in Figure 7.2. Iso-octane was used as fuel; it has a high anti-knock property, RON of 100 and this ensured that the combustion proceeds in a normal mode for a wide initial pressure region. Under naturally aspirated condition, knock experiments have been conducted by Roberts [2010]. This study found that the knock occurred in more than 90% of the firing cycles when the spark timing was advanced to 15^o bTDC and about 100 knock cycles have been collected as samples to analyze the knock properties. In this study, the initial pressure in the inlet was increased from 1.6 bar to 2.1 bar, and the spark timing was varied starting from the TDC position, and advancing by one degree of the crank angle until more than 90% of cycles became knocking. This spark timing was defined as the knock boundary. It can be seen that the spark timing had to be retarded towards the TDC position with increasing initial pressure, and there was an approximately linear relationship between initial pressure and spark timing for the knock boundary. The spark timing of knock boundaries for intake pressures of initial 1.6 bar, 1.8 bar, and 2.1 bar, are

[1] Usually, knock boundary is defined at which the number of knock cycles is above 10% of all firing cycles. In this study, 90% was chosen in order to acquire as much as knock cycle samples for statistical analysis.

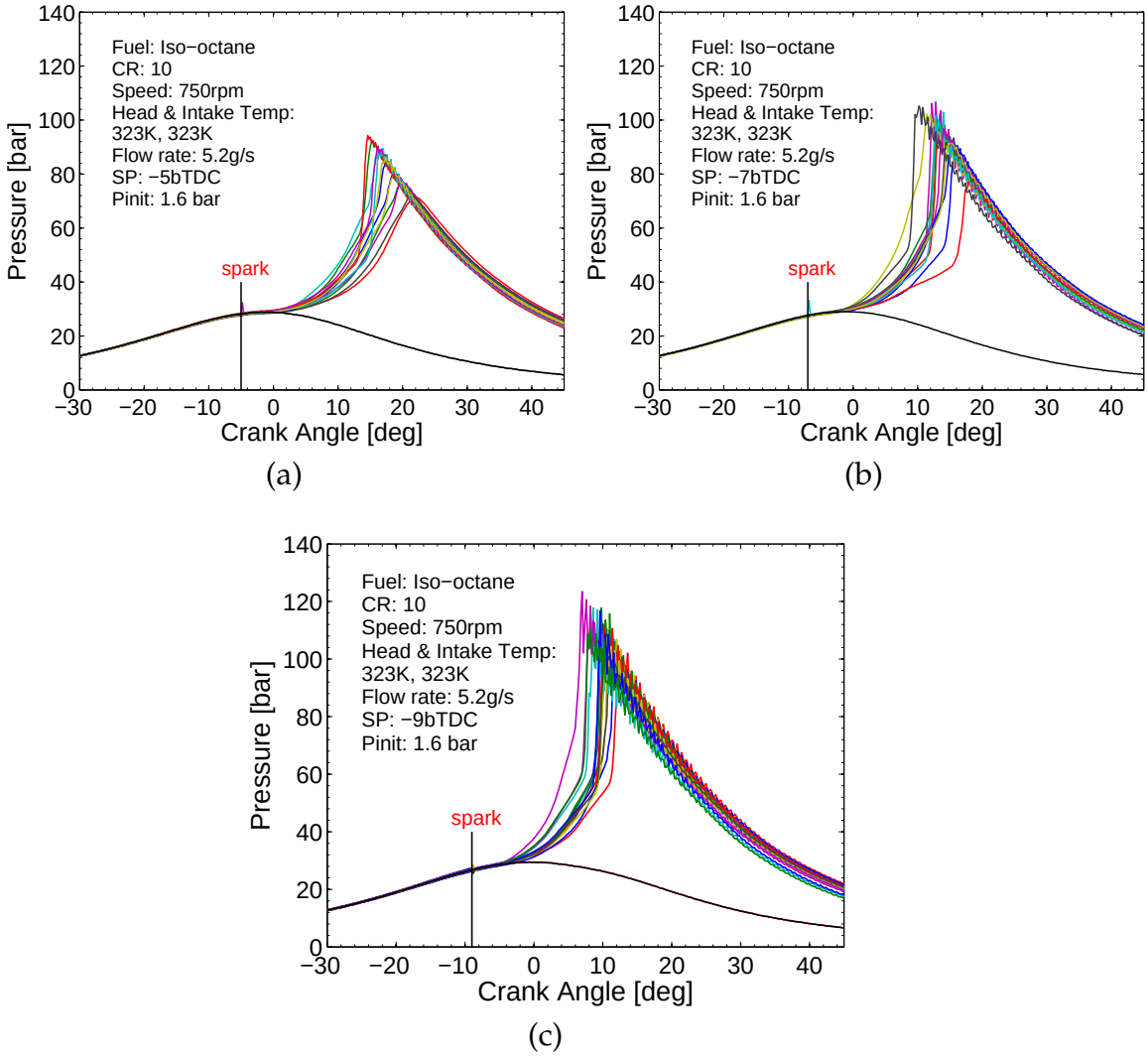

Figure 7.1: Pressure traces near the knock boundary at initial pressure 1.6 bar: (a) slight knocking, (b) "average" knocking, (c) severe knocking. Other operation parameters are listed in the Figures.

7^o bTDC, 4^o bTDC, and 2^o bTDC respectively. The peak in-cylinder pressure of normal cycles near the knock boundary reached approximately 100 bar.

The experimental data have been also collected at an initial pressure of 2.1 bar and spark timing 2^o bTDC at the engine speed of 750 rpm with only pressure measurement for a further clarification of the role of the pressure. Surprisingly enough, extreme knock was only randomly found at the very strongly boosted conditions. Although there is no strict definition of extreme knock, it can be considered as a kind of knock where a pressure oscillation amplitude exceeds 50 bar and occurs at random. In order to observe this phenomena under the acceptable maximum pressure that the optical window can withstand, an imaging method was employed with spark timing of 2^o bTDC, and initial

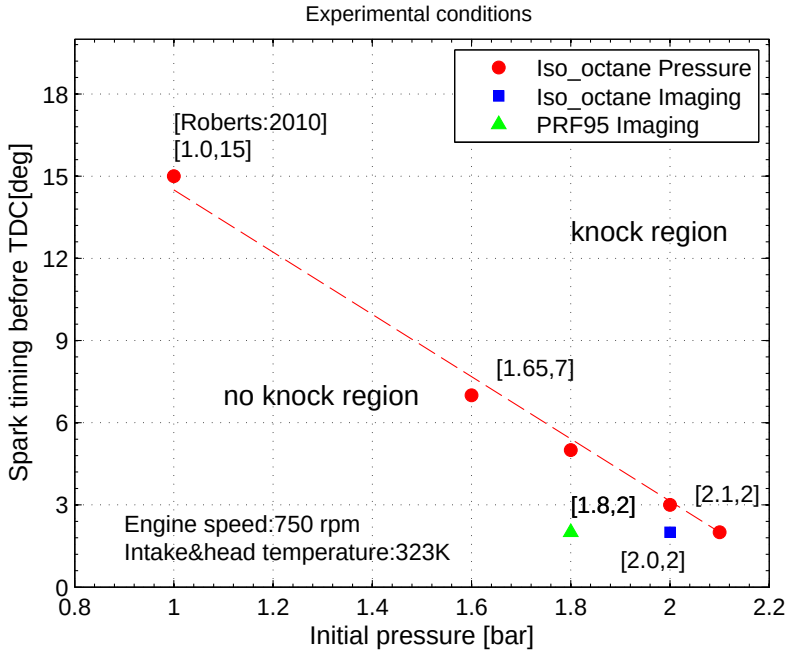

Figure 7.2: Engine knock map of the LUPOE 2D boosted engine at a speed of 750 rpm, the temperature of engine intake and head were kept at 323K. The numbers in the square bracket are coordinates.

pressure was decreased to 2.0 bar; in this region, most cycles were normal or only slightly knocking. The probability of the extreme knock occurrence is low. These images with corresponding pressure traces will be presented in Section 7.2 to show how autoignition develops in different abnormal combustion phenomena. Nevertheless, the rare occurrence of knock for the high octane number fuel, i.e. iso-octane renders its capture more difficult. Moreover, it was found that once the knock occurs, its intensity for an iso-octane and air mixture has a high magnitude pressure oscillation quite capable of destroying the engine windows. Therefore, a mixture of 95% iso-octane and 5% n-heptane by volume, referred to as PRF95 was used. This fuel has a shorter ignition delay time and it tends to cause knock more easily. The knock intensities of the PRF fuel show a wide spread of magnitudes at the same operation conditions. At the same spark timing setting at 2^o bTDC of iso-octane fuel, the knock boundary of PRF95 fuel is at a lower initial pressure of 1.8 bar, thus, this condition was selected to collect different knock intensity cycles with the imaging method. PRF95 fuel data will be analyzed in Section 7.5.

The pressure signal frequencies, amplitudes and phase could all be varied by changing the location of the pressure transducers (Heywood [1988]). Since there is only one dynamic pressure transducer installed in the LUPOE 2D engine, the relationship between location and the pressure profile was not studied in the present study. Engine resonant

frequencies and appropriate cut-off bandwidth frequencies were evaluated from the previous LUPOE 2D engine studies (Conway [2013]; Roberts [2010]; Smallbone [2004]). The frequency of knock oscillation in the LUPOE 2D engine is usually in the range of 2.5 to 12 kHz. Therefore, a wide bandwidth filter 2.5 kHz-12 kHz was selected to remove the noise at low and extremely high frequency regions in the following analysis of knock intensity. Peak pressure was defined as the maximum value of the band-filtered pressure.

7.2 Observations of autoignition

This Section shows images of different abnormal combustion phenomena, including end gas self-ignition, extreme knock and auto-ignition. These images were recorded simultaneously with pressure data recording in the LUPOE 2D boosted engine at fixed operation conditions .

7.2.1 End gas self-ignition

Sequential frames from a natural light high speed camera, see Chapter 4 for description, set at 10,000 frames per seconds, are presented in Figure 7.3 for a typical slight knock cycle, The optical LUPOE 2D engine was operated near the knock boundary and close to the knock-free region as shown in Figure 7.2. The engine would be stopped immediately after the extreme knock was detected. The operational conditions chosen were determined as follows. The engine speed was set at 750 rpm and the intake temperature was kept at 323K, while the equivalence ratio was 1. The spark timing was set at 2^o bTDC, and the initial boost pressure was 2.0 bar. Iso-octane was used as fuel.

A large autoigntion site can be discerned quite clearly in the image 6 at around six o'clock position in Figure 7.3; it occurred at the late stage of combustion process, where a small volume of unburnt mixture was left in a high pressure and temperature environment. A second autoignition site can be observed at the left hand side of this image with a negative curvature of the regular flame front ahead of it. In the next image, these autoignition sites grew larger, and the local movement of main flame in front of these sites became slow compared to the other directions. In the next two milliseconds, the rest of the end gas was engulfed, usually this process happened in only 1^o CA interval.

From the pressure trace shown in Figure 7.4, there was a little acceleration of the pressure rise, after the onset of autoignition at point 6. The mild pressure oscillations arise not at the moment of the autoignition, but several milliseconds later at point 8.

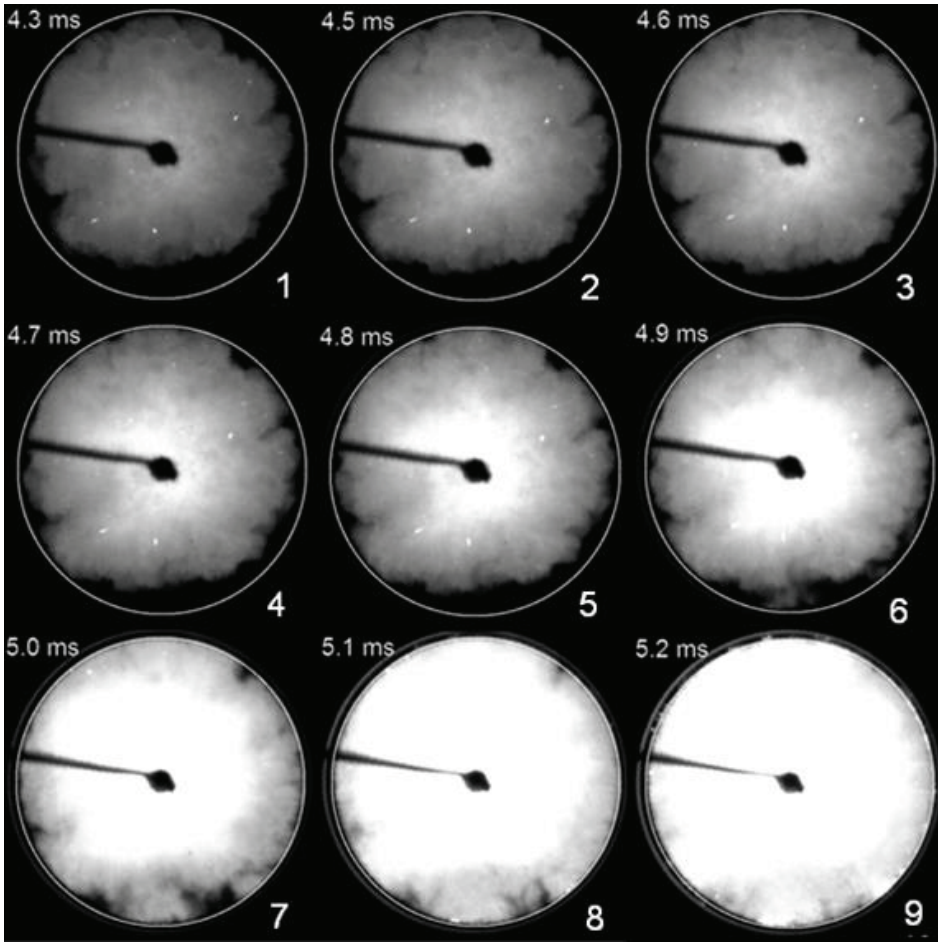

Figure 7.3: End gas self-ignition, the operating condition and the corresponding pressure trace can be seen in the Figure 7.4. The times shown are the time elapsed from the spark discharge.

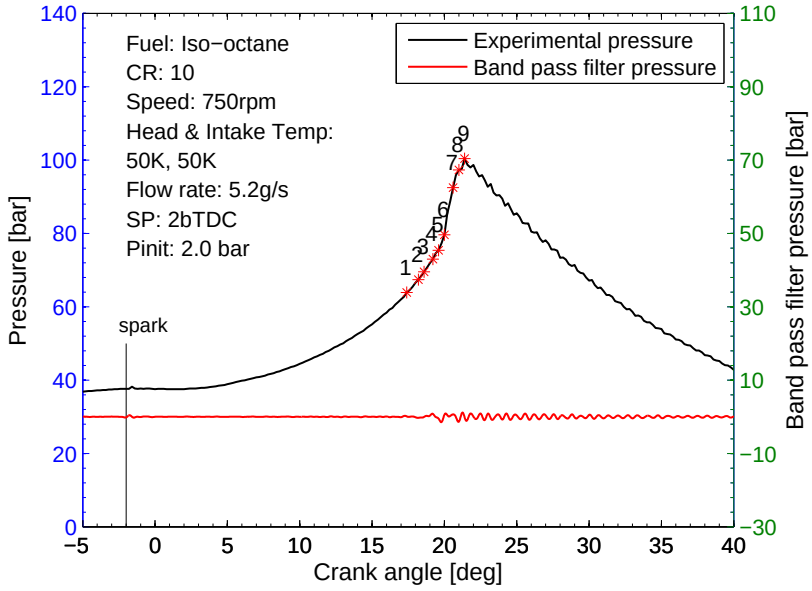

Figure 7.4: Pressure trace of a self-ignition cycle in Figure 7.3, the number of the images in Figure 7.3 are shown next to the pressure points at which the images were taken.

The self-ignition of the end gas produces slight knock and ensuing pressure oscillations which are relatively small. Occasionally, the knock phenomena may not happen, and the engine might benefit from the rapid heat release from self-ignition. This kind of knock has been widely observed in engine knock experiments in naturally aspirated engines (Konig and Sheppard [1990]; Pan and Sheppard [1994]), it also exists at current strongly boosted engine conditions. The autoignition delay time of the fuel, and the inhomogeneous pressure and temperature environment in the unburnt end gas are believed to be the main factors which influence the onset of self-ignition. The weak knock intensity may be related to only a small volume of unburnt mixture resided in the engine cylinder after autoignition onset.

7.2.2 Extreme knock

With the rise of the initial boosted pressure at low speed in a supercharged engine, besides the slight knock phenomena induced by the end gas self-ignition, a sporadic extreme knock has been observed at the same engine operation conditions. The maximum amplitude of this kind of knock pressure tends to be extremely high compared to the knock combustion pressure in a naturally aspirated engine. Previous research has found that extreme knock usually accompanied the pre-ignition in the modern supercharged engine (Zahdeh et al. [2011]). However, an extreme knock could also occur after regular spark ignition, especially for very advanced spark timing.

Figure 7.5 represents a sequence of images of an extreme knock cycle captured with camera speed 10,000 fps, captured are about 300 firing cycles at identical conditions. The operation conditions of the engine presented in Figure 7.6, essentially the same conditions as the self-ignition experiment described in Section 7.2.1: the engine speed was 750 rpm, spark timing was 2^o bTDC, and the initial pressure was 2.0 bar. Iso-octane was used as fuel and mixed at equivalence ratio 1. A different behaviour of combustion in the end unburnt gas was observed during an extreme knock event. After first 2.5 msec elapsed since ignition, and while the main flame was very small, see frame 4 in Figure 7.5, there appeared a hot spot ahead of the flame, and at some small distance away from the wall. The autoignition kernel does not seem to be in a direct contact with the wall, therefore a surface ignition may be ruled out. At the onset of autoigniton, the volume of autoigniton flame tended to be equal with that of the main flame, only approximately 50% of the mixture of fuel and air has been burnt and the left part of mixture burnt after autoigniton happened in an interval of as little as 2^o crank angles. This contrasts strongly with the slight knock occurred at the same engine operating condition.

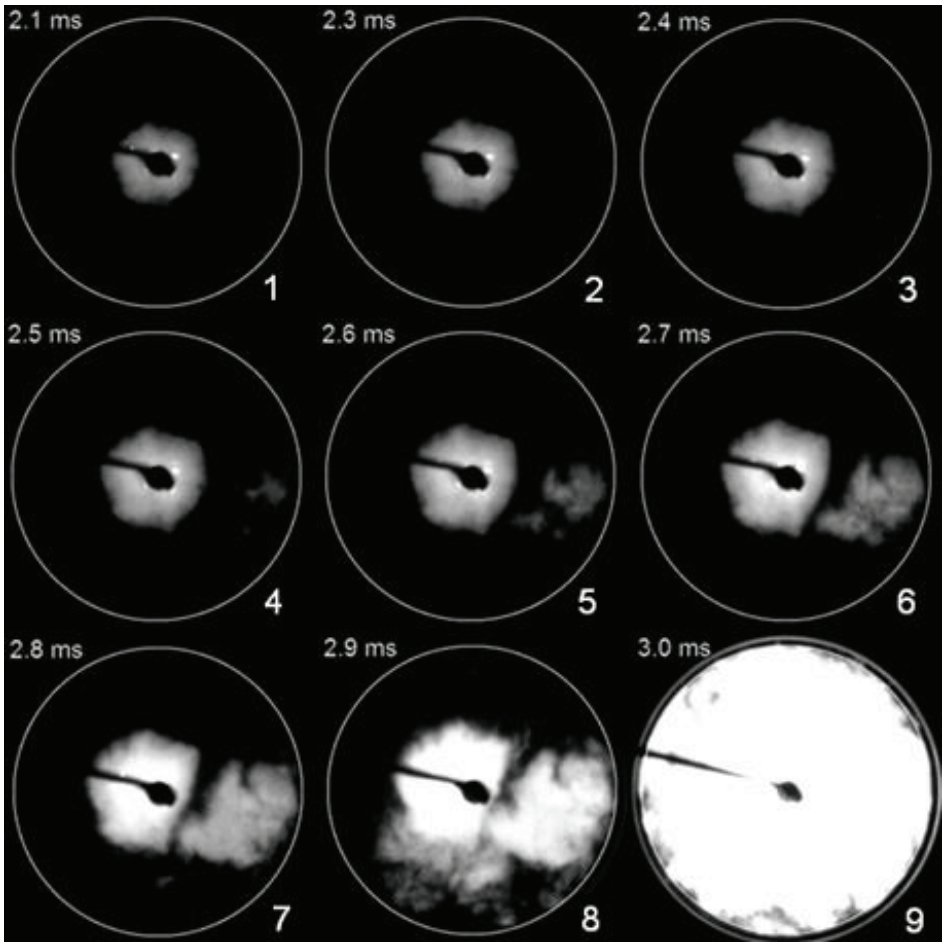

Figure 7.5: Extreme knock, the operating condition and the corresponding pressure trace can be seen in the Figure 7.6. The times shown are the time elapsed from the spark discharge.

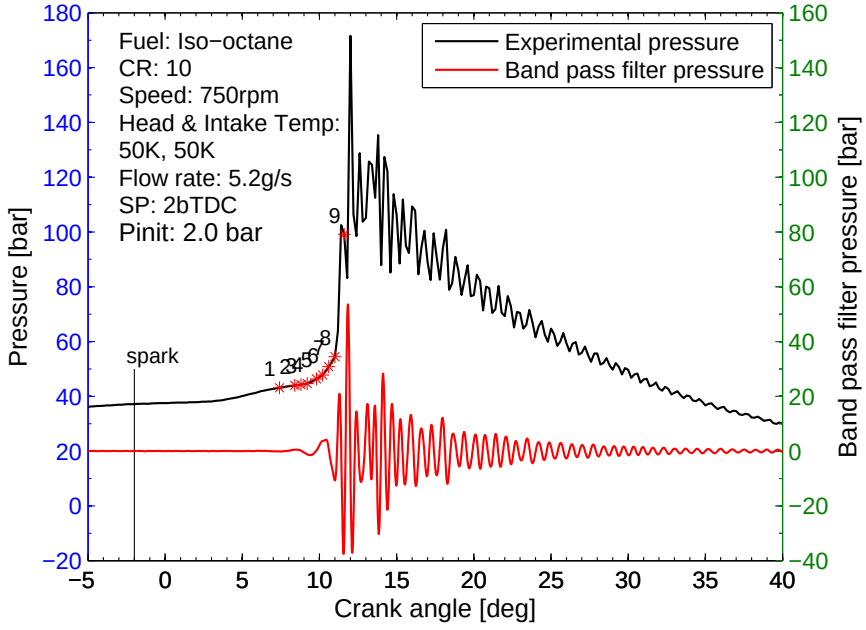

Figure 7.6: Pressure trace of an extreme knock cycle in Figure 7.5, the number of the images in Figure 7.5 are shown next to the pressure points at which the images were taken.

Subsequently, it generated a second fast growing flame pushing the main flame backwards, cf. frames 6-9 in Figure 7.5. No pressure oscillations could be discerned neither at the instant of the auto-ignition nor the subsequent flame propagation. In the frame 8, the flame originated from autoigniton interacted with the main flame, and a secondary self-ignition of the end gas can be seen clearly in the areas at 7-8 o'clock in this frame, resulting in a fast rapid heat released and a pressure increasing. As a consequence, a first pressure peak was generated in the point 9 in Figure 7.6. Then strong pressure waves travelled across the engine cylinder, leading to pressure oscillations in the chamber. It should be noted that the second peak pressure has a much higher oscillation amplitude than the first one after 0.4^o CA (0.9 ms). The maximum amplitude of the pressure oscillation can reach 100 bar. It may be in the form of a detonation-like wave, which is the most dangerous hazard for an engine (Rudloff et al. [2013]). The following image frames were extremely bright so that nothing could have been observed. The light was emitted by strong heat release and soot formation throughout the entire chamber area.

The filming speed 10,000 fps (10 thousand frames per second) proved barely adequate for autoignition centre development. Presented in Figure 7.7 is another extreme knock cycle recorded at a faster imaging speed 25 kfps, with CH* chemiluminescence technique, i.e. with 430 nm interference filter. The engine was operated under the same conditions as the above cases, and listed in Figure 7.8. Compared to the first extreme cycle, this extreme knock has lower peak pressure, about 130 bar, however the maximum amplitude of pressure oscillation of both cycles are similar. By using the CH* chemiluminescence technique, the reaction front could be discriminated well, the bright multi-autoignition centres appears in the image 5, i.e. 2.68 ms after spark ignition, which is about 0.2 ms later than the first extreme knock cycle. The unburnt mixture might generate more autoignition events due to local temperature imhomogenity and pressure waves induced by the initial autoignition event. Compared to the ignited flame, luminescence intensities of the autoignition centres are higher, thus indicating a stronger heat release. These autogintion centres occurred between the engine walls and flame front, then expanded toward different directions merging with neighbouring centres. Thereafter, from Figure 2.7, it is clearly seen that the reaction front, indicated by bright CH* emission, propagates along a ring encircling the main flame front and the wall. This development process might contribute to two effects: the reaction front propagation of auto-ignition, and subsequently continuing autoignitions occurring in front of the reaction front. Essentially, the auto-ignition induced a reaction front propagation as a second "flame". At the same time, new autoignition centres continue to appear in the unburnt gas see e.g. image 13 in Figure 7.7, until they covered all the end-gas region. During this process, the main flame seems to be virtually frozen and there is a clear boundary between ignited

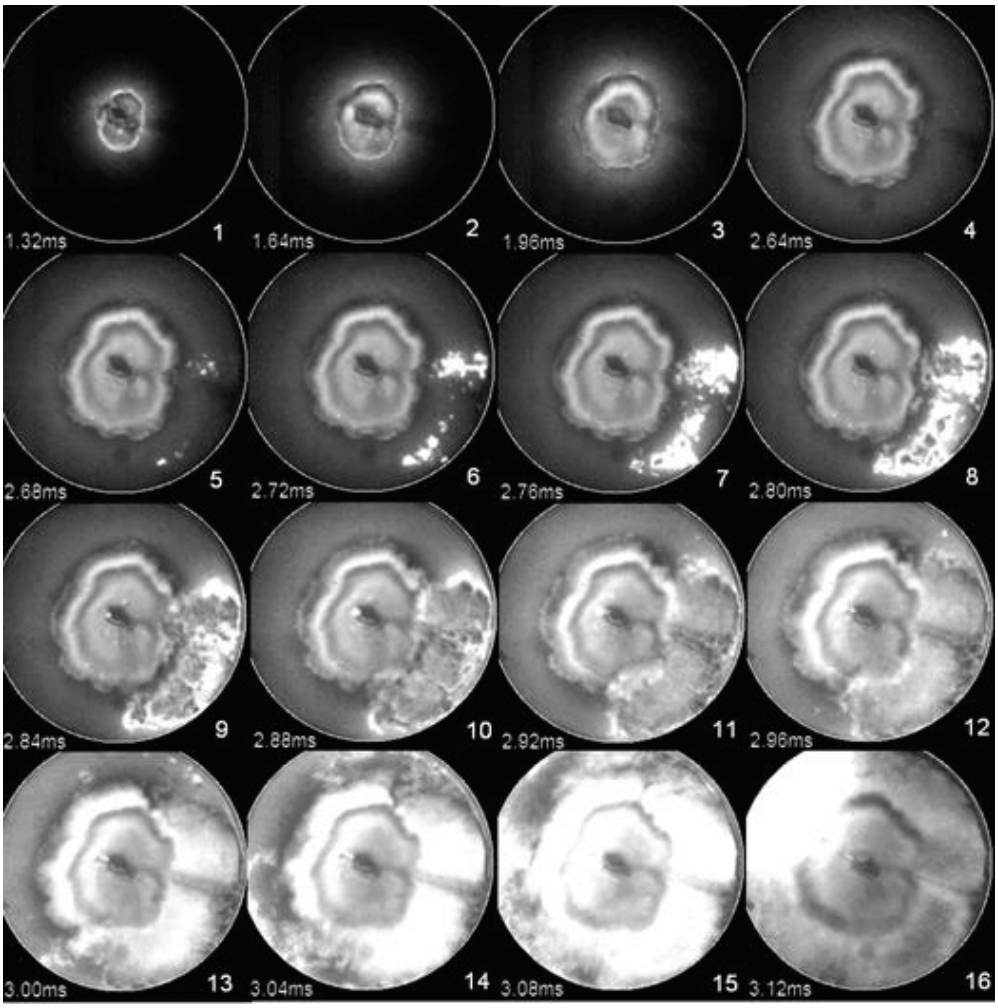

Figure 7.7: An extreme knock with high speed imaging 25 kfps. The operating condition and the corresponding pressure trace can be seen in the Figure 7.8. The times shown are the time elapsed from the spark discharge.

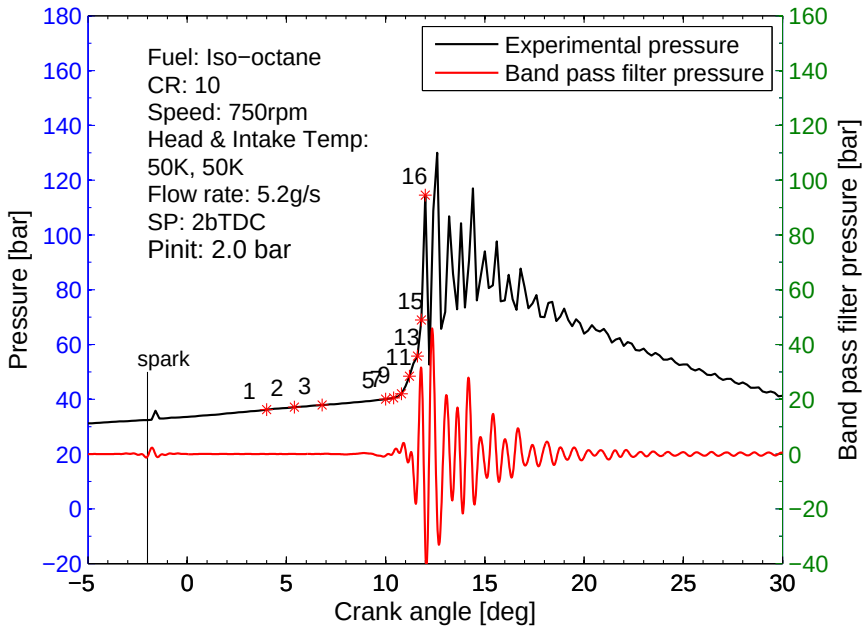

Figure 7.8: Pressure trace of an extreme knock cycle in Figure 7.7, the number of the images in Figure 7.7 are shown next to the pressure points at which the images were taken.

flame and autoignition flame. The pressure increases smoothly without any oscillation until image 16, where a peak pressure was achieved with an approximate 50 bar difference compared to the pressure at image 15. A bright region was generated around the 10 o'clock direction where the autoignition reaction fronts from the two sides around the ignited flame met. In the same way as the first extreme knock, the maximum pressure of the cycle happened after the first peak pressure. That may indicate a more rapid consumption of the end gas after image 15, because the autoignition might continue reacting with a relatively large volume of unburnt gas in front of the main flame.

Even with this high imaging speed, it is still not clear whether the strong pressure increase in a short interval time was caused by the detonation or not. However, these images provided some clues that detonation might be created when autoignition centres developed as a "flame" after a long distance travel around the circumference of the chamber, and generated a second ignition by interference of the new autoignition sites. The autoignition in extreme knock cycles may happen in several stages. At the initial stage, the autoignition was generated near the wall, then it developed with self-propagation or merging of more autoignition centres with the space restriction of ignited flame and wall. During this period, no pressure oscillation was detected. New autoignition may appear far from the first autoignition developed "flame". Once this "flame" passed these new autoignition sites, the visible regions were covered immediately, and a peak pressure was generated at the same time. The reaction still continued to generate a second peak pressure, which might be higher than the first one. Once there is a fast strong pressure pulse, as seen in Figure 7.8 between the images 15 and 16, the derivation of the burning rate from the pressure becomes impossible because of an extremely fast rate of heat release, equally the imaging is of little help because the unburnt gas region is hidden from the view by the bright glow.

7.2.3 Abnormal combustion in a skip-fired cycle

An autoignition cycle accidentally recorded in a skip-fired cycle provided an opportunity to observe the autoignition kernel development process much more clearly. The images and the pressure history of this event are shown in Figure 7.9 and 7.10. The engine operating conditions were exactly the same as for the previous cycle, engine speed was 750 rpm, initial pressure was 2.0 bar, engine head and intake temperature set at 323 K. The imaging acquisition system is for CH* chemiluminescence with a filming rate of 25 kfps.

The first autoignition center could just be observed in the first frame image close to the wall. Then more self-ignition centres appear in images 2-4 and become more appar-

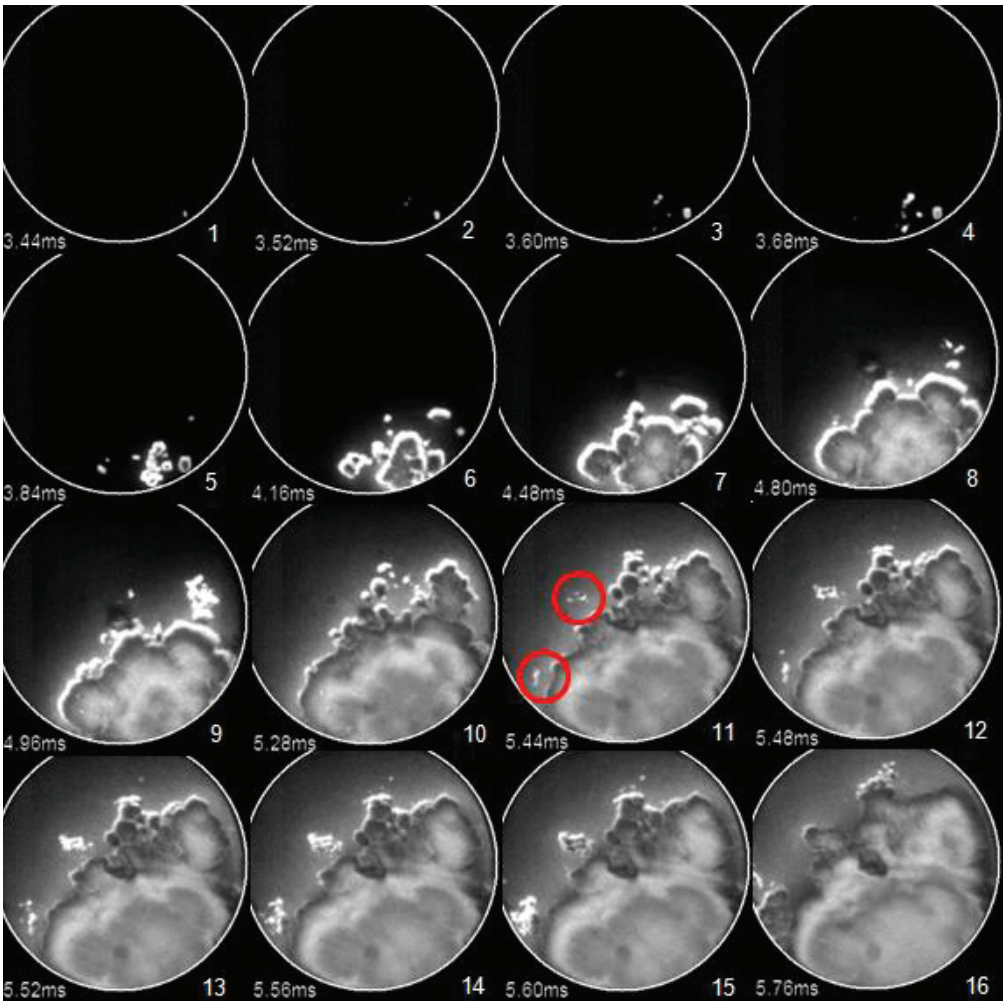

Figure 7.9: Autoignition process captured in a misfire cycle. The operating condition and the corresponding pressure trace can be seen in the Figure 7.10. The times shown are the time elapsed from the spark discharge. The red circles indicate the onset moment of two autoignition sites.

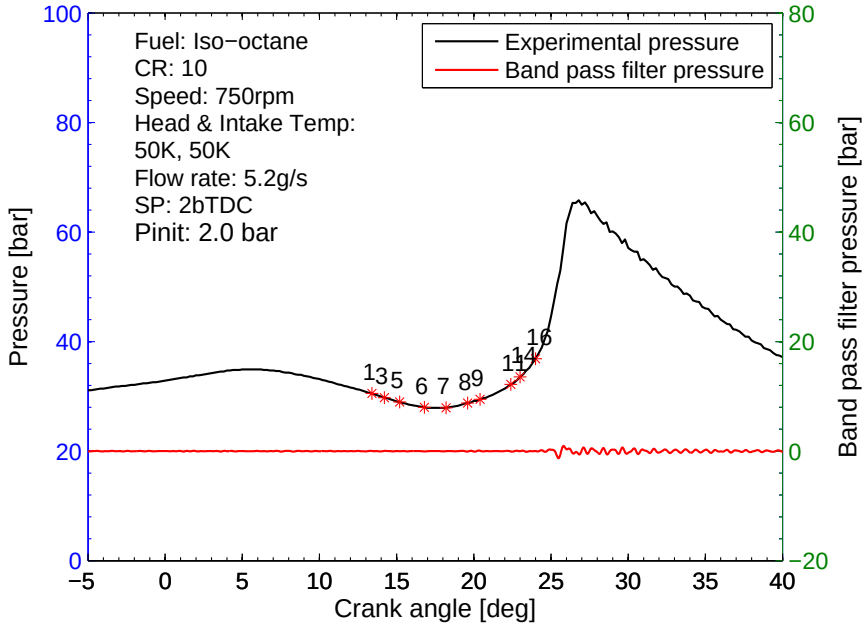

Figure 7.10: Pressure trace of an autoignition cycle in Figure 7.9, the number of the images in Figure 7.9 are shown next to the pressure points at which the images were taken.

ent in the vicinity of the first one. They are bright and associated with rapid consumption of the unburnt gas. After these autoignition sites merged together, they form a propagating flame front, indicated by CH* luminescence. Flame propagation is accompanied by appearance of new self-ignition centres ahead of it. A process of autoignition geneated in front of the "flame front" can be observed in the sequence of images 11 to 14: the shape of one close to the wall was affected by the compression of the burnt gas, while the one in the center area of chamber developed more freely, later they are engulfed by the flame. In the following frame, the whole end gas is engulfed by the flame, and no pressure oscillation was detected in this cycle. In a sense, this sequence is very similar to HCCI combustion with an important distinction that the charge is stoichiometric without dilution.

7.3 Knock onset and intensity

Knock onset and intensity are usually the two main parameters to characterize the knock properties (Heywood [1988]). From previous knock images, the knock onset can be further discriminated as an autoignition onset, where the autoignition sites appear and only cause a slight pressure increase. Yet, the knock onset is usually the starting point of strong pressure oscillations, at which the autoignition sites have been developed across the entire cylinder in the visible image. The pressure trace of the extreme knock shown in Section 7.2 is selected here to illustrate the definitions of autoignition and knock onset in this study. The knock cycle pressure trace was separated into a low band pass part and a high pass part firstly as shown in Figure 7.11. The high band pass filtered pressure represents the pressure oscillations induced by knock; the signal shown in Figure 7.11 corresponds to the cut-off frequency bandwidth of 2.5-12 kHz. Some weak oscillations can be observed after the autoignition sites appear before the detected knock onset, and then the amplitude of pressure increases progressively until knock occurs. At the knock onset time, the amplitude of pressure increased steeply and then reached a peak value in a short time. After this, the amplitude of the pressure decreased and the oscillations lasted for few milliseconds, slowly decaying.

A threshold value was adopted to determine the autoignition onset, that is the filtered pressure oscillations were scanned until a certain threshold value was exceeded (Worret et al. [2002]). The threshold was usually set below the maximum amplitude of the knock-related oscillations and above that of the noise signals. However, a universal threshold setting for all engine operation conditions does not exist. Even for the same operation condition, it was found that decreasing the threshold leads to mark incor-

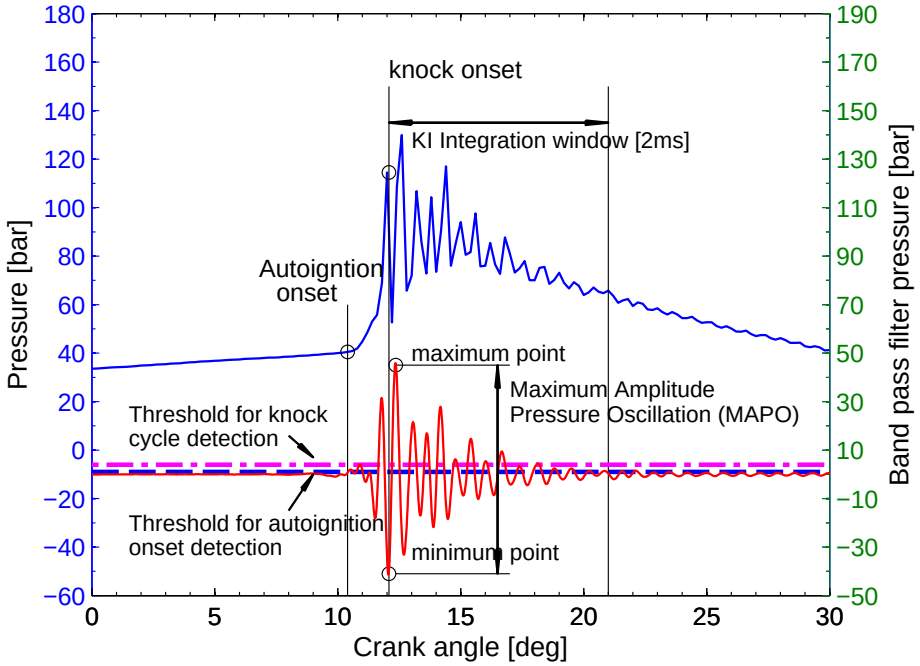

Figure 7.11: Illustration of the definitions of knock parameters.

rectly some non-knocking cycles as knocking because of larger noise, whilst increasing the threshold excluded some slightly knocking cycles; it also produced late onset in some heavy knock cycles (Mittal et al. [2007]). In order to overcome this problem, a second threshold was used to determine a cycle to be a knock cycle or a non-knock cycle. As observed in Figure 7.11, a knock cycle has a maximum oscillation point, which is significantly larger than the noise signal. By setting a threshold lower than the maximum oscillation point, the knock cycles could be selected. Then, the second threshold could be set at a lower value to determine the autoignition onset, where the pressure has a slight increase. The threshold values should be set by comparing the filtered pressure trace of non-knocking cycles with that of knocking cycles. The knock onset can be defined at the crank angle where is the last lowest oscillation pressure ahead of the peak point, at which the pressure commences to rise rapidly rather than reach an extremely high value. In the present study, the threshold for knock cycle detection was set at 1.0 bar, while the threshold for autoignition onset detection was 0.5 bar. Actually, it is not clear if any cycle that has autoignition without any pressure oscillation (lower than 1 bar) exists, because it was not observed in the imaging experiment, these cycles will be recognized as normal combustion cycles using this method if they really existed.

Detected autoigntion onset from images were compared with detected autoigntion onset from pressures for 7 knock cycle samples at two operating conditions, this is shown

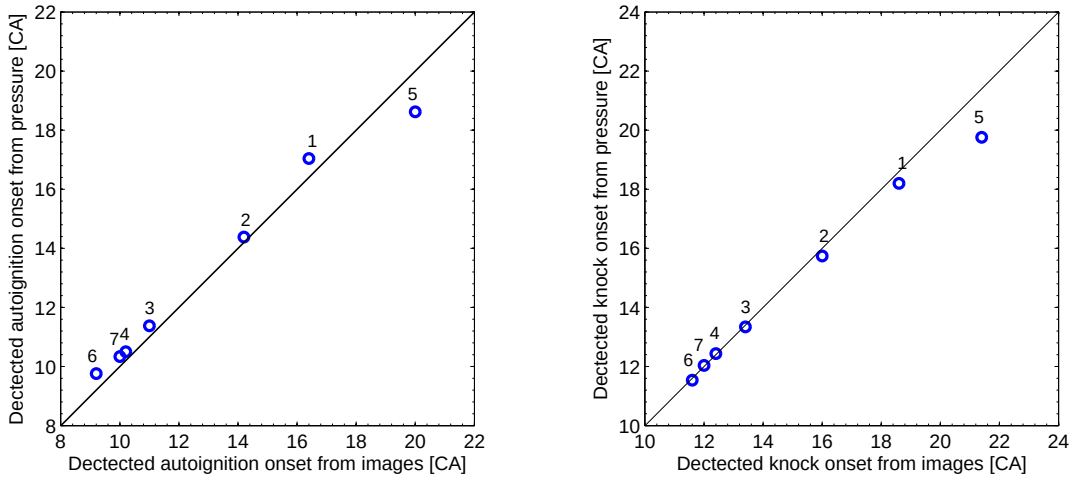

Figure 7.12: Comparison of (a) detected autoignition onset, and (b) knock onset from pressure and images. The cycles number 1 to 4 are from the PRF95 fuel experiment in Section 7.5, while the cycles number 5, 6 and 7 correspond to the cycles: self-ignition, and two extreme knock cycles described in Section 7.2.

in Figure 7.12 (a). The cycles numbers 1 to 4 are from the PRF95 fuel experiment, which will be presented in Section 7.5, while the cycles numbers 5, 6 and 7 corresponds to the cycles described in Section 7.2, these are self-ignition and "extreme knock" cycles. If the two methods correspond well, then all symbols would reside on the 1:1 slope line, which means that the autoignition onset can be perfectly detected by present threshold method to the nearest 0.2^o CA. The onset moment of autoignition was determined manually by observation of the knock images, the resolution depends on the imaging frame rate, i.e 0.1 ms at 10 kfps. It can be seen that the detected autoignition onset from pressure is slightly delayed compared to that from images. This is due to the minimum pressure change at the occurrence of autoignition sites, however the difference is smaller than 0.4 CA. By comparing the knock onset detected by pressure and imaging methods, the knock onset detected from two methods also is plotted in the Figure 7.12 (b). It was found that the symbols distribution along the 1:1 slope line with small errors. There is a good linear relationship between autoignition onset and knock onset, because the difference of interval time between autoignition onset and knock onset usually is smaller than 0.2^o degree, which is less than the resolution of the measurement. In order to compare the pressure and temperature at autoignition onset, in the following sections, autoignition onset will be adopted.

Knock intensity has been widely defined to characterize the knock severity of an individual knocking cycle. Two kinds of knock intensity parameters were evaluated here. The maximum amplitude of the pressure oscillation (MAPO) of the band pass filtered

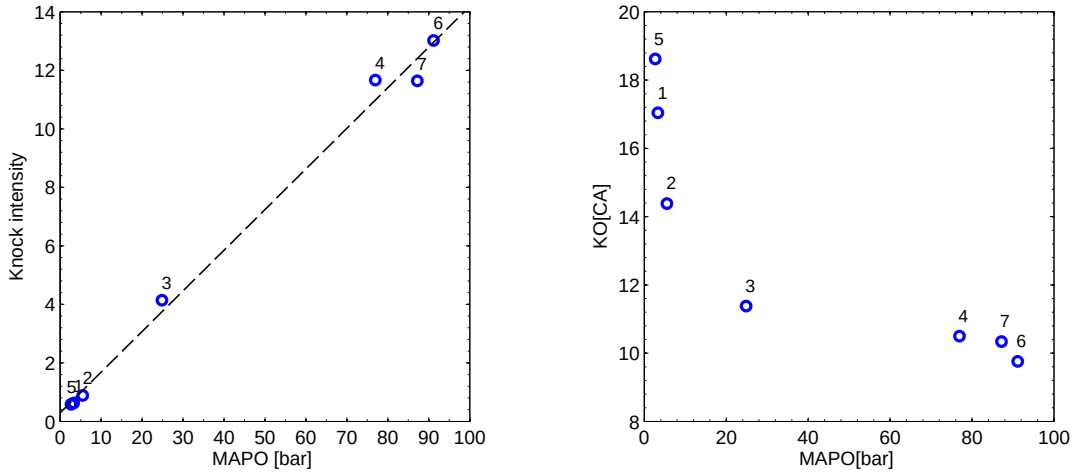

Figure 7.13: (a) Comparison of knock intensity and MAPO, (b) The relationship between knock onset and knock intensity of 7 sample cycles. The cycles number 1 to 4 are from the PRF95 fuel experiment in Section 7.5, while the cycles number 5,6 and 7 correspond to the cycles: self-ignition, two extreme knock cycles described in Section 7.2.

pressure, and another definition proposed in the previous Leeds work (Konig and Sheppard [1990]; Pan and Sheppard [1994]) can be expressed as:

$$KI = \sqrt{\frac{1}{N}\sum_{i=1}^{N}(P_i - P_{mean})^2} \tag{7.1}$$

Where KI is the calculated knock intensity, P_i is the instantaneous band-pass filtered pressure, P_{mean} is the mean value of band-pass filtered pressure, N is the number of samples collected during a period of 2 ms from the detected knock onset. A 2 ms period allowed time for approximately 10 reflections of a pressure wave travelling at typical combustion chamber at sonic velocities (Konig and Sheppard [1990]).

A comparison of these two methods is shown in Figure 7.13 (a), where a linear relationship can be observed. Actually, these two parameters show a similar characteristic of knock intensity, therefore only MAPO was adopted in the following analysis as an indication of knock intensity. A quick scan of knock onset and knock intensity was plotted in the Figure 7.13 (b). There does not exist a linear relationship between these two values, because the knock intensity is also related to the development of autoignition after autoignition onset. The knock amplitude is very sensitive to the timing of autoignition and for the studied conditions, a change of the latter by 10^o CA results in a ten-fold increase of pressure oscillations intensity.

7.4 Influence of intake pressure on the knock characteristics

More knock cycles have been collected at the strongly charged LUPOE 2D boosted engine i.e. intake pressure of 2.1 bar, with engine metal head. Only the pressure signals have been recorded. The experiment was carried out at the engine speed of 750 rpm and spark timing was set at 2^o bTDC at the knock boundary, iso-octane was used as fuel. At the same operation condition, naturally aspirated (NA) LUPOE 2D engine knock experiments have been conducted by (Roberts [2010]), the spark timing was 15^o bTDC was the knock boundary for naturally aspirated engine conditions. This section will compare the characteristics of knock properties under these two different engine inlet initial pressures by using autoignition onset and knock intensity defined in the previous section. The raw pressure data of these two conditions are shown in Figure 7.14.

In order to study effects of the cycle-to-cycle variability on a single knock cycle, fast, medium and slow cycles, shown in Figure 7.14, were separated into three groups, depending on their rate of the combustion. The fast, medium and slow cycles are shown in red, blue and green, respectively in Figure 7.14. It can be clearly seen that for the NA operation, gas autoignition events cause only very mild pressure oscillations. At the same time, the cycle-to-cycle variability is much greater for the boosted operation; thus, the slow cycles seem to have no knock even though the autoignition may be discerned on a few slow cycles shown in green lines. Virtually every fast cycle ends in auto-ignition and many autoignition events lead to very violent pressure oscillations at the high inlet pressure combustion.

Figure 7.15 show scatter plots of maximum pressure as a function of the time at which it is achieved. For both NA and boosted operation there is an approximately linear proportionality between the crank angle at which the pressure reaches the maximum and the pressure magnitude. This is somewhat surprising as the adopted method of data processing includes cycles with knock, and the peak pressure in those are determined by the pressure oscillations. One could surmise that, if the knock, i.e. pressure oscillations, is caused by detonation, which is much faster than the normal turbulent flame propagation, it would produce much earlier timing of the maximum pressure, and this is clearly not the case, see Figure 7.15 (b). Another observation which can easily be derived from Figure 7.15 is that the cyclic variability increases with the initial pressure, peak pressure of extreme knock events could exceed the average value plus two standard deviations.

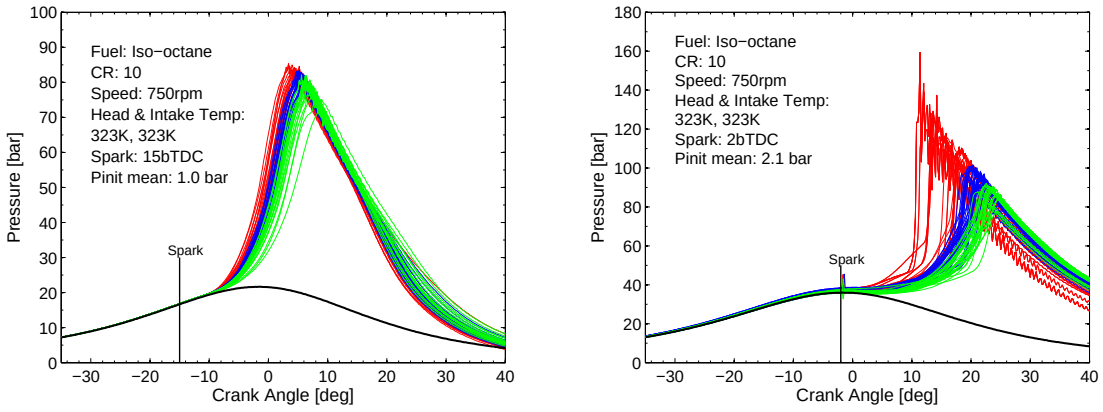

Figure 7.14: Knock pressure traces for the naturally aspirated (a) and charged (b) operation of LUPOE 2D. The fast cycles are shown in red, medium in blue and slow in green colors, respectively. "Pinit mean" means the inlet pressure.

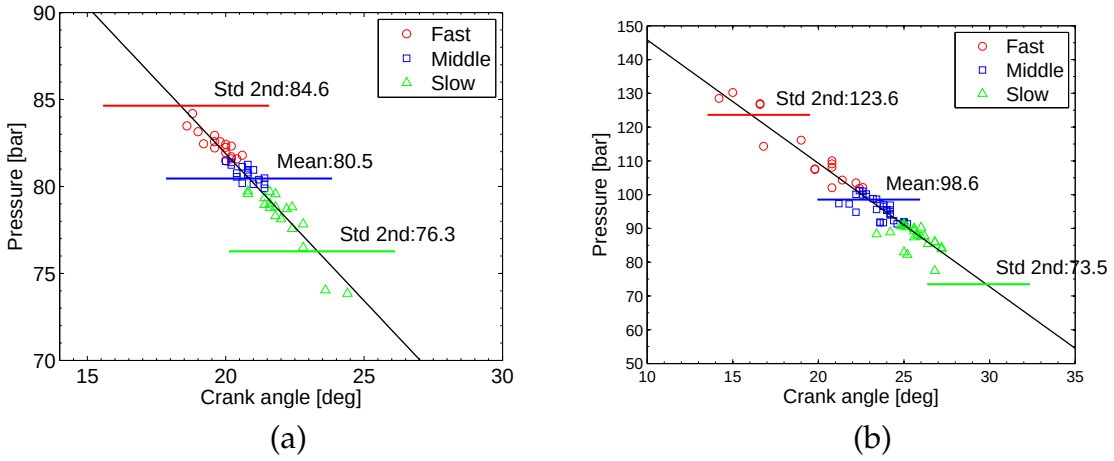

Figure 7.15: Maximum pressure as a function of the crank angle at which it is achieved for the naturally aspirated (a) and charged (b) operation of LUPOE 2D. "Std 2nd" means the two standard deviations.

Figure 7.16 and Figure 7.17 show autoignition onset and knock intensity distributions. For the NA condition, knock onset is distributed approximately normally about the mean value with a standard deviation of about 2 crank angle degrees. For the boosted condition, another peak distribution appears, which represents the extreme knock cycles, and the other is slight knock. The slight knock has a normal distribution, the extreme knock occurs earlier than slight knock, with higher corresponding knock intensity. By comparing NA to boosted cycles, the knock intensity of charged operation is much higher than that of NA. It could be described that, in the beginning of initial pressure increasing, the knock onset is advanced and results in higher knock intensity, when the initial pressure is increased extremely high, some extreme knock cycles occur with an early knock onset time and higher knock intensity, however, the possibility of occurrence

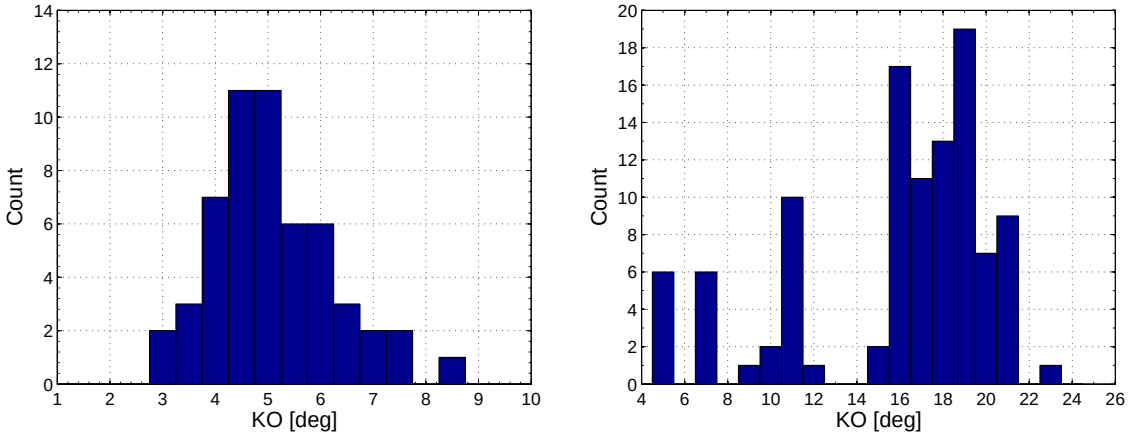

Figure 7.16: Knock onset distribution for the naturally aspirated (a) and charged (b) operation of LUPOE 2D engine. The operation parameters are listed in the Figure 7.14.

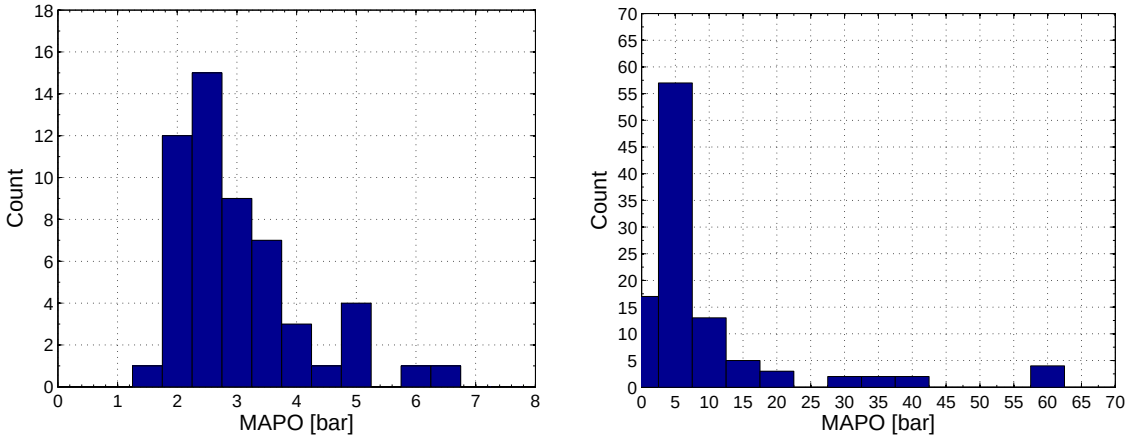

Figure 7.17: Knock intensity distribution for the naturally aspirated (a) and charged (b) operation of LUPOE 2D engine. The operation parameters are listed in the Figure 7.14.

of these extreme knock cycle is low and the other knock cycles in the same condition appear the similar property as the natural aspirated engine knocking.

Figure 7.18 shows the mass fraction burnt (mfb) at the moment of the autoignition onset (AO) versus knock intensity (MAPO) for the naturally aspirated and charged operation of LUPOE 2D engine. The unburnt mass fraction can be calculated from the heat release history of combustion pressure trace using LUSIEDA. With an increase of the intake pressure, the density of the air-fuel mixture in the cylinder also increases, therefore, at the same value of AO, the supercharged engine has more unburnt mass in the cylinder. It is natural to suppose that the larger amount of the end-gas available for the rapid self-ignition would result in larger pressure fluctuations. It can be seen that at the

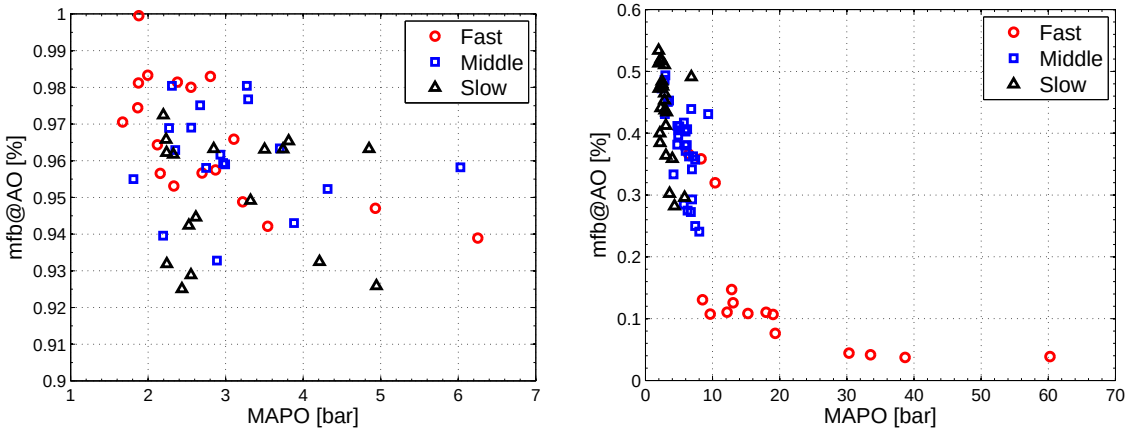

Figure 7.18: Autoignition onset versus knock intensity (MAPO) for the naturally aspirated (a) and charged (b) operation of LUPOE 2D engine. The operation parameters are listed in the Figure 7.14.

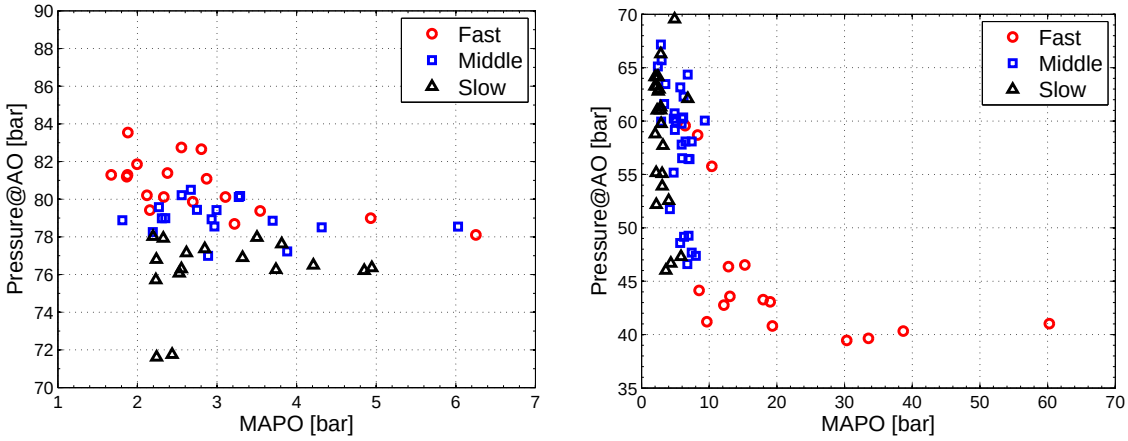

Figure 7.19: Pressure at the moment of autoignition onset versus knock intensity (MAPO) for the naturally aspirated (a) and charged (b) operation of LUPOE 2D engine. The operation parameters are listed in the Figure 7.14.

boosted operation while the more violent knock in fast cycles does tend to happen at the low mass fraction burnt. However, a low proportion of the burnt gas does not necessarily result in more violent knock. The difference in mfb in Figure 7.18 is huge; at the atmospheric intake pressure, it is never below 90%, at the charged operation it is never above 60%.

It can be inferred from Figure 7.18 that the amplitude of the knock arising at the strongly boosted operation has a strong dependency upon the mass of the end gas available for the self-ignition. While the end-gas self-ignition at the NA operation consumes no more than 8% of the total charge mass, at the boosted conditions the strongest knock, with MAPO of more than 10 bar occurs when less than half the charge is burnt in the

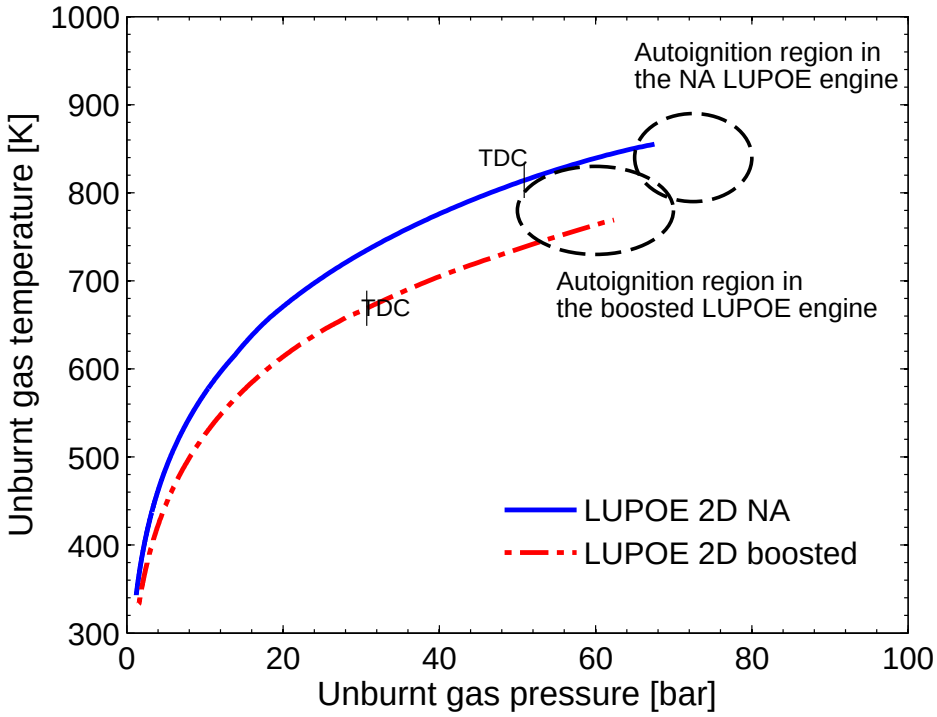

Figure 7.20: The pressure and temperature history of the end gas for the naturally aspirated (NA) and the boosted LUPOE 2D engines with the potential autoignition regions. The reverse cycle software LUSIEDA was used to predict the unburnt gas temperatures based on experimentally gathered cylinder pressure data.

main combustion event. The higher end gas pressure and temperature, the higher is the possibility of end gas autoignition. In the applied engine modelling it is sometimes assumed that knock will occur if the pressure reaches some threshold value. Figure 7.19 shows influence of the pressure at the moment of knock onset on the knock intensity. It is clear that, with charged operation, the extreme knock events happen at relatively low pressures. Unexpectedly, some cycles develop knock at pressures lower than for NA operation. It is perhaps reasonable to assume that the auto-ignition events at the lowest pressures correspond to the smallest flame advance, hence the largest proportion of the total charge energy is available to sustain the knock. Therefore, counter-intuitively, the conditions for the extreme knock, even though it arises at the elevated intake pressures, are associated with processes at fairly low end-gas temperatures and pressures, see Figure 7.19.

The mean unburnt gas temperature and pressure histories in the naturally aspirated (NA) and boosted LUPOE 2D engine have been calculated using the reverse thermodynamic engine software LUSIEDA and are shown in Figure 7.20. Only a minor variation of the intake temperature existed between the NA and boosted operation. The

calculated results show the temperature of the boosted LUPOE 2D engine is lower than that of the NA engine at the TDC position and the potential autoignition region. However, the spark timing of the boosted engine is closer to TDC than that of NA engine, thus the difference of the temperature at the spark timing is not large for two conditions. This implied that extreme knock occurrence may be not governed by auto-igniton of unburnt end gas, which is sensitive to the pressure and temperature. Since there does not exist valves or spray injection deposits in the LUPOE 2D engine, the lubrication oil released from piston crevice could be a potential reason for the extreme knock.

7.5 Comparison of self-ignition and extreme knock

Several knock cycles selected from the same boosted condition will be used for a further study on the difference between self-ignition and extreme knock. Although the number of knock cycles with image recording is too small to derive reliable statistical results, an attempt at establishing a relationship of knock development process with knock intensity could still be undertaken. Here, knock cycles with different knock intensities are analyzed, the engine was operated at 750 rpm, and fuelled with a mixture of 95% iso-octane and 5% n-heptane by volume (PRF95). Due to the short ignition delay time of PRF95, at the same spark timing, the knock boundary occurred at a lower initial pressure of 1.8 bar compared to iso-octane at the spark timing 2^o bTDC. Four knock cycles are selected, representing a transition from a slight knock to an extreme knock. The pressure traces and filtered pressure oscillations are compared in Figure 7.21 and Figure 7.22.

It can be seen that there existed a small pressure deviation at spark timing; the cycle 1 has the lowest pressure at that moment, and it also shows the lowest rate of combustion and a weakest barely detectable knock. Cycle 3 has much smaller pressure at the spark timing and, yet, it shows very similar fast burning rate and onset of knock to the cycle 4 which has the highest pressure at the spark instance. Cycle 2 and 4 have the same ignition pressure but the subsequent combustion is very different. The autoignition onsets detected from the images are marked in the pressure traces, with the advance of autoigniton onset time, the peak pressure raised and the pressure oscillation become more violent. The amplitude of pressure oscillation can be seen in Figure 7.22, which clearly show a gradually increase of the magnitude of the pressure oscillations.

These pressure traces were transformed into the frequency domain by using Fast Fourier Transform (FFT) in Matlab. The FFT results are plotted in Figure 7.23. Generally, the position of the maximum frequency does not change much with the knock intensity

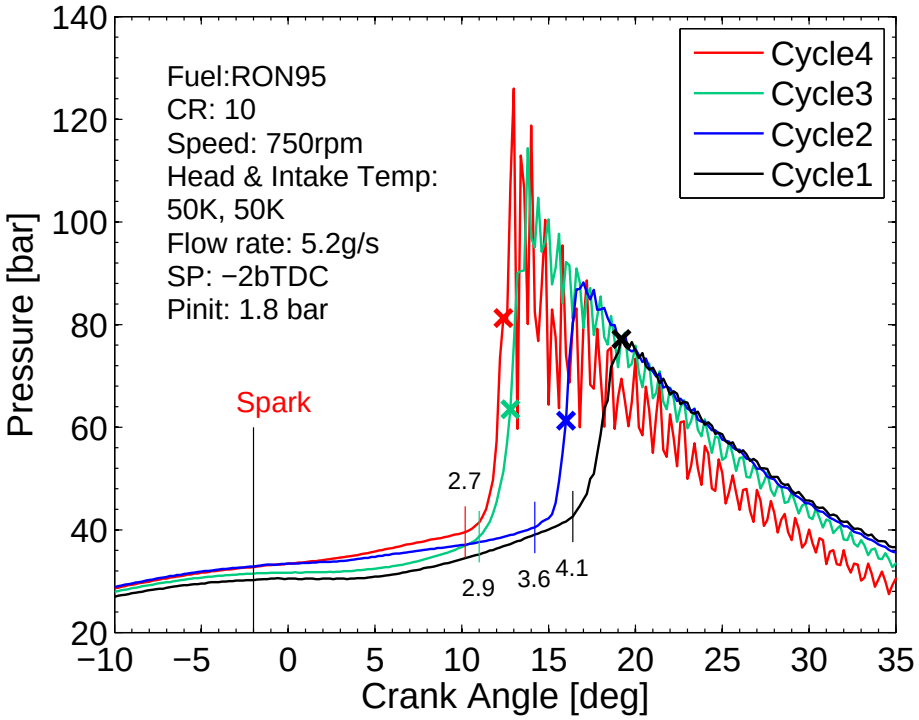

Figure 7.21: Pressure traces of four different knock intensity cycles selected from the same engine operation condition, in the LUPOE 2D boosted engine running at a speed of 750 rpm and a spark timing 2^o bTDC, stoichiometric PRF95 fuel. The numbers are time (ms) of the autoignition onset after ignition.

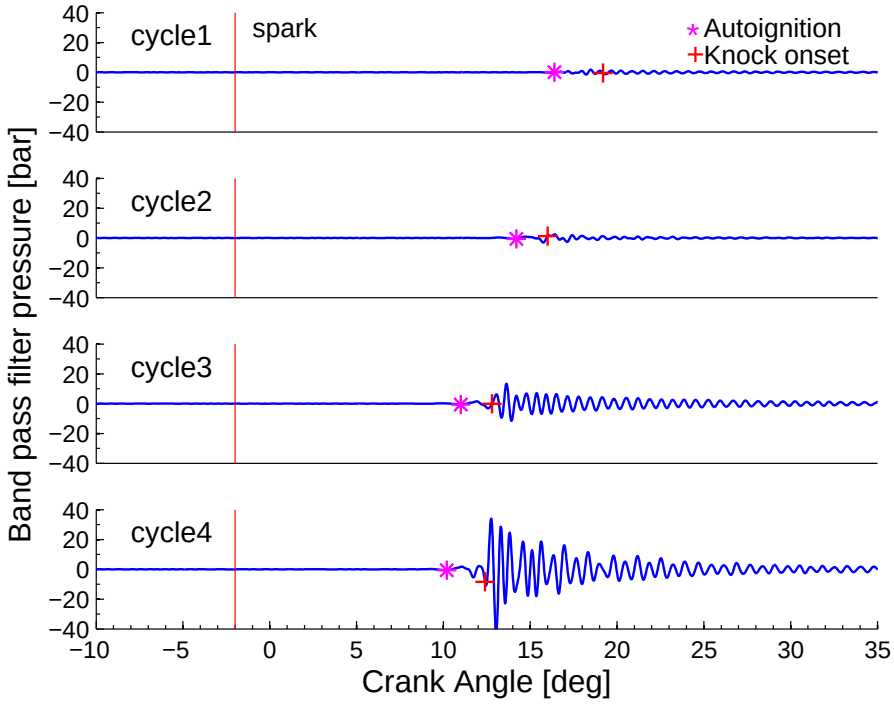

Figure 7.22: Band pass filter pressure traces of four different knock intensity cycles selected from the same engine operation condition, in the LUPOE 2D boosted engine running at a speed of 750 rpm and a spark timing 2^o bTDC, stoichiometric PRF95 fuel.

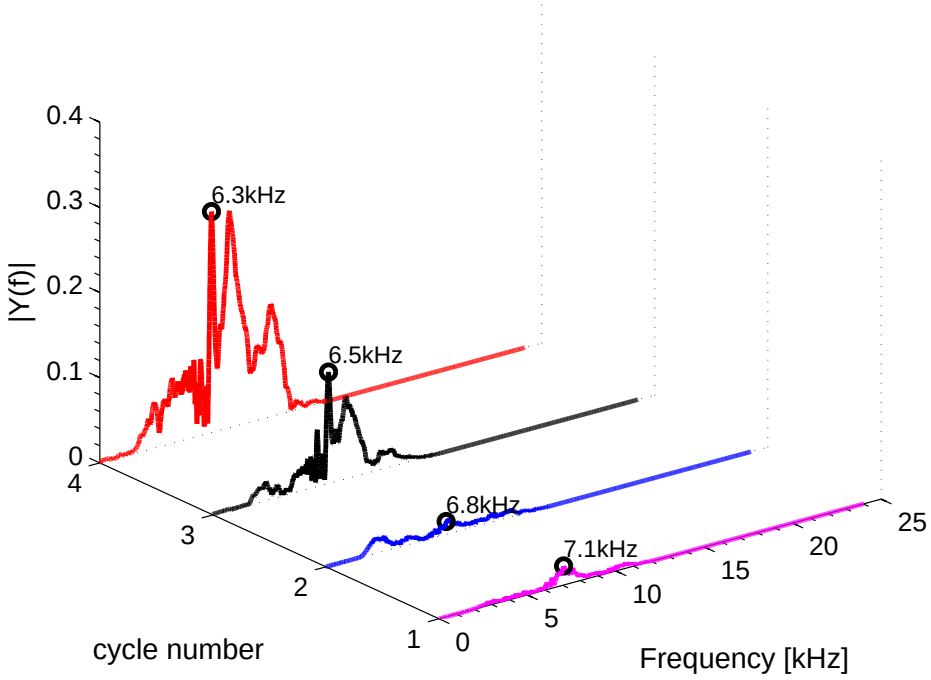

Figure 7.23: FFT transform of four different knock intensity cycles selected from the same engine operation condition, in the LUPOE 2D boosted engine running at a speed of 750 rpm and a spark timing 2^o bTDC, stoichiometric PRF95 fuel.

increasing, and locates around 6.5 kHz, which is corresponding to a first approximation of the tangential and longitudinal mode frequencies of engine cylinder. With an increase of knock intensity, the frequency region tends to be wider and there are several small peak frequencies appearing. These small peak frequencies may become dominant with the knock intensity rise, see cycle 4. It may imply that more pressure waves travel across the cylinder, which were generated by several autoignition centres. The magnitudes of frequency of an extreme knock cycle are higher than that of a slight knock cycle.

The temperature and pressure histories of 4 cycles between spark ignition and autoignition onset were calculated by LUSIEDA and shown in Figure 7.24. It should be noted that these temperature values are considered as global mean values, and the local temperature may be higher or lower than these due to the temperature inhomogeneity in the cylinder. As shown in the pressure traces, there is a small difference of pressure at spark timing, which are mainly caused by cycle-to-cycle variability. The maximum differences of pressure and temperature between four cycles are about 1.7 bar and 9 K, when the cycle 1 and cycle 4 are compared. However, the temperature variance in the engine may exceed this difference, therefore it is not reliable to draw any conclusion using these four cycles here about the effects of pressure and temperature on autoignition onset.

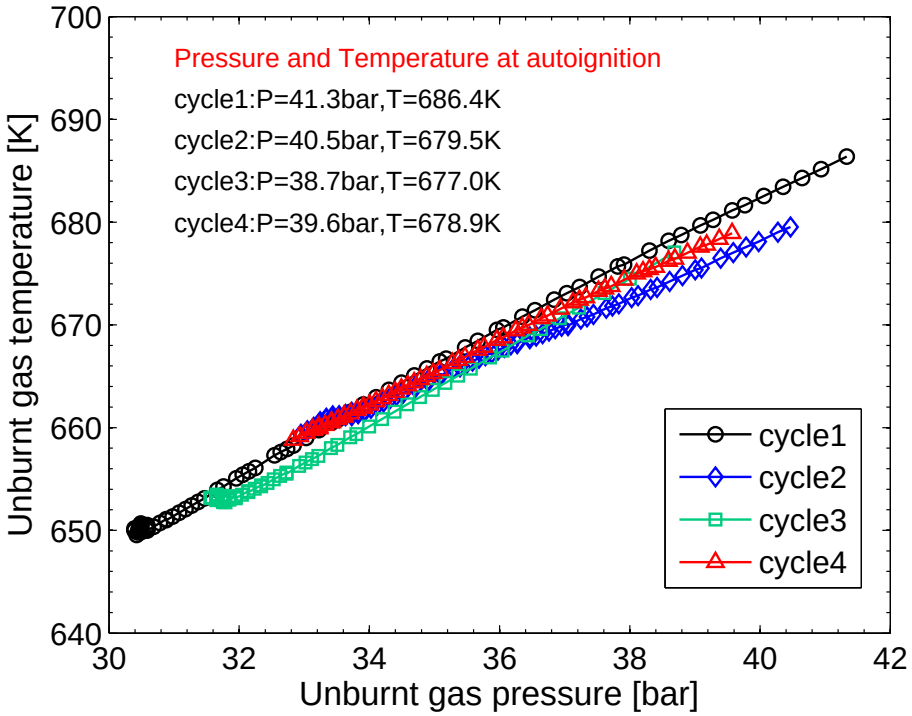

Figure 7.24: Temperature and pressure histories of four different knock intensity cycles selected from the same engine operation condition, in the LUPOE 2D boosted engine running at speed of 750 rpm and spark timing 2^o bTDC, stoichiometric PRF95 fuel.

The autoignition moment and the following 0.3 ms of images are shown in Figure 7.25. During the flame propagation, several bright spots were detected in the burnt gas, see cycle 1, image 2. These bright spots may be created by local fuel-rich combustion. All the autoignition sites occurred near the wall. For cycle 1, it appeared in the flame front, most close to the wall at 3-4 o'clock direction. Then, second autoignition happened in a flame cusp. Clearly, it is an end gas self-ignition knock, which only generated a slight pressure oscillation. The autoignition started at the flame front of cycle 2; later more autoigniton sites appeared around the flame. However, this autoignition did not cause a strong pressure oscillation, similarly to cycle 1, whilst this cycle achieved a higher peak pressure than that of cycle 1. This confirmed that the autoignition can release the heat energy rapidly without large pressure oscillations. Cycle 3 and cycle 4 have similar autoignition onset position and development process, with only about 0.1 ms difference between their autoignition onset times. However, the magnitude of pressure oscillation of cycle 4 is twice larger than that of cycle 3. There is a clear autoignition centre in the 6 o'clock direction in the image 4 of cycle 4. It is evident that the second autoignition, which is far from the first one, may trigger the strong reaction energy release and shock wave when the reaction front generated by the first autoignition passes it.

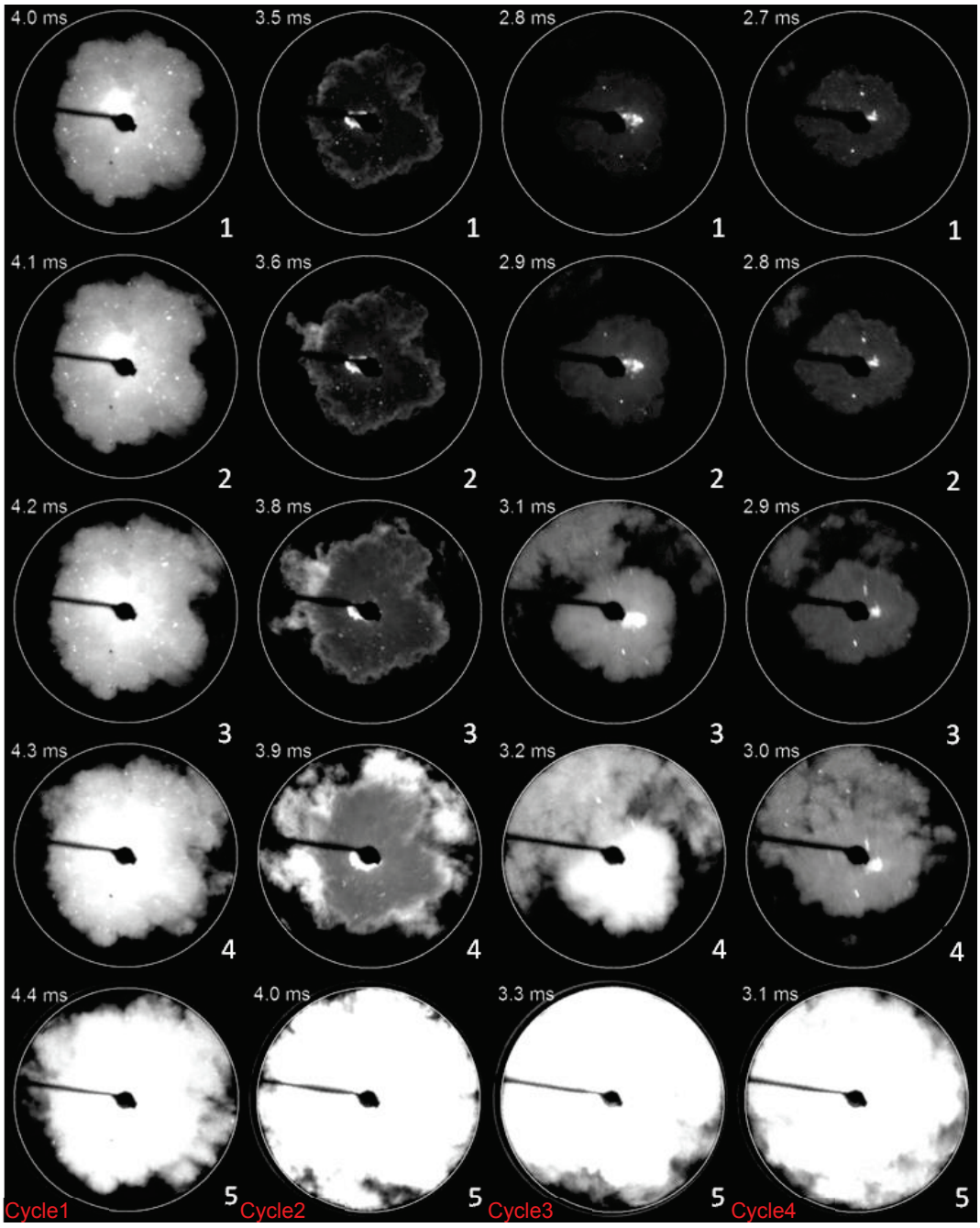

Figure 7.25: Images of autoignition development for four different knock intensity cycles selected from the same engine operation condition, in the LUPOE 2D boosted engine running at a speed of 750 rpm and a spark timing 2^o bTDC, stoichiometric PRF95 fuel. The cycle numbers are the same as shown in Figure 7.21.

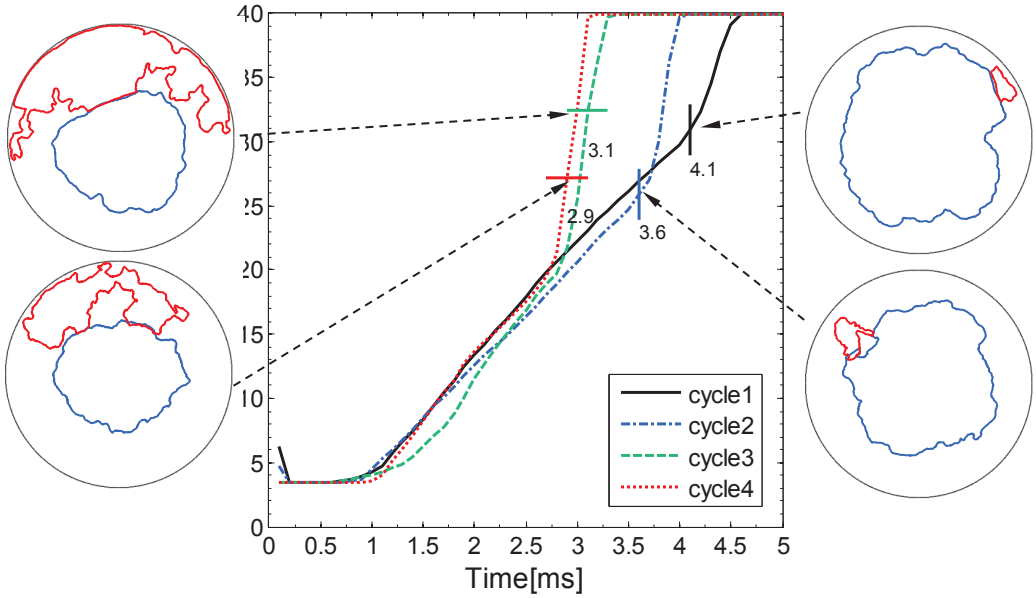

Figure 7.26: Flame radius development of four different knock intensity cycles selected from the same engine operation condition, in the LUPOE 2D boosted engine running at a speed of 750 rpm and a spark timing 2^o bTDC, with stoichiometric PRF95 fuel.

There was about 3^o-4^o CA difference of autoigniton occurrence time between the light knock and the extreme knock. Earlier autoignition usually means stronger knock. However, it should be noted that even a minimal earlier autoigniton occurrence could lead to a large difference in the pressure oscillation as e.g. see on the comparison of cycle 3 to cycle 4. On the other hand, a large different between two cycles' autoignition onset may result both in small pressure oscillations, if cycle 1 and cycle 2 were compared. Therefore, the knock intensity is not necessarily related to autoignition onset time. It is also governed by the autoignition development process. Earlier autoignition often indicates a larger unburnt space, as well as a longer time for autoignition propagation, hence it may easily develop into a "detonation" with a second autoignition. Although the camera did not capture any evidence to prove the existence of detonation, the strong oscillation pressure indicates that a strong reaction process exists. The huge magnitude of pressure oscillation may be not caused by the large unburnt gas heat release, it is likely that gas dynamics of autoignition play an important role for the pressure oscillation.

Flame speed before autoignition impeded the main flame propagation are compared in Figure 7.26, the flame radii were calculated from a circle which has the same area as the flame, once autoignition starts, the flame area also includes the autoignition. There are no significant differences between the four cycles, and actually the strongest knock and slight knock have almost the same flame radius development history, which indicates that the flame speed did not have a direct effect on the knock onset and inten-

sity under the same engine operation condition. The area of autoignition at the moment that the autognition contacted the ignited flame are also shown in Figure 7.26. It can be seen knock intensity is not related to autoignition area when it interacts with the flame.

A narrow horizontal section of image was taken from the full-bore image of extreme knock shown in Figure 7.5 in Section 7.2, to calculate the local flame propagation speed. A sequence of the local propagation of the spark-ignited flame and the autoignition is shown in Figure 7.27. The mean flame radius was measured to represent the flame position in each image, the blue line is derived main flame front, the red line is the autoignition reaction front, the yellow one is an extrapolation line to predict the flame position without autoigntion effect. Then, the speed of flame and autoignition was obtained in Figure 7.28. The detected maximum velocities of flame and autoignition were approximate 9 m/s and 60 m/s, respectively. Both velocities decreased when the autoignition flame approached the main flame. The camera frame rate is not fast enough to capture the initial stage of auto-ignition; however, the propagating velocity of it indicated that a detonative reaction could not occur before flame and autoignition interaction. Hence a detonation can be ruled out, at least during the early observed period.

The direct initiation of detonation can be due to inhomogeneities, according to the description of Zeldovich [1980], and this phenomena was observed by Pan and Sheppard [1994], and this may not be accurate to describe the extreme knock. The second possibility of detonation onset is a second ignition as a consequence of interaction between the autoignition generated "flame" and more autoignition sites in front of it, following a process that the pressure waves were reflected and focused by the cylinder wall. "The bidirectional coupling of heat release and pressure wave is established once the pressure wave is strong enough and the gas mixture is reactive enough", this detonation mechanism was described by Pöschl and Sattelmayer [2008] and be supported by the experimental data from a rapid compression and expansion machine. A reaction front travelling in the opposite direction to the original temperature gradient was observed at a speed up to v = 1400 m/s. A simulation of interaction between a shock and a flame in a channel has been done by Oran and Gamezo [2007]. Although the first purpose of this simulation can not be extrapolated to the conditions for the engine, the configuration of their simulation was similar to the current initial stages of extreme knock conditions. A deflagration-to-detonation transition (DDT) could occur after the energy release accelerated due to the increased surface of the flame and the increased temperature behind the strong reflected shock. However, it is not yet clear whether flame to flame interactions can lead to DDT in any realistic situations; at least none could have been observed in the experiments presented here.

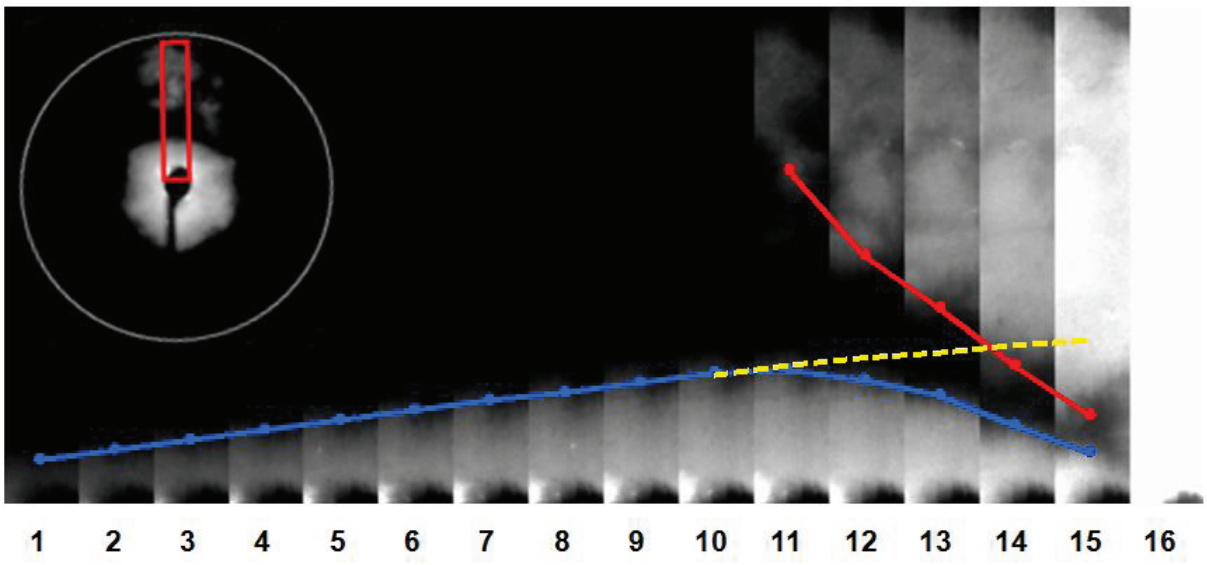

Figure 7.27: A narrow horizontal section taken from the full-bore image for derivation of flame displacement speed under extreme knock case shown in Figure 7.5, the blue line is derived ignited flame front, the red line is the autoignition reaction front, the yellow line is an extrapolation line to predict the flame position without autoigntion effect.

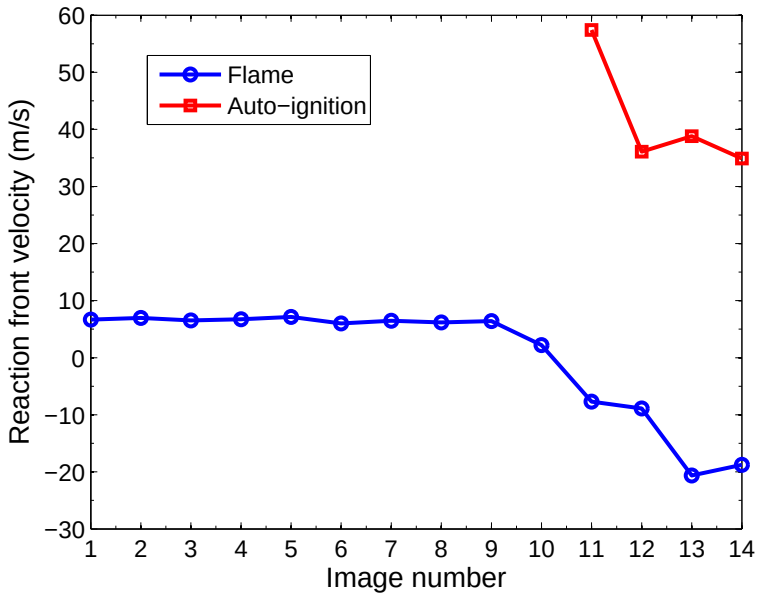

Figure 7.28: Local ignited flame velocity and the reaction front velocity developed from an autoignition site, calculated from Figure 7.27.

Chapter 8

Conclusions and Recommendations

8.1 Introduction

This thesis aimed an investigation of the flame propagation and autoignition in a high pressure single-cylinder optical research engine used here. The LUPOE 2D boosted engine has a disc-shaped combustion chamber with full-bore overhead optical access. A new boosting method with control system has been developed to increase the inlet pressure while maintaining well-controlled turbulence intensity under safe operating conditions. Subsequently, three main groups of experiments have been conducted:

- Measurement of iso-octane flame speed in a turbulence-free engine relevant environment;
- Study of turbulent flame development at supercharged engine conditions, emphasizing on the pressure effects on different flame development stages and flame structure;
- Investigation of characteristics of auto-ignition and extreme knock in a strongly boosted engine.

In these experiments, in-cylinder pressure signals were recorded, and have been analyzed using the Leeds University Spark Ignition Data Analysis (LUSIEDA) reverse

thermodynamic code. Various optical diagnostic methods have been applied. The Particle image velocimetry (PIV) was employed to investigate effects of engine speed, intake flow rate, and pressure on the turbulent flow in the engine. Flame chemiluminescence signals were captured with a high speed imaging acquisition system with an interference filter; flame propagation speeds under different conditions were derived from these images. The detailed flame structure was obtained by laser sheet visualization technique, where the cross section of a 3D flame has been visualized by cross-cuuting it with a laser sheet. These data collected under well controlled conditions yielded a comprehensive database for engine combustion theory validation, and also for modelling work by colleagues in the School of Mechanical Engineering at Leeds University. Conclusions drawn from the previous Chapters of this thesis are presented here. Furthermore, some suggestions arising from this study are proposed for future works.

8.1.1 Conclusions of Iso-octane flame speed experiments

Presented in the current section are conclusions from the measurements of iso-octane flame speed in a turbulence-free engine-relevant environment.

- The engine flow fields at the mid plane of the clearance volume of LUPOE-2D engine were measured using a PIV system near the TDC position, at engine speeds of 100, 150, 200, and 250 rpm. There was no significant swirl motion detected in the bulk flow, and the flow tends to be homogeneous and uniform near the TDC position. The ensemble mean velocity decreased when the engine speed was reduced. At the engine speed of 100 rpm, the mean gas velocity in the chamber was lower than 0.1 m/s. The RMS turbulent velocity near TDC was linearly proportional to the engine speed, and declined to approximately zero when the engine speed decreased to zero. At the same time, the integral length scale at TDC also decreased with the engine speed; the longitudinal integral length scales were approximately twice larger than the transverse integral length scales. These results confirmed that LUPOE engine could generate an almost homogeneous and turbulence-free environment when it runs at extremely low speed, i.e. less than 100 rpm, and so it could be used as a reciprocating combustion rig for laminar flame speed measurement under engine relevant conditions.

- Pressure traces recorded in the LUPOE engine at an engine speed of 100 rpm, with various equivalence ratios, show that the cycle variability was extremely small at the stoichiometric and rich conditions. These observations further support the

claim that the LUPOE engine can provide minimum turbulence intensity and homogeneous mixture conditions. The spark timing was set at 10 deg bTDC, where a high pressure of 12 bar and high temperature of 600k (calculated from LUSEIDA) could be achieved.

- Laser sheet visualization measurements provided the cross-section information of flame shape. Comparing the results from engine speeds at 150 rpm and 750 rpm, it was shown clearly that the flame contour was closer to a circle at the low engine speed. The variability of mean flame radius at the same crank angle also had a significant drop with the engine speed decreasing.

- After a comprehensive assessment of experimental conditions, direct measurement of flame propagation in a turbulent-free environment has been conducted using CH* chemiluminescience. The sequence of images captured at various equivalence ratios show the development process of flame. A smooth flame front was observed after ignition, and it became wrinkled as the flame was approaching the wall. However, the flame front attained more regular cellular shapes, which was different from the randomly wrinkled flame front induced by turbulence. These cellular structures could be generated by a flame instability at the high pressure.

- In order to eliminate effects exerted by the ignition and engine side walls on the flame speed measurement, only the flame radius range from 10 to 22 mm was chosen for the burning velocity calculation. During this stage, the volume height changed only about 0.4 mm at the engine speed of 100 rpm, which is equal to 5% of the total volume. This combustion duration could be considered as a constant volume process. The visible flame speed S_n was derived from the slope of the fitting line of flame radius from 10 to 22 mm, the burning velocity was calculated as $U = \rho_b/\rho_u S_n$, and the value of the thermal expansion ratio was calculated using LUSIEDA. The burning velocity of iso-octane had a similar value of 1.1 m/s for stoichiometric and rich mixtures of equivalence ratio, while 0.6 m/s and 0.8 m/s were for lean mixture 0.6 and 0.8 respectively.

- Since the rms velocity was linearly proportional to the engine speed, and decreased to approximately zero if the engine was stopped, a new method of measuring a laminar burning velocity at turbulence-free conditions was explored. This method is based on extrapolating the burning velocities from different engine speeds from 300 rpm to 150 rpm. In order to keep the pressures and temperatures similar at spark timing, different spark timings have been selected, at a high pressure of 15 bar and a high temperature of 600K. Flame speeds with equivalence ratios 0.8, 1

and 1.2 under four engine speeds have been measured. The results show that the burning velocity has linearly decreased with the reduction of the engine speed for lean and stoichiometric mixture, while the rich flame speed shows an opposite tendency. The extrapolated burning velocity for three equivalence ratios are 0.78 m/s for the lean mixture, 0.94 m/s for the stoichiometric and 1.15 m/s for the rich mixture. The difference between the values from the direct measurement at engine speed 100 rpm and that derived from extrapolation from engine speed 150 to 300 rpm is small.

- It is very difficult to measure the laminar burning velocity of iso-octane at a high pressure of 15 bar, and high temperature of 600K at constant pressure in a constant volume combustion vessel. The experimental data which can be used to validate the current measurement results are not available in the literature. For this reason, correlations for laminar flame speed and reaction mechanism computations have been adopted. Nevertheless, these equations and a reaction mechanism need to be evaluated using the available experimental data before applying them to calculate burning velocity at high pressure. 4 sets of experimental data of iso-octane burning velocity, 3 correlation equations and a chemical reaction mechanism were selected and evaluated comprehensively.

- Comparing current measured burning velocities to values derived from correlation equations at high temperature and pressure, a difference between the magnitude of measured and computed results was observed. The measured flame speed is about 1.5-2 times larger than that from calculation. This may be attributed to the acceleration of the flame front due to flame instabilities and stretch effects. Since the Markstein number of iso-octane-air mixtures at high temperatures and pressures was low, instabilities which arise at increasing pressure, may play a more important role on flame speed, and result in an acceleration of the flame speed.

8.1.2 Conclusions of high pressure turbulent flame experiments

The following conclusions could be derived from the investigation of turbulent flame development at supercharged engine conditions.

- The boosting methods were tested by using exhaust valve installed in the exhaust system and increasing the inlet flow rate, and a map of initial pressure with these two methods was realized. Based on the map, a reference condition was decided as a starting point for subsequent inlet pressure increasing before the knock cycle

happened. Two conditions for each boosting method were selected as the following test conditions.

- The effects of increasing inlet flow rate on the turbulence intensity in the LUPOE 2D engine was investigated using a PIV system. The measurements were conducted at the mid plane of the clearance volume of LUPOE-2D engine near the TDC position, at engine speeds of 750 rpm. The maximum flow speed in the LUPOE engine was about 4m/s, where no significant bulk flow, e.g. swirl motion, was detected. Increasing the inlet flow rate by 50% caused stronger turbulence intensity by up to 40%, while the exhaust valve closing could keep the RMS velocity at almost the same level. For the highest and lowest levels of tested mass flow rate, the mean velocity of an engine flow field had a similar mean value and standard deviation along both the X and Y axes. These results confirmed that the new boosting configuration using the exhaust valve enabled the intake mass flow rate and the initial pressure to be independently controlled.

- The integral length scales were calculated from the mean PIV vector fields at 2 degrees before TDC. It could be observed that, in general, average values of the longitudinal integral length scales were between 8-10 mm, approximately twice the transverse integral length scales 4 mm. The flow field near the TDC could thus be considered as a homogeneous turbulence flow.

- Pressure traces and images of flame propagation of 100 cycles have been recorded at the selected conditions. The entrainment flame radius was defined as the radius of a circle having the same area as the observed irregular flame boundary. In order to take the cycle variability effect into analysis, the recorded pressure traces and flame radius were separated into fast, middle and slow cycles. The cycle was classified by using peak pressure below, within, or above two standard deviations from the ensemble average value.

- The experimental conditions were plotted on the Borghi diagram, the turbulence intensity and integral length scales were measured by the PIV system, the laminar flame speeds were calculated with Metghalchi and Keck's power law correlation equation. The selected conditions were located in the boundary between wrinkled flamelets and wrinkled flamelets with pockets. Molecular transport parameters were calculated at initial temperature estimated with the LUSEIDA, and its value was around 620K.

- The effects of pressure on flame development were assessed at the different combustion phases i.e. initiation, main phase, and termination phase. Overall, the re-

sults show that the pressure rise decreased the flame burning velocity very weakly. However, it had different effects upon the acceleration at early stages, and deceleration at final stages. Increasing the initial pressure had slightly negative effects on the flame acceleration; turbulence was the main factor at the initial stage. Increasing initial pressure could decrease slightly the burning velocity in the fully developed stage. Yet, this decrease may mainly be caused by decreasing flame acceleration. The burning velocity was slightly rising with pressure increasing. Pressure decreased the flame deceleration near the walls, resulting in longer combustion duration. However, the burning rate increased with higher pressure in this region.

- The flame acceleration speed curves for fast, middle, and slow cycles at three initial pressure conditions have been compared with the flame acceleration model proposed by Lipatnikov and Chomiak, which was characterized by two turbulent parameters. The models predicted a faster initial rate of flame acceleration than the measured value, and slower rate at the later stage of the flame acceleration.

- The flame deceleration speed curves of fast, middle, and slow cycles at three initial pressure conditions are well fitted by the error functions erfc(x), which was characterized by two parameters: the flame radius time, and flame deceleration duration. For the fast cycle, the flame deceleration duration value of the equation is the main value to be adjusted to fit the curve shape, whilst for the slow cycle, the flame radius time value is more important.

- Under the same experimental conditions, the structure of the flame at high pressure and its response to pressure effects were also investigated. A Laser sheet visualization method was applied, and a new algorithm for image processing was developed to derive the detailed cross section flame front topology. Self-similar properties of flames were evaluated with mean progress variable maps. The results show that the initial pressure has only a slightly effect on the flame structure in the aspects of flame wrinkle and curvature. The mean progress variable profiles could be collapsed by the error function well. Flames at high pressure have the same ”self-similar” properties as those observed at low pressure.

8.1.3 Conclusions of autoignition and extreme knock experiments

The following conclusions may be drawn from the experimental investigation of autoignition and extreme knock in a strongly boosted engine.

- An engine knocking map was made for the LUPOE 2D boosted engine at an engine speed of 750 rpm. The intake and cylinder head temperature were kept at 323K. When the initial pressure was increased from 1.0 bar to 2.1bar, the spark timing had to be retarded from 15^oCA bTDC to 2^oCA bTDC. At these spark timings, above 90% of the cycles were knocking cycles and this spark timing was defined as the knock boundary.

- A rise of the initial pressure promoted appearance of the extreme knock characterized with very large pressure oscillations and low probability of appearance. In this study, the extreme knock was defined as a kind of knock, where the pressure oscillation amplitude exceeded 50 bar and occurred at random.

- Images of self-ignition and the extreme knock process have been obtained; the end gas self-ignition happened at the late stage of combustion, and produced slight pressure oscillations. In contrast, the extreme knock was caused by earlier autoignition sites and following strong pressure oscillation. The development process of autoignition in an extreme knock event can generate a new "flame", which could be a result of the reaction front propagation of auto-ignition, or subsequently continuing from the autoignition occurring in front of the reaction front. This process was restricted by the main flame and engine walls.

- Knock onset and autoignition onset have been discriminated using an accurate detection of pressure oscillation, and be validated by the collected knocking images. The raw knock pressure trace was filtered with a bandwidth of 2.5-12 kHz to derive the pressure oscillations induced by knock. Two knock intensity characteristic methods, the MAPO maximum amplitude of the pressure oscillation of band pass filtered pressure, and the one developed by previous workers in Leeds were compared. These methods produced similar results.

- Effects of cyclic variability on knock onset and intensity were strongly amplified by engine charging. In particular, the magnitude of cyclic variability of the maximum pressure within a cycle increased with the initial pressure.

- At the initial stage, the autoignition was generated at some small distance away from the wall. The autoignition kernel did not seem to be in direct contact with the wall, therefore surface ignition may be ruled out.

- Compared with slight knock, the extreme knock occurred at a lower pressure and larger mass fraction burnt. Since the LUPOE engine does not have valves or spray injection deposits, the lubrication oil from piston crevice could be a potential reason for the extreme knock.

- It was not observed that the flame speed had a direct effect on the knock onset and intensity under the same engine operation condition. Knock intensity also did not relate to autoignition area when it interacted with the main flame.
- In the frequency domain, the frequency of the most intense pressure oscillations did not change upon a transition to extreme knock, and this might be only related to engine chamber size. However, the width of the frequency distribution tended to be longer and showed more harmonics when the knock became stronger.
- The knock intensity was not necessarily related to the autoignition onset time. The gas dynamics of autoignition, and flame-autoignition interaction played an important role for the pressure oscillations. The earlier autoignition occurrence provided more time and space for autoignition sites to propagate, achieved a higher speed to impede the main flame, and generated a second ignition by interference from the new autoignition sites. This could result in strong pressure oscillations.
- From measurements of the local speed of the reaction front developed from an autoignition site it was found that the velocity remained subsonic. Thus a direct detonation did not exist in the observed extreme knocks. However, an extremely fast rate of heat release could be observed from the pressure in the several milliseconds which followed the autoignition onset.

8.1.4 Recommendations for future work

Listed below are pointed some empirical observations related to the possibility to extend further this study to explore related areas. I am articulating a series of suggestions in order to address some of these empirical and theoretical issues that remain unsorted within the temporal and logistic conditions, as well as the equipment limitations of this research.

- The direct measurement of laminar flame in a disc-shape engine chamber could be affected by the heat release and the flame geometry restricted by the engine walls, the effects of these factors on the burning velocity measurement need to be taken into account and corrected.
- The quasi-laminar flame speed measured in the current study is twice faster than the one expected from the existing literature; flame instability could be the main factor accelerating the flame speed, according to the image observation and exclusive method. Nevertheless, the mechanism behind this is still not clear, and the method to characterise this flame instability effect also needs to be developed to

derive the "real" flame burning velocity. Furthermore, whether the flame speed carrying the flame instability information is suitable for the turbulent flame speed modelling, also requires additional discussions.

- The engine temperature was calculated by using reverse thermodynamic models, the accuracy of the results relays on the models and input parameters. Direct temperature measurement could be applied by using advanced laser diagnostics such as PLIF. This is useful for current models validation and investigation of the temperature imhomogeities in the engine chamber. Spatial temperature measurement is also important for the further studies of autoignition and knock.

- Laminar flame speed measurement in this experiment can be explored in a wider range of experimental conditions. The maximum pressure could be increased by changing the engine compression ratio, while the temperature could also be varied by setting different heater values for the engine body.

- The exhaust valve used in the current study consisted of three solenoid valves. Although it can fulfill the requirements of increasing the inlet pressure at the engine speed of 750 rpm very well, the response time of exhaust valves is still slow if the engine speed is increased above 1500 rpm. The iris diaphragm and butterfly valve actuated by a brushless DC motor could be a solution to achieve a faster response time with large flow rate across. Thereafter, the engine speed could be further increased to study the high pressure combustion behaviour at high engine speeds.

- The Particle Image Velocimetry (PIV) system used in this study has the low repetition rate of 15 Hz, hence, only one flow field could be captured in each engine cycle. The dynamic flow field with flame propagation could be evaluated by using a fast PIV system i.e. repetition rate is larger than 5 kHz. Furthermore, the burning velocity might also be directly derived from the flow information in front of the flame front.

- With a fast PIV system, the relationship between turbulence and autoignition sites generation could be studied. It is also interesting to see how the turbulence flow field changes with the autoignition sites development. The local flow speed around the autoignition sites also can derived from PIV images.

- The flame development near the engine walls could be further studied, the accuracy of the measurement is strongly compromised by the light refection from the engine walls. New measurement methods should be developed to observe this process with a higher resolution.

- Although some clues from this study have shown that the extreme knock may be caused by the engine lubricants, see Section 8.3, direct evidence lacks. Autoignition properties of various lubricants and lubricant-fuel combinations should be studied, and the mechanism of interaction between engine knock and lubricant system need to be investigated. Interestingly, the lubricant's effect on the knock was only observed in the supercharged engines.

- During this study, an attempt for the development of fast C_2 PLIF has been made. A test platform was built to test if it was possible that by applying a high repetition copper vapour laser to excite the C_2 (2,2) band near 509.7 nm, and to detect fluorescence signals from the (2,1) band near 471.5 nm. Owing to the experiment equipment limitations, no positive results were obtained.

- At the final stage of this study, the lab received a new copper vapour laser. This new copper vapour laser has been installed near the LUPOE 2D boosted engine. Fast laser sheet visualization experiments could be applied to obtain more information of flame structure development at the high pressure with the flame contour spectrum analysis method.

Appendix A: Photograph of the LUPOE 2D engine

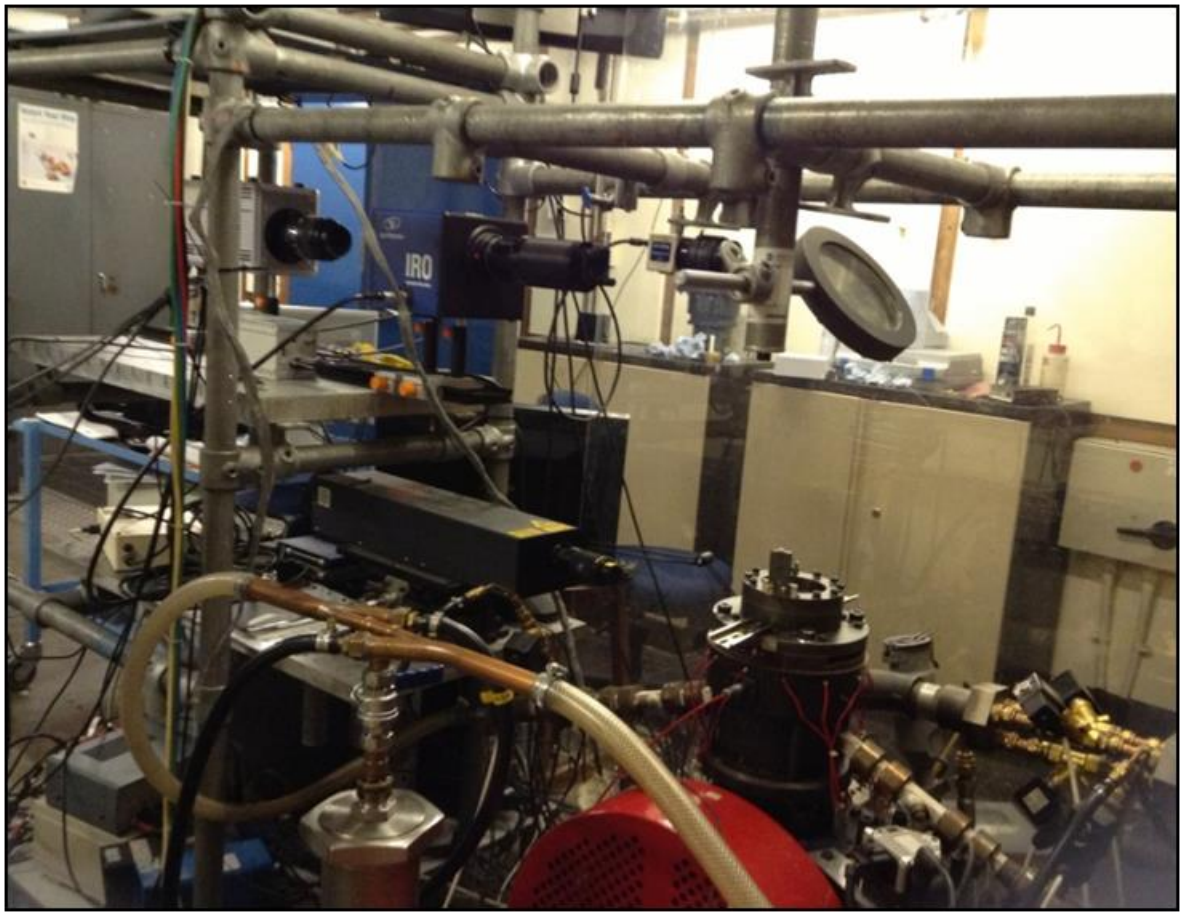

Photograph of the LUPOE 2D boosted engine with optical measurement equipment.

Appendix B: Equation 3.1 derivation

The equation of an ideal gas state is:

$$PV = mRT \tag{1}$$

where P is pressure, V is volume, T is temperature, m is mass, R is the specific gas constant, Taking the logarithm of Equation 1 and differentiating according to crank angle θ (Ferguson and Kirkpatrick [2001]) gives:

$$\frac{1}{P}\frac{dP}{d\theta} + \frac{1}{V}\frac{dV}{d\theta} = \frac{1}{m}\frac{dm}{d\theta} + \frac{1}{T}\frac{dT}{d\theta} \tag{2}$$

The first law of thermodynamics for an ideal gas within an open system:

$$mc_v\frac{dT}{d\theta} + c_vT\frac{dV}{d\theta} = \frac{dQ}{d\theta} - P\frac{dV}{d\theta} + c_pT\frac{dm}{d\theta} \tag{3}$$

Combining Equation 2 and Equation 3:

$$\frac{dP}{d\theta} = -\gamma\frac{P}{V}\frac{dV}{d\theta} + \frac{\gamma - 1}{V}\frac{dQ}{d\theta} + \gamma\frac{dm}{d\theta} \tag{4}$$

The fluid mass conservation in the system with m_{in} and m_{out} at the angle speed of ω is:

$$\frac{dm}{d\theta} = \frac{\dot{m}}{\omega} = \frac{\dot{m_{in}} - \dot{m_{out}}}{\omega} \tag{5}$$

Suppose the engine compression is a adiabatic process, and combine Equation 4 and Equation 5:

$$\frac{dP}{d\theta} = -\gamma\left(\frac{P}{V}\frac{dV}{d\theta} + \frac{\dot{m}_{in} - \dot{m}_{out}}{\omega}\right) \tag{6}$$

Appendix C

Zhengyang Ling, A.A. Burluka, U. Azimov. **Knock Properties of Oxygenated Blends in Strongly Charged and Variable Compression Ratio Engines**, *in SAE 2014 international Powertrain, Fuels&Lubricants Meeting*, Birmingham, UK, October 20-30, 2014. SAE Technical Paper, 2014-01-2608.

14FFL-0202/2014-01-2608

Knock properties of oxygenated blends in strongly charged and variable compression ratio engines

Zhengyang Ling[1], A. A. Burluka[1], Ulugbed Azimov[2]

1.University of Leeds, 2.Northumbria University

Abstract

Replacing the conventional fossil fuel totally or partially with alcohols or ethers in spark-ignition (SI) engine is a promising way to reduce pollutant emissions. A large number of studies on alcohol-containing blends in SI engines could be found in the literature. Nonetheless, investigations of ether-containing blends are by far much less numerous, especially for modern boosted engines. Blending with ether compounds might change the burning rate at high pressure, which consequently changes the anti-knock properties of these fuels and leads to a deterioration in the vehicle drivability.

This work reports experiments carried out in two one-cylinder engines: one is a naturally aspirated, variable compression ratio engine, and the other is a strongly charged optical engine. Three fuels with different RON and MON numbers were tested: Iso-octane, a blend Ethyl Tert Butyl Ether (ETBE) with a primary reference fuel, and a commercial gasoline fuel containing 5% by volume of ethanol (E05).

The experimental results show a significant difference of knock boundaries of three fuels in the boosted engine at the initial, i.e. equivalent of the intake manifold, pressure of 1.6bar, and almost similar knock boundaries under different compression ratios in the naturally aspirated engine. The fuel sensitivity upon the knock boundary of oxygenated blends was identified in order to compare the fuels' performance in different engines. The burning rate was determined at the same compression ratio for the two engines from the high speed flame imaging and a reverse-thermodynamic analysis, in order to clarify the effects of the burning rate on the anti-knock behaviour.

Introduction

Raising concentration of carbon dioxide (CO2) in the air is one of the main causes of environmental concerns. Automotive companies are under political pressures, and they are taking seriously this issue by seeking cost-effective solutions which combine an eco-friendly approach with the reduced costs of fuel [1]. One such solution is a wider use of bio-derived petrol substitutes, such as ethanol or alkyl ter-butyl ethers, e.g. ETBE. Oxygenated fuel admixtures also allow the gasoline in vehicles to burn more completely, resulting in reducing air pollution such as carbon monoxide emission and smog.

The idea of using alcohol as an alternative fuel is not new, but only recently ethanol has become the additive of choice for oxygenated fuel in many places around the world. Alcohols are more competitive among the other alternatives, because they are compatible with existing fuelling distribution infrastructure and are easily stored in a vehicle [2]. Blending ethanol to gasoline has another beneficial effect of improving inherent or chemical resistance to engine knock owing to their high octane numbers (RON 109). Auto-ignition delay time also is further increased by the high sensitivity, i.e. difference between the research (RON) and motor (MON) octane number of ethanol, resulting in greater knock resistance as combustion phasing is retarded due to reduced unburned gas temperature [3]. In general, compared to "standard" gasoline, oxygenated fuels have high Motor Octane Number (MON) and Research Octane Number (RON) which results in high anti-knock Index. In contrast, the sensitivity of the gasoline increases with increasing the oxygenates content, which may cause difficulties in the operation under different engine operation conditions.

Furthermore, the alcohols have a higher latent heat of evaporation compared to gasoline; this reduces the temperature of the inlet manifold and increases the volumetric efficiency [4]. Especially, it is beneficial in supercharged engines, where, by injecting the alcohol-gasoline blends into a supercharger inlet, both the cooling effect and the compressor efficiency are enhanced [5].

For many years, MTBE was another common additive for oxygenated fuel. However, MTBE can easily foul up water in artesian wells because of its low sorption into soils and high water solubility. As a result, legislative efforts have been made by some governments to phase out the use of MTBE [6]. Possible alternative to MTBE, Ethyl Tert-Butyl Ether (ETBE), has much smaller impact on our water supply due to its lower water solubility [7]. ETBE is synthesised from mixtures of ethanol with isobutylene in an endothermic catalytic reaction [2]. ETBE is considered as a biofuel thus having the potential to play a significant role in the future of alternative biofuels [8]. One of advantages of ETBE as a blending component compared to ethanol is that it does not increase the volatility of gasoline. It has higher octane boost than MTBE, and a higher MON than ethanol [9, 10]. Its saturated vapour pressure is lower than that of either MTBE or ethanol. ETBE has better sensitivity compared to other alcohols [11].

Downsizing, i.e. reduction of engine displacement volume, accompanied with supercharging is becoming an important strategy in the engine industry for improving the efficiency of gasoline engines. It has shown to have an excellent potential, allowing a reduction in pumping losses, friction and heat transfer losses, through boosting the inlet air flow. However, abnormal combustion, such as knock, limits both compression ratio and boost levels [12, 13]. Investigations of knock properties of oxygenated fuel blends fuel in high compression ratio and boost levels are few. And this motivates the present work exploring the anti-knock properties of oxygenated blends under widely differing operating conditions. The effects of compression ratios, boost levels, and spark timing on engine knock limit for oxygenated fuel blends were studied.

Experimental engines

The experiments have been performed in two single cylinder research engines: Leeds University Ported Optical Engine, MK2, Disk chamber (LUPOE 2D-boosted engine) [14] and a naturally aspirated Ricardo E6 variable compression ratio engine.

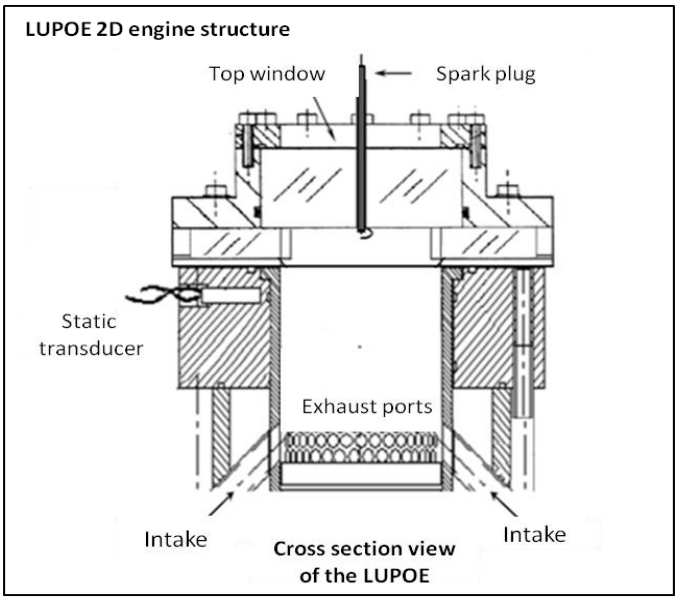

Figure 1. Arrangement of LUPOE-2D boosted engine showing the details of the optical windows, and intake and exhaust systems.

LUPOE-2D boosted engine has a disc-shaped combustion chamber with a full-bore overhead optical access. It replaces the overhead valves by side ports to avoid obstructing the full-bore optical access, provided by top and side windows. LUPOE-2D has two diametrically opposed intake ports of rectangular cross section and an exhaust passage consisting of two rings of circular exhaust holes drilled in the liner, communicating with a void between a liner and barrel, leading to one exhaust duct. The exhaust holes have been positioned in such a way that the exhaust port is already cut-off by the piston while the intake port is still open. The intakes are connected to a high pressure compressed air line, allowing to obtain a desired initial pressure. The employed ported breathing arrangement, in particular the ports dimensions and inclination, allow one to eliminate swirl and tumble motion often existing in valves engines, and to generate in-cylinder flow field uniform in both average and root mean square properties. The air and fuel mass flow rates were set and maintained constant by mass flow rate controllers, respectively. In this work, a central spark ignition was employed. The quartz optical window only was used in normal combustion experiments; it was replaced by a more robust metal blanking plate to avoid the damage to the quartz window under knocking conditions.

A Ricardo E6 variable compression ratio engine, which is a 4-stroke, poppet valve engine with real exhaust residual, was also used in this study. Ricardo E6 engine is a better approximation to a serial production passenger car engine than the LUPOE engine. For the E6 engine, many continuous cycles were recorded over a range of compression ratios. The engine combustion chamber also was “disc-shaped”, with a spark plug located 4mm from the side wall. The clearance height and compression ratio was altered by a worm-gear mechanism changing the position of the cylinder head relative to the engine body.

Table 1. LUPOE-2D boosted and Ricardo E6 engines specifications.

	LUPOE2D-boosted	Ricardo E6
Engine type	Two-stroke	Four-stroke
Bore(mm)	80	76.2
Stroke(mm)	110	111.1
Connecting rod	232	244
Compression ratio	11.5	Variable 10-14
Spark position	center	side
Valves timing	Intake ports	Inlet valve
	Closes -108 deg BTDC Opens -108 deg ATDC	Opens -9 deg BTDC Closes -38deg ABDC
	Exhaust ports	Exhaust valve
	Closes -121 deg BTDC Opens -121 deg ATDC	Opens -45 deg BBDC Closes -9 deg ATDC
Engine Speed (rpm)	750	1500
Equivalence ratio	1	1
Mass flow rate of air (g/sec)	9	4
Intake and cylinder head temperature(K)	323	323
Initial pressure (bar)	1.6	1

Both engines shared similar control and data acquisition systems. Piezoelectric pressure transducer type 601A was mounted to the cylinder head flush to the wall. In LUPOE 2D engine, an absolute pressure level was measured by Kistler piezoresistive sensor, type 4045A5, which was fixed to the cylinder barrel opened at 60^{o} CA before top dead center (bTDC) to avoid exposing it to high temperatures and

pressures caused by compression and combustion. In-cylinder pressure data were collected at 0.2° crank angle resolution. The trigger timing was controlled by a custom micro-controller system synchronized with the shaft encoder signal; the data acquisition frequency was set at 200 kHz.

The high speed flame imaging was employed for derivation of flame speed in LUPOE-2D boosted optical engine, see Fig.1. The imaging system comprised a Photron Ultima APX-RS CMOS camera, using a Nikon 50 mm lens. Natural light imaging technique was used with a view from the top of the chamber to record the flame edge propagation. Images were acquired at a frame rate of 10 kHz with an image resolution of 512 by 512 pixels.

During experiments, the LUPOE-2D boosted engine speed was set at 750 rpm, and the charge initial temperature was 323K, and the equivalence ratio was 1. The engine was used in skip-fired mode where only every 11th cycle was fired and 10 skipped firing, this was done to purge the chamber of any noticeable amount of the exhaust residual gas. The spark timing was advanced until the fraction of cycles with knock was above 90% of all firing cycles. The fuel was introduced into well-controlled heated intake manifold well upstream of the ports.

The Ricardo engine speed was set at 1500 rpm and the intake temperature was maintained constant at 323K, the equivalence ratio was 1, and the compression ratio was varied from10 to13.5. Knocking combustion, also, was induced by advancing the spark timing until the knock onset time was clearly defined. The specifications of the two engines and experimental conditions are listed in Table 1. Ricardo E6 is a carburetted engine. The aim of this study was primarily fuel effects, leaving the influence of engine speed and turbulence intensity beyond the scope of this work. Because of this and different modes of ignition, LUPOE2D employing central, and E6 side spark position, therefore, comparison at the same rpm is not included. Such comparison is left for a follow-up work. Three fuels were employed in the present work: 100% Iso-octane, mixture of 10% by volume of EBTE with 90% of primary reference fuel (PRF), i.e. mixture of n-heptane with iso-octane, and, finally, a commercial gasoline fuel containing 5% by volume of ethanol (E05) were tested and compared.

Table 2.Properties of the fuels used in the current study.

Fuel name	Blend (by volume)	RON	MON	Sensitivity RON-MON	Density @ 20°C (kg/m3)	Air/Fuel=1
ISO100	Iso-octane	100	100	100	691.3	15.04
E05	gasoline with 5% ethanol	95	88.6	6.4	726.7	14.2
ETBE10	90% 95PRF, 10% ETBE	97.5	95.5	2	695.8	14.73

Data processing

In order to isolate the knock-related pressure oscillation, an appropriate selection of cut-off frequencies was chosen. A variety of cut-off frequency settings of different bandwidths have been adopted in many studies for the different purposes [15, 16]. According to these reports, a wide bandwidth FFT filter, e.g. 2.5-12 kHz was selected to remove the noise in low and extremely high frequency region. Peak pressure was defined as the maximum value of low-pass-filtered pressure, or, Maximum Amplitude Pressure Oscillation (MAPO); this is the maximum amplitude of oscillation of band pass filtered pressure, see Fig.2.

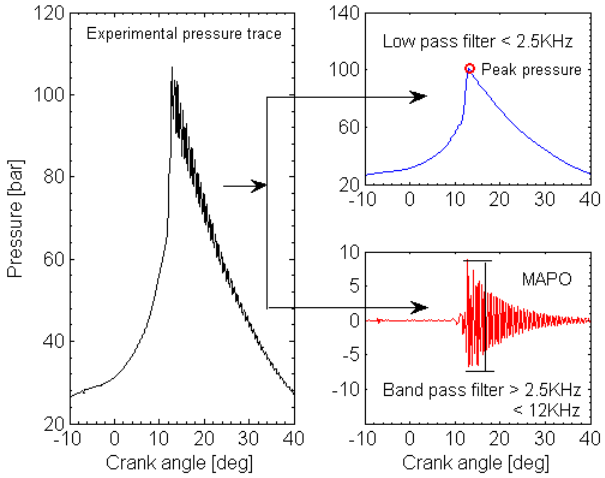

Figure 2. Illustration of FFT filter for the knocking pressure trace and the definitions of Peak pressure and Maximum Amplitude Pressure Oscillation (MAPO).

Knock onset is usually detected by scanning the filtered pressure oscillations until a certain threshold value is exceeded [17]. However, a universal threshold is difficult to define, because of the cycle variability invariably present in an engine. In the present study, a dynamic threshold was set, where the threshold was adjusted with the peak value of high-pass-filtered motoring pressure before spark timing. This method can distinguish the pressure caused by engine vibration from knock. The detected knock onset is defined at the last zero-crossing point before the first threshold-limited point, where the pressure starts rising rapidly rather than reaching the peak value [18], see Fig.2.

A knock intensity definition, adopted from the previous research [15], was employed to quantify the knock severity as a compensation for MAPO by taking into the knock duration time account. This can be expressed as:

$$KI = \sqrt{\frac{1}{N}\sum_{i=1}^{N}\left(P_i - P_{mean}\right)^2} \quad (1)$$

where KI is the calculated knock intensity, P_i is the instantaneous band-pass filtered pressure, P_{mean} is the mean value of band-pass filtered pressure, N is the number of samples collected during a period of 2 ms from the detected knock onset. 2 ms period allowed time for approximately 10 reflections of a pressure wave travelling at typical combustion chamber at sonic velocities.

Engine tests data were analysed with a quasi-dimensional thermodynamics computer code, known as LUSIEDA, an acronym for Leeds University Spark Ignition Engine Data Analysis, which analyses the closed part of the engine cycle and derives the mass fraction of the burnt gas from the pressure signal [19]. The LUSIEDA code employs a reverse thermodynamic analysis assuming spherical flame shape and accounting for heat losses and blow-by flow. Further details of procedure may be found in [19,20]. In this study, LUSIEDA was used for the calculation of unburned pressure and temperature history during engine combustion, and for the derivation of the burnt flame radius for Ricardo E6 engine.

Results and Discussion

In-cylinder conditions

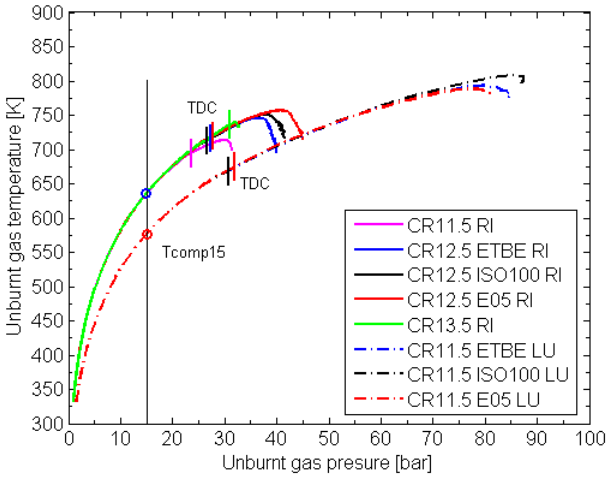

Figure 3. The pressure –temperature history of the end gas for the Ricardo E6 (RI) and LUPOE-2D boosted (LU) engines at spark timing 7bTDC, the reverse software LUSIEDA was used to predict the unburned gas temperature based on experimentally gathered cylinder pressure data.

Although LUPOE 2D boosted engine and Ricardo E6 engine have similar chamber geometry and size, they operate under very different conditions, as can be seen in Figure 3. This figure shows the pressure and temperature history of the end gas plotted for two engines. The pressure for both engines is taken from measured in-cylinder data, while the gas temperature has been calculated using the LUSIEDA reverse cycle analysis package. It can be seen that there is a large spread in the unburned pressure - temperature regime between the two engines; LUPOE-2D boosted engine has higher initial pressure and lower temperature during compression, the fuel-air mixture density was increased by the boosted initial pressure, resulting in higher combustion peak pressure and higher temperature in the end of combustion stage. The peak motoring pressure and the temperature at the TDC rises with increasing of compression ratio. The auto-ignition behavior of the engine usually will largely be determined by the pressure-temperature history, therefore the wide operating range of two engines should be an ideal set for testing the knock properties of oxygenated blend fuel.

For each test condition, Figure 3 highlights the unburned gas temperature taken when the in-cylinder pressure equaled 15bar during compression. This value was used to calculate the constant K in the Kalghatgi octane index correction method [21] and a subsequent octane index (OI) for each operating condition [21, 22]. The derived values are presented in Table3. The octane index is defined as:

$$OI = (1-K)\,RON + KMON = RON - KS \quad (2)$$

where S=RON-MON is the fuel sensitivity, and K is calculated from on the temperature of the gas when the pressure inside the engine the compression stroke reaches 15 bar, T_{comp15}

$$K = (T_{comp15}\,0.0056) - 4.68 \quad (3)$$

Table 3.The Kalghatgi K factor for the three engines

Engine	Tcomp15(K)	KalghatgiKfactor
LUPOE -2D	661	-0.98
LUPOE-2D boosted	573	-1.45
Ricardo-E6	635	-1.1

The Kalghatgi K factors for the LUPOE 2D boosted and Ricardo E6 engines are listed in Table 3. Value for the normally aspirated LUPOE 2D engine also was calculated as a reference. All three engines have negative values of K. This means that fuels might have octane index greater than RON if MON is smaller than RON; this is usually the case. With the inlet boosting, the K value was decreased toward larger negative value. The 'old' Ricardo-E6 engine also has a negative K value, this is caused by low heating temperature (323K) of the intakes. This K is also smaller than that for naturally aspiration LUPOE 2D engine under higher compression ratio. It is should be noticed that Iso-octane (100RON, 100MON) has zero sensitivity, (RON=MON=100), therefore its anti-knock behavior should not be affected by the K factor.

Turbulence, particularly during ignition and flame propagation, has a major influence on the burning rate and cycle variability. Measurement of turbulence at LUPOE 2D boosted optical engine has been conducted by using PIV [23, 24]. The turbulence intensity near TDC at an engine speed of 750 rpm was about 0.88m/s, however, application of laser diagnostic to Ricardo E6 engine bereft of any optical access is not possible. Daneshyar reported turbulence rms velocity in Ricardo E6 0.37m/s at TDC; the value was measured with hot-wire anemometry at 260 rpm [25]. Ahmet Erdil [26] measured the turbulence intensity using the same method, and reported rms

velocity u' of approximately 1.24 m/s at engine speed of 1500 rpm. It can be deduced that Ricardo E6 engine's turbulence intensity is about twice higher than that in the LUPOE 2D boosted engine.

Characteristics of normal combustion

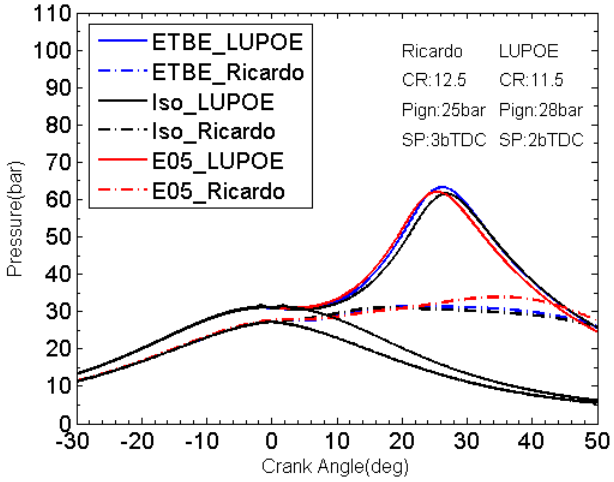

Figure 4. Normal combustion in-cylinder mean pressure traces for ETBE10, iso-octane and E05 in the LUPOE-2D boosted and Ricardo E6 engine at similar spark timing and operation conditions were listed in Table 1. Compression ratio in Ricardo E6 was set at 12.5.

The mean pressure traces of normal combustion cycles recorded in the both engines are presented in terms of crank angle in Figure 4. Further crank-resolved data for all conditions are presented in the Appendix 1. For the shown cycles, the spark timing was set at 2CA bTDC to avoid any knock in the LUPOE 2D optical engine. Ricardo E6 engine at the similar spark advance, (3 CA bTDC), produced peak pressures which were unsurprisingly much lower and occurring later. The peak pressure in Ricardo E6 engine at these conditions was approximately 35bar, which is almost half of the peak pressure at LUPOE-2D boosted engine. E05 has the highest mean peak pressure among the three fuels at Ricardo E6, however the difference among the three fuels in LUPOE 2D is not significant.

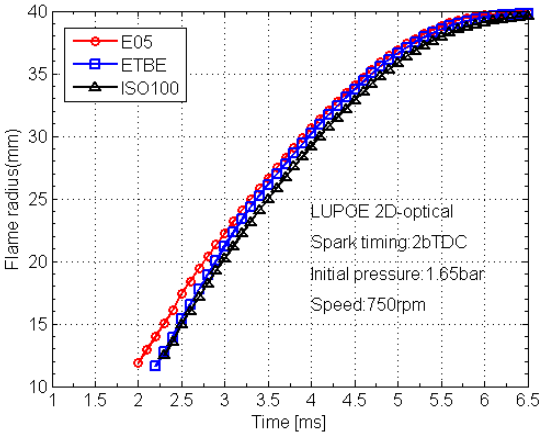

Figure 5. Entrainment flame radius development recorded by high speed camera in the LUPOE-2D boosted engine for three fuels.

The flame radius for three fuels derived from the flame images in the optical LUPOE 2D boosted engine is shown in Fig.5. The mean entrainment flame radius was defined as the radius of a circle having the same area as enflamed cross-sectional area, calculated from an image. For Ricardo E6 engine, the burnt flame radius was derived from LUSEIDA by using averaged pressure curve as input. The difference between entrainment flame radius and burnt gas radius is supposed to be the turbulent flame brush thickness.

Three main stages of turbulent flame propagation in SI engines were discerned: an initial acceleration, propagation with approximately constant speed and the final deceleration caused by the proximity of walls [20]. In both engines, E05 has a slightly stronger initial acceleration, ETBE blend and iso-octane show very similar performance at this stage. At the period when the flame radius is between 15mm to 30 mm, the flame speed tends to be constant. Using a linear approximation, flame speeds were calculated for this period; the values are listed in Table 4, it can be seen that the difference of the flame speed between the three fuels' is small, while ETBE has slightly highest flame speed, the difference of about 5-10%.

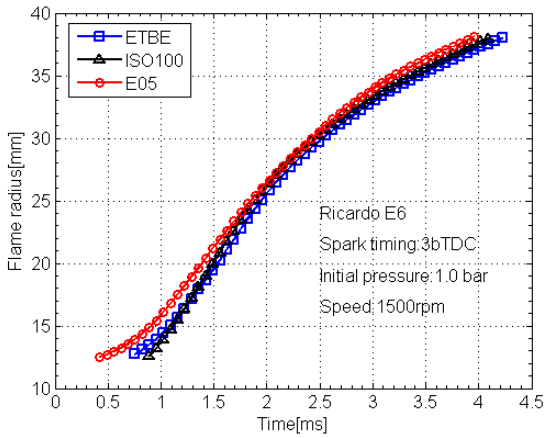

Figure 6. Burnt flame radius vs. time derived from the reverse thermodynamic analysis from the crank-resolved pressure trace in the Ricardo E6 for three fuels.

Table 4. Entrainment flame speed in the LUPOE-2D boosted engine and burnt flame speed at Ricardo E6.

Fuel	Entrainment flame speed (m/s) LUPOE-2D boosted	Burnt flame speed (m/s) Ricardo E6
E05	9.6	10.8
ETBE	10.5	11.4
ISO100	9.9	10.2

In general, E05 shows the fastest flame radius development during the first half of combustion because it has high initial acceleration. This phenomenon may be related to the highest laminar burning velocity of ethanol. The flame development of ETBE was slower than that of E05 in the beginning, however it

has slightly larger “developed” turbulent flame speed. At some point, when the flame is approximately half-way to the wall, ETBE blend flames reach the same radius as E05 owing to its faster entrainment flame speed. Isooctane was the slowest fuel of the three. These results derived from optical observation are corroborated by the results derived from the mean pressure signal.

Despite the turbulence being approximately twice stronger in Ricardo E6, the time required for the flame to grow from 15 to 35mm in size was slightly larger, circa 2.5 msec, in Ricardo E6 as compared to approximately 2 msec in LUPOE 2D, see Figs. 5 and 6. It may indicate a possible greater role of the flame instabilities at the higher pressures in LUPOE 2D, however, detailed investigation of this effect is beyond the scope of this paper. Nonetheless, it is worth noticing that, the combustion duration times are very similar in the two engines, the combustion duration angle in Ricardo E6 is almost double the one in the LUPOE 2D boosted engine, because the former runs at 1500 rpm. The spark timing was set close to TDC, therefore, combustion happened in the expansion stroke, with a strong drop of the peak combustion pressure with the increasing chamber volume. Moreover, Ricardo E6 engine has the side spark plug configuration. These factors result in much lower and later observed peak pressures in the Ricardo E6 engine.

Slow flame speeds weakened the linear relationship between maximum pressure, and crank angle at which the maximum pressures achieved. The linear relationship have been widely observed in several engines [19] . In Fig 7, the fastest fuel E05 still show a somewhat proportional relationship, while the slowest fuel Iso-octane may have the higher peak pressure in the late combustion angle. According to these figures, coefficient of variation of peak pressure COV-pmax was calculated for cyclic variability comparison, it is presented in Table 5. The cyclic variation of peak pressure for E05 is lower than that for iso-octane and EBTE10 at the LUPOE engine. However it becomes the highest one in Ricardo E6 engine.

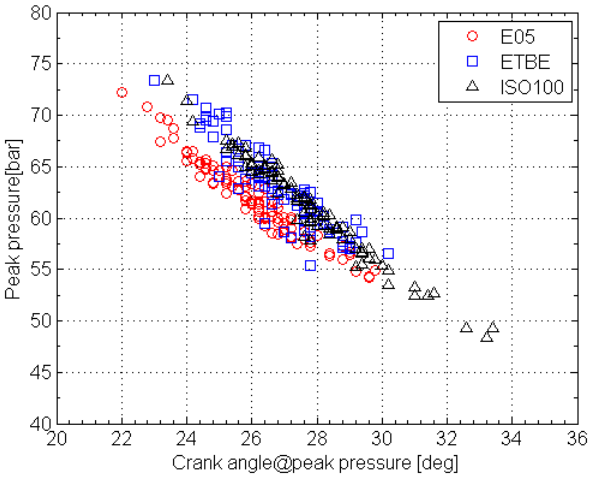

Figure 7. Peak pressure versus corresponding crank angle for its occurrence for ISO100, E05 and ETBE at LUPOE -2D boosted engine.

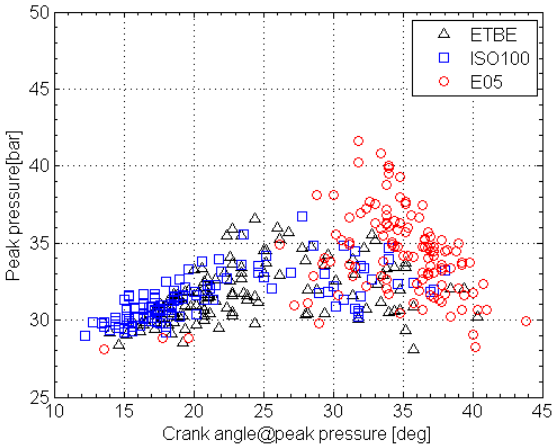

Figure 8. Peak pressure versus corresponding crank angle for its occurrence for ISO100, E05 and ETBE at Ricardo-E6.

Table 5. Coefficient of variation (COV) in peak pressure in the two engines for the three fuels.

Fuel	COV-pmax LUPOE-2Dboosted	COV-pmax Ricardo-E6
E05	12.2	12.3
ETBE	12.4	10.4
ISO100	13.2	11.0

Characteristics of knocking combustion

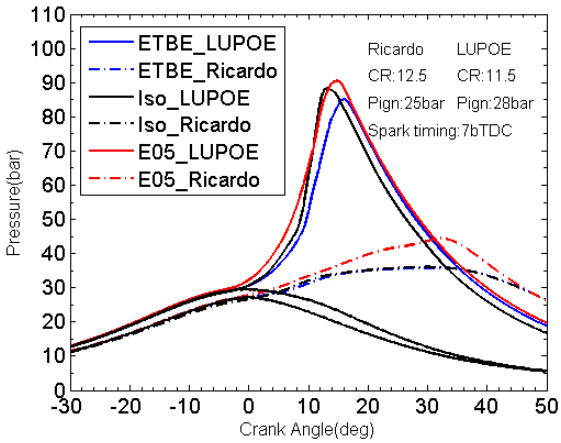

Figure 9. Knock combustion in-cylinder mean pressure traces for ETBE10, iso-octane and E05 in the LUPOE-2D boosted and Ricardo E6 engine at spark timing 7bTDC and operation conditions were listed in Table 1.

Under the same operational conditions as the normal combustion discussed above, the spark time was advanced to 7^{o} bTDC, at which point a larger proportion of the cycles was knocking. The mean low-pass filtered pressures for three fuels in the two engines are presented in Figure 9 and the individual

instantaneous cycles are shown in Appendix 2. Knock cycles appear accompanying with other normal combustion cycles. The onset of knock and its intensity vary cycle-by-cycle due to different end-gas temperature, pressure histories and mixture non-uniformities.

In LUPOE 2D engine, both ETBE blend and isooctane show very strong knock oscillation, while the knock-caused oscillations of E05-air mixture are much smaller. It indicates that E05 had better knock resistance than iso-octane or EBTE10 even though it has a lower nominal RON value. 100% iso-octane shows the most severe knock, the amplitude of which is approximately twice greater than that of E05. At the same time, the difference between knock intensities of the three fuels in Ricardo E6 is not significant.

Iso-octane has the RON of 100, ETBE-PRF blend has the RON value of 97.5, while the commercial gasoline E05 has the nominal RON of 95. At the conditions studied here, the end-gas auto-ignition occurs in the temperature interval of 750-800K and the pressures between 40 and 85 bar, these values belong to the so-called negative temperature coefficient region for the PRF fuels [22].

It has been said that when the original RON and MON tests were devised, values of K were approximately 1 [27]; therefore the OI was the average of the RON and MON. With the modern engines operating at lower temperatures as compared to the adiabatic compression of the end gas, owing to improved materials technology, use of direct injection and intercooled turbocharging, values of K are falling; therefore, when K is 0, the MON test is no longer relevant. More importantly for the latest series of downsized engines, K values can be negative, e.g. shown in Table 4, which brings about the situation of where OI value exceeds RON for a fuel of high sensitivity. This is confirmed in the present experiment, E05 has octane index (OI) of 104.3, while ETBE is 100.4. E05 shows better anti-knock properties than ETBE in the boosted engine condition, which is consistent to use of OI calculated from Eq.2. However, how K value influences the knock onset and intensity would still benefit from further investigation.

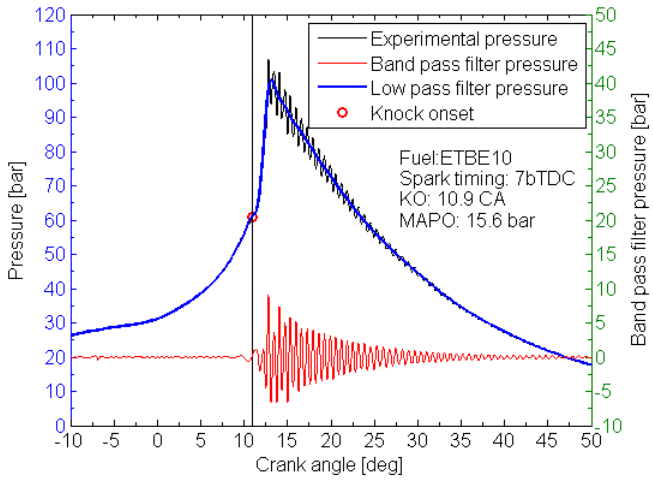

Figure 10. Typical knock cycle pressure in LUPOE-2D boosted engine and it was separated into low pass filter pressure and band pass filter pressure.

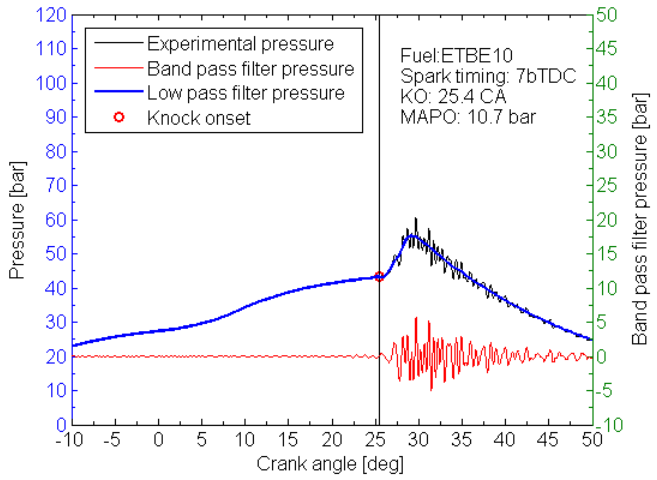

Figure 11. Typical knock cycle pressure in Ricardo E6 engine and it was separated into low pass filter pressure and band pass filter pressure.

Another significant difference of knock cycles between two engines is the knock pressure trace shape and heat release profile. Two typical knock cycles from LUPOE 2D boosted and Ricardo E6 engine were shown in Figures 10 and 11. It can be seen that the knock onset in LUPOE 2D is earlier than that in Ricardo; Knock onset in LUPOE 2D is about 11 ATDC, which approximately corresponds to 70% flame propagation across the cylinder chamber. After separating the knock pressure into low-passed filtered pressure and high-passed filtered pressure by using FFT filter, the maximum amplitude pressure oscillation (MAPO) can be acquired. The pressure oscillations magnitude in the first knocking cycle can reach the value up to 15.6 bar, much higher than for the second knocking cycle occurring at the later crank angle. In the Ricardo E6 engine the auto-ignition usually sets on when about 90% of mass is consumed in the normal flame propagation.

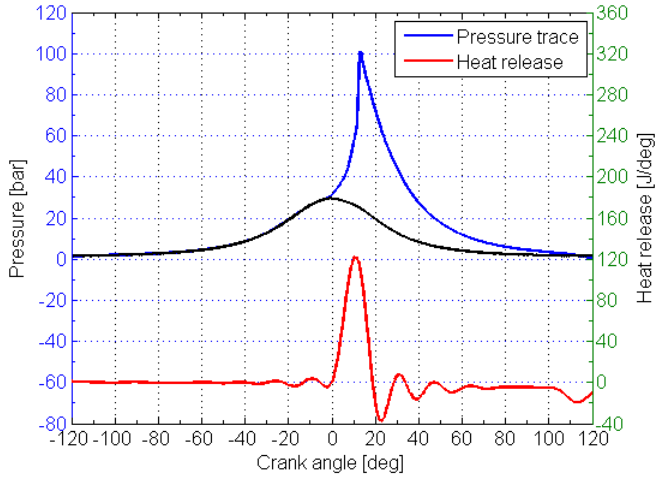

Figure 12. Corresponding low pass filter pressure of knock cycle presented in Fig 10 and its heat release.

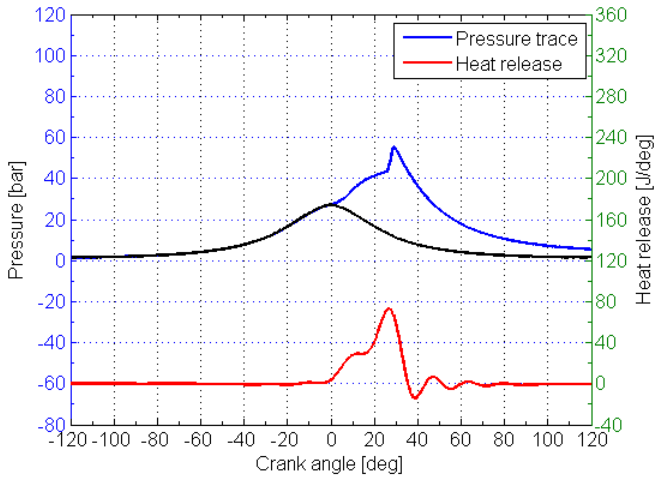

Figure 13. Corresponding low pass filter pressure of knock cycle presented in Fig 11 and its heat release.

Calculation of the heat release from the low-pass filtered pressure reveals two distinct heat release profiles. In the Ricardo E6 engine, two peak points can be observed in the heat release history, see Fig 13, the first, smaller, one comes from the flame propagation and the following, larger, and maximum is caused by auto-ignition. In LUPOE 2D engine, auto-ignition occurs before the peak heat release from flame propagation, and it consequently cannot be readily determined from the abnormal inflection point in the heat release rate history, see Fig 12. This is particularly remarkable for weaker auto-ignitions [28]. The difference between the two kinds of heat release can be used to explain the difference of MAPO. The autoignition occurring after heat release caused by flame propagation, has less energy left in the unburned air-fuel mixture, hence it has much smaller propensity to trigger violent pressure oscillations. When the auto-ignition happened before or along with main flame heat release stage, it may generate a very strong knock. This shows that a correlation for the knock intensity must take into account the mass fraction of the burnt gas at the moment of self-ignition.

Effects of boost

The average peak combustion pressure and knock MAPO were calculated by averaging individual cycles. The results for the two engines are shown in Figures 14 and 15. As the spark timing is advanced, average knock MAPO increases and knock tends to occur earlier. The shown average knock MAPO actually includes non-knocking cycles as well; for any set conditions at the knock borderline there is always a proportion of cycles showing very mild or no pressure oscillations; thus further confirming the influence of the main flame propagation stage on the auto-ignition of the end gas. These effects of cyclic variability are worth taking into account, in particular, when using the engine data for the chemical kinetics simulations of auto-ignition.

For any of the three fuels studied, no knock was detected in the LUPOE 2D engine operated in the naturally aspirated mode, i.e with initial pressure of 1.0bar at the instant of ports closure. In LUPOE 2D boosted engine, the knock transition of E05 occurs at a spark advance of 8 to 10 degrees CA bTDC; that is to say that 100% cycles exhibit pressure oscillations at the ignition timing of 10^0CA bTDC while the proportion of knocking cycles is about 50% at the ignition timing of 8^0CA bTDC. Similar knock transition occurs at the spark timing of 10-11^0CA bTDC in the Ricardo E6 run at the same compression ratio as LUPOE2-D. For ETBE-10 and iso-octane, a spark timing advance from 5 to 7 CA degrees bTDC makes the transition from no knock to all cycles knocking in the supercharged LUPOE 2D. The same fuels exhibit the similar knock transition at more advanced ignition of 12-13 degrees bTDC in Ricardo E6. The knock boundaries for the three fuels are very close in Ricardo E6. E05 has a knock-limited spark advance difference of about 1-2 degrees CA compared to ETBE blend and iso-octane; this is consistent with their nominal RON values. However, the situation is very different in LUPOE 2D boosted engine, where E05 shows markedly better anti-knock properties than ETBE or iso-octane.

Fig. 7 and the previous work [23] show that the peak pressure is a proxy measure of the burning rate in an individual cycle. Fig. 14 shows that at the most retarded spark, at 3^0CA bTDC, the fastest burning fuel is ETBE-10; it is also the only one exhibiting knock at this timing. E05 is the slowest burning fuel in the LUPOE2D and it is the most resilient to auto-ignition even though it has lowest RON of the three fuels. For the intermediate spark timing of 5-6^0CA bTDC where all three fuels show approximately the same peak pressures from normal combustion, hence similar burning rates they also show similar knock MAPO's.

The relative order of the burning rates is inverted in the naturally aspirated Ricardo E6, see Fig. 15. Here, the E05 is the fastest burning fuel showing at the same time the highest average peak pressures and the worst knock amplitudes. It is perhaps worth noticing that for common ignition timings of around 10^0CA bTDC the auto-ignition resistance of the three fuels is very similar even though E05 burns slightly faster; very likely, this comes as a result of optimisation of the composition of this pump gasoline. Another interesting remark is that, despite its high RON, the iso-octane performs worst at the most retarded spark timings and it is the only fuel for which some cycles do show auto-ignition.

Figures 16 and 17 show the timing of auto-ignition averaged only for knocking cycles. As discussed previously the auto-ignition onset varies from on knocking cycle to another. It is interesting to notice that the average knock onset is, for a given fuel in a given engine, is a linear function of the spark advance, see Fig. 16 for LUPOE 2D and Fig. 17 for Ricardo E6. Comparison of Figs. 15 and 17 for iso-octane shows that variation of ignition timing results in a very significant variation of the auto-ignition timing but it only slightly affects the MAPO. Ricardo engine has higher end-gas temperature near the TDC at the spark timing closer to TDC. It is difficult to ascertain the effects caused by lower temperatures at the TDC in the LUPOE-2D come from the fact the end-gas conditions fall into the so-called negative temperature coefficient (NTC) region where further increase in temperature leads to an increase of the ignition delay. This difficulty arises because of a sensitivity of the NTC region to the pressure and even small variations in fuel composition, especially oxygenated compounds.

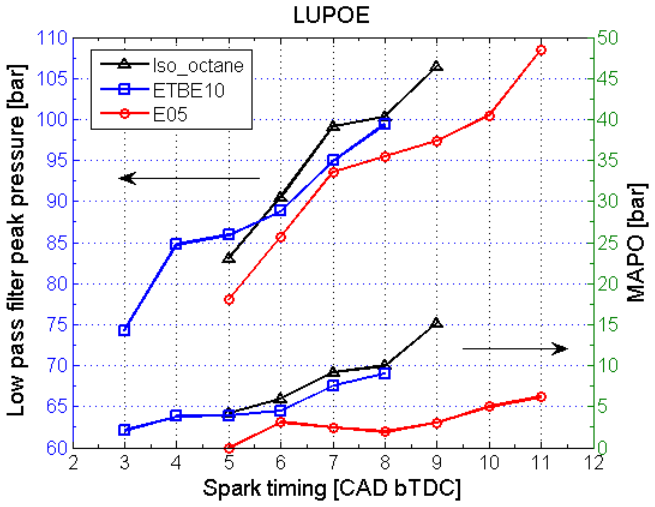

Figure 14. Effect of spark timing on peak pressure and MAPO in the LUPOE -2D boosted engine.

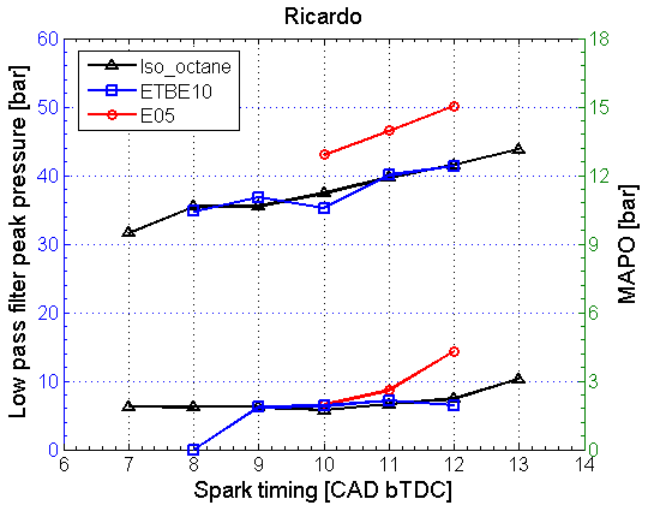

Figure 15. Effect of spark timing on peak pressure and MAPO in the Ricardo E6 engine.

Leaving aside the possible effects of the chemical kinetics, the previous work in the supercharged optical engine [14] has shown that there is a large amount of cyclic variability in the knock intensity even when the auto-ignition occurs at the same crank angle and the engine is run at the nominally the same conditions. The general observation was that faster main combustion stage generates earlier auto-ignition and stronger pressure oscillations. These previous findings are in a perfect qualitative agreement with the present results.

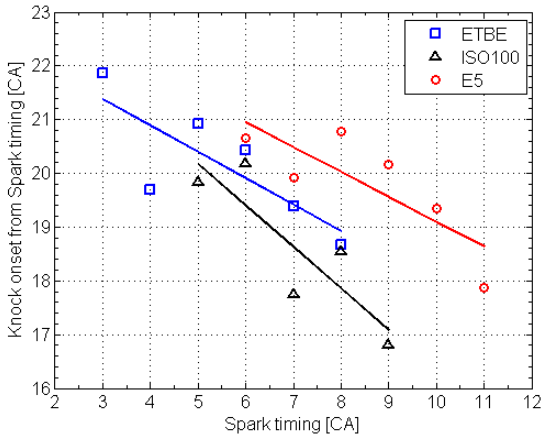

Figure 16. Effect of spark timing on knock onset in the LUPOE -2D boosted engine.

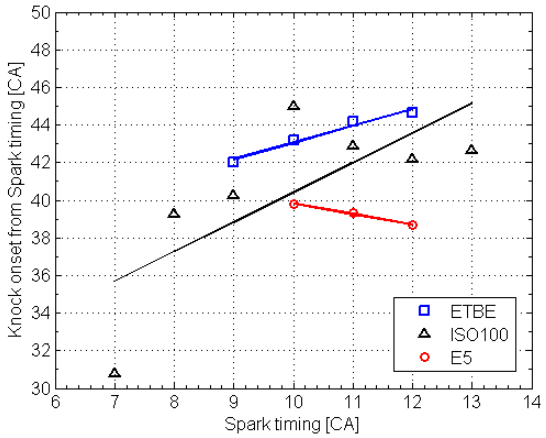

Figure 17. Effect of spark timing on knock onset in the Ricardo E6 engine.

Effects of compression ratio

The knock intensity values for three fuels measured in Ricardo E6 at the different compression ratios are shown in Figure 18as carpet plots. As the compression ratio increases, the knock boundary is shifted towards the top dead centre. At higher compression ratios, the pressure in cylinder increases and leads to knock. Similarly to the above-shown results for Ricardo E6, the iso-octane seems to have best anti-knock characteristics among three fuels. It was found that spark timing at the knock boundary is advanced by about 1 deg CA for ETBE-10 and 2 deg CA for E05 as compared with iso-octane. At the same spark timing, higher compression ratio causes more severe knock. It should be noticed that there exists a region at high compression ratio where cycles might have auto-ignition with quite small pressure oscillations. E05 has larger such region than ETBE blend, it indicates that E05 also has better anti-knock property at high compression ratios in a naturally aspirated engine. This kind of combustion mode may provide a way to gain high efficiency operation with modern oxygenated fuel blends.

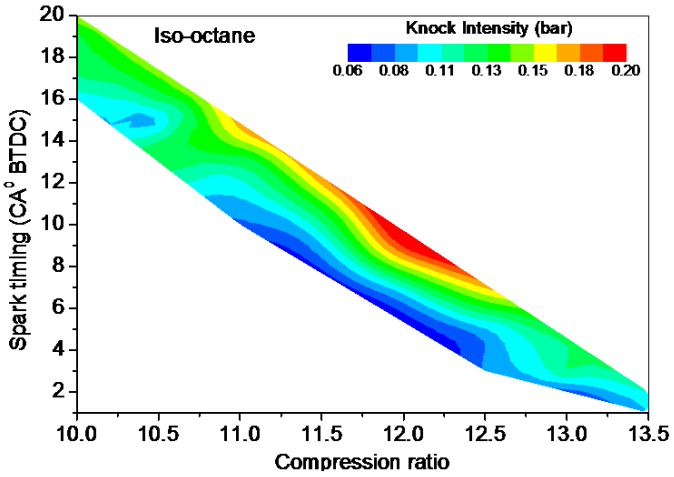

(a)

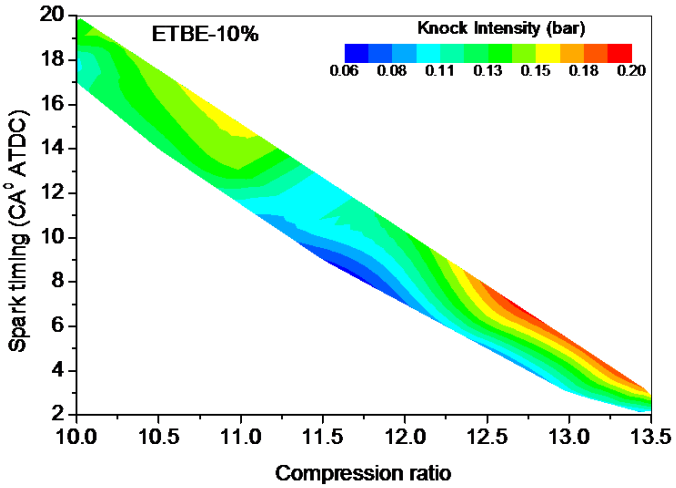

(b)

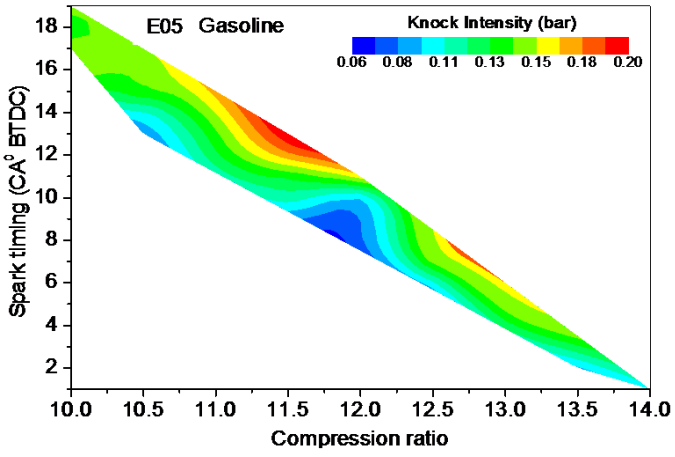

(c)

Figure 18. Knock intensity map with variable compression ratios and spark timing for Iso-octane (a),ETBE-10%(b) and E05 (c).

Conclusions

Presented in this paper are the experimental findings and conclusions from two one-cylinder spark ignition engines: LUPOE 2D boosted and Ricardo E6 naturally aspirated engine, with testing fuels of primary reference fuel (Iso-octane), blends of ETBE with 95PRF, and ethanol-gasoline commercial fuel (E05). In both engines, E05 has highest initial flame acceleration during the flame development period while ETBE blend has the fastest established turbulent flame speed.

Boosted LUPOE 2D engine has lower K value than the Ricardo E6 engine under different compression ratios, resulting in lower temperature during engine compression.

The significant difference of knock boundaries of three fuels have been found in the boosted LUPOE 2D boosted engine at the intake manifold (initial) pressure of 1.6bar, and almost similar knock boundaries under different compression ratios in the naturally aspirated engine.

100% iso-octane has the best anti-knock characteristic in naturally aspirated engine. However, the anti-knock tendency was reversed in strongly charged engine. E05 show the best anti-knock properties among three fuels under boosted condition, and knock onset was influenced slightly by inlet boosted pressure.

The knock onset and intensity is determined mainly by the temperature-pressure history which, in its turn, depends upon the burning rates. The general trend is that the fuel with the faster burning rate will result in an earlier auto-ignition of the end gas and larger MAPO.

Knock intensity maps for three fuels under a wide range of compression ratios have been made, there exists a region that auto-ignition occurs with slightly pressure oscillation at high compression ratio, which may be exploited with the high anti-knock oxygenated fuels.

References

1. A.A.Kumar. "Biofuels (Alcohols and Biodiesel) Applications as Fuels for Internal Combustion Engines." *Progress in energy and combustion science* 33, no. 3 (2007): 233-71.
2. A.E.Hussin. *New and Renewable Energy: Reewable Fuels in Internal Combustion Engines*, PhD thesis, in *School of Mechaincal Engineering*. 2012, University of Leeds: Leeds.
3. R.A.Stein, J.E.Anderson,and T.J.Wallington."An Overview of the Effects of Ethanol-Gasoline Blends on Si Engine Performance, Fuel Efficiency, and Emissions." *SAE Int. J. Engines* 6, no. 1 (2013): 470-87.
4. F.Yüksel, and B.Yüksel. "The Use of Ethanol–Gasoline Blend as a Fuel in an Si Engine." *Renewable energy* 29, no. 7 (2004): 1181-91.
5. J. W. G.Turner, R. J. Pearson, B. Holland, and R. Peck. "Alcohol-Based Fuels in High Performance Engines." SAE Technical Paper 2007-01-0056, 2007, doi:10.4271/2007-01-0056.
6. R, Magnusson. and C. Nilsson. "The Influence of Oxygenated Fuels on Emissions of Aldehydes and Ketones from a Two-Stroke Spark Ignition Engine." *Fuel* 90, no. 3 (2011): 1145-54.

7. C. M. Shiblom, G. A. Schoonveld, R. K. Riley, and R. H. Pahl. "Use of Ethyl-T-Butyl Ether (Etbe) as a Gasoline Blending Component." SAE Technical Paper 902132, 1990, doi:10.4271/902132.
8. G, Wallace, J. Blondy, W. Mirabella, E. Schulte-Körne, and J. Viljanen. "Ethyl Tertiary Butyl Ether - a Review of the Technical Literature." *SAE Int. J. Fuels Lubr.* 2, no. 1 (2009): 940-52.
9. K. Koseki, M. Wakita, N. Okabe, T. Kaneko, M. Watanabe, K. Horie, T. Kikuchi*, et al.* "Investigations of Compatibility of Etbe Gasoline with Current Gasoline Vehicles." SAE Technical Paper 2007-01-2039, 2007, doi:10.4271/2007-01-2039.
10. P. E. Jenkins, Y-S. Cho, and B. Kim. "Performance Analysis of a Spark Ignited Engine with Etbe as a Blending Agent." SAE Technical Paper 901520, 1990, doi:10.4271/901520.
11. D. Karonis, G. Anastopoulos, E. Lois, and S. Stournas. "Impact of Simultaneous Etbe and Ethanol Addition on Motor Gasoline Properties." *SAE Int. J. Fuels Lubr.* 1, no. 1 (2008): 1584-94.
12. J. Milpied, N, Jeuland, G, Plassat, S, Guichaous, N, Dioc, A. Marchal, and P. Schmelzle. "Impact of Fuel Properties on the Performances and Knock Behaviour of a Downsized Turbocharged Di Si Engine - Focus on Octane Numbers and Latent Heat of Vaporization." *SAE Int. J. Fuels Lubr.* 2, no. 1 (2009): 118-26.
13. J. S. Young, R. Lewis, L. Bromberg, and J. Heywood. "Performance Maps of Turbocharged Si Engines with Gasoline-Ethanol Blends: Torque, Efficiency, Compression Ratio, Knock Limits, and Octane." SAE Technical Paper 2014-01-1206, 2014, doi:10.4271/2014-01-1206.
14. Z.Y. Ling, A.A.Burluka., *Self-ignition and knock in normally aspirated and strongly charged SI engine.*, in *European Combustion Meeting 2013*. 2013: Lund, Sweden.
15. J. Pan, and C. G. W. Sheppard. "A Theoretical and Experimental Study of the Modes of End Gas Autoignition Leading to Knock in S. I. Engines." SAE Technical Paper 942060, 1994, doi:10.4271/942060.
16. P,J, Roberts, and C. G. W. Sheppard. "The Influence of Residual Gas No Content on Knock Onset of Iso-Octane, Prf, Trf and Ulg Mixtures in Si Engines." *SAE Int. J. Engines* 6, no. 4 (2013): 2028-43.
17. R. Worret, S. Bernhardt, F. Schwarz, and U. Spicher. "Application of Different Cylinder Pressure Based Knock Detection Methods in Spark Ignition Engines." SAE Technical Paper 2002-01-1668, 2002, doi:10.4271/2002-01-1668.
18. V.Mittal, B. M. Revier, and J. B. Heywood. "Phenomena That Determine Knock Onset in Spark-Ignition Engines." SAE Technical Paper 2007-01-0007, 2007, doi:10.4271/2007-01-0007.
19. A. A. Burluka, K. X. Liu, C. G. W. Sheppard, A. J. Smallbone, and R. Woolley. "The Influence of Simulated Residual and No Concentrations on Knock Onset for Prfs and Gasolines." SAE Technical Paper 2004-01-2998, 2004, doi:10.4271/2004-01-2998.
20. K.X.Liu, A. A. Burluka, and C. G. W. Sheppard. "Turbulent Flame and Mass Burning Rate in a Spark Ignition Engine." *Fuel* 107 (2013): 202-08.
21. G.T.Kalghatgi. "Auto-Ignition Quality of Practical Fuels and Implications for Fuel Requirements of Future Si and Hcci Engines." SAE Technical Paper 2003-01-3215, 2003, doi:10.4271/2003-01-3215.
22. G.T.Kalghatgi, K. Nakata, and K. Mogi. "Octane Appetite Studies in Direct Injection Spark Ignition (Disi) Engines." SAE Technical Paper 2005-01-0244, 2005, doi:10.4271/2005-01-0244.
23. A.A.Burluka, A. E. Hussin, Z.Y. Ling, and C.G.W. Sheppard. "Effects of Large-Scale Turbulence on Cyclic Variability in Spark-Ignition Engine." *Experimental Thermal and Fluid Science* 43 (2012): 13-22.
24. Z.Y. Ling, A.A.Burluka., *Effect of increased initial pressure on premixed turbulent flame development in SI Engines*, in *the 7th Biennial Meeting for the Scandinavian-Nordic Section*. 2014: Cambridge,UK.
25. H.Daneshyar, and D.E. Fuller, *Definition and Measurement of Turbulence Parameters in Reciprocating I.C. Engines*. SAE Technical Paper 861529, 1986
26. A,Erdil., et al. *"Decomposition of Turbulent Velocity Signals Using Moving Average Filter"*. in *ELECO" 2001 International Conference on Electrical and Electronics Engineering*.
27. V.Mittal, and John B. Heywood. "The Shift in Relevance of Fuel Ron and Mon to Knock Onset in Modern Si Engines over the Last 70 Years." *SAE Int. J. Engines* 2, no. 2 (2009): 1-10.
28. J.M.Borg, and A.C.Alkidas. "Characterization of Autoignition in a Knocking Si Engine Using Heat Release Analysis." SAE Technical Paper 2006-01-3341, 2006, doi:10.4271/2006-01-3341.

Acknowledgments

Zheng-Yang Ling gratefully acknowledges the financial support of the China Scholarship Council.

Definitions/Abbreviations

CR	Compression Ratio
bTDC	Before Top Dead Center
aTDC	After Top Dead Center
KO	Knock Onset
KI	Knock Intensity
MAPO	Maximum Amplitude Pressure Oscillation

Appendix

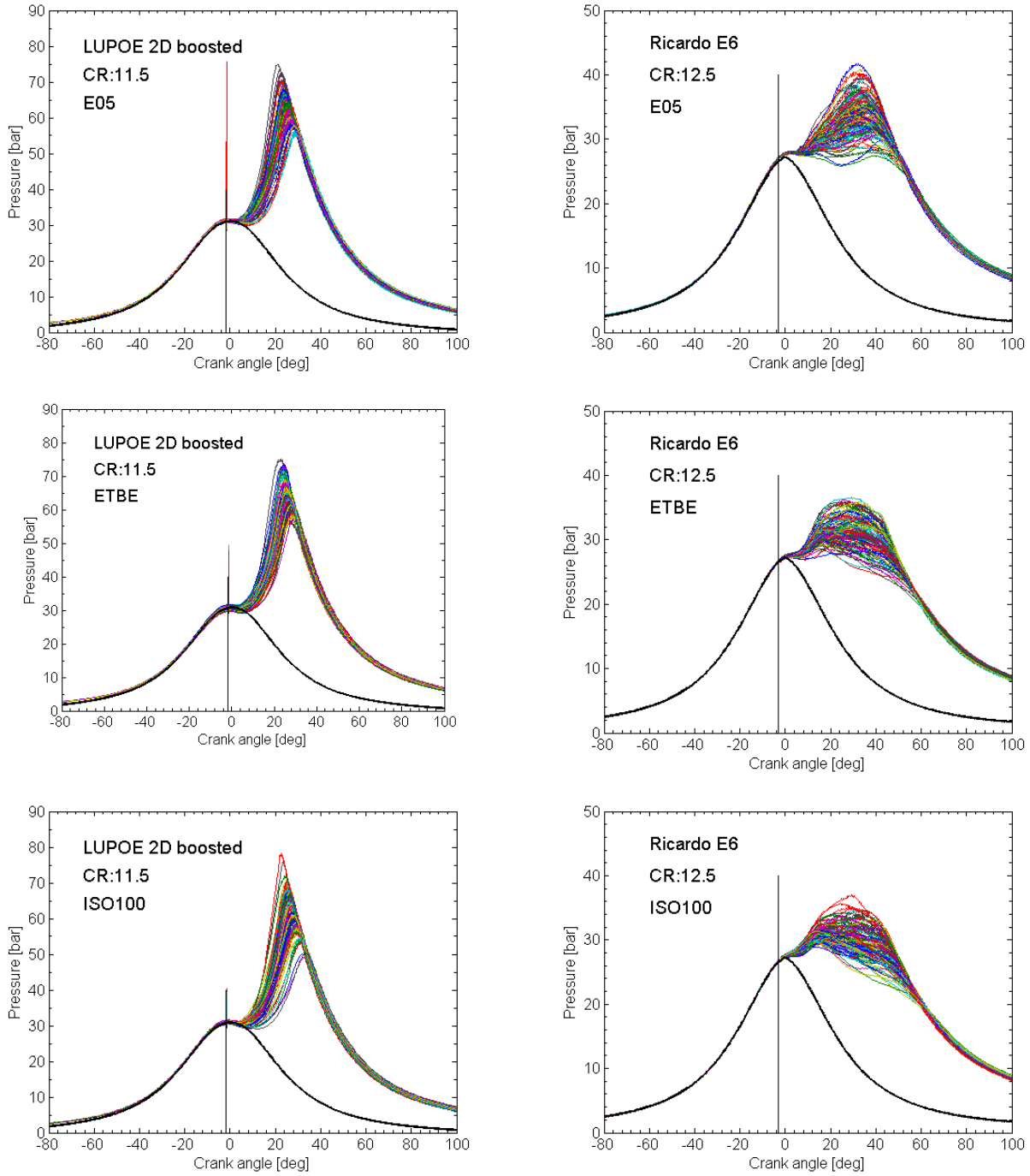

Figure 19. Normal combustion cycles for three fuels, compression ratio of LUPOE-2D boosted is 11.5, compression ratio of Ricardo E6 is 12.5. spark timing is 2 degrees bTDC for LUPOE-2D, 3 degrees bTDC for Ricardo E6.

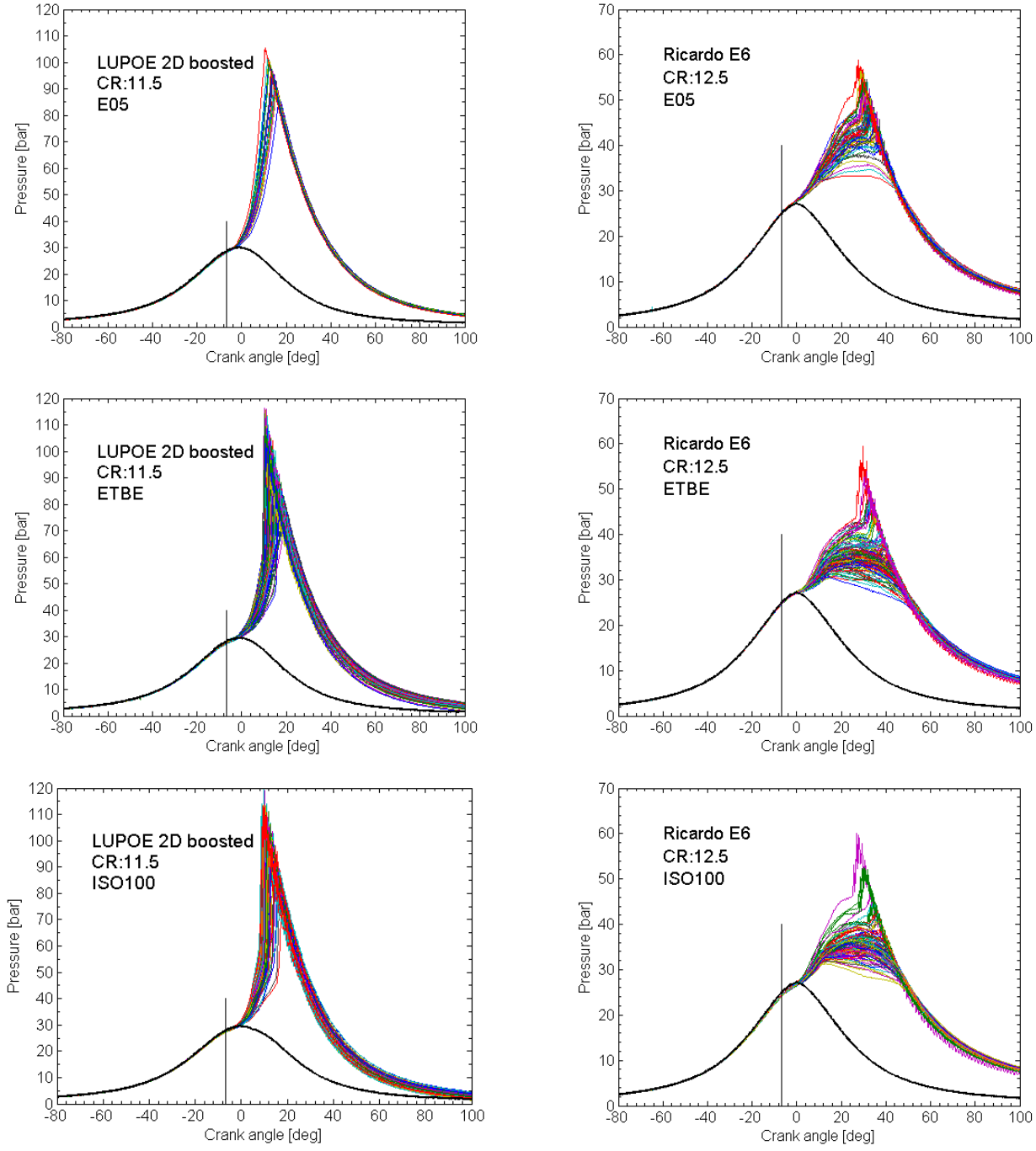

Figure 20. Knock cycles at same spark timing: 7deg bTDC for three fuels, compression ratio of LUPOE-2D boosted is 11.5, compression ratio of Ricardo E6 is 12.5.

References

Abdel-Gayed, R., Bradley, D., and Lung, F.-K. (1989). Combustion regimes and the straining of turbulent premixed flames. *Combustion and Flame*, 76(2):213–218. 25

Abdel-Gayed, R. G., Bradley, D., and Lawes, M. (1987). Turbulent burning velocities: A general correlation in terms of straining rates. *Proceedings of the Royal Society of London. A. Mathematical and Physical Sciences*, 414:389–413. 12, 13, 157, 158

Abdi Aghdam, E. (2003). *Improvement and Validation of a Thermodynamic S.I. Engine Simulation Code*. PhD thesis, Department of Mechanical Engineering, The University of Leeds. 19, 61, 63, 157, 159

Abraham, J., Williams, F. A., and Bracco, F. V. (1985). A discussion of turbulent flame structure in premixed charges. *Society of Automotive Engineers*, SAE Technical Paper 850345. 16

Al-Shahrany, A. S., Bradley, D., Lawes, M., and Woolley, R. (2005). Measurement of unstable burning velocities of iso-octane-air mixtures at high pressure and the derivation of laminar burning velocities. *Proceedings of the Combustion Institute*, 30:225–232. 30, 117, 118, 124

Aleiferis, P., Serras-Pereira, J., and Richardson, D. (2013). Characterisation of flame development with ethanol, butanol, iso-octane, gasoline and methane in a direct-injection spark-ignition engine. *Fuel*, 109:256–278. 40

Aleiferis, P., Serras-Pereira, J., Van Romunde, Z., Caine, J., and Wirth, M. (2010). Mechanisms of spray formation and combustion from a multi-hole injector with e85 and gasoline. *Combustion and Flame*, 157(4):735–756. 40

Aleiferis, P., Taylor, A., Ishii, K., and Urata, Y. (2004). The nature of early flame development in a lean-burn stratified-charge spark-ignition engine. *Combustion and Flame*, 136(3):283–302. 32, 40, 165

Atashkari, K. (1997). *Laser Diagnostics in Combustion and In-Cylinder Flow*. PhD thesis, Department of Mechanical Engineering, The University of Leeds. 7

Attard, W. P., Toulson, E., Watson, H., and Hamori, F. (2010). Abnormal combustion including mega knock in a 60% downsized highly turbocharged PFI engine. *Society of Automotive Engineers*, SAE Technical Paper 2010-01-1456. 2, 3, 34

Baratta, M., Catania, A. E., Spessa, E., and Vassallo, A. (2006). Development and assessment of a multizone combustion simulation code for SI engines based on a novel fractal model. *Society of Automotive Engineers*, SAE Technical Paper 2006-01-0048. 158

Bates, S. C. (1991). Further insights into SI four-stroke combustion using flame imaging. *Combustion and Flame*, 85(3):331–352. 40

Beretta, G., Rashidi, M., and Keck, J. (1983). Turbulent flame propagation and combustion in spark ignition engines. *Combustion and Flame*, 52:217–245. 27, 40

Borghi, R. and Destriau, M. (1998). *Combustion and flames: chemical and physical principles*. Editions Technip, Paris, 1st edition. 22, 24

Bradley, D. and Head, R. (2006). Engine autoignition: The relationship between octane numbers and autoignition delay times. *Combustion and flame*, 147(3):171–184. 38

Bradley, D., Hicks, R. A., Lawes, M., and Sheppard, C. G. W. (1998). The measurement of laminar burning velocities and markstein numbers for iso-octane-air and iso-octane-n-heptane-air mixtures at elevated temperatures and pressures in an explosion bomb. *Combustion and Flame*, 115:126–144. xiv, 29, 30, 115, 116, 117, 123

Bradley, D. and Kalghatgi, G. (2009). Influence of autoignition delay time characteristics of different fuels on pressure waves and knock in reciprocating engines. *Combustion and flame*, 156(12):2307–2318. 35, 39, 40

Bradley, D., Lau, A. K. C., and Lawes, M. (1992). Flame stretch rate as a determinant of turbulent burning velocity. *Philosophical Transactions of the Royal Society : Physical and Engineering Sciences*, 338(1650):359–387. 7, 16

Bradley, D., Morley, C., Gu, X., and Emerson, D. (2002). Amplified pressure waves during autoignition: relevance to cai engines. *Society of Automotive Engineers*, SAE Technical Paper 2002-01-2868. 39

Burke, M. P., Chen, Z., Ju, Y., and Dryer, F. L. (2009). Effect of cylindrical confinement on the determination of laminar flame speeds using outwardly propagating flames. *Combustion and Flame*, 156(4):771–779. 123

Buschbeck, M., Bittner, N., Halfmann, T., and Arndt, S. (2012). Dependence of combustion dynamics in a gasoline engine upon the in-cylinder flow field, determined by high-speed PIV. *Experiments in fluids*, 53(6):1701–1712. 40

Cairns, A. (2001). *Turbulent Flame Development in a Spark Ignition Engine*. PhD thesis, Department of Mechanical Engineering, The University of Leeds. 47, 76, 82, 87, 132, 165

Chen, L., Stone, R., and Richardson, D. (2012). A study of mixture preparation and pm emissions using a direct injection engine fuelled with stoichiometric gasoline/ethanol blends. *fuel*, 96:120–130. 40

Chen, Y.-C., Peters, N., Schneemann, G., Wruck, N., Renz, U., and Mansour, M. S. (1996). The detailed flame structure of highly stretched turbulent premixed methane-air flames. *Combustion and flame*, 107(3):223–IN2. 25

Conway, G. (2010). High pressure autoignition modelling in S.I. engines - transfer report. *Department of Mechanical Engineering, The University of Leeds*. 49

Conway, G. T. (2013). *Cyclic variability of flame propagation and autoignition in supercharged and naturally aspirated SI engines*. PhD thesis, Department of Mechanical Engineering, The University of Leeds. x, 49, 174

Cruz, P., Vianna, J., and Moreira, C. S. (2003). Study of the turbulence intensity variation within the combustion chamber of an S.I engine due to turbocharging. *Society of Automotive Engineers*, SAE Technical Paper 2003-01-3687. 14

Curran, H. J., Gaffuri, P., Pitz, W., and Westbrook, C. (2002). A comprehensive modeling study of iso-octane oxidation. *Combustion and flame*, 129(3):253–280. 36

Dahnz, C. and Spicher, U. (2010). Irregular combustion in supercharged spark ignition engines- pre-ignition and other phenomena. *International Journal of Engine Research*, 11:485–499. 2, 34, 38

Dawood, A. (2010). *Combustion and Flow Characteristics in a Disc-Shaped Spark Ignition Engine*. PhD thesis, Department of Mechanical Engineering, The University of Leeds. 14, 41, 69, 71, 76, 77, 129, 137

Desoky, A. (1981). *An experiental and theoretical study of the combustion process in a divided chamber spark ignition engine*. PhD thesis, Department of Mechanical Engineering, The University of Leeds. 61

DoE, U. (2014). International energy outlook 2014. *In: Energy Information Administration Office of Integrated Analysis and Forecasting U.S. Department of Energy Washington, D. (Ed.). http://www.eia.gov/forecasts/ieo/*. 1

Driscoll, J. F. (2008). Turbulent premixed combustion: Flamelet structure and its effect on turbulent burning velocities. *Progress in Energy and Combustion Science*, 34(1):91–134. 24

Eckbreth, A. C. (1996). *Laser diagnostics for combustion temperature and species*. CRC Press. 76, 86

Fajardo, C. and Sick, V. (2009). Development of a high-speed uv particle image velocimetry technique and application for measurements in internal combustion engines. *Experiments in Fluids*, 46(1):43–53. 67

Ferguson, R. C. and Kirkpatrick, T. A. (2001). *Internal Combustion Engines: Applied Thermosciences*. John Wiley & Sons, New York, 2nd edition. 210

Firey, J. (1957). A detonation wave theory of gasoline engine knock. *Symposium (International) on Combustion*, 6(1):878–886. 35

Foucher, F. and Mounaïm-Rousselle, C. (2005). Fractal approach to the evaluation of burning rates in the vicinity of the piston in a spark-ignition engine. *Combustion and flame*, 143(3):323–332. 40

Fraser, N., Blaxill, H., Lumsden, G., and Bassett, M. (2009). Challenges for increased efficiency through gasoline engine downsizing. *Society of Automotive Engineers*, SAE Technical Paper 2009-01-1053. 2

Galmiche, B., Halter, F., and Foucher, F. (2012). Effects of high pressure, high temperature and dilution on laminar burning velocities and markstein lengths of iso-octane/air mixtures. *Combustion and Flame*, 159(11):3286–3299. xiv, 115, 116, 117

Gatowski, J. A., Heywood, J. B., and Deleplace, C. (1984). Flame photographs in a spark-ignition engine. *Combustion and flame*, 56(1):71–81. 40, 75

Gaydon, A. G. (1957). *The spectroscopy of flames*. Chapman and Hall London. 32, 84

Gerke, U., Steurs, K., Rebecchi, P., and Boulouchos, K. (2010). Derivation of burning velocities of premixed hydrogen/air flames at engine-relevant conditions using a single-cylinder compression machine with optical access. *International Journal of Hydrogen Energy*, 35(6):2566–2577. 93, 123

Gillespie, L., Lawes, M., Sheppard, C. G. W., and Woolley, R. (2000). Aspects of laminar and turbulent burning velocity relevant to SI engines. *Society of Automotive Engineers*, SAE Technical Paper 2000-01-0192. 28

Griebel, P., Siewert, P., and Jansohn, P. (2007). Flame characteristics of turbulent lean premixed methane/air flames at high pressure: Turbulent flame speed and flame brush thickness. *proceedings of the Combustion Institute*, 31(2):3083–3090. 30

Griffiths, J. F. and Barnard, J. A. (1995). *Flame and Combustion*. Blackie Academic & Professional, Glasgow, 3rd edition. 15, 16, 33, 36

Groff, E. G. and Matekunas, F. A. (1980). The nature of turbulent flame propagation in a homogeneous spark-ignited engine. *Society of Automotive Engineers*, SAE Technical Paper 800133. 27

Groot, G., Van Oijen, J., De Goey, L., Seshadri, K., and Peters, N. (2002). The effects of strain and curvature on the mass burning rate of premixed laminar flames. *Combustion Theory and Modelling*, 6(4):675–695. 21

Gu, X., Emerson, D., and Bradley, D. (2003). Modes of reaction front propagation from hot spots. *Combustion and flame*, 133(1):63–74. 38, 40

Hall, M. J. and Bracco, F. V. (1987). A study of velocities and turbulence intensities measured in firing and motored engines. *Society of Automotive Engineers*, SAE Technical Paper 870453. 94

Hardalupas, Y. and Orain, M. (2004). Local measurements of the time-dependent heat release rate and equivalence ratio using chemiluminescent emission from a flame. *Combustion and Flame*, 139(3):188–207. 32

Hattrell, T. (2007). *A Computational and Experimental Study of Spark Ignition Combustion*. PhD thesis, Department of Mechanical Engineering, The University of Leeds. 61, 76, 162

Heywood, J. B. (1988). *Internal Combustion Engine Fundamentals*. McGraw-Hill, New York, international edition edition. 7, 8, 34, 36, 42, 52, 173, 182

Hicks, R., Lawes, M., Sheppard, C., and Whitaker, B. (1994). Multiple laser sheet imaging investigation of turbulent flame structure in a spark ignition engine. *Society of Automotive Engineers*, SAE Technical Paper 941992. x, 41, 90, 169

Hill, P. and Zhang, D. (1994). The effects of swirl and tumble on combustion in spark-ignition engines. *Progress in energy and combustion science*, 20(5):373–429. 7

Hinze, J. (1975). *Turbulence: an introduction to its mechanism and theory*. McGraw-Hill, New York, 2nd edition. 10

Hult, J., Richter, M., Nygren, J., Aldén, M., Hultqvist, A., Christensen, M., and Johansson, B. (2002). Application of a high-repetition-rate laser diagnostic system for single-cycle-resolved imaging in internal combustion engines. *Applied optics*, 41(24):5002–5014. 77

Hussin, A. (2012). *New and Renewable Energy:Renewable Fuels in Internal Combustion Engines*. PhD thesis, Department of Mechanical Engineering, The University of Leeds. 71, 75, 77, 129, 140, 161

Hynes, J. (1986). *A Computational and Experimental Study of Spark Ignition Combustion*. PhD thesis, Department of Mechanical Engineering, The University of Leeds. 61

Ihracska, B., Korakianitis, T., Ruiz, P., Emberson, D. R., Crookes, R. J., Diez, A., and Wen, D. (2014). Assessment of elliptic flame front propagation characteristics of iso-octane, gasoline, M85 and E85 in an optical engine. *Combustion and Flame*, 161(3):696–710. 41

Ikeda, Y., Nishihara, H., and Nakajima, T. (2001). Measurement of flame front structure and its thickness by planar and local chemiluminescence of OH*, CH* and C2*. *Society of Automotive Engineers*, SAE Technical Paper 2001-01-0920. 32, 76

Inoue, T., Inoue, Y., and Ishikawa, M. (2012). Abnormal combustion in a highly boosted SI engine-the occurrence of super knock. *Society of Automotive Engineers*, SAE Technical Paper 2012-01-1141. 2

Jerzembeck, S., Peters, N., Pepiot-Desjarins, P., and Pitsch, H. (2009). Laminar burning velocities at high pressure for primary reference fuels and gasoline: Experimental and numerical investigation. *Combustion and Flame*, 156:292–301. x, xiv, 29, 37, 115, 116, 117

Kalghatgi, G. and Bradley, D. (2012). Pre-ignition and 'super-knock' in turbo-charged spark-ignition engines. *International Journal of Engine Research*, 0:1–16. x, 33, 38, 39, 40

Kawahara, N., Tomita, E., and Sakata, Y. (2007). Auto-ignited kernels during knocking combustion in a spark-ignition engine. *Combustion Institute*, pages 2999–3006. 36

Kelley, A., Smallbone, A., Zhu, D., and Law, C. (2011). Laminar flame speeds of C5 to C8n-alkanes at elevated pressures: Experimental determination, fuel similarity, and stretch sensitivity. *Proceedings of the Combustion Institute*, 33(1):963–970. xiv, 116, 117, 124

Kheirkhah, S. and Gülder, Ö. (2013). Turbulent premixed combustion in v-shaped flames: Characteristics of flame front. *Physics of Fluids (1994-present)*, 25(5):055107. 169

Knaus, D. A., Gouldin, F. C., Hinze, P. C., and Miles, P. C. (1999). Measurement of instantaneous flamelet surface normals and the burning rate in a SI engine. *Society of Automotive Engineers*, SAE Technical Paper 1999-01-3543. 40

Kobayashi, H., Kawahata, T., Seyama, K., Fujimari, T., and Kim, J.-S. (2002). Relationship between the smallest scale of flame wrinkles and turbulence characteristics of high-pressure, high-temperature turbulent premixed flames. *Proceedings of the Combustion Institute*, 29(2):1793–1800. 22, 30, 130

Kobayashi, H., Nakashina, T., Tamura, T., Maruta, K., and Niioka, T. (1997). Turbulence measurements and observations of turbulent premixed flames at elevated pressure up to 3.0mpa. *Combustion Institute*, 108(1-2):104–110. 14, 30

Konig, G. and Sheppard, C. G. W. (1990). End gas autoignition and knock in a spark ignition engine. *Society of Automotive Engineers*, SAE Technical Paper 902135. 38, 41, 176, 185

Lake, T., Stokes, J., Murphy, R., Osborne, R., and Schamel, A. (2004). Turbocharging concepts for downsized D.I gasoline engines. *Society of Automotive Engineers*, SAE Technical Paper 2004-01-0036. 1

Lancaster, D. R. (1976). Effects of engine variables on turbulence in a spark-ignition engine. *Society of Automotive Engineers*, SAE Technical Paper 760159. 9

Landry, L., Halter, F., Foucher, F., Samson, E., and Rousselle, C. (2008). Effect of pressure and dilution on flame front displacement in boosted spark-ignition engine combustion. *Society of Automotive Engineers*, SAE Technical Paper 2008-01-1625. 14, 30, 42, 127, 137, 155

Langridge, S. (1995). *Imaging and thermodynamic analysis of autoignition and knock in SI engines*. PhD thesis, Department of Mechanical Engineering, The University of Leeds. 61

Larsson, G. (2009). *Turbulence Related Cyclic Variation in Combustion*. PhD thesis, Department of Mechanical Engineering, The University of Leeds. 74, 130

Lauer, M. and Sattelmayer, T. (2010). On the adequacy of chemiluminescence as a measure for heat release in turbulent flames with mixture gradients. *Journal of Engineering for Gas Turbines and Power*, 132(6):061502. 20

Lavision (2012). High-speed IRO. Technical report, Lavision. xi, 77, 78, 79

Law, C. K. (2006). *Combustion physics*. Cambridge University Press. 12, 17, 20, 29

Lawes, M., Ormsby, M. P., Sheppard, C. G. W., and Woolley, R. (2012). The turbulent burning velocities of iso-octane/air mixtures. *Combustion and Flame*, 159:19491959. 29, 31

Lecointe, B. and Monnier, G. (2003). Downsizing a gasoline engine using turbocharging with direct injection. *Progress in Energy and Combustion Science*, 28:1–74. 3

Ling, Z. (2011). Characterization of knock and autoignition in a boosted spark ignition engine- transfer report. *Department of Mechanical Engineering, The University of Leeds*. 52, 56

Liou, T.-M., Hall, M., Santavicca, D., and Bracco, F. (1984). Laser doppler velocimetry measurements in valved and ported engines. *Society of Automotive Engineers*, SAE Technical Paper 840375. 9

Lipatnikov, A. N. (1996). Some issues of using markstein number for modeling premixed turbulent combustion. *Combustion science and technology*, 119(1-6):131–154. 21

Lipatnikov, A. N. (2013). *Fundamentals of Premixed Turbulent Combustion*. CRC Press, Boca Raton, Florida, 1st edition. ix, 22, 24, 27, 28

Lipatnikov, A. N. and Chomiak, J. (1997). A simple model of unsteady turbulent flame propagation. *Society of Automotive Engineers*, SAE Technical Paper 972993. 158, 159

Lipatnikov, A. N. and Chomiak, J. (2000). Modeling of pressure and non-stationary effects in spark-ignition engine combustion: A comparison of different approaches. *Society of Automotive Engineers*, SAE Technical Paper 2000-01-2034. 162

Lipatnikov, A. N. and Chomiak, J. (2002). Turbulent flame speed and thickness: phenomenology, evaluation and application in multi-dimensional applications. *Progress in Energy and Combustion Science*, 28:1–74. 2, 151, 157

Liu, C.-C., Shy, S., Chen, H.-C., and Peng, M.-W. (2011). On interaction of centrally-ignited, outwardly-propagating premixed flames with fully-developed isotropic turbulence at elevated pressure. *Proceedings of the Combustion Institute*, 33(1):1293–1299. 29

Liu, C.-C., Shy, S. S., Peng, M.-W., Chiu, C.-W., and Dong, Y.-C. (2012). High-pressure burning velocities measurements for centrally-ignited premixed methane/air flames interacting with intense near-isotropic turbulence at constant reynolds numbers. *Combustion and Flame*, 159(8):2608–2619. 31

Liu, K., Burluka, A., and Sheppard, C. (2013). Turbulent flame and mass burning rate in a spark ignition engine. *Fuel*, 107:202–208. 27, 151

Mandilas, C. (2008). *Laminar and Turbulent Burning Characteristics of Hydrocarbon Fuels*. PhD thesis, Department of Mechanical Engineering, The University of Leeds. xi, 80, 81

Markstein, G. Non-steady flame propagation,(1964). *McMillan Publication, New York*. 21

Marshall, S., Taylor, S., Stone, C., Davies, T., and Cracknell, R. (2011). Laminar burning velocity measurements of liquid fuels at elevated pressures and temperatures with combustion residuals. *Combustion and Flame*, 158(10):1920–1932. 19, 29

Martz, J., Middleton, R., Lavoie, G., Babajimopoulos, A., and Assanis, D. (2011). A computational study and correlation of premixed isooctane–air laminar reaction front properties under spark ignited and spark assisted compression ignition engine conditions. *Combustion and Flame*, 158(6):1089–1096. 118

Mathieu, J. and Scott, J. (2000). *An introduction to turbulent flow*. Cambridge University Press, Cambridge, 1st edition. 6, 7, 10, 11, 12, 13

Merola, S., Sementa, P., Tornatore, C., and Vaglieco, B. (2009). Spectroscopic investigations and high resolution visualization of the combustion phenomena in a boosted PFI SI engine. *Society of Automotive Engineers*, SAE Technical Paper 2009-01-1814. ix, 32, 33

Merola, S., Vaglieco, B., Formisano, G., Lucignano, G., and Mastrangelo, G. (2007). Flame diagnostics in the combustion chamber of boosted PFI SI engine. *Society of Automotive Engineers*, SAE Technical Paper 2007-24-0003. 31, 127

Metghalchi, M. and Keck, J. C. (1982). Burning velocities of mixtures of air with methanol, isooctane, and indolene at high pressure and temperature. *Combustion and Flame*, 48:191–210. 19, 29, 115, 117, 118, 119, 149

Miller, C. D. (1947). Roles of detonation waves and autoignition in spark-ignition engine knock as shown by photographs taken at 40,000 and 200,000 frames per sec. *Society of Automotive Engineers*, SAE Technical Paper 470207. 35

Mittal, V., Revier, B. M., and Heywood, J. B. (2007). Phenomena that determine knock onset in spark-ignition engines. *Society of Automotive Engineers*, SAE Technical Paper 2007-01-0007. 183

Moisy, F. (2007). PIVMat: A PIV post-processing and data analysis toolbox for matlab. `http://www.fast.u-psud.fr/pivmat/`. 74

Morley, C. (2005). Gaseq: a chemical equilibrium program for windows. *http:// www. gaseq. co. uk*. 149

Mounaïm-Rousselle, C., Landry, L., Halter, F., and Foucher, F. (2013). Experimental characteristics of turbulent premixed flame in a boosted spark-ignition engine. *Proceedings of the Combustion Institute*, 34(2):2941–2949. 31, 42

Muard, A. E. M. A. (2006). *Flow and combustion in disc and pent roof SI engines*. PhD thesis, Department of Mechanical Engineering, The University of Leeds. 43, 76

Muller, U. C., Bollig, M., and Peters, N. (1997). Approximations for burning velocities and markstein numbers for lean hydrocarbon and methanol flames. *Combustion and Flame*, 108:349–356. 118

Neij, H., Johansson, B., and Aldén, M. (1994). Development and demonstration of 2D-LIF for studies of mixture preparation in SI engines. *Combustion and Flame*, 99(2):449–457. 77

Oran, E. S. and Gamezo, V. N. (2007). Origins of the deflagration-to-detonation transition in gas-phase combustion. *Combustion and Flame*, 148(1):4–47. 197

Otsu, N. (1975). A threshold selection method from gray-level histograms. *Automatica*, 11(285-296):23–27. 82

Pan, J., Sheppard, C., Tindall, A., Berzins, M., Pennington, S., and Ware, J. (1998). End gas inhomogeneity, autoignition and knock. *Society of Automotive Engineers*, SAE Technical Paper 982616. 39

Pan, J. and Sheppard, C. G. W. (1994). A theoretical and experimental study of the modes of end gas autoignition leading to knock in s.i. engines. *Society of Automotive Engineers*, SAETechnical Paper 942060. 34, 176, 185, 197

Peterson, B., Reuss, D. L., and Sick, V. (2014). On the ignition and flame development in a spray-guided direct-injection spark-ignition engine. *Combustion and Flame*, 161(1):240–255. 40

Pierce, P. H., Ghandhi, J. B., and Martin, J. K. (1992). Near-wall velocity characteristics in valved and ported motored engines. *Society of Automotive Engineers*, SAE Technical Paper 920152. 10

Pöschl, M. and Sattelmayer, T. (2008). Influence of temperature inhomogeneities on knocking combustion. *Combustion and Flame*, 153(4):562–573. 197

Prudnikov, A. (1964). Combustion of homogeneous fuel-air mixtures in turbulent flows. *Physical basis of processes in combustion chambers of airbreathing engines. Moscow: Mashinostroenie*, pages 255–347. 28

Raffel, M., Willert, C., and Kompenhans, J. (2007). *Particle Image Velocimetry: a practical guide*. Springer. 67, 68, 69, 71, 72, 73

Rallis, C. J. and Garforth, A. M. (1980). The determination of laminar burning velocity. *Progress in Energy and Combustion Science*, 6(4):303–329. 17, 20

Reuss, D. and Rosalik, M. (2000). PIV measurements during combustion in a reciprocating internal combustion engine. In *Laser Techniques Applied to Fluid Mechanics*, pages 441–456. Springer. 67

Robert, J. (1989). Chemkin-II: A fortran chemical kinetics package for the analysis of gas-phase chemical kinetics. *Sandia National Laboratories Report*, pages SAND89–8009B. x, 37, 119

Roberts, P. (2010). *Fuel and Exhaust Residual Effects in Spark Ignition and HCCI engines.* PhD thesis, Department of Mechanical Engineering, The University of Leeds. x, xi, 43, 45, 47, 49, 64, 171, 174, 186

Roudnitzky, S., Druault, P., and Guibert, P. (2006). Proper orthogonal decomposition of in-cylinder engine flow into mean component, coherent structures and random gaussian fluctuations. *Journal of Turbulence*, (7). 9

Rudloff, J., Zaccardi, J.-M., Richard, S., and Anderlohr, J. (2013). Analysis of pre-ignition in highly charged SI engines: Emphasis on the auto-ignition mode. *Proceedings of the Combustion Institute*, 34(2):2959–2967. 40, 178

Ryan, T. W. and Lestz, S. S. (1980). The laminar burning velocity of isooctane, n-heptane, methanol, methane, and propane at elevated temperature and pressures in the presence of a diluent. *Society of Automotive Engineers*, SAE Technical Paper 800103. 115

Schießl, R. and Maas, U. (2003). Analysis of endgas temperature fluctuations in an SI engine by laser-induced fluorescence. *Combustion and flame*, 133(1):19–27. 41

Scott, M, J. (1992). *Distributions of strain rate and temperature in turbulent combustion*. PhD thesis, Department of Mechanical Engineering, The University of Leeds. 12, 13, 130

Serras-Pereira, J., Aleiferis, P., and Richardson, D. (2012). Imaging and heat flux measurements of wall impinging sprays of hydrocarbons and alcohols in a direct-injection spark-ignition engine. *Fuel*, 91(1):264–297. 41

Shahed, S. M. and Bauer, K. H. (2009). Parametric studies of the impact of turbocharging on gasoline engine downsizing. *Society of Automotive Engineers*, SAE Technical Paper 2009-01-1472. 3

Smallbone, A. (2004). *Fuel and Residual Effects in Spark Ignition Engines*. PhD thesis, Department of Mechanical Engineering, The University of Leeds. 43, 174

Soika, A., Dinkelacker, F., and Leipertz, A. (2003). Pressure influence on the flame front curvature of turbulent premixed flames: comparison between experiment and theory. *Combustion and flame*, 132(3):451–462. 14, 15, 29, 30, 166

Sounasis, J. (Accessed 23 June 2013). World vehicle population tops 1 billion units. `http://wardsauto.com/ar/world_vehicle_population_110815`. 1

Stone, C. R. (1999). *Introduction to Internal Combustion Engines*. Palgrave Macmillan, New York, 3rd edition. x, 8, 9, 41

Tabaczynski, R. J. (1976). Turbulence and turbulent combustion in spark-ignition engines. *Progress in Energy and Combustion Science*, pages 143–165. 7, 10

Tennekes, H. and Lumley, J. L. (1972). *A First Course in Turbulence*. MIT, Cambridge, MA, 1st edition. 6, 11

Tornatore, C., Marchitto, L., Valentino, G., Esposito Corcione, F., and Merola, S. S. (2012). Optical diagnostics of the combustion process in a PFI SI boosted engine fueled with butanol–gasoline blend. *Energy*, 45(1):277–287. 42

Towers, D. and Towers, C. (2004). Cyclic variability measurements of in-cylinder engine flows using high-speed particle image velocimetry. *Measurement Science and Technology*, 15(9):1917. 67

Vagelopoulos, C. M. and Egolfopoulos, F. N. (1998). Direct experimental determination of laminar flame speeds. 27(1):513–519. 19

Veynante, D. and Vervisch, L. (2002). Turbulent combustion modeling. *Progress in energy and combustion science*, 28(3):193–266. 25, 26

Witze, P. O. (1980). A critical comparison of hot-wire anemometry and laser doppler velocimetry for IC engine applications. *Society of Automotive Engineers*, SAE Technical Paper 800132. 66

Worret, R., Bernhardt, S., Schwarz, F., and Spicher, U. (2002). Application of different cylinder pressure based knock detection methods in spark ignition engines. *Society of Automotive Engineers*, SAE Technical Paper 2002-01-1668. 182

Woschni, G. (1967). A universally applicable equation for the instantaneous heat transfer coefficient in the internal combustion engine. *Society of Automotive Engineers*, SAE Technical Paper 670931. 62

Wu, C.-H. (2006). *Turbulence and Combustion Studies in a Naturally Aspirated and Pressure Charged Spark Ignition Engine*. PhD thesis, Department of Mechanical Engineering, The University of Leeds. x, 48

Yoo, C. S., Luo, Z., Lu, T., Kim, H., and Chen, J. H. (2013). A DNS study of ignition characteristics of a lean iso-octane/air mixture under HCCI and SACI conditions. *Proceedings of the Combustion Institute*, 34(2):2985–2993. 119

Zahdeh, A., Rothenberger, P., Nguyen, W., Anbarasu, M., Schmuch-Solda, S., Schaefer, J., and T., G. (2011). Fundamental approach to investigate pre-ignition in boosted SI engines. *Society of Automotive Engineers*, SAE Technical Paper 2011-01-0340. 176

Zeldovich, Y. B. (1980). Regime classification of an exothermic reaction with nonuniform initial conditions. *Combustion and Flame*, 39(2):211–214. 34, 197

Zhao, H. and Ladommatos, N. (2001). *Engine combustion instrumentation and diagnostics*. Warrendale, PA: Society of Automotive Engineers, 2001. 842. 40, 77, 86

Ziegler, G., Zettlitz, A., Meinhardt, P., Herweg, R., Maly, R., and Pfister, W. (1988). Cycle-resolved two-dimensional flame visualization in a spark-ignition engine. *Society of Automotive Engineers*, SAE Technical Paper 881634. 40

Zimont, V. L. (1979). Theory of turbulent combustion on a homogeneous fuel mixture at high reynolds numbers. *Combustion, Explosions & Shockwaves*, 15:305–311. 157

Zur Loye, A. O. (1987). Two-dimensional visualization of premixed charge flame structure in an IC engine. *Society of Automotive Engineers*, SAE Technical Paper 870454. 41